UNIVERSITY OF
BIRMINGHAM

DISSOLUTION OF SPRAY-DRIED POROUS PARTICLES:

FROM SINGLE TO BULK

By

DIMITRIS KARAMPALIS

A thesis submitted to
the University of Birmingham
for the degree of
DOCTOR OF PHILOSOPHY

School of Chemical Engineering
College of Engineering and Physical Sciences
University of Birmingham

May 2018

ABSTRACT

This thesis demonstrates a detailed understanding and investigation of the dissolution behaviour of spray dried porous structured particles. This topic is crucially important for many industries as the control of the dissolution performance of the powders will allow them to modulate their essential properties.

The formulation of the slurry was linked to the physicochemical properties of the detergent particles via characterisation techniques. SEM and XRT results show that high slurry mix moisture (62%) results in mush less amount of undissolved Na_2SO_4 (0.6%) and high levels of porosity (82%) which has been confirmed by Mercury Porosimetry. On the other hand, the presence of binder in the formulation results in high bulk density, lower porosity and high degree of agglomeration.

Focusing on the effect of material components, dissolution conditions and particle structure on dissolution, a combination of experimental measurements and numerical simulation have been used. Novel dissolution methods have been developed for conducting single particle diffusion and convective dissolution. The single particle dissolution mechanisms have been visualised for the first time. Results indicate that under stagnant conditions the effects of binder and porosity on dissolution are dominant. Powder samples with high slurry mix moisture dissolve smoother, faster (up to 68%) and more controllable than the low slurry mix moisture samples. Silicate binder due to polymerisation slows down the dissolution while the presence of Citric Acid in the binder formulation is critical as it enhances disintegration and as a result dissolution.

However, in convective dissolution significant role play the hydrodynamic conditions. Single particle convective dissolution results indicate dissolution under laminar flow is up to 42% and up to 79% faster than diffusion for particles below 250 μm and 250-500

μm respectively. Numerical models developed to link single particle diffusion dissolution to bulk and to predict single particle convective dissolution using experimentally evaluated particle velocity. Results show good fitting for both conditions.

Bulk dissolution experiments on the chemical release of components demonstrate that Conductivity can be used as an accurate tool for the detection of chemical release of Na_2SO_4 while UV-Vis and $CatSO_3$ titration can measure the release of the anionic surfactant, linear alkyl benzene sulphonate (LAS). At the initial moments of dissolution, the release of Na_2SO_4 is blocked by either LAS or binder. A dissolution model found in the literature has been used to predict LAS (R^2=0.833 ± 0.18) and Na_2SO_4 (R^2=0.972 ± 0.01) release.

In general, the generated insights, and the assays developed in this study can be of critical importance for the industry on powder performance evaluation. Also, can be used in the development of a new formulation strategy to produce highly soluble, and fast releasing spray-dried powders.

ACKNOWLEDGMENTS

First, I am very grateful to my academic supervisors, Professor Serafim Bakalis and Professor Yulong Ding for providing me with this opportunity and for their consistent advice and support over the course of my PhD.

I would also like to express my gratitude to Dr. Hui Cao for her invaluable guidance, encouragement and mentorship throughout this project and for her inputs and corrections on this thesis.

I would like to acknowledge Procter & Gamble Ltd., Newcastle Innovation Centre and Department for Bussiness, Innovation and Skills United Kingdom for the research support via project CHARIOT. Special thanks to Mr. Joel Caragay from P&G for his help and guidance.

Finally, and most importantly, to my family, Vanta, Zenia and Angelos, goes out my sincerest thanks for their love, understanding and support, despite the geographical distance. And to Despoina, I want to say a big thank you for always being there for me, through your constant encouragement and support, and for making our time in Birmingham enjoyable.

" Πάντα κατ` αριθμόν γίγνονται "

Πυθαγόρας

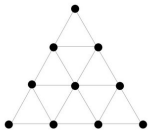

TABLE OF CONTENTS

ABSTRACT ..... **i**

ACKNOWLEDGMENTS ..... **iii**

TABLE OF CONTENTS ..... **iv**

LIST OF FIGURES ..... **ix**

LIST OF TABLES ..... **xxiii**

NOMENCLATURE ..... **xxvi**

CHAPTER 1 INTRODUCTION ..... **- 1 -**

1.1 Aims and Objectives ..... **- 4 -**

1.2 Structure of the Thesis ..... **- 5 -**

1.3 Publications and Conferences ..... **- 6 -**

1.3.1 Publications ..... - 6 -

1.3.2 Oral Presentations (Speaker Underlined) ..... - 7 -

CHAPTER 2 LITERATURE REVIEW ..... **- 8 -**

2.1 Dissolution principles ..... **- 9 -**

2.1.1 Dissolution theories ..... - 9 -

2.1.2 Diffusion coefficient ..... - 13 -

2.1.3 Dissolution rate ..... - 17 -

2.1.4 Convective mass transport ..... - 18 -

2.1.5 Numerical models ..... - 21 -

2.2 Parameters influencing dissolution in a liquid medium ..... **- 25 -**

2.2.1 Physicochemical Characteristics ..... - 25 -

2.2.2 Fluid Characteristics ..... - 34 -

2.3 Single particle dissolution ..... **- 38 -**

2.3.1 Single particle diffusion dissolution theory ..... - 40 -
2.3.2 Single particle diffusion dissolution experimental studies ..... - 43 -
2.3.3 Single particle diffusion dissolution simulation studies ..... - 47 -
2.3.4 Single particle convective dissolution theory ..... - 49 -
2.3.5 Single particle convective dissolution experimental studies ..... - 50 -
2.3.6 Single particle convective dissolution simulation studies ..... - 54 -
2.4 Bulk particle dissolution ..... - 57 -
2.4.1 Bulk particle dissolution theory ..... - 57 -
2.4.2 Bulk particle dissolution studies ..... - 60 -
2.4.3 Chemical release of bulk particles ingredients ..... - 62 -
2.5 Dissolution measurement techniques ..... - 65 -
2.5.1 Rotating basket method (USP Apparatus 1) ..... - 65 -
2.5.2 Paddle method (USP Apparatus 2) ..... - 65 -
2.5.3 Reciprocating cylinder apparatus (USP Apparatus 3) ..... - 67 -
2.5.4 Flow-through cell apparatus (USP Apparatus 4) ..... - 67 -
2.5.5 Other USP dissolution apparatus ..... - 68 -
2.5.6 Small-scale dissolution methods ..... - 68 -
2.5.7 The use of optical microscopy as a dissolution method ..... - 70 -
2.5.8 Image processing on single particle dissolution ..... - 71 -
2.5.9 Concluding Remarks ..... - 73 -
CHAPTER 3 MATERIALS AND CHARACTERISATION ..... - 74 -
3.1 Introduction ..... - 75 -
3.2 Materials ..... - 75 -
3.3 Fluid related properties ..... - 80 -
3.3.1 Density of the fluid ..... - 80 -
3.3.2 Viscosity of the fluid ..... - 80 -

3.4 Characterization of the samples ..... - 81 -

3.4.1 Solubility ..... - 81 -

3.4.2 Diffusivity ..... - 83 -

3.4.3 Particle Size Distribution (PSD) ..... - 84 -

3.4.4 Bulk Density & Porosity ..... - 86 -

3.4.5 Particle Density ..... - 89 -

3.4.6 Surface morphology ..... - 92 -

3.4.7 Microstructure analysis ..... - 97 -

3.5 Conclusions ..... - 111 -

CHAPTER 4 SINGLE PARTICLE DIFFUSION DISSOLUTION ..... - 113 -

4.1 Introduction ..... - 115 -

4.2 Materials and Methods ..... - 117 -

4.2.1 Materials ..... - 117 -

4.2.2 Diffusion dissolution experimental setup ..... - 118 -

4.2.3 Image Processing ..... - 119 -

4.3 Results and Discussion ..... - 119 -

4.3.1 Dissolution phenomena ..... - 119 -

4.3.2 Disintegration phenomenon ..... - 123 -

4.3.3 Effect of particle size and microstructure on dissolution times ..... - 126 -

4.3.4 Dissolution profiles ..... - 129 -

4.3.5 Effect of particle size on dissolution rate ..... - 132 -

4.3.6 Effect of particle size on dissolution rate constant ***k*** ..... - 135 -

4.3.7 From single particle dissolution to bulk dissolution ..... - 137 -

4.4 Conclusions ..... - 144 -

CHAPTER 5 SINGLE PARTICLE CONVECTIVE DISSOLUTION ..... - 147 -

5.1 Introduction ..... - 149 -

5.2 Materials and Methods ..... - 150 -

5.2.1 Materials ..... - 150 -

5.2.2 Convective dissolution experimental setup ..... - 151 -

5.2.3 Manufacturing protocol of the microfluidic device ..... - 153 -

5.2.4 Image Processing ..... - 153 -

5.2.5 Ghost Particle Velocimetry (GPV) ..... - 154 -

5.2.6 COMSOL simulation ..... - 155 -

5.3 Results and Discussion ..... - 156 -

5.3.1 Theoretical analysis of the system ..... - 156 -

5.3.2 Calibration of the microfluidic device ..... - 164 -

5.3.3 Dissolution phenomena ..... - 170 -

5.3.4 Effect of flow rate and temperature on dissolution times ..... - 172 -

5.3.5 Dissolution profiles ..... - 176 -

5.3.6 Effect of flow rate and temperature on dissolution rate ..... - 184 -

5.3.7 Effect of flow rate and temperature on dissolution rate constant $\boldsymbol{k}$ ..... - 199 -

5.3.8 Derivation of single particle dissolution equation ..... - 206 -

5.4 Conclusions ..... - 226 -

CHAPTER 6 INVESTIGATION OF Na_2SO_4 AND LAS DISSOLUTION FROM GRANULES ..... - 227 -

6.1 Introduction ..... - 229 -

6.2 Materials and Methods ..... - 230 -

6.2.1 Materials ..... - 230 -

6.2.2 Dissolution studies ..... - 230 -

6.2.3 Conductivity ..... - 231 -

6.2.4 UV-Vis Spectrophotometer ..... - 231 -

6.2.5 $CatSO_3$ titration ..... - 232 -

6.3 Results and Discussion ..... - 233 -

6.3.1 Chemical release of Na_2SO_4 ..... - 233 -

6.3.2 Chemical release of LAS ..... - 235 -

6.3.3 Dissolution rate of LAS and Na_2SO_4 ..... - 244 -

6.3.4 Model to predict dissolution of LAS and Na_2SO_4 ..... - 249 -

6.4 Conclusions ..... - 257 -

CHAPTER 7 OVERALL CONCLUSIONS AND FUTURE WORK ..... - 259 -

7.1 Overall conclusions ..... - 260 -

7.2 Future Work ..... - 262 -

BIBLIOGRAPHY ..... - 264 -

APPENDIX A ..... - 286 -

APPENDIX B ..... - 288 -

APPENDIX C ..... - 290 -

LIST OF FIGURES

Figure 2-1 Representation of the level of concentration difference for a continuous surface dissolution in the (a) diffusion layer model, (b) interfacial barrier model, and (c) Dankwert's model (C_s is saturated concentration, C_t is concentration of bulk at time t, h is diffusion layer thickness) [32]. ..... - 11 -

Figure 2-2 Polar and Non-Polar relationships in dissolution. ..... - 26 -

Figure 2-3 Influence of particle size on dissolution time [4]. ..... - 27 -

Figure 2-4 Zingg's categorisation of particle shape. ..... - 29 -

Figure 2-5 (a) Dissolution of sugar grain in an aqueous medium using optical method; (b) Simulation images of the dissolution process of the same sample [24]. ..... - 30 -

Figure 2-6 Comparison of dissolution profiles of crystalline and amorphous forms.- 33 -

Figure 2-7 Relationship of dissolution enthalpy and dissolution rate constant (k) for sucrose spherical particles [1]. ..... - 34 -

Figure 2-8 Effect of pH on the dissolution rate of humid acid particles [83]. ..... - 36 -

Figure 2-9 Dissolution of performance of ibuprofen tablets containing different acidic and basic additives using FTIR imaging data [85]. ..... - 36 -

Figure 2-10 Representation of convective diffusion equation for a rectangular surface [89]. ..... - 38 -

Figure 2-11 Schematic representation of dissolution stages of the agglomerated particle [8]. ..... - 40 -

Figure 2-12 Pseudo-steady state concentration gradient around a spherical particle (radius = r_p and x = the distance from the center of the particle) [11]. ..... - 42 -

Figure 2-13 Diffusion dissolution of sucrose crystal in sorbitol melt at 130dC using optical microscopy [21]. ..... - 44 -

Figure 2-14 Optical images of dissolution process of a sucrose sphere at different concentrations of polyethylene glycol (molecular weight 1000) solutions showing the moving boundaries as a function of time [1]. ..... - 45 -

Figure 2-15 Single particle diffusion dissolution of (a) skim milk powder and (b) freeze-dried skim milk powder in water at 30dC as a function of time [16]. ..... - 45 -

Figure 2-16 Evaluation of diameter of dissolving sodium carbonate granule as a function of time [95]..... - 46 -

Figure 2-17 Illustration of the simulation of diffusion-limited dissolution of a virtual granule [102]. ..... - 48 -

Figure 2-18 (a) Optical images of a dissolving particle cluster of sodium mono glutamate crystals and brown sugar particles in water; (b) simulated dissolution procedure of the cluster [24]. ..... - 49 -

Figure 2-19 Dissolution plot of phosphate rock crystal under equal time intervals [105].. ..... - 51 -

Figure 2-20 (a) Schematic representation of the single sodium caseinate particles convective dissolution experimental setup; (b) the relationship between mean particle dissolution rate and fluid velocity [17]. ..... - 52 -

Figure 2-21 Schematic overview of the modified Einstein's teacup method developed by Svanbäck et al., [18]..... - 53 -

Figure 2-22 Schematic representation of the three main disintegration mechanisms in single particle dissolution (a) leaching, (b) surface erosion and (c) break-up, followed by a change in particle size distribution [107]. ..... - 53 -

Figure 2-23 Dissolution of a virtual particle. (a) Streamlines presenting the velocity profile around a partially dissolved particle; (b) Concentration profile of a main compound around a partially dissolved particle [77]. ..... - 55 -

Figure 2-24 Simulation dissolution profiles of (a) standalone component particles and their agglomerate under diffusion-only conditions and (b) components of the same agglomerate under flow conditions [23]. ..... - 56 -

Figure 2-25 Structure of the model for linking energy input of the mixing system with the dissolution of particles [27]. ..... - 57 -

Figure 2-26 NIR images for the distribution of (a) ionised HCl salt form, (b) water and (c) free based on a pharmaceutical tablet dissolution [134]. ..... - 64 -

Figure 2-27 Dissolution of multi-compound pharmaceutical formulation using three different spectroscopic imaging methods. (a) MRI images of the interface of the tablet, (b) ATR-FTIR images and (c) Raman maps of the crystalline compound [134]. ..... - 64 -

Figure 2-28 Schematic representation of (a) Rotating basket method (USP Apparatus 1); (b) Paddle method (USP Apparatus 2). ..... - 66 -

Figure 2-29 6+6 position vessel dissolution tergotometer [138]. ..... - 66 -

Figure 2-30 Schematic representation of reciprocating cylinder apparatus (USP Apparatus 3) [140]. ..... - 67 -

Figure 2-31 Schematic representation of flow through cell apparatus (USP Apparatus 4) [141]. ..... - 68 -

Figure 2-32 Schematic representation of a “mini-paddle” apparatus. ..... - 69 -

Figure 3-1 The transition from the Today’s Blown Powder to the Future Simple Blown Powder..... - 77 -

Figure 3-2 Solubility test of (a) Sample1, (b) Sample2, (c) Sample3, (d) Sample4 and (e) Sample5 at different temperatures in 100 mL of water..... - 82 -

Figure 3-3 Comparison of solubilities of the five samples at 20dC, 40dC and 60dC. ..... ……- 83 -

Figure 3-4 Diffusivity D of the spray dried powder samples at 20dC, 40dC and 60dC. ..... ….- 83 -

Figure 3-5 Schematic representation of dynamic image analysis optical setup for the measurement of particle size distribution [156]..... - 84 -

Figure 3-6 Characterisation of the particle size distribution for all the spray dried powder samples utilised in this study..... - 85 -

Figure 3-7 Cross section of a penetrometer (up) filled with mercury (down) which pressure has forced some mercury into the pores of the powder and almost 50% of the stem capacity has been used..... - 88 -

Figure 3-8 Schematic representation of a gas pycnometer [160]..... - 90 -

Figure 3-9 Absolute density $\rho_{absolute}$ as a function of porosity..... - 91 -

Figure 3-10 Particle envelope density $\rho_{envelope}$ as a function of porosity. ..... - 92 -

Figure 3-11 SEM images of the bulk, at low and high magnification, and each size fraction for the five detergent powder samples. The green line represents characteristic holes, while the red line shows typical agglomerates. ..... - 94 -

Figure 3-12 EDX analysis of singles particles for each powder sample..... - 96 -

Figure 3-13 Schematic representation of XRT scanning instrument [163]. ..... - 97 -

Figure 3-14 Sample holder for XRT scan using 0.3 g of each powder sample. ..... - 98 -

Figure 3-15 Sample holder for XRT scan using a single particle of each size fraction of every powder sample..... - 98 -

Figure 3-16 XRT scanning area of bulk particles (red line presents one cross-section). ..... …- 101 -

Figure 3-17 XRT images of Sample1 (a) to (d), Sample2 (e) to (i), Sample3 (j) to (m), Sample4 (n) to (q) and Sample5 (r) to (u). (a) is cross-section of bulk particles at one position, (b) (c) (d) are cross sections of the particle dash circled in (a). Same as (e) to (i), (j) to (m), (n) to (q) and (r) to (u). ..... - 103 -

Figure 3-18 (a) Pore size distribution by volume (%) and (b) Crystal size distribution by volume (%) based on XRT 3D analysis of bulk. ..... - 106 -

Figure 3-19 XRT images of different sized individual granules of (a) Sample1, (b) Sample2, (c) Sample3, (d) Sample4 and (e) Sample5. ..... - 109 -

Figure 3-20 Pore size distribution by volume (%) based on XRT 3D analysis of (a) below 250 μm, (b) 250 to 500 μm, (c) 500 to 710 μm and (d) 710 μm to 1 mm single particles. ..... .- 110 -

Figure 3-21 Crystal size distribution by volume (%) based on XRT 3D analysis of (a) below 250 μm, (b) 250 to 500 μm, (c) 500 to 710 μm and (d) 710 μm to 1 mm single particles. ..... - 111 -

Figure 4-1 Schematic of single particle diffusion dissolution experimental setup. - 118 -

Figure 4-2 Overview of the dissolution stages (first line: raw images; second line: images after image processing). ..... - 120 -

Figure 4-3 Different dissolution behavior: the first and second line represent the dissolution of single and multiple particles without binder respectively; the third and fourth line show the dissolution of single and multiple particles with Silicate binder respectively; and the fifth and sixth line present the dissolution of single and multiple particles with mix binder (Citric Acid + $MgSO_4$ + Zeolite). ..... - 123 -

Figure 4-4 Typical different dissolution phenomena summarized in image sequences of which particles dissolve in water at 20dC: first row A~E represent a granule dissolves in water and disintegration happens at 3 s, second row I~V particle dissolves and disintegration happens at 1.4 s, third row (1)~(5) represents particle dissolution and disintegration happens at 2.2 s, fourth row (a)~(d) are granule dissolving and no disintegration happens, fifth row (i)~(v) particle swells (not significantly) instead of disintegrates, and last row ①~④ particle dissolving and no disintegration happens. ..... ……- 125 -

Figure 4-5 Flowchart of single spray dried particle diffusion dissolution phenomena…… ..... - 126 -

Figure 4-6 (a) Total dissolution time t_f (s) versus particle size (μm) of the samples for each size fraction, (b) the ratio between the early stage disintegration time t_b and t_f (t_b/t_f) versus powder porosity (%), (c) the ratio between the later stage disintegration time t_d and t_f (t_d/t_f) versus powder porosity (%). ..... - 129 -

Figure 4-7 Dissolution profiles based on surface area (mm^2) versus time (s) for (a) below 250 μm, (b) 250-500 μm, (c) 500-710 μm and (d) 710 μm-1 mm. ..... - 131 -

Figure 4-8 Dissolution rate dW/dt (μg/s) per mm^2 versus time (s) for (a) below 250 μm, (b) 250-500 μm, (c) 500-710 μm and (d) 710 μm-1 mm. The dissolution rate dW/dt (kg/s) versus time (s) is embedded in each graph. ..... - 134 -

Figure 4-9 Surface specific dissolution rate G (μg/smm^2) versus time (s) for (a) below 250 μm, (b) 250-500 μm, (c) 500-710 μm and (d) 710 μm-1 mm. ..... - 135 -

Figure 4-10 Dissolution rate constant k (m/s) versus time (s) for (a) below 250 μm, (b) 250-500 μm, (c) 500-710 μm and (d) 710 μm-1 mm. ..... - 137 -

Figure 4-11 Comparison of dissolution profiles of 1g of (a) Sample1, (b) Sample2, (c) Sample3, (d) Sample4 and (e) Sample5 using Equation (4-11) with conductivity data. ..... - 143 -

Figure 4-12 Comparison of Monte Carlo analysis single to bulk approach for (a) Sample1, (b) Sample2, (c) Sample3 and (d) Sample4 with conductivity data. ..... - 144 -

Figure 5-1 Schematic of single particle convective dissolution experimental setup. ..... - 152 -

Figure 5-2 (a)Diagram and (b)Top view of the microfluidic device used in experiments. ..... - 153 -

Figure 5-3 The aluminium mould of the microfluidic device. ..... - 153 -

Figure 5-4 GPV experimental setup. ..... - 155 -

Figure 5-5 The geometry of the model (a) without and (b) with the sphere. ..... - 156 -

Figure 5-6 Linear relationship between flow rate Q (µL/s) and velocity of water u_{water} (mm/s). ..... - 157 -

Figure 5-7 (a) Reynolds number Re and (b) Length to fully developed velocity profile, l_e (mm) as a function of flow rate Q (µL/s). ..... - 158 -

Figure 5-8 Friction factor f_D as a function of Re. ..... - 159 -

Figure 5-9 Pressure drop across the channel $\Delta P/L$ (Pa/m) as a function of (a) flow rate Q (µL/s) and (b) dynamic viscosity of the water μ_{water} (kg/m*s). ..... - 160 -

Figure 5-10 Reynolds of the particle Re_p as a function of flow rate Q (µL/s) for (a) d_p=200 µm, (b) d_p=300 µm, (c) d_p=400 µm and (d) d_p=500 µm. ..... - 161 -

Figure 5-11 Drag coefficient C_D as a function of flow rate Q (µL/s) for (a) (a) d_p=200 µm, (b) d_p=300 µm, (c) d_p=400 µm and (d) d_p=500 µm. ..... - 163 -

Figure 5-12 Total drag force on the sphere F_D (μN) as a function of flow rate Q (μL/s) for (a) (a) d_p=200 μm, (b) d_p=300 μm, (c) d_p=400 μm and (d) d_p=500 μm. ..... - 164 -

Figure 5-13 (a) Bright field image of 200 nm polystyrene particles (concentration 0.2% by weight) dispersed in deionised water flowing through a microchannel (c) containing a 250 μm glass bead and (e) containing a 500 μm glass bead. (b), (d) and (f) Speckle patterns of the bright field images (a), (c) and (e) respectively obtained by subtraction of the median image. Scale bars are 200 μm. ..... - 165 -

Figure 5-14 Comparison of the flow velocity field within a microchannel obtained experimentally (left column) via GPV and (right column) via COMSOL simulations for flow rate 1 μL/s for three different conditions (a) (b) empty channel, (c) (d) 250 μm and (e) (f) 500 μm. ..... - 167 -

Figure 5-15 Comparison of the experimental and simulation flow velocity results for a line crossing the middle of the empty channel for a flow rate of (a) 0.2 μL/s, (b) 0.4 μL/s, (c) 0.6 μL/s, (d) 0.8 μL/s and (e) 1 μL/s. ..... - 168 -

Figure 5-16 Comparison of the experimental and simulation flow velocity results for a line crossing the middle of a channel with a 250 μm glass bead for a flow rate of (a) 0.2 μL/s, (b) 0.4 μL/s, (c) 0.6 μL/s, (d) 0.8 μL/s and (e) 1 μL/s. ..... - 169 -

Figure 5-17 Comparison of the experimental and simulation flow velocity results for a line crossing the middle of a channel with a 500 μm glass bead for a flow rate of (a) 0.2 μL/s, (b) 0.4 μL/s, (c) 0.6 μL/s, (d) 0.8 μL/s and (e) 1 μL/s. ..... - 170 -

Figure 5-18 Overview of the convective dissolution stages. Each row represents the convective dissolution of a characteristic particle of each sample at a certain flow rate, from 0.2 μL/s to 1 μL/s at 20dC water temperature. ..... - 172 -

Figure 5-19 (a), (c), (e) Total dissolution time t_f (s) versus flow rate Q (μL/s) of the samples for particle size below 250 μm at 20dC, 40dC and 60dC respectively; (b), (d), (f) The ratio between the later stage disintegration time t_d and t_f (t_d/t_f) versus flow rate Q (μL/s) for particle size below 250 μm at 20dC, 40dC and 60dC respectively. ..... - 175 -

Figure 5-20 (a), (c), (e) Total dissolution time t_f (s) versus flow rate Q (μL/s) of the samples for particle size 250-500 μm at 20dC, 40dC and 60dC respectively; (b), (d), (f) The ratio between the later stage disintegration time t_d and t_f (t_d/t_f) versus flow rate Q (μL/s) for particle size 250-500 μm at 20dC, 40dC and 60dC respectively. ..... - 176 -

Figure 5-21 Dissolution profiles based on surface area (mm^2) versus time (s) of particle size below 250 μm for (a) 0.2 μL/s, (b) 0.4 μL/s, (c) 0.6 μL/s, (d) 0.8 μL/s and (e) 1 μL/s at 20dC. ..... - 179 -

Figure 5-22 Dissolution profiles based on surface area (mm^2) versus time (s) of particle size below 250 μm for ((a) 0.2 μL/s, (b) 0.4 μL/s, (c) 0.6 μL/s, (d) 0.8 μL/s and (e) 1 μL/s at 40dC. ..... - 180 -

Figure 5-23 Dissolution profiles based on surface area (mm^2) versus time (s) of particle size below 250 μm for (a) 0.2 μL/s, (b) 0.4 μL/s, (c) 0.6 μL/s, (d) 0.8 μL/s and (e) 1 μL/s at 60dC. ..... - 181 -

Figure 5-24 Dissolution profiles based on surface area (mm^2) versus time (s) of particle size 250-500 μm for (a) 0.2 μL/s, (b) 0.4 μL/s, (c) 0.6 μL/s, (d) 0.8 μL/s and (e) 1 μL/s at 20dC. ..... - 182 -

Figure 5-25 Dissolution profiles based on surface area (mm^2) versus time (s) of particle size 250-500 μm for (a) 0.2 μL/s, (b) 0.4 μL/s, (c) 0.6 μL/s, (d) 0.8 μL/s and (e) 1 μL/s at 40dC. ..... - 183 -

Figure 5-26 Dissolution profiles based on surface area (mm^2) versus time (s) of particle size 250-500 μm for (a) 0.2 μL/s, (b) 0.4 μL/s, (c) 0.6 μL/s, (d) 0.8 μL/s and (e) 1 μL/s at 60dC. ..... - 184 -

Figure 5-27 Dissolution rate dW/dt (μg/s) per mm^2 versus time (s) of particle size below 250 μm for (a) 0.2 μL/s, (b) 0.4 μL/s, (c) 0.6 μL/s, (d) 0.8 μL/s and (e) 1 μL/s at 20dC. The dissolution rate dW/dt (kg/s) versus time (s) is embedded in each graph. ..... - 187 -

Figure 5-28 Dissolution rate dW/dt (μg/s) per mm^2 versus time (s) of particle size below 250 μm for (a) 0.2 μL/s, (b) 0.4 μL/s, (c) 0.6 μL/s, (d) 0.8 μL/s and (e) 1 μL/s at 40dC. The dissolution rate dW/dt (kg/s) versus time (s) is embedded in each graph. ..... - 188 -

Figure 5-29 Dissolution rate dW/dt (μg/s) per mm^2 versus time (s) of particle size below 250 μm for (a) 0.2 μL/s, (b) 0.4 μL/s, (c) 0.6 μL/s, (d) 0.8 μL/s and (e) 1 μL/s at 60dC. The dissolution rate dW/dt (kg/s) versus time (s) is embedded in each graph. ..... - 189 -

Figure 5-30 Dissolution rate dW/dt (μg/s) per mm^2 versus time (s) of particle size 250-500 μm for (a) 0.2 μL/s, (b) 0.4 μL/s, (c) 0.6 μL/s, (d) 0.8 μL/s and (e) 1 μL/s at 20dC. The dissolution rate dW/dt (kg/s) versus time (s) is embedded in each graph. ..... - 190 -

Figure 5-31 Dissolution rate dW/dt (μg/s) per mm^2 versus time (s) of particle size 250-500 μm for (a) 0.2 μL/s, (b) 0.4 μL/s, (c) 0.6 μL/s, (d) 0.8 μL/s and (e) 1 μL/s at 40dC. The dissolution rate dW/dt (kg/s) versus time (s) is embedded in each graph. ..... - 191 -

Figure 5-32 Dissolution rate dW/dt (μg/s) per mm^2 versus time (s) of particle size 250-500 μm for (a) 0.2 μL/s, (b) 0.4 μL/s, (c) 0.6 μL/s, (d) 0.8 μL/s and (e) 1 μL/s at 60dC. The dissolution rate dW/dt (kg/s) versus time (s) is embedded in each graph. ..... - 192 -

Figure 5-33 Surface specific dissolution rate G (μg/smm^2) versus time (s) of particle size below 250 μm for (a) 0.2 μL/s, (b) 0.4 μL/s, (c) 0.6 μL/s, (d) 0.8 μL/s and (e) 1 μL/s at 20dC. ..... - 194 -

Figure 5-34 Surface specific dissolution rate G (μg/smm^2) versus time (s) of particle size below 250 μm for (a) 0.2 μL/s, (b) 0.4 μL/s, (c) 0.6 μL/s, (d) 0.8 μL/s and (e) 1 μL/s at 40dC. ..... - 195 -

Figure 5-35 Surface specific dissolution rate G (μg/smm^2) versus time (s) of particle size below 250 μm for (a) 0.2 μL/s, (b) 0.4 μL/s, (c) 0.6 μL/s, (d) 0.8 μL/s and (e) 1 μL/s at 60dC. ..... - 196 -

Figure 5-36 Surface specific dissolution rate G (μg/smm^2) versus time (s) of particle size 250-500 μm for (a) 0.2 μL/s, (b) 0.4 μL/s, (c) 0.6 μL/s, (d) 0.8 μL/s and (e) 1 μL/s at 20dC. ..... - 197 -

Figure 5-37 Surface specific dissolution rate G (μg/smm^2) versus time (s) of particle size 250-500 μm for (a) 0.2 μL/s, (b) 0.4 μL/s, (c) 0.6 μL/s, (d) 0.8 μL/s and (e) 1 μL/s at 40dC. ..... - 198 -

Figure 5-38 Surface specific dissolution rate G (μg/smm^2) versus time (s) of particle size 250-500 μm for (a) 0.2 μL/s, (b) 0.4 μL/s, (c) 0.6 μL/s, (d) 0.8 μL/s and (e) 1 μL/s at 60dC. ..... - 199 -

Figure 5-39 Dissolution rate constant k (m/s) versus time (s) of particle size below 250 μm for (a) 0.2 μL/s, (b) 0.4 μL/s, (c) 0.6 μL/s, (d) 0.8 μL/s and (e) 1 μL/s at 20dC.- 201 -

Figure 5-40 Dissolution rate constant k (m/s) versus time (s) of particle size below 250 μm for (a) 0.2 μL/s, (b) 0.4 μL/s, (c) 0.6 μL/s, (d) 0.8 μL/s and (e) 1 μL/s at 40dC.- 202 -

Figure 5-41 Dissolution rate constant k (m/s) versus time (s) of particle size below 250 μm for (a) 0.2 μL/s, (b) 0.4 μL/s, (c) 0.6 μL/s, (d) 0.8 μL/s and (e) 1 μL/s at 60dC.- 203 -

Figure 5-42 Dissolution rate constant k (m/s) versus time (s) of particle size 250-500 μm for (a) 0.2 μL/s, (b) 0.4 μL/s, (c) 0.6 μL/s, (d) 0.8 μL/s and (e) 1 μL/s at 20dC..... - 204 -

Figure 5-43 Dissolution rate constant k (m/s) versus time (s) of particle size 250-500 μm for (a) 0.2 μL/s, (b) 0.4 μL/s, (c) 0.6 μL/s, (d) 0.8 μL/s and (e) 1 μL/s at 40dC..... - 205 -

Figure 5-44 Dissolution rate constant k (m/s) versus time (s) of particle size 250-500 μm for (a) 0.2 μL/s, (b) 0.4 μL/s, (c) 0.6 μL/s, (d) 0.8 μL/s and (e) 1 μL/s at 60dC..... - 206 -

Figure 5-45 Sherwood number Sh as a function of Reynolds number of the particle Re_p of each powder sample. Left column represents particle size below 250 μm, while right column represents particle size 250 to 500 μm. ..... - 213 -

Figure 5-46 Below 250 μm dissolution profiles of experiment data vs modelling for (a) 0.2 μL/s, (b) 0.4 μL/s, (c) 0.6 μL/s, (d) 0.8 μL/s and 1 μL/s at 20dC for each powder sample. ..... - 214 -

Figure 5-47 Below 250 μm dissolution profiles of experiment data vs modelling for (a) 0.2 μL/s, (b) 0.4 μL/s, (c) 0.6 μL/s, (d) 0.8 μL/s and 1 μL/s at 40dC for each powder sample. ..... - 215 -

Figure 5-48 Below 250 μm dissolution profiles of experiment data vs modelling for (a) 0.2 μL/s, (b) 0.4 μL/s, (c) 0.6 μL/s, (d) 0.8 μL/s and 1 μL/s at 60dC for each powder sample. ..... - 216 -

Figure 5-49 250-500 μm dissolution profiles of experiment data vs modelling for (a) 0.2 μL/s, (b) 0.4 μL/s, (c) 0.6 μL/s, (d) 0.8 μL/s and 1 μL/s at 20dC for each powder sample. ..... - 217 -

Figure 5-50 250-500 μm dissolution profiles of experiment data vs modelling for (a) 0.2 μL/s, (b) 0.4 μL/s, (c) 0.6 μL/s, (d) 0.8 μL/s and 1 μL/s at 40dC for each powder sample. ..... - 218 -

Figure 5-51 250-500 μm dissolution profiles of experiment data vs modelling for (a) 0.2 μL/s, (b) 0.4 μL/s, (c) 0.6 μL/s, (d) 0.8 μL/s and 1 μL/s at 60dC for each powder sample. ..... - 219 -

Figure 6-1 (a) Experimental setup of $CatSO_3$ titration, (b) Two phases of solution before titration, yellow: soluble Dichloromethane and pink: anionic surfactant cationic dye complex. ..... - 233 -

Figure 6-2 Calibration of Conductivity of LAS and Na_2SO_4. ..... - 233 -

Figure 6-3 Conductivity dissolution profiles of powder samples at (a) 20dC 100rpm, (b) 20dC 200rpm and (c) 40dC 100rpm. ..... - 235 -

Figure 6-4 (a) UV-Vis absorption spectra of LAS; (b)UV-Vis absorbance at 225 nm versus LAS concentration (ppm). ..... - 236 -

Figure 6-5 Comparison of chemical release of Na_2SO_4 (conductivity) and LAS (UV-Vis) for (a) Sample1, (b) Sample2, (c) Sample3, (d) Sample4 and (e) Sample5 at 20dC 100 rpm. ..... - 238 -

Figure 6-6 Comparison of chemical release of Na_2SO_4 (conductivity) and LAS (UV-Vis) for (a) Sample1, (b) Sample2, (c) Sample3, (d) Sample4 and (e) Sample5 at 20dC 200 rpm. ..... - 239 -

Figure 6-7 Comparison of chemical release of Na_2SO_4 (conductivity) and LAS (UV-Vis) for (a) Sample1, (b) Sample2, (c) Sample3, (d) Sample4 and (e) Sample5 at 40dC 100 rpm. ..... - 240 -

Figure 6-8 Comparison of chemical release of Na_2SO_4 (conductivity) and LAS (UV-Vis and $CatSO_3$ titration) for (a) Sample1, (b) Sample2, (c) Sample3, (d) Sample4 and (e) Sample5 at 20dC 100 rpm. ..... - 242 -

Figure 6-9 Comparison of chemical release of Na_2SO_4 (conductivity) and LAS (UV-Vis and $CatSO_3$ titration) for (a) Sample1, (b) Sample2, (c) Sample3, (d) Sample4 and (e) Sample5 at 20dC 200 rpm. ..... - 243 -

Figure 6-10 Comparison of chemical release of Na_2SO_4 (conductivity) and LAS (UV-Vis and $CatSO_3$ titration) for (a) Sample1, (b) Sample2, (c) Sample3, (d) Sample4 and (e) Sample5 at 40dC 100 rpm. ..... - 244 -

Figure 6-11 Comparison of dW/dt (kg/s) of Na_2SO_4 (conductivity) and LAS (UV-Vis and $CatSO_3$ titration) for (a) Sample1, (b) Sample2, (c) Sample3, (d) Sample4 and (e) Sample5 at 20dC 100 rpm. ..... - 247 -

Figure 6-12 Comparison of dW/dt (kg/s) of Na_2SO_4 (conductivity) and LAS (UV-Vis and $CatSO_3$ titration) for (a) Sample1, (b) Sample2, (c) Sample3, (d) Sample4 and (e) Sample5 at 20dC 200 rpm. ..... - 248 -

Figure 6-13 Comparison of dW/dt (kg/s) of Na_2SO_4 (conductivity) and LAS (UV-Vis and $CatSO_3$ titration) for (a) Sample1, (b) Sample2, (c) Sample3, (d) Sample4 and (e) Sample5 at 40dC 100 rpm. ..... - 249 -

Figure 6-14 Dissolution profiles of experiment data vs modelling of Na_2SO_4 and LAS for (a) Sample1, (b) Sample2, (c) Sample3, (d) Sample4 and (e) Sample5 at 20dC 100 rpm. ..... - 255 -

Figure 6-15 Dissolution profiles of experiment data vs modelling of Na_2SO_4 and LAS for (a) Sample1, (b) Sample2, (c) Sample3, (d) Sample4 and (e) Sample5 at 20dC 200 rpm. ..... - 256 -

Figure 6-16 Dissolution profiles of experiment data vs modelling of Na_2SO_4 and LAS for (a) Sample1, (b) Sample2, (c) Sample3, (d) Sample4 and (e) Sample5 at 40dC 100 rpm. ..... - 257 -

LIST OF TABLES

Table 2.1 Summary of characteristic ionic conductance's at infinite dilution in water at 25°C [41], [42]. ..... - 16 -

Table 2.2 Summary of numerical dissolution expressions. ..... - 24 -

Table 3.1 Batch codes of the five spray dried powder samples provided by Procter and Gamble, Newcastle Innovation Centre. ..... - 78 -

Table 3.2 Overview of the chemical composition of the spray dried detergent powder samples. ..... - 79 -

Table 3.3 Density of D. I. water ρ_{water} (kg/m^3) at 20dC, 40dC and 60dC. ..... - 80 -

Table 3.4 Dynamic viscosity of D.I water μ_{water} (kg/sm) and kinematic viscosity of water v_{water} (m^2/s) at 20dC, 40dC and 60dC. ..... - 80 -

Table 3.5 Main parameters of particle size distribution of the samples. ..... - 86 -

Table 3.6 Initial bulk density ρ_b (kg/m^3) and porosity ε_b (%) for the five powder samples. ..... - 89 -

Table 3.7 XRT settings of the bulk and the individual granule. ..... - 99 -

Table 3.8 The effect of slurry water concentration on undissolved Na_2SO_4 (%) and porosity (%) results evaluated from XRT 3D analysis of bulk. ..... - 105 -

Table 4.1 Experimental conditions of Low and High concentration (ppm) of bulk dissolution testing for each powder sample. ..... - 139 -

Table 5.1 Average velocity of the particle u_p of for each flow rate, temperature and size fraction of Sample1. ..... - 209 -

Table 5.2 Average velocity of the particle u_p of for each flow rate, temperature and size fraction of Sample2. ..... - 210 -

Table 5.3 Average velocity of the particle u_p of for each flow rate, temperature and size fraction of Sample3. ..... - 210 -

Table 5.4 Average velocity of the particle u_p of for each flow rate, temperature and size fraction of Sample4. ..... - 211 -

Table 5.5 Average velocity of the particle u_p of for each flow rate, temperature and size fraction of Sample5. ..... - 211 -

Table 5.6 Comparison of diffusivity from Figure 3-4 and experiment fitting results D_{fit} at different temperatures for Sample1 below 250 μm. The R^2 for each experimental condition is also presented. ..... - 221 -

Table 5.7 Comparison of diffusivity from Figure 3-4 and experiment fitting results D_{fit} at different temperatures for Sample1 250-500 μm. The R^2 for each experimental condition is also presented. ..... - 221 -

Table 5.8 Comparison of diffusivity from Figure 3-4 and experiment fitting results D_{fit} at different temperatures for Sample2 below 250 μm. The R^2 for each experimental condition is also presented. ..... - 222 -

Table 5.9 Comparison of diffusivity from Figure 3-4 and experiment fitting results D_{fit} at different temperatures for Sample2 250-500 μm. The R^2 for each experimental condition is also presented. ..... - 222 -

Table 5.10 Comparison of diffusivity from Figure 3-4 and experiment fitting results D_{fit} at different temperatures for Sample3 below 250 μm. The R^2 for each experimental condition is also presented. ..... - 223 -

Table 5.11 Comparison of diffusivity from Figure 3-4 and experiment fitting results D_{fit} at different temperatures for Sample3 250-500 μm. The R^2 for each experimental condition is also presented. ..... - 223 -

Table 5.12 Comparison of diffusivity from Figure 3-4 and experiment fitting results D_{fit} at different temperatures for Sample4 below 250 μm. The R^2 for each experimental condition is also presented. ..... - 224 -

Table 5.13 Comparison of diffusivity from Figure 3-4 and experiment fitting results D_{fit} at different temperatures for Sample4 250-500 μm. The R^2 for each experimental condition is also presented. ..... - 224 -

Table 5.14 Comparison of diffusivity from Figure 3-4 and experiment fitting results D_{fit} at different temperatures for Sample5 below 250 μm. The R^2 for each experimental condition is also presented. ..... - 225 -

Table 5.15 Comparison of diffusivity from Figure 3-4 and experiment fitting results D_{fit} at different temperatures for Sample5 250-500 μm. The R^2 for each experimental condition is also presented. ..... - 225 -

Table 6.1 g of LAS and Na_2SO_4 in bulk dissolution testing. ..... - 245 -

Table 6.2 Values of determination coefficient R^2 from measurement data of the ingredients of each powder sample for dissolution models at 20dC 100rpm. ..... - 251 -

Table 6.3 Power input P (W) and turbulent energy dissipation rate ε (W/kg) in mixing tank with 800 mL of water [27]. ..... - 252 -

Table 6.4 Bulk density ρ_b (kg/m^3) and solubility C_s (kg/m^3) of LAS and Na_2SO_4 (values provided by P&G). ..... - 253 -

Table 6.5 Comparison of diffusivity obtained from Nernst equation (2-10) and Table 2.1 and experiment fitting results D_{fit} at 20dC 100rpm, 200rpm and 40dC 100rpm for LAS and Na_2SO_4 each powder sample. The R^2 is also presented. ..... - 254 -

NOMENCLATURE

Latin Characters

A exposed surface area of solid, m^2

$A_{channel}$ cross-sectional area of the channel, m^2

Al amount of aliquot, m^3

A_p surface area of particle, m^2

$A_{p,t}$ projected surface area of particle at time t, m^2

$A_{particles}$ surface area of particles, m^2

$A_{particles,size}$ area of particles of each particle size category of the distribution, m^2

A_t exposed surface area at time t, m^2

A_v volume specific surface, m^2

A_0 initial surface area of the granule, m^2

C scalar concentration, kg/m^3

C_b initial concentration of the bulk solution, kg/m^3

C_D drag coefficient

C_p initial concentration of the particle, kg/m^3

$C_{p,t}$ concentration of the particle at time t, kg/m^3

C_s saturated concentration, kg/m^3

$C_{s,h=0}$ solubility under sink conditions as diffusion layer thickness h reaches zero, kg/m^3

C_0 initial concentration of solid in the solution, kg/m^3

C_t concentration of bulk at time t, kg/m^3

D diffusivity/diffusion coefficient, m^2/s

D_{AB} diffusion coefficient of dilute solutions, m^2/s

D_{AB}^{o} diffusion coefficient at infinite dilution, m^2/s

D_{fit} diffusivity from fitting results, m^2/s

D_H hydraulic diameter of the pipe, m

F_c Faraday constant

F_D total drag force on the sphere, N

G surface specific dissolution rate, kg/sm^2

H height, m

K, $K_{1/3}$, $K_{1/2}$, $K_{2/3}$ dissolution rate constant, m/s

K_T equilibrium constant at temperature T

K_{T_0} equilibrium constant at absolute temperature T_0

K_0 zero-order release constant, mol/m^3s

K_1 new equivalent constant, m/s

L length, m

L_T length of the tablet, in the direction of flow, m

M mobility, m^2/Vs

M_B molecular weight of solvent, kg/mol

Mwt analyte molecular weight, kg/mol

N agitation speed, rpm

$N_{particles}$ number of particles

N_t titrant normality, mol/m^3

P power input, W

P_{wet} wetted perimeter of the cross-section, m

Q flow rate, m^3/s

R ideal gas constant, J/Kmol

Re Reynolds number

Re_p Reynolds number of the particle

Sc Schmidt number

Sh Sherwood number

T absolute temperature, K

T_i titration reading, m^3

T_t lag time before the progression of dissolution, s

V volume of the liquid medium, m^3

V_A solute molar volume, mol/m^3

$V_{container}$ volume of container, m^3

V_p, $V_{particle}$ volume of the particle, m^3

V_{pore} volume of pores, m^3

W width, m

$W_{avgsize(<250\mu m)}$ mass of the average size for particles of size fraction below 250 μm, kg

$W_{avgsize(710\mu m-1mm)}$ mass of the average size for particles of size fraction 710 μm – 1 mm, kg

$W_{b,0}$ initial weight of bulk particles, kg

$W_{b,t}$ weight of bulk particles at time t, kg

W_{bulk} weight of the bulk particles, kg

$W_{bulk,t}$ weight of the bulk particles at time t, kg

W_i weight of ingredient, kg

$W_{i,t}$ weight of ingredient at time t, kg

W_p, $W_{p,0}$ particle weight, kg

$W_{p,t}$ weight of the particle at time t, kg

W_{powder} mass of the powder, kg

$W_{sizefraction}$ the weight that lies on each particle size category of the distribution, kg

W_t amount of solid dissolved in time t, kg

W_τ undissolved weight, kg

W_0 initial amount of solid in the solution, kg

W_∞ total amount of solid dissolve in the solution, kg

Z_+ cation valence

Z_- anion valence

a constant

a_0 initial radius for a sphere or cylinder or the half-thickness for a slab, m

b constant

b_w width of the tablet, m

$d_{impeller}$ diameter of the impeller, m

d_p diameter of the particle, m

$d_{p,t}$ diameter of the particle at time t, m

d_{psv} is the size of a spherical granule that, if the bulk contained only of this kind of particles, would have equivalent effective surface area as the original sample, m

d_{tank} diameter of the tank, m

dW/dt dissolution rate, kg/s

f_D Darcy's friction factor for laminar flow

h diffusion layer thickness, m

k dissolution rate constant, m/s

k_B Boltzmann's constant, J/K

k_0 erosion rate constant, mol/m^{3}s

k' constant

l_e length to fully developed velocity profile for laminar flow, m

$l_{particle}$ length of the particle, m

m accumulate portion of the solid in solution, kg

n dissolution exponent

n_i total number of time intervals

r radius, m

r_p particle radius, m

$r_{p,0}$ initial particle radius, m

t time, s

t_b early stage disintegration time, s

t_d later stage disintegration time, s

u fluid velocity, m^3/s

u_p relative velocity of the particle in the fluid, m/s

u_{water} velocity of water, m/s

u_x, u_y, u_z fluid velocity components, m^3/s

$\bar{u}$ vector fluid velocity, m^3/s

v_{water} kinematic viscosity of water, m^2/s

x, y, z spatial coordinates

Greek Characters

ΔH_R^0 standard enthalpy of the reaction, KJ/mol

ΔP pressure drop, Pa

Δt_i timescale between two time intervals, s

Δx_i distance that each granule covered, m

P pressure, Pa

$\dot{\gamma}$ shear rate in the boundary layer, 1/s

ε turbulent energy dissipation rate, W/kg

$\varepsilon_{particle}$ particle porosity, %

ε_b powder porosity, %

λ_+^o anionic conductance at infinite dilution

λ_-^o cationic conductance at infinite solution

μ mean particle diameter, m

μ_f dynamic viscosity of the fluid, kg/sm

μ_{water} dynamic viscosity of D.I water, kg/sm

ξ_B association parameter of solvent

ρ_a air density, kg/m^3

$\rho_{absolute}$ absolute particle density, kg/m^3

$\rho_{apparent}$ apparent particle density, kg/m^3

ρ_b bulk density, kg/m^3

$\rho_{envelope}$ envelope particle density, kg/m^3

ρ, ρ_p, ρ_s particle density, kg/m^3

ρ_f density of the fluid, kg/m^3

ρ_{water} water density, kg/m^3

σ standard deviation

τ_d time needed to complete dissolution, s

CHAPTER 1 INTRODUCTION

Dissolution kinetics of powders have been investigated for more than a century and are crucially important in various fast moving consumer goods, especially food, pharmaceutical, personal care and household products [1]. The control of the dissolution performance enables researchers to modulate the essential properties of these goods.

In this work, spray-dried detergent powders were used to study the dissolution process. Spray-drying process is the most preferred method for manufacturing thermal sensitive materials. Particles produced from this method usually have controllable particle size, bulk density, degree of crystallinity, moisture content, as well as dissolution performance. 60-70% of the commercially accessible detergent washing powders are manufactured from this method [2]. These powders usually have highly porous microstructures and multi compounds [3]. Therefore, analytically study of the dissolution kinetics of these powders remains challenging because gas (porosity), liquid or soft solid (detergent) and solid (primary particles) phases are all involved in this process [4].

Researchers [1], [5], [6] proposed three subsequent stages regarding the dissolution process of a solid particle: diffusion of solvent to the dissolving particle surface, the transformation of dissolved material from solid to solute condition immediately at the dissolving surface, and the transfer of solute (by diffusion and/or convection) from the surface to the bulk solution. In these steps, the kinetics of the dissolution mechanisms are influenced not only by the physical but also the chemical characteristics of the liquid medium (e.g. surface tension, viscosity, density, temperature) and those of the powders (e.g., particle size, density, porosity, chemical composition) [1]. In the case of a porous particle, e.g. detergent powder, numerous steps consist the dissolution process: i) intrusion of liquid into pores via capillary action, ii) submersion of granule in the solvent,

iii) disintegration of the primary particles within the solvent and iv) the dissolution of primary particles [7], [8].

In general, studying dissolution rates of small sample amounts has thus far been through a bulk approach [1]. The most common method for conducting dissolution experiments is a USP (U.S. Pharmacopeia) dissolution apparatus. Multi-particle systems are usually investigated by combining chemical analytical technology, i.e. UV spectrophotometer [9]–[11], conductivity meter [12], viscometer [13]–[16], rheometer [17], calorimeter [18], rheometrics fluid spectrometer [14], [15] and an immersion refractometer [19].

However, dissolution of bulk-particles is very challenging and complicate to understand precisely [20]. This is due to critical parameters influencing the dissolution rate of powders such as the particle size and shape, degree of aggregation and agglomeration and the interactions between the particles are difficult to explain accurately [21]–[23]. The difficulty is enhanced if we consider the dynamic change of these parameters through the dissolution. Therefore, the accuracy of the measurements obtained from bulk particles relies on the efficiency of the statistical predictions [24]. The dissolution rate of single particles can solve this obstacle. With the examination of single granules, the cohesive interactions between particles can be neglected. Therefore, the single-particle theory can minimise the hypothesis considering parameters affecting the dissolution behaviour, and the results can be considered as more trustworthy.

Nevertheless, diffusion [1], [25]–[29] and convective [30]–[35] dissolution experiments of single particles have been carried out in limited cases. All previous single-particle studies were focused on solid structured granules and no understanding on the dissolution phenomena/kinetics of porous particles has been developed. Furthermore, no link of the single particle understanding to the bulk has been performed.

In this study, spray-dried detergent powders were used to study the dissolution behaviour of highly porous structured particles with different bind material. Systematic studies and data at this level of detail are extremely rare in the literature, so this study will make a valuable contribution to the knowledge base in this particular area. The aim is to help the industry to develop an easy to manufacture internally/externally, highly soluble and fast releasing washing powder of the future.

1.1 Aims and Objectives

The primary aim of this study is to develop a better fundamental understanding of the relationship between the material components (binder), dissolution conditions (e.g. temperature, time, flow rate) and particle structure (e.g. porosity). For this reason, a combination of theoretical understanding, experimental measurements and numerical simulation were used. The findings of the relationship will allow the industry to improve the performance of detergent products.

The objectives of this work include:

1) To link formulation in the slurry to post-dried particle structure properties using characterization techniques;
2) To develop novel experimental technique based on optical microscopy for conducting single particle diffusion and convective dissolution to understand dissolution mechanisms on different conditions, e.g. flow rate, temperature, and the impact of particle structure;
3) To develop a link using single particle dissolution understanding to predict bulk dissolution through dissolution models or statistical methods (Monte Carlo analysis);
4) To study the effect of binder on the chemical release of ingredients on different dissolution conditions, e.g. stirring speed and temperature.

1.2 Structure of the Thesis

A description of the subject of each chapter is summarized below:

CHAPTER 2 A detailed review of the literature is described first covering subjects of fundamental dissolution theories, experimental methods, numerical models and parameters influencing dissolution. Then, literatures of particle dissolution are reviewed focusing on single particle diffusion and convection dissolution, and bulk particle convection dissolution in both simulation and experimental study.

CHAPTER 3 In this chapter the materials, the methodology and the results of particle characterisation are presented.

CHAPTER 4 The diffusion dissolution of single particles is examined. The dissolution phenomenon is visualised, and related times and kinetics are analysed. Image Processing is used to obtain the release rates. The effect of particle size, porosity and binder content are examined. The results are used to predict bulk particle dissolution with two different methods. One is based on Noyes-Whitney Equation with the implementation of particle size distribution, and the other is via Monte Carlo analysis. Results are compared with conductivity measurements of bulk particle dissolving in USP Apparatus 2.

CHAPTER 5 The convective dissolution of single particles under different conditions (particle size, temperature, flow rate) is studied. A novel microfluidic approach is used for this purpose. Ghost Particle Velocimetry and Nanofluids are used for the optimisation of the microfluidic chambers and compared with COMSOL simulations data. Dissolution times and profiles are extracted, the kinetics are analysed, and phenomena are visualised. The effect of fluid related properties as well as particle size, porosity and binder are examined. The velocity around the particle is evaluated and implemented in a dissolution

model based on Noyes-Whitney Equation to predict single particle convective dissolution.

CHAPTER 6 This chapter studies the effect of binder on the chemical release of components during bulk particle dissolution. Different chemical analytical methods (Conductivity, UV-Vis Spectrophotometer and Cat-SO_3 titration) are used to detect the release of salt and LAS. The effect of binder on their dissolution rate is also presented. Results are fitted in current dissolution models to point out the most applicable model for the prediction of ingredients chemical release.

CHAPTER 7 General conclusions of this research is given. Future work is also proposed.

1.3 Publications and Conferences

Results presented in this thesis have been published in the following journals and presented at the following conferences

1.3.1 Publications

H. Cao, **D. Karampalis**, Y. Li, J. Caragay, A. Alexiadis, Z. Zhang, P. J. Fryer, and S. Bakalis, "Abrupt disintegration of highly porous particles in early stage dissolution," *Powder Technology*, vol. 333, pp. 394–403, 2018.

D. Karampalis, H. Cao, J. Caragay, P. J. Fryer, Y. Ding and S. Bakalis, "A novel method to predict bulk dissolution based on a single particle dissolution understanding," In: *Proceedings of Formula IX – Multiscale Structures and Functionalities for Future Formulation*, Beijing, China, pp.123-125, 2017.

D. Karampalis, H. Cao, J. Caragay, S. Bakalis and Y. Ding, "Effect of particle interactions on chemical release of spray dried powders," In: *Proceedings of the UK-China International Particle Technology Forum VI*, Yangzhou, China, pp. 77-79, 2017.

D. Karampalis, H. Cao, J. Caragay, P. J. Fryer, Y. Ding and S. Bakalis, "Dissolution phenomena of spray dried powders by single particle approach," In: *Proceedings of the Royal Society of Chemistry 1st Food Chemistry Conference*, Amsterdam, Netherlands, pp. 32-33, 2016.

1.3.2 Oral Presentations (Speaker Underlined)

D. Karampalis, H. Cao, J. Caragay, P. J. Fryer, Y. Ding and S. Bakalis, "A novel method to predict bulk dissolution based on a single particle dissolution understanding," *Formula IX – Multiscale Structures and Functionalities for Future Formulation*, Beijing, China, 2017.

D. Karampalis, H. Cao, J. Caragay, S. Bakalis and Y. Ding, "Effect of particle interactions on chemical release of spray dried powders," *UK-China International Particle Technology Forum VI*, Yangzhou, China, 2017.

D. Karampalis, H. Cao, J. Caragay, D. Vigolo, Y. Ding and S. Bakalis, "Convective dissolution of spray dried particles using microfluidics," Icheme ChemEngDayUK 2017, Birmingham, United Kingdom, 2017.

D. Karampalis, H. Cao, J. Caragay, P. J. Fryer, Y. Ding and S. Bakalis, "Dissolution phenomena of spray dried powders by single particle approach," *Royal Society of Chemistry 1st Food Chemistry Conference*, Amsterdam, Netherlands, 2016.

CHAPTER 2 LITERATURE REVIEW

The analysis focuses on: i) dissolution principles, ii) parameters influencing dissolution in liquid medium, iii) dissolution of porous particles, iv) dissolution methods and v) the use of optical microscopy as a dissolution method.

2.1 Dissolution principles

Dissolution is the process in which a solid substance is disintegrating/disassociating in a solvent, composing a molecular-level, physicochemical uniform dispersion, called a solution.

The first research in dissolution was in 1897 when Noyes and Whitney [36] published a paper called "*The Rate of Solution of Solid Substances in Their Own Solution*" concluded that the rate of dissolution controlled by a layer of saturated solution that forms immediately around the dissolving substance.

Dissolution research has been expanding for about a century, and several methods have been developed to estimate the dissolution rate and phenomena of many industrial and consumer applications ranging from food to pharmaceuticals, chemicals etc.

The dissolution process of multi-ingredient particles is highly complex because compared to the fixed shape tablets, the surface area and/or shape changes as the dissolution proceeds [37]. Wetting of particles succeeded by the intrusion of liquid into pores on particle shell via capillary action, followed by disintegration of main particles into liquid medium and dissolution of the soluble main particles are the main stages of particle dissolution [7], [8].

2.1.1 Dissolution theories

The dissolution, of a solid substance in a liquid medium, is a two-step process: i) The interfacial step in which molecules dissociated from the solid surface and become

solvated and ii) mass transfer of the dissolved molecules (by diffusion and/or convection) to the bulk of solvent [37].

As dissolution is a process of disintegration and diffusion, the dissolution rate is a parameter driven by the following rates of diffusion [38]. The diffusional mass transfer mechanism defines the sudden motion of molecules which result in a transition of the substance from one part of a system to the other. In 1855 Fick pointed out the correlation of diffusion and heat conduction and explained this diffusional flux. Fick's law of diffusion was the base for the development of the first dissolution models in early 1900s.

Zero order kinetics

The dissolution of solid substances that do not disperse and dissolve slowly (hypothesise that the area remains constant and the solution cannot reach equilibrium stage) can be described by

$$W_t = W_0 + K_0 t \tag{2-1}$$

where W_t is the amount of solid dissolved in time t, W_0 is the initial amount of solid in the solution and K_0 is the zero-order release constant [39]. Equation (2-1) implies that the same portion of solid substances solubilises in the solvent during time. However, the conditions for this model to be applied make its use almost impossible.

Three physical models of dissolution

Three are the most frequent physical models used to model the dissolution of multi-compound particles in a given liquid medium [40]. The diffusion layer model, the interfacial barrier model and Dankwert's model (Figure 2-1).

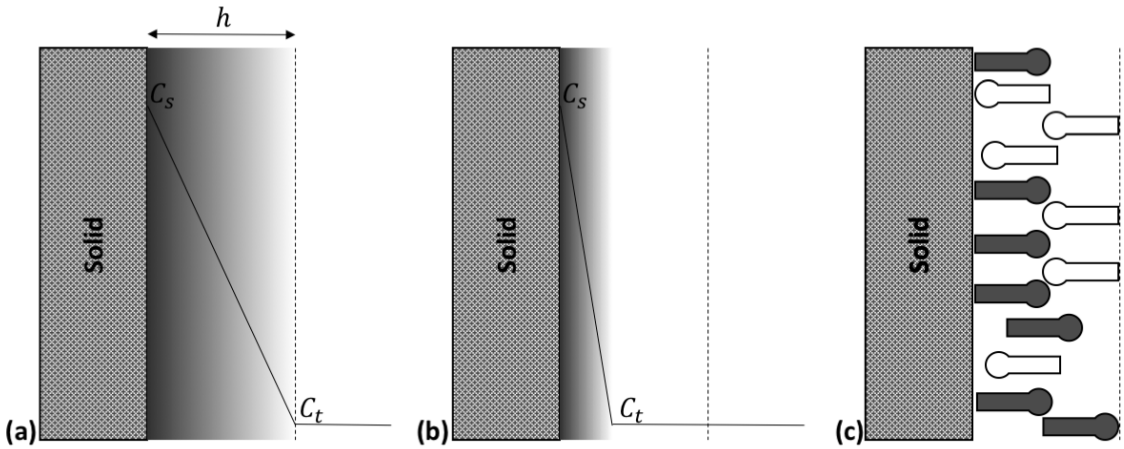

Figure 2-1 Representation of the level of concentration difference for a continuous surface dissolution in the (a) diffusion layer model, (b) interfacial barrier model, and (c) Dankwert's model (C_s is saturated concentration, C_t is concentration of bulk at time t, h is diffusion layer thickness) [40].

Diffusion layer model

In 1897 Noyes and Whitney developed the basic diffusion layer model of solid substances by conducting dissolution experiments of benzoic acid and lead chloride. Because of their experimental work, the authors concluded that the dissolution rate is proportional to the difference between the concentration of the solution and equilibrium concentration (Figure 2-1(a)). This declaration expressed as Noyes-Whitney equation [36].

$$V\frac{dC}{dt} = K(C_s - C_t) \tag{2-2}$$

where V is the volume of the liquid medium, K is the dissolution rate constant, C_t is the concentration of solution at time t, and C_s is the concentration when it is saturated. In general, they suggested that a layer of saturated solution that is created immediately in the perimeter of the solid particle controls the dissolution rate [36].

Three years later in 1900, the Noyes-Whitney dissolution equation has been modified by Brunner and Tolloczko to show that the dissolution rate depends on the surface area of the dissolving interface, the physicochemical properties of the solid substance, the medium related properties e.g. rate of agitation, temperature and the configuration of the

dissolution apparatus. They altered the Noyes-Whitney equation, to implement the value of the exposed surface area of solid, A [41].

$$V\frac{dC}{dt} = K_1 A(C_s - C_t) \tag{2-3}$$

where K_1 is the new equivalent constant.

Later, in 1904, Brunner collaborated with Walther Nernst to examine the relationship between the constants. Based on the diffusion layer concept and Fick's second law of diffusion, they evolved the equation (2-3), and the result was the mathematical expression called Nernst-Brunner equation [38], [42].

$$V\frac{dC}{dt} = \frac{D}{h}A(C_s - C_t) \tag{2-4}$$

where D is the diffusion coefficient, and h is the thickness of the diffusion layer.

In 1931, Hixson and Crowell [43] developed another diffusion controlled model for dissolution of solid particles under sink conditions. They modified the equation (2-3) and expressed solid surface area, A in respect to weight W, by letting A to be proportional to $W^{1/3}$. When this hypothesis is fitted in equation (2-3), integrates and generates a cubic-root law

$$W_0^{1/3} - W_t^{1/3} = K_{1/3}t \tag{2-5}$$

where $K_{1/3} = \left(\frac{4\pi\rho N_{particles}}{3}\right)^{1/3}\frac{DC_s}{\rho h}$.

where $K_{1/3}$ is the dissolution rate constant, ρ is the density of the particle and $N_{particles}$ is the number of the particles.

Hixson and Crowell equation or "cube root law" represented as equation (2-5) is based on the following assumptions: i) the concentration of the solute remains constant during

dissolution process (ideal sink conditions), ii) the particles retain their spherical shape across the process and iii) there is no disintegration of particles during dissolution.

Although the diffusion layer model has been the most suitable path to understand dissolution, it has gained much criticism, due to the hypothesis of the immediate formation of equilibrium concentration at dissolving interface.

Interfacial barrier model

The interfacial barrier model considered that interfacial transport, rather than diffusion through the film, is the limiting step due to a high activation energy level for the former. The interfacial transport of dispersing solid molecules into the liquid medium is the main principle (Figure 2-1(b)). The first analysis of this approach has been published in 1909 by Wilderman [44] but has not been examined thoroughly through the years and an explicit mathematical description for the dissolution kinetics is not available.

Dankwert's model

The Dankwert's theory uses a different approach. It considers that macroscopic packets of liquid medium swirl due to fluid velocity and reaches the solid-liquid interface. Then they absorb solute using diffusion principles. These packets are continuously substituted by new packets that exhibit new solid surface area every time (Figure 2-1(c)). For this reason, is called surface renewal process [40].

2.1.2 Diffusion coefficient

Diffusion is the phenomenon in which random movement of atoms, molecules or small particles occurs from a high concentration area to a lower concentration. It takes place in gas, liquid or solid conditions and in between them. The concept of diffusion it is widely used in dissolution.

Diffusion in dilute solutions is highly complex because except the random motion of atoms existing in the gas phase, forces between molecules of solute and solvent are also contributing in the process [45]. The liquid phase consists of groups of randomly arranged atoms or molecules which occur in an activated state and face irregular motion thus the complexity of handling it.

During the years, many researchers tried to evaluate molecular diffusivities in liquid phase based on hydrodynamical, quasi-crystalline and fluctuation approach. Most of the equations developed based on hydrodynamical approach, which links the diffusion coefficient to the viscosity of the liquid or to a friction constant, which can be linked to viscosity.

A theoretical explanation of the diffusivity of spherical solute particles that are large compared to the liquid medium in which they move is described by the Stokes-Einstein equation [46]. This equation based on the hypothesis that the particles are hard spheres moving continuously in a fluid with a consistent velocity under an applied force F.

Stokes' law explaining the force acting on an atom

$$F = 6\pi\mu_f r_p u_p \tag{2-6}$$

Then Einstein correlated the diffusion coefficient to the mobility M and developed the equation

$$D = k_B T M \tag{2-7}$$

As mobility M expressed as the ratio of particle's velocity to an applied force, the implementation of equation (2-6) to equation (2-7) gives the Stokes-Einstein equation

$$D = \frac{k_B T}{6\pi r_p \mu_f} \tag{2-8}$$

where D is the self-diffusion coefficient or diffusivity, k_B is Boltzmann's constant, T is the absolute temperature, r_p is the radius of the dissolving particle, μ_f is the dynamic viscosity of the liquid, and u_p is the velocity of the diffusing particle.

The use of this equations lies in the fact that it can predict diffusion coefficients with the correct order of magnitude. However, there are many of controversies against it.

Stokes-Einstein equation has been used as a base for the development of many practical approaches. Wilke and Chang [45] examined the interactions of diffusion coefficients in dilute solutions using a range of hydrocarbon solvents, and they established the equation

$$D_{AB} = 7.4 * 10^{-8} \frac{(\xi_B M_B)^{1/2} T}{V_A^{0.6} \mu_f} \tag{2-9}$$

where D_{AB} is the diffusion coefficient of dilute solutions, V_A is the solute molar volume, M_B is solvent molecular weight, and ξ_B is an association parameter of solvent. Association parameter ξ_B lies between the values of 1.0 for non-associated solvents, 1.5 for ethanol, 1.9 for methanol and 2.6 for water.

Wilke and Chang's equation can be used for the estimation of diffusion coefficients in dilute solutions with sufficient accuracy, about 10% average error is unavoidable. However, errors can achieve values higher than 200% when water is used as a solute [47].

In 1888, Nernst [48] linked the diffusion coefficient of electrolyte solutions to electrical conductivities at infinite dilution (Equation (2-10)). In an electrolyte solution, the solute separates into cations and anions. Their mobility via solvent will vary since the size of the ions is dissimilar than the initial molecule. Probably, the larger ion will diffuse slower than the smaller one. However, the electric charge does not disassociate, so both ionic classes must diffuse at the same rate.

$$D_{AB}^{o} = \frac{RT}{F_c^2}\frac{\lambda_+^o \lambda_-^o}{\lambda_+^o + \lambda_-^o}\frac{|Z_+| + |Z_-|}{|Z_+ Z_-|} = 8.931 * 10^{-14} T \frac{\lambda_+^o \lambda_-^o}{\lambda_+^o + \lambda_-^o}\frac{|Z_+| + |Z_-|}{|Z_+ Z_-|} \quad (2\text{-}10)$$

where D_{AB}^{o} is the diffusion coefficient at infinite dilution, F_c is the Faraday constant, λ_+^o is the anionic conductance at infinite dilution, λ_-^o is the cationic conductance at an infinite solution, Z_+ is cation valence and Z_- is anion valence.

Table 2.1 summarises characteristic ionic conductance's at infinite dilution [49], while Robinson and Stokes published a comprehensive list [50]. This table will be used for the evaluation of powder samples diffusivity in 3.4.2 .

Table 2.1 Summary of characteristic ionic conductance's at infinite dilution in water at 25°C [49], [50].

Cation	λ_+^o	Anion	λ_-^o
Ag^+	61.9	Br^-	78.4
H^+	349.8	Cl^-	76.35
Li^+	38.7	ClO_3^-	64.6
Na^+	50.1	ClO_4^-	67.4
K^+	73.5	F^-	55.4
NH^+	73.6	I^-	76.8
Ca^{2+}	59.5	NO_3^-	71.46
Cu^{2+}	56.6	OH^-	198.6
Mg^{2+}	53	CO_3^{2-}	69.3
Zn^{2+}	52.8	SO_4^{2-}	80.0

2.1.3 Dissolution rate

The rate of dissolution is the quantity of a solid substance that moves in solution per unit time under controlled conditions of temperature, solvent composition and interfacial area.

Dissolution rate constant

So far, a specific definition of dissolution rate has not been developed, and its explanation is based on experimental statements. The same statements have been used to develop Fick's law.

Equation (2-3) shows that the solution's concentration difference and the interfacial surface area are equivalent to the amount of solid substance moved into the liquid medium. This correlation is expressed by K_1 which is called dissolution rate constant.

Dissolution rate physical explanation can be considered as the rate constant to transfer one molecule from the boundary to the bulk solution [51]. If the value of dissolution rate constant K_1 is high, then the mass transfer will be fast otherwise if it is low it will be slow. It is expressed per surface area of the interface. Therefore, its measurement unit is equivalent to velocity and not to dissolution time.

Dissolution rate defines the dissolution speed. It depends on the chemical nature of the solvent and solute, the temperature, the degree of undersaturation, the presence of mixing, the surface area of the interface, and the existence of inhibitors (e.g. substances adsorbed on the surface).

Noyes-Whitney equation reveals that a substance with high solubility will face high dissolution rate while low dissolution rate will exhibit a substance with low solubility. Therefore, the order of magnitude of dissolution rate ranges in different conditions.

Intrinsic dissolution rate (IDR)

According to United States Pharmacopoeia (USP) [52] the intrinsic dissolution rate (IDR) is the rate of mass transfer per area of dissolving surface and time during constant temperature, pH, ionic strength and agitation and is usually expressed as kg/m^2s. Sink conditions should be applied, and the surface area of the dissolving substance should be kept constant during dissolution.

2.1.4 Convective mass transport

According to the movement of the solvent dissolving the solute, dissolution can be categorised into two types, i) diffusive transport or ii) convective transport

Dissolution can be determined as particular categories of several complex reactions in which a mass transfer is influenced by the final outcome of release and deposition of solute molecules at a solid surface. These reactions can be categorised based on the following three classes [53]:

i) The reaction or interaction at the interface happens much faster than the transfer rate of reactants to and molecules from the interface. Thus, the rate is defined by the transfer procedure. In dissolution, this would be the diffusion or convective transfer of solute from the interfacial boundary layer to the solution.

ii) The rate of reaction at the interface is much slower than the mass transfer and thus dominates the rate. In dissolution, the diffusion and deposition of the solute molecules at the interface would govern the rate.

iii) The order of magnitude of intrinsic rates and rate constants is similar, therefore, the overall rate is a determined by both processes.

In the case of convection in a stirred solvent the reaction at the interface and the transfer procedure coexist.

Nernst and Brunner diffusion layer theory has been opposed by researchers supporting that the movement of the fluid, as well as the turbulence, expands in an area very close to the solid surface. Van Name and Hill [54], [55] and King [56] has stated the argument that the fluid motion component vertical to the surface becomes small so it does not physically act on the transport rate. Moreover, Fage and Townsend [57] by measuring velocity distributions detected only laminar movement horizontal to the interface in areas close to the interface. The summary of the above researcher's output points out that convective transport would support the transfer of solute only in the distant regions of the film.

The general expression for convective diffusion in three dimensions -x, -y, -z, is given by

$$\frac{\partial C}{\partial t} = D\left(\frac{\partial^2 C}{\partial x^2} + \frac{\partial^2 C}{\partial y^2} + \frac{\partial^2 C}{\partial z^2}\right) - u_x \frac{\partial C}{\partial x} - u_y \frac{\partial C}{\partial y} - u_z \frac{\partial C}{\partial z} \tag{2-11}$$

where u_x, u_y, u_z are fluid velocities in the three dimensions. This model is an extension of Fick's second diffusion law with the inclusion of convection factors [58].

A dimensionless number is initiated to symbolise the ratio of convective to diffusive mass transfer, called Sherwood number (Sh). It is described as

$$Sh = \frac{KL}{D} \tag{2-12}$$

where L is the characteristic length.

Frösling equation can be used to define the Sherwood number for single spheres when $2 \leq Re_p \leq 12000$ and $0.6 \leq Sc \leq 2.7$

$$Sh = 2 + 0.552\left(Re_p\right)^{1/2}(Sc)^{1/3} \tag{2-13}$$

where Re_p is Reynolds of the particle. Sc is the Schmidt number which represents the ratio between momentum diffusivity and mass diffusivity and is given by

$$Sc = \frac{\mu_f}{\rho_f D} \tag{2-14}$$

where ρ_f and μ_f are the density and the dynamic viscosity of the fluid respectively.

Various approaches have been developed to estimate the Sherwood number for a spherical particle that takes into consideration many parameters especially the associated size of the particle and the laminar or turbulent flow inside the stirred tank reactor. In general, powders have a broad particle distribution, and the size of the particle changes during dissolution, an equation that can be used across the different particle sizes is required.

Levins and Glastonbury [59] modified the Frössling equation and proposed the following equation for a well-mixed system

$$Sh = 2 + 0.47\left(Re_p\right)^{0.62}(Sc)^{0.36}\left(\frac{d_{impeller}}{d_{tank}}\right)^{0.17} \tag{2-15}$$

where particle Reynolds number, Re_p is described as

$$Re_p = \frac{\rho_f \varepsilon^{1/3} d_p^{4/3}}{\mu_f} \tag{2-16}$$

where ε is the turbulent energy dissipation rate, d_p is the diameter of the particle, $d_{impeller}$ is the diameter of the impeller and d_{tank} is the diameter of the tank.

For particles with high density than the fluid the following equation of Sherwood number is used

$$Sh = 2 + 0.44\left(\frac{\rho_f u_p d_p}{\mu_f}\right)^{0.5}\left(\frac{\mu_f}{\rho_f D}\right)^{0.38} \quad (2\text{-}17)$$

where u_p is the relative velocity of the particle in the fluid [60].

2.1.5 Numerical models

The description of dissolution kinetics using dissolution models is widely developed in many industrial sectors ranging from pharmaceuticals and chemicals to foods etc. The main aim of the development and perfection of new numerical models is to manufacture optimum and effective products. Numerical measurements can be used to validate experimental data and evaluate parameters related to the dissolution process. Using a model, the dissolution behaviour of a product can be predicted, and the outcomes can be used to finalise products formulation and dissolution performance before it reaches the markets.

The fundamental equations often used to describe the diffusion dissolution process are based on Fick's laws of diffusion [61], [62], such as the Noyes and Whitney equation(2-2) [36], Nernst and Brunner equation(2-4) [38], [42] and the Hixson and Crowell cube root model, equation (2-5) [43] as described in Section 2.1.1 . Other relevant models describe the dissolution process including the first order kinetics and those developed by Weibull [63], Niebergall et al. [64], Higuchi and Hiestand [65], [66], Baker-Lonsdale [67], Korsmeyer-Peppas [68] and Hopfenberg [69]. Hixson and Crowell cube root model, Niebergall et. al. model and Higuchi and Hiestand model are more related to particulate products. The cube-root law is most relevant when the particle size is much larger than the diffusion layer thickness, the Higuchi and Hiestand equation is used when the particle size is much smaller than the diffusion layer thickness. The Niebergall et. al. model

expression is in-between the other two models [62]. A summary of the most relevant numerical models to describe the dissolution process of a solid is given in Table 2.2.

First order kinetics

The use of this model to dissolution studies was first suggested by Gribaldi and Feldman [70] and later by Wagner [71]. If a solid substance with a constant surface area is dissolving under sink conditions, the integration of equation (2-5) will become

$$W_t = W_0 e^{-K_1 t} \text{ or } \ln W_t = \ln W_0 K t \quad (2\text{-}18)$$

Weibull model

Weibull characterised the dissolution process with a general empirical equation [72]. When applied to powder dissolution, the Weibull equation defines the accumulated portion of the solid, m, in solution at time t

$$m = 1 - exp\left[\frac{-(t - T_t)^b}{a}\right] \quad (2\text{-}19)$$

where a defines the dissolution time scale, T_t is the lag time before the progression of dissolution and usually is zero and b is a shape parameter (b=1 the curve is exponential, b>1 the curve is sigmoid, b<1 the curve is parabolic).

Niebergall et al. model

Niebergall et al., [64] based on equation (2-5) developed a semi-empirical equation which has a square root dependency on weight

$$W_0^{1/2} - W_t^{1/2} = K_{1/2} t \quad (2\text{-}20)$$

where $K_{1/2} = \left(\frac{3\pi\rho N_{particles}}{2}\right)^{1/2} \frac{DC_s}{k'\rho}$.

where $K_{1/2}$ is the dissolution rate constant and k' is a constant.

Higuchi and Hiestand model

Higuchi and Hiestand, [65], [66] based on equation (2-5) developed a two-thirds-root dependency on weight

$$W_0^{2/3} - W_t^{2/3} = K_{2/3}t \tag{2-21}$$

where $K_{2/3} = \left(\frac{4\pi\rho N_{particles}}{3}\right)^{2/3} \frac{2DC_s}{\rho}$.

Baker-Lonsdale model

Modified Higuchi and Hiestand equation (2-21), Baker and Lonsdale [67] described the dissolution of a solid substance from a spherical matrix

$$\frac{3}{2}\left[1 - \left(1 - \frac{W_t}{W_\infty}\right)^{2/3}\right] - \frac{W_t}{W_\infty} = Kt \tag{2-22}$$

where W_∞ is the total amount of solid dissolve in the solution.

Korsmeyer-Peppas model

Korsmeyer et al., [68] developed a semi-empirical model to relate the dissolution of the solid exponentially to the dissolution time t.

$$\frac{W_t}{W_\infty} = at^n \tag{2-23}$$

where a is a constant related to structural characteristics of solid and n is the dissolution exponent (n=0.5 for Fick's diffusion and $0.5<n\leq1$ for mass transfer following Fick's diffusion).

Hopfenberg model

A numerical equation on the dissolution of slabs, spheres and cylinders facing heterogeneous erosion established by Hopfenberg [69].

$$\frac{W_t}{W_\infty} = 1 - \left[1 - \frac{k_0 t}{C_0 a_0}\right]^n \tag{2-24}$$

where k_0 is the erosion rate constant, C_0 is the initial concentration of solid in the solution and a_0 is the initial radius for a sphere or cylinder or the half-thickness for a slab. The value of n is 1, 2 and 3 for a slab, cylinder and sphere accordingly.

Table 2.2 Summary of numerical dissolution expressions.

Noyes and Whitney	$V\frac{dC}{dt} = k(C_s - C_t)$
Nernst Brunner	$V\frac{dC}{dt} = \frac{D}{h}A(C_s - C_t)$
Zero order	$W_t = W_0 + k_0 t$
First order	$W_t = W_0 e^{-K_1 t}$ or $\ln W_t = \ln W_0 + K_1 t$
Hixson – Crowell	$W_0^{1/3} - W_t{}^{1/3} = K_{1/3}t,$ $K_{1/3} = \left(\frac{4\pi\rho N_{particles}}{3}\right)^{1/3}\frac{DC_s}{\rho h}$
Weibull	$m = 1 - exp\left[\frac{-(t - T_t)^b}{a}\right]$
Niebergall et. al.	$W_0^{1/2} - W_t{}^{1/2} = K_{1/2}t,$ $K_{1/2} = \left(\frac{3\pi\rho N_{particles}}{2}\right)^{1/2}\frac{DC_s}{k'\rho}$
Higuchi and Hiestand	$W_0^{2/3} - W_t{}^{2/3} = K_{2/3}t,$ $K_{2/3} = \left(\frac{4\pi\rho N_{particles}}{3}\right)^{2/3}\frac{2DC_s}{\rho}$
Baker-Lonsdale	$\frac{3}{2}\left[1 - \left(1 - \frac{W_t}{W_\infty}\right)^{2/3}\right] - \frac{W_t}{W_\infty} = Kt$
Korsmeyer-Peppas	$\frac{W_t}{W_\infty} = at^n$
Hopfenberg	$\frac{W_t}{W_\infty} = 1 - \left[1 - \frac{k_0 t}{C_0 a_0}\right]^n$

2.2 Parameters influencing dissolution in a liquid medium

Dissolution of particles in a liquid medium is determined by many parameters like the solvent in which the solute is dissolving, the temperature and the pH of the solvent and the attraction forces of the solute to dissolve in the solution. Furthermore, the dissolution rate is also governed by the particle size and shape, porosity, the solid-state properties and the exposed surface area of solute to solvent.

2.2.1 Physicochemical Characteristics

The physicochemical properties of the particles and the fluid are one of the main factors that dissolution depends on. The solubility, diffusivity, particle size, shape and surface area, porosity as well as the solid-state properties are all affecting the process.

Solubility

Solubility scope is to indicate how much chemical substance (solid, liquid or gaseous) will eventually dissolve in a quantity of solvent (solid, liquid or gaseous) to form a homogeneous solution. It is the resting limit for the equilibrium between undissolved substance and solubilised substance.

The ability of a solute to dissolve in a solvent depends on the attraction forces between the solute and solvent particles. When the attraction forces of different particles are stronger than the forces between similar particles, a solution is generated. The degree to which the attraction forces prevail is related to the amount of solvent in which a substance can dissolve. This quantity will also be dependent on certain conditions of temperature, pressure and pH, as solubility usually differs with alteration of these three parameters.

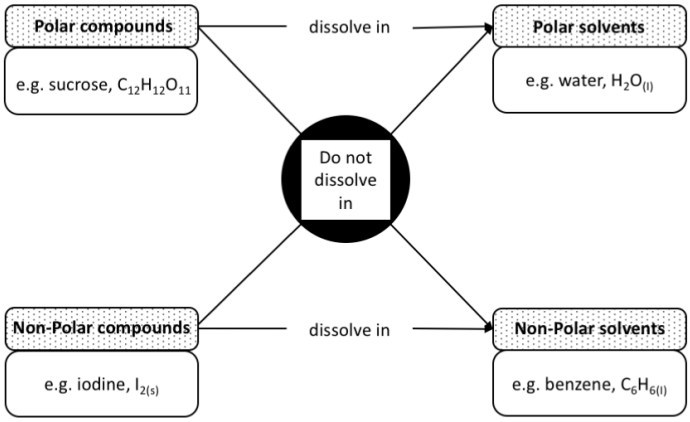

Figure 2-2 Polar and Non-Polar relationships in dissolution.

When the amount of solvent to dissolve any further solute is achieved, adding more solute will not enhance the concentration of the solution and will start to precipitate the surplus of solute. This is indicated as saturation concentration.

As suggested by Noyes and Whitney a layer of saturated solution that is created immediately in the perimeter of the solid particle controls the dissolution rate. In this saturated layer, the solubility of the solute at a given temperature is the quantity of a solid substance in the solvent. By decreasing solubility, the saturated layer concentration will decrease; therefore, the movement of the molecules is governed by a more prominent force due to the high concentration difference between the layer and the bulk solution.

Diffusivity

Diffusivity is the degree of diffusion. The correlation of Noyes-Whitney equation (2-2) and Nernst-Brunner equation (2-4) links the dissolution rate constant with the diffusion coefficient

$$K_1 = \frac{D}{h} \tag{2-25}$$

Based on that we can conclude that the dissolution rate constant is equivalent to the diffusivity. The higher the diffusion, the faster the mass transfer.

Diffusivity is affected by the size and shape of the molecule, the viscosity of the solvent and the properties of the bulk solution e.g. pH, temperature, salt concentration etc. By increasing the temperature, the viscosity will decrease, thus the diffusivity will increase and as a result the speed of dissolution will increase as well.

Particle size

The impact of particle size on dissolution rate is critical. Increasing the particle size, the dissolution rate decreases. When a solid substance disperses into small parts, the interfacial surface area increases, therefore, the dissolution process will be faster (Figure 2-3).

Based on equation (2-4) the rate of diffusion dissolution is directly proportional to the interfacial surface area of the dissolving solid substance [64]. Therefore, a decrease in particle size will result in an increase in dissolution rate. However, Bisrat and Nyström has shown that a decrease in particle size results in a higher increase in dissolution rate that can be explained solely by the increase in surface area [73].

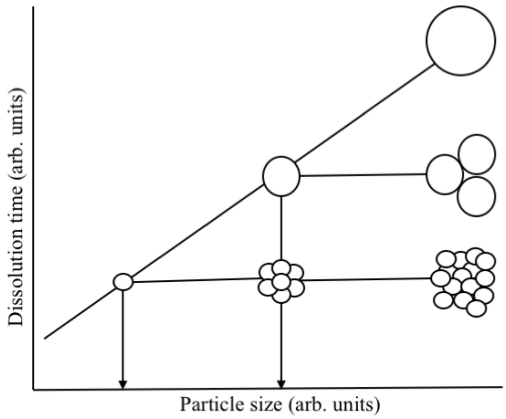

Figure 2-3 Influence of particle size on dissolution time [4].

In dispersed solid-liquid systems, particle size reduction seems to result in an increase of the dissolution rate of a sparingly soluble material by decreasing the thickness of the diffusion layer around each particle [64], [73] and also by exhibiting a large interfacial

area [36], [42], [48], [74]. In the case of particles above 50 μm the hydrodynamic boundary layer thickness has been determined to be constant and about 30 μm [75]. Particles below 50 μm, though, do not have sufficient surface area and associated friction force to sustain a boundary and a diffusion layer of this size.

According to the Prandtl boundary layer theory for particles below 50 μm, the hydrodynamic boundary layer is almost equal to the particle radius or diameter [22], [64], [74].

In 1995, Mosharraf and Nyström [22] examined the joined effect of particle size (from 1.8 μm to 3.8 μm) and particle shape (from spherical to irregular granules) on the dissolution rate of granules below 5 μm. The data showed that the dissolution rates of dispersed pharmaceuticals are linked to the granule size and shape. The dissolution rate of similarly sized particles reduced as the degree of flakiness and irregularity increased. The hypothesis concerning this is that the increasing irregularity of the particles increases the hydrodynamic boundary layer thickness.

Particle shape

The shape is mainly used to characterise the outer geometrical appearance of a particle. Form, roundness, irregularity and sphericity are the four significant parameters that define the particle shape [76]. Form is the three-dimensional projection of particles length width and thickness, the associated angularity of the particle called roundness, the divergence of the particle's three-dimensional projection called irregularity and sphericity is the magnitude of particles which can be considered as a sphere. For the evaluation of all these parameters, the length, width and thickness measurements need to be determined. In 1935, Zingg [77] identified the four primary shapes using the relationship of thickness to

with and width to length (Figure 2-4). In general, the information that researchers use for the evaluation of particle size distribution hypothesizes that all granules are spheres.

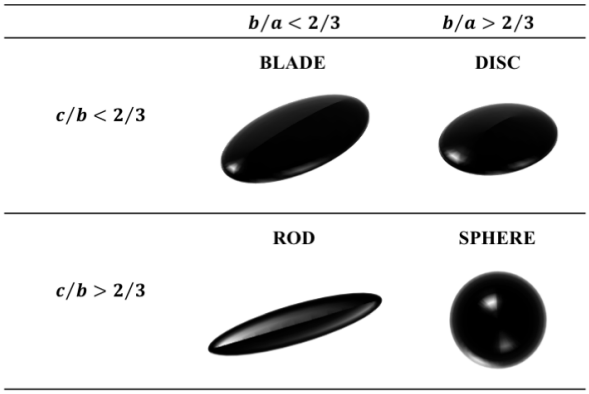

Figure 2-4 Zingg's categorisation of particle shape.

Keith and Bouza [78] used smoothness, aspect ratio and equivalent circular area for the image analysis of particle dissolution process. Results showed an increase of particle smoothness as the dissolution progresses.

Jia and Williams [79] modelled the influence of particle shape on dissolution process with the use of a custom developed software named *DigiDiss*. They used three irregular shaped particles with an equivalent surface area, and they showed that their dissolution behaviour differs significantly. Moreover, they suggested that the spatial distribution of the surface area might have an impact on the concentration C_t of equation (2-2).

More recently, in 2013, Yuan et al. [80] compared dissolution experiments of differently shaped sugar grain using optical methods with *DigiDiss* simulation results of the same samples and studied the impact of particle shape. The curved elements of particle surface area dissolve faster than the void spaces due to the larger surface area exposed to the liquid medium which results in higher diffusion rate and smoother edges and corners.

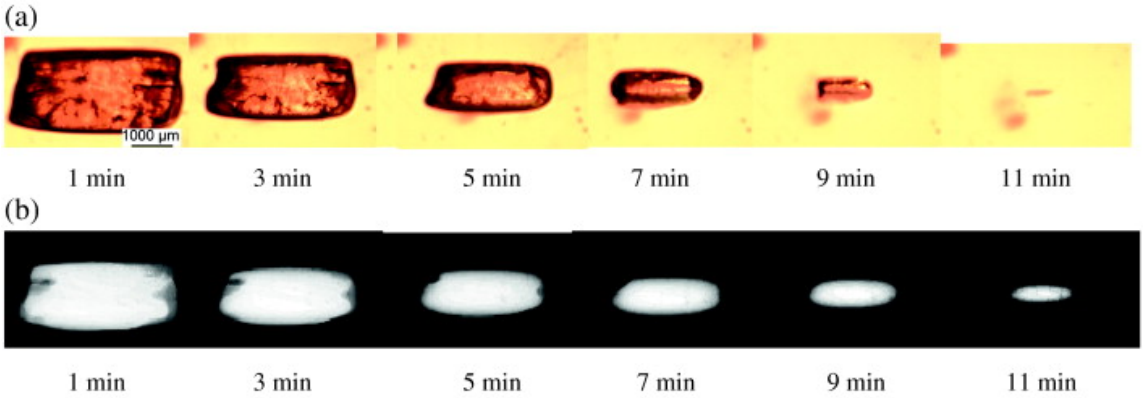

Figure 2-5 (a) Dissolution of sugar grain in an aqueous medium using optical method; (b) Simulation images of the dissolution process of the same sample [80].

Surface area

It is usually preferred the dissolution rate to be defined by a particular surface measurement (e.g., μg/min per cm2). This approach can be accomplished either by exposing a fixed solid surface area to the solvent or by gradually measuring or recording the alteration of surface area, as a function of time. G frequently expresses the surface specific dissolution rate in the bibliography and is occasionally as well mentioned as the intrinsic dissolution rate. In 1985 Nyström et al., [81] calculated the remaining surface area (cm^2), and the weight dissolved (μg) as a function of time (min).

$$G = \frac{W_0 - W_t}{t\left((A + A_t)/2\right)} \tag{2-26}$$

where A_t is the exposed surface area at time t. This equation assumes that the shape of the granule remains the same during particle dissolution [82].

One year earlier, Nicklasson and Brodin [83] demonstrated the chance of measuring the maximum dissolution rate of a substance from the equation

$$\log C_s = \log G + 1.94 \tag{2-27}$$

Their theory assumes that diffusion controls the dissolution rate. By conducting measurements at increasing rotational velocities for a rotating disc, they stated that equation (2-27) was accurate only for conditions where the diffusional mass transfer could be neglected, i.e., reflecting the maximum dissolution rate.

An inverse relationship usually occurs between particle size and surface area. Surface can be separated into two categories, the effective surface area and the absolute surface area. Absolute is the entire surface area of the granule, while effective is the exposed surface area to dissolution medium. The effective surface area has a significant effect on dissolution rate. Based on equation (2-4) the higher the effective surface area is, the greater the contact between the surface of the solute and the solvent and thus the faster the dissolution process becomes. Overall, any surface-related phenomenon can be potentially used for surface area evaluation. Permeametry and gas adsorption are the most common methods used for the evaluation of effective surface area in many industrial applications [84]. The effective surface measured by any method can be translated into an analogous mean spherical particle diameter d_{psv}, by

$$d_{psv} = 6/A_v \tag{2-28}$$

where A_v is the volume specific surface. The d_{psv} is the size of a spherical granule that, if the bulk contained only of this kind of granules, would have an equivalent effective surface area as the original product.

Porosity

Dissolution speed can be expressed as the time needed for a portion of material per disperse element to move into the bulk solution. This can change by the particle porosity. Experimental [85], [86] and numerical [87] results showed that porosity could influence the dissolution rate of particles significantly. The higher the particle porosity, the smaller

the available volume of the particle for dissolution and thus, the faster the dissolution. Porosity can be manipulated by the portion of binder content appear within the particle [88] so it can vary from 0 for binder-saturated particles to 1 for non-binder particles.

In 2004, Stepanek [87] related particle porosity to dissolution via virtual dissolution experiments. Results showed that porosity could have a significant (for fast-dissolving particles) or insignificant (almost nil) (for slow-dissolving particles) influence on dissolution rate.

To validate this conclusion, Ansari and Stepanek [19] used sugar spheres and D-mannitol particles with polyethylene glycol (PEG) and polyvinyl pyrrolidone (PVP) as a binder, respectively to represent the above two cases. They found that in the case of sugar-PEG particles dissolution rate is controlled by the dissolution of primary particles and hence particle porosity does not affect. However, in the case of D-mannitol-PVP granules, the effect of particle porosity on dissolution is very strong.

Solid-phase characteristics

Another parameter with a significant influence on dissolution rate is the solid-phase, i.e. amorphicity, crystallinity, state of hydration and polymorphic structures. The impact on the dissolution rate of the solid-phase characteristics is related to the different lattice energies (and entropies) of the correlated physical forms (crystallinity, amorphous, polymorphism). The difference in dissolution rate between different polymorphs and hydrate/anhydrate forms of the same solid substance differ up to two times, in contrast, the difference in dissolution rate between amorphous and crystalline ingredients can change up to 100 times [89] (Figure 2-6). Anhydrous forms dissolve faster than hydrated because their thermodynamic action is higher than hydrates. Furthermore, metastable

(high activation energy) polymorphic forms have higher dissolution rate than stable forms.

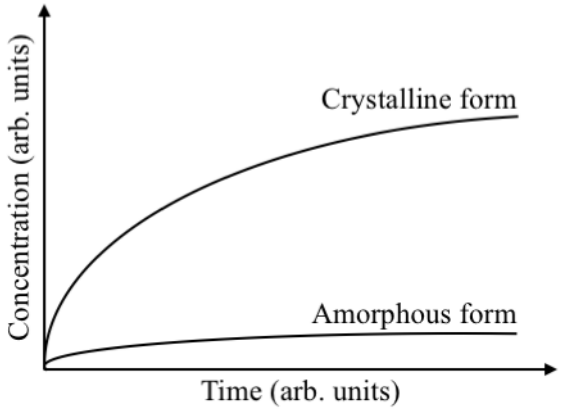

Figure 2-6 Comparison of dissolution profiles of crystalline and amorphous forms.

Marabi et al., [1], [18] conducted an extensive research on the dissolution kinetics of food powders using a differential scanning calorimeter. Results showed that dissolution enthalpy was varying if no phase change took place in the solid substance but was influenced when a part of the solid exhibit crystallisation. Since in general, amorphous ingredients reveal an exothermic reaction during dissolution process, while crystals face an endothermic reaction, the existence of crystals in powders would lead in a lower release of energy during dissolution. Consequently, this could slow down dissolution due to a decrease in the free energy of the process. They proved that there is a link between dissolution enthalpy and dissolution rate. More exothermic behaviours lead in a faster dissolution process (Figure 2-7).

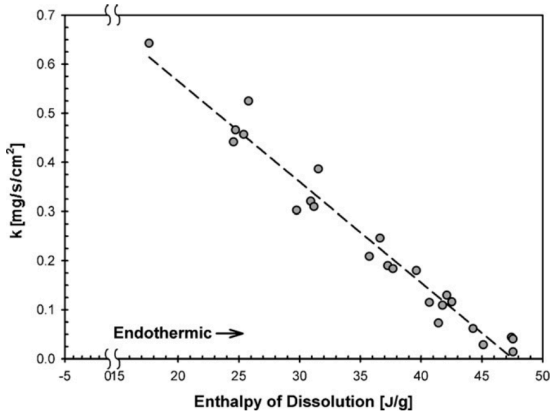

Figure 2-7 Relationship of dissolution enthalpy and dissolution rate constant (k) for sucrose spherical particles [1].

2.2.2 Fluid Characteristics

Except the physicochemical properties of the granule and the fluid, the fluid related properties have similar effects on dissolution performance.

Temperature

The influence of solvent temperature on solubility and dissolution rate is significant. The solubility of a gas as a function of temperature is given by the derivation of van't Hoff equation [51]

$$\ln\left(\frac{K_T}{K_{T_0}}\right) = -\left(\frac{\Delta H_R^0}{R}\right)\left(\frac{1}{T} - \frac{1}{T_0}\right) \tag{2-29}$$

where K_T and K_{T_0} is the equilibrium constant at temperature T and absolute temperature T_0 respectively, ΔH_R^0 is the standard enthalpy of the reaction and R is an ideal gas constant.

Increasing the temperature, the higher the dissolution rate of most solute substances becomes. At higher solution temperatures, the energy that is added (heating) into dissolution system increases the motion of the solute molecules. The increase in the moving speed of solvent molecules conflicts with the attraction between molecules and

usually makes them separate efficiently. Also, it makes more of the solvent molecules to reach solute molecules and drag them with force, which results in faster dissolution.

Since different solutes consist of different atoms, ions, or molecules the increase in the temperature will influence their dissolution at different levels.

pH

The dissolution process of a solid substance in a liquid medium is a complex process. The value of the pH is one the main parameters related to the fluid that can influence the solubility of a solute. Therefore, the alteration of the pH value of the solvent can have a critical effect on the dissolution rate of a solid compound. Several studies have been conducted to examine this phenomenon.

In 1985, Serajuddin and Jarowski [90], [91] examined the dissolution kinetics of pharmaceutical acids and bases and their hydrochloride and sodium salts respectively, by linking the pH-solubility profiles with the pH-dissolution rate profiles. An approach for the prediction of dissolution rates of acid/base or salts at different pH has been demonstrated. Good agreement with the Noyes-Whitney equation was shown when solubilities under sink conditions as the diffusion layer thickness h reaches zero ($C_{s,h=0}$) were applied compare to solubilities of the bulk solution (C_s).

Brigante et al., [92], [93] have studied the effect of pH on the dissolution speed of humid acid granules. These particles are aggregates of humid acid molecules which are connected by interaction forces. By sinking a particle in an aqueous medium, the forces attenuate, the aggregated disperse and the dissolution becomes faster. Results showed that the rate of dissolution increases at high pH level, while it slows down by decreasing pH (Figure 2-8).

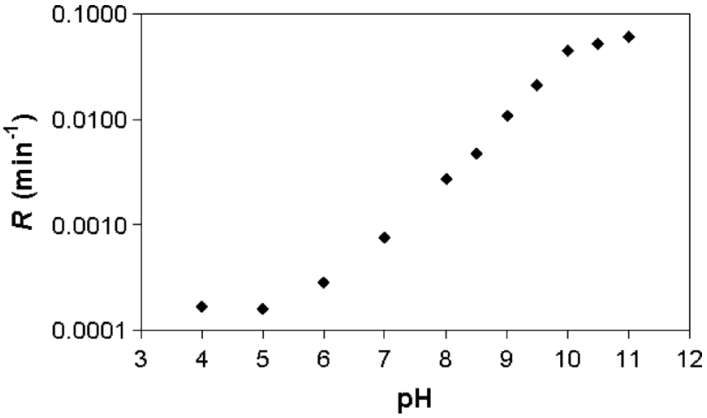

Figure 2-8 Effect of pH on the dissolution rate of humid acid particles [92].

More recently, a research on the dissolution of ibuprofen tablets by changing the pH of the dissolution system using acidic and basic powders in the formulation has been published [94]. Ibuprofen tablets containing basic pH additives showed faster dissolution performance than the ones including acid pH additives (Figure 2-9).

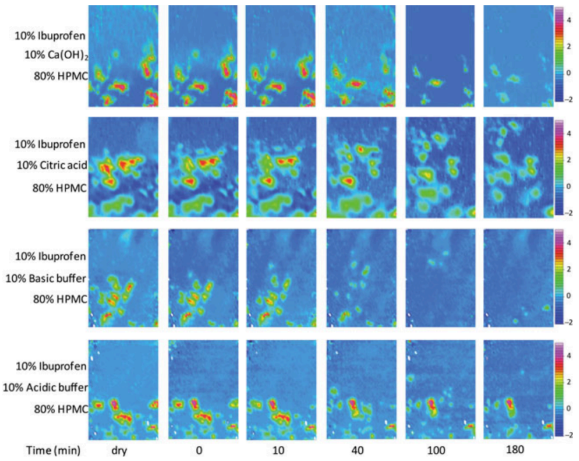

Figure 2-9 Dissolution performance of ibuprofen tablets containing different acidic and basic additives using FTIR imaging data [94].

Agitation

Hydrodynamics and the agitation speed, or the stirring conditions, is one of the most important factors affecting the dissolution rate via the effect of mixing [41], [43]. Stirring of the bulk solution generates an extension of high concentration areas, enhancing the contact area of lower concentration areas and therefore the concentration reaches an

equilibrium [43]. It is obvious, due to the Nernst-Brunner diffusion layer theory [38], [42], that agitation can have a significant effect on diffusion dissolution as the diffusion layer thickness is inversely proportional to the speed of agitation. The following equation has been demonstrated by Wurster and Taylor [95]

$$K = a(N)^b \tag{2-30}$$

where N is the agitation speed and a, b are constants. If dissolution rate is diffusion-controlled b should be 1. However, in case that the reaction (dissolution) is interfacial-rate-controlled, agitation intensity will not control the dissolution rate, and constant b should be equal to 0. If both processes are controlling the dissolution rate and many different agitation intensities are applied, then the value of b should vary between 0 and 1. Considering that as the distance from the interface increases due to the change of the fluid motion from laminar to turbulent, the price of constant b might also differ with the model of stirring used. Hixson and Baum [96] examined this phenomenon when they used data from the dissolution of benzoic acid pellets as a parameter for agitation efficiency. They conducted a dimensional analysis and selected a critical Reynolds number for the moment where the relationship of the variables changed. Then, they associated this alteration to the turbulence motion and acquired different relationships for low and high Reynolds numbers. In a following study [97], they changed only the model of agitation, and they showed that a different experimental relationship should be developed.

A transport controlled-convective numerical diffusion model has been developed by Nelson and Shah [98] and validated by rotating-filter-stationary basket experiments. They chose suitable boundary conditions and solved the convective diffusion differential

equation. For a rectangular surface, the equation given by convective diffusion theory for the dissolution rate constant is

$$K = 0.808 D^{2/3} C_s \dot{\gamma}^{1/3} b_w L_T^{2/3} \tag{2-31}$$

where $\dot{\gamma}$ is the shear rate in the boundary layer, L_T is the length of the tablet, in the direction of flow, and b_w is the width of the tablet.

For a circular surface of radius r, the equation of K is given by

$$K = 2.157 D^{2/3} C_s \dot{\gamma}^{1/3} r^{5/3} \tag{2-32}$$

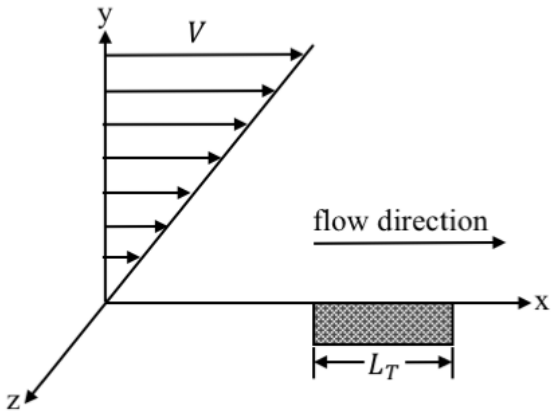

Figure 2-10 Representation of convective diffusion equation for a rectangular surface [98].

2.3 Single particle dissolution

In general, dissolution of small quantities has been examined through a bulk approach [1]. However, multi-particle systems are highly complex and therefore difficult to model accurately [20]. This is because critical parameters influencing the dissolution of solid samples such as the particle size and shape, level of aggregation and agglomeration and the interaction between the particles are difficult to analyse accurately [21]–[23]. The continuous change of these parameters throughout the dissolution enhance this difficulty. Therefore, the accuracy of results obtained from multi-particle systems counts on the reliability of the fundamental analytical measurements [24]. This problem can be

prevented by estimating the dissolution rate from single granules. By examining single particles, the cohesive interactions between particles can be neglected. The single-particle approach thus eliminates the hypothesis concerning parameters affecting the dissolution behaviour, and the results can, therefore, be noted as more trustworthy. Furthermore, knowing the specific size and shape of a granule enables the correlation between these parameters and the dissolution kinetics. This in return enables the extrapolation of the obtained data to any granule size distributions, shape distributions or active surface areas. The dissolution behaviour of a porous particle relies upon the solubility of particle compounds. Based on that, granules can be separated into two categories, dissolvable and non-dissolvable. Most particles used in the new industrial applications consist of several chemical compounds which have different solubilities. At the same time, multi compound particles usually have porous microstructure. Therefore, their dissolution process is more complex than the dissolution of one ingredient solid granules.

Researchers [1], [5], [6] proposed, three subsequent stages regarding the dissolution process of a solid particle: diffusion of solvent to the dissolving particle surface, the transformation of dissolved material from solid to solute condition instantly at the dissolution surface, and the transfer of solute (by diffusion and/or convection) from the surface to the bulk solution. In these steps, the kinetics of the dissolution mechanisms are influenced not only by the physical but also the chemical characteristics of the liquid medium (e.g. surface tension, viscosity, density, temperature) and those of the powder itself (e.g., particle size, density, porosity, chemical composition) [1]. However, in a case of a porous sample, e.g. detergent powder, numerous steps consist the dissolution process: i) wetting, intrusion of liquid into pores via capillary action, ii) sinking, submersion of

granule in the solvent, iii) disintegration of the primary particles within the solvent and iv) the dissolution of primary particles [7], [8].

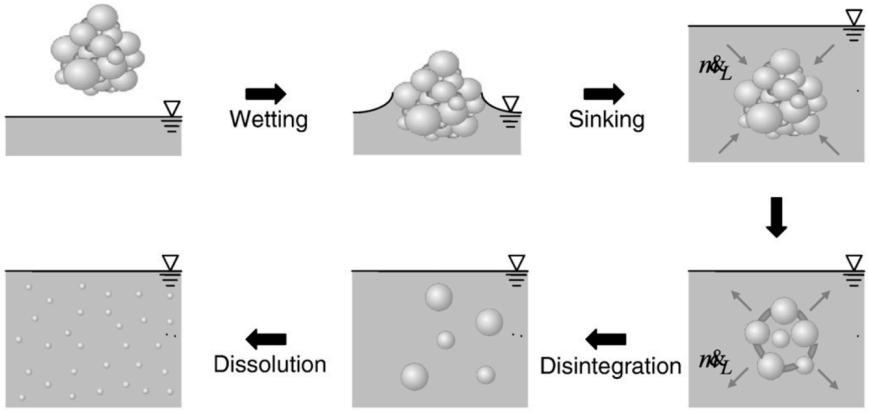

Figure 2-11 Schematic representation of dissolution stages of the agglomerated particle [8].

The corresponding four stages of dissolution can exhibit independently, but some overlapping may happen, depending upon the amount of material and enhance the difficulty to understand the mechanism of dissolution.

2.3.1 Single particle diffusion dissolution theory

The investigation of the dissolution rate of single granules was based on the theory of diffusion. Single particle diffusion dissolution is more complex than that of fixed surface area tablets due to changes in surface area and/or shape during time. Also, the variability of the size and shape of the granules, promotes the difficulty to model their dissolution process.

The hypothesis regarding the theory of diffusion for dissolution of individual particles is that there is a stagnant diffusion layer covering the granules and that diffusion of solute dominates the dissolution rate of the particles via the stagnant layer. Different hypothesis about the diffusion layer thickness, and the concentration gradient of solute across the

layer covering a single granule, resulted to the derivation of various single particle diffusion dissolution models.

Three diffusion-controlled models Hixson and Crowell, “cube-root law” (see Equation (2-5)), Niebergall et al., “square-root law” (see Equation (2-20)) and Higuchi and Hiestand, “two-thirds-root law” (see Equation (2-21)) have been presented for single spherical particle diffusion dissolution. Each one of these dissolution models provides a sufficient fit to specific experimental dissolution measurements [43], [64], [66]. But, the selection of the model to fit experimental measurements is to some extent subjective. Although they seem different, the three numerical solutions are frequently hard to differentiate when experimental data are implemented. Pedersen and Brown [99] validated these three approaches by conducting dissolution experiments of tolbutamide powder. Considering the particle size distribution in their numerical analysis, they identified that the fitted curve of the cube-root model had the smallest deviation compared to the rest. Nevertheless, the fitting data of the cube-root and the square-root models were relatively evenly good.

A general solution for single particle diffusion dissolution was developed by Wang and Flanagan [23] by taking into account the curve of the concentration gradient in the diffusion layer around a spherical granule. Their research presents that the concentration gradient in the diffusion layer of a spherical granule is not linear at pseudo-steady-state conditions (see Figure 2-12) as is for planar surface dissolution (see Figure 2-1(a)).

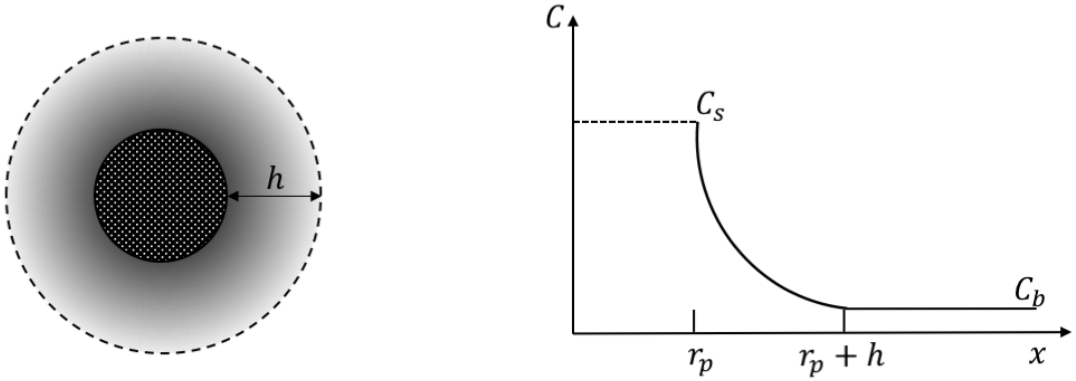

Figure 2-12 Pseudo-steady state concentration gradient around a spherical particle (radius = r_p and x = the distance from the center of the particle) [23].

In Wang and Flanagan's research, it was hypothesised that:

i) The particle is spherical and dissolves isotropically;

ii) The diffusion layer thickness around the granule (h) is constant;

iii) During dissolution, a pseudo-steady-state condition is set with only limited solid dissolution, after which the overall mass transport rates across the inner and outer spherical surfaces (at $x = r_p$ and $r_p + h$) of the diffusion layer are assumed to be equal;

iv) The solid-liquid saturated concentration (C_s) and solubility are not influenced by particle size;

v) The concentration of the bulk solution (C_b) is considered as zero, and the diffusion coefficient (D) is a constant across the diffusion layer.

Due to the concentration gradient throughout the diffusion layer on granule's surface is not linear, it is a function of distance from the centre of the particle and is determined as

$$\frac{\partial C}{\partial x} = -C_s\left(\frac{1}{r_p} + \frac{1}{h}\right) \tag{2-33}$$

Using the theory of diffusion and the mass balance law, the single particle diffusion dissolution equation becomes

$$\frac{DC_s}{\rho h}t = r_{p,0} - r_p - h\ln\frac{h + r_{p,0}}{h + r_p} \tag{2-34}$$

where $r_{p,0}$ is the initial spherical particle radius.

And the time needed to complete dissolution, τ_d at r_p= 0 is given by

$$\tau_d = \frac{\rho h}{DC_s}\left(r_{p,0} - h\ln\frac{h + r_{p,0}}{h}\right) \tag{2-35}$$

Introducing spherical particle weight W_p in Equation (2-34)

$$\frac{DC_s}{\rho h}t = \left(\frac{3W_{p,0}}{4\pi\rho}\right)^{1/3} - \left(\frac{3W_p}{4\pi\rho}\right)^{1/3} - h\ln\frac{h + \left(\frac{3W_{p,0}}{4\pi\rho}\right)^{1/3}}{h + \left(\frac{3W_p}{4\pi\rho}\right)^{1/3}} \tag{2-36}$$

where $W_{p,0}$ is the initial spherical particle weight.

Wang and Flanagan also presented that the three-single particle diffusion-controlled models are approximate solutions to the general model. The general equation is transformed to "cube-root law" for particles much larger than h and to "two-thirds-root law" for particles much smaller than h.

General single particle diffusion dissolution model also showed that the surface specific dissolution rate relies upon particle size, where bigger granules exhibit lower values.

$$G = DC_s\left(\frac{1}{h} + \frac{1}{r_p}\right) \tag{2-37}$$

2.3.2 Single particle diffusion dissolution experimental studies

A limited amount of research on single particle diffusion dissolution was conducted through the years. In 2001, Bechtloff et al. [25] studied the dissolution of single borax crystals in propionic acid and presented that the macro kinetics of solid-liquid reactions and their rates can be determined by an initially added amount of the product or by-product, but no numerical explanation of the dissolution kinetics was demonstrated. Two

years later, Bhandari and Roos [26] examined the dissolution of single sucrose crystals in molten sorbitol at different conditions using DSC and a microscope. The dissolution indicated by the increased glass transition of the melt decreased melting endotherm of sucrose, decreased enthalpy of sorbitol in glass transition and microscopic observations.

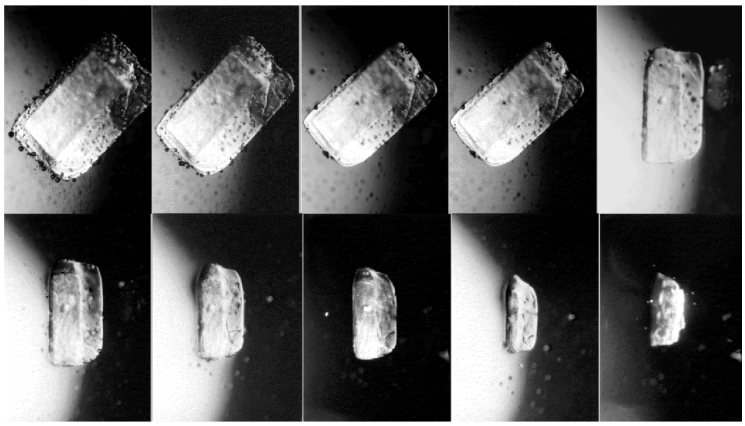

Figure 2-13 Diffusion dissolution of sucrose crystal in sorbitol melt at 130dC using optical microscopy [26].

A research focusing on single particle dissolution has been conducted by Marabi et al., [1], in 2008, who measured the dissolution kinetics of individual spherical sucrose granules in stagnant conditions using a microscope. Via image processing of the recorded data, they extracted the dissolution rates of the single particles. They also simulated the impact of the liquid viscosity on the dissolution kinetics using a shrinking sphere model. Furthermore, they showed that the granule kept its spherical shape throughout the process. A calorimeter has been used to measure dissolution enthalpy and showed that high endothermic response leads to slower dissolution rate. Later, to prove the feasibility of their approach used the same experimental principles to investigate the dissolution of maltodextrin and skim milk powder [18].

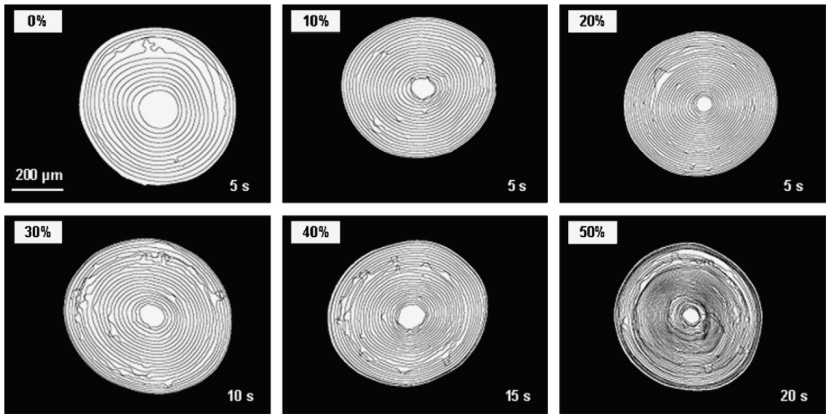

Figure 2-14 Optical images of dissolution process of a sucrose sphere at different concentrations of polyethylene glycol (molecular weight 1000) solutions showing the moving boundaries as a function of time [1].

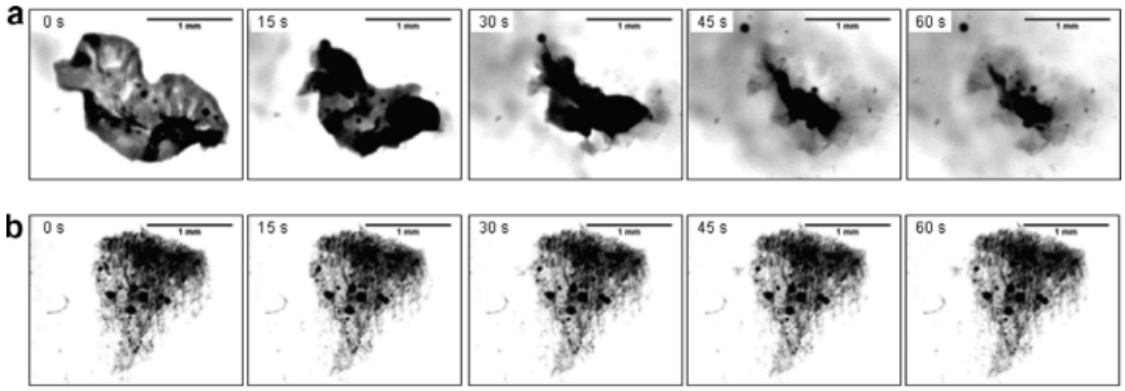

Figure 2-15 Single particle diffusion dissolution of (a) skim milk powder and (b) freeze-dried skim milk powder in water at 30dC as a function of time [18].

In 2011, Østergaard et al. [100] used a commercially available UV imaging detector to measure the dissolution of lidocaine from a single crystal into the aqueous buffer but faced limitations regarding the crystal size and dimensions, the position of the crystal as well as hydrodynamics. The results demonstrated that salt could alter the local pH (and the dependent phenomena) of the dissolution medium. More recently, in 2014, Svanbäck et al., [28] compared image analysis and UV-Vis single pellet dissolution data to evaluate the applicability of microscope as a method for measuring dissolution. They showed that image analysis could potentially be used as an analytical method for single particle dissolution experiments. The last single particle diffusion dissolution study conducted by

Li et al., [29]. They examined the effect of temperature and pH on diffusion dissolution kinetics of individual spherical sodium carbonate particles. The obtained release profiles were fitted using a Noyes-Whitney based surface reaction model, while the extracted dissolution rate constant was simulated using a mass transport model. Results showed that the dissolution rate constant increases with the increasement in temperature but decreases with the increasement in pH.

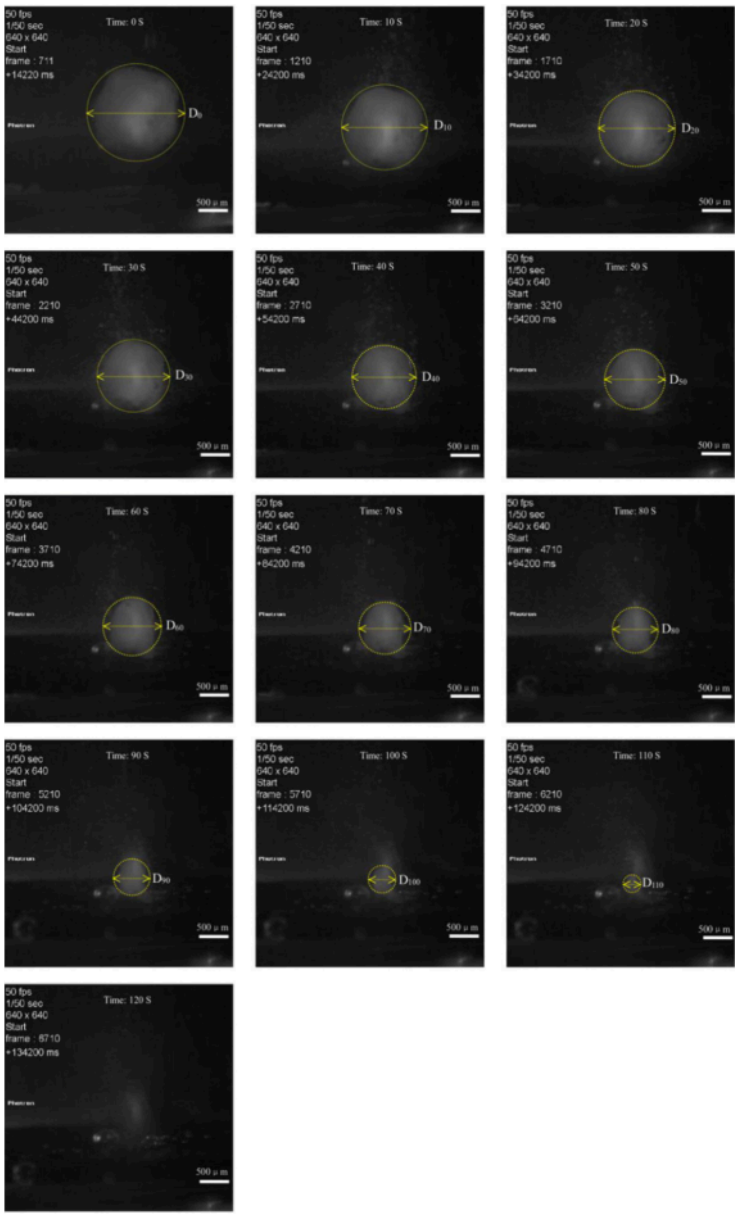

Figure 2-16 Evaluation of diameter of dissolving sodium carbonate granule, sitting on a flat surface, as a function of time [29].

2.3.3 Single particle diffusion dissolution simulation studies

One of the most significant challenges of simulation of particle dissolution (either diffusion or convective) are the moving boundaries. The complication of pursuing the movement of the interface is due to the discontinuity of concentration in this section.

To simulate effectively the dissolution process researchers developed different mathematical models by generating their own codes.

In 1966, Readey and Cooper [101] published the differential equations dominating the dissolution of a sphere dominated by diffusive mass transfer where the effects of a moving boundary and of the resulting radial convective mass trasnefer were examined.

Vrentas and Shin [102], [103] evaluated the slow and fast evolution of dissolution rates of single spheres and presented a different solution for the moving boundary obstacle.

Vermolen et al., [104] have developed a semi-numerical model for the prediction of the dissolution of spherical granules in liquid medium as a relation of initial concentration differences between particle and matrix and interface concentration. A good agreement between semi-analytical and numerical results was obtained for most conditions. A Monte Carlo statistical analysis on the effect of surface roughness on the dissolution of SiO_2 aerogels conducted by Prokop'ev et al., [105]. They commented that the dissolution rate increased as the surface area of roughness increased for small diameter primary particles (2.9 nm and 3.5 nm). For these, the value of dissolution time is in a similar manner as the time required to reach steady-state roughness. However, the numerical values were not validated with experimental results.

In 2004, a modified shrinking sphere model developed by Mgaidi et al., [106] for the dissolution of sand at increased temperature and pressure considering the effect of particle size, temperature and hydroxide ion molality. A good agreement between predicted

values and experimental data has been noticed. They also expressed their will to investigate the effect of stirring speed.

Ansari and Stepanek [107] presented a 3D virtual diffusion dissolution of a single particle with varying porosity and binders. The solid-liquid interface was removed according to the local diffusion mass flux, gathered by determining the diffusion numerical solution in the boundary layer in-between the surrounding fluid. However, they have not shown any validation of their modelling results with experimental measurements.

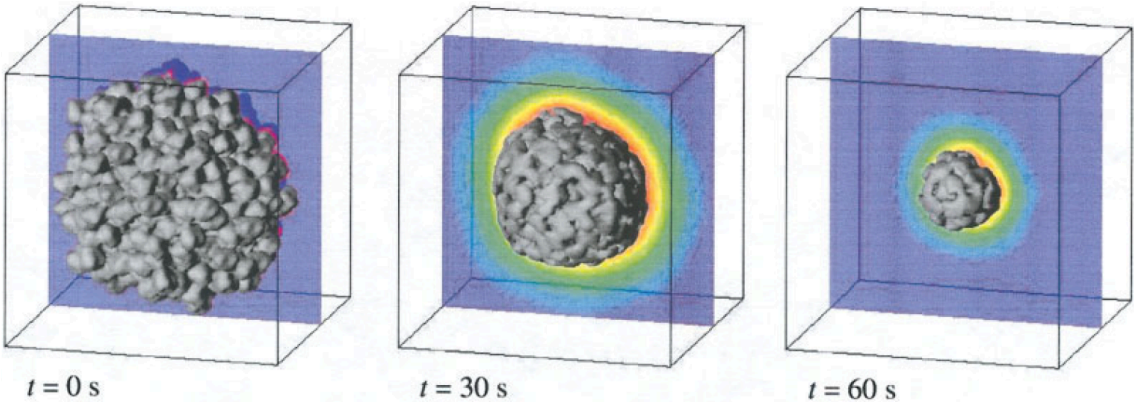

Figure 2-17 Illustration of the simulation of diffusion-limited dissolution of a virtual granule [107].

More recently, in 2013, Yuan et al. [80] validated the "DigiDiss" code developed by Jia et al., [79] (a combination of X-ray Micro tomography (XRT) and Lattice-Boltzmann method (LBM)) by correlating simulation and experimental measurements. XRT has been used to scan single crystals (sugars) and the cluster to obtain a digital approach of their microstructures. Then they were implanted in the "DigiDiss" to simulate their diffusion dissolution. Furthermore, the same granules were dissolved in aqueous solution, and the dissolution procedure was recorded using an optical setup. The total dissolution times and pictures of granule size and shape during dissolution were evaluated.

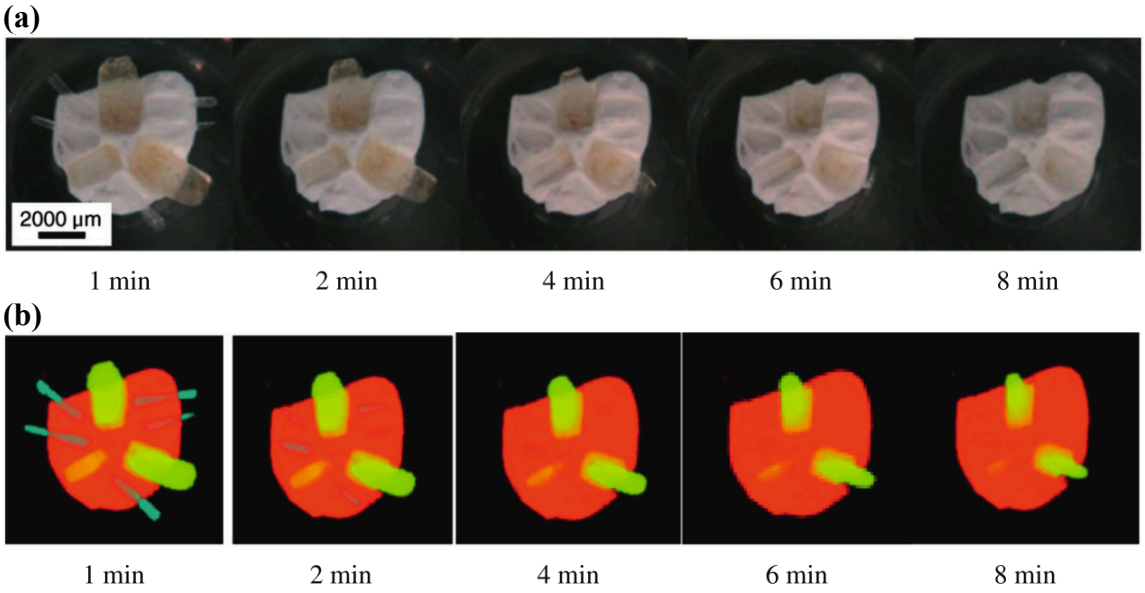

Figure 2-18 (a) Optical images of a dissolving particle cluster of sodium mono glutamate crystals and brown sugar particles in water; (b) simulated dissolution procedure of the cluster [80].

To increase the accuracy of dissolution predictions of polydisperse particles Wang et al., [108], in 2015, developed a diffusion-controlled "hierarchical" model considering the role of particle-size distribution width with various dose level and the importance of "confinement" on dissolution.

2.3.4 Single particle convective dissolution theory

The single particle convective dissolution model has the benefit to be more hydro-dynamically realistic than the single particle diffusion dissolution one. Using convective diffusion principles to single spherical particle dissolution has the advantage to be able to model dissolution rate precisely.

A convective diffusion model for a sphere was developed by Levich [109]. Hypothesized that the flow of the solvent around a granule is in creeping condition, while the boundary layer is small compared to granule size, Levich generated an equation for mass transfer to a free-falling sphere based on convective diffusion

$$\nabla(D\nabla C) = \bar{u}\nabla C \tag{2-38}$$

where C is scalar concentration and $\bar{u}$ is vector fluid velocity.

This equation can be used when the Reynolds number is much less than 1, while the Peclet number is greater than 1. When this equation is used for spherical particle dissolution, it can be stated as

$$V\frac{dC}{dt} = 7.98C_s D^{2/3}u^{1/3}r_p^{4/3} \tag{2-39}$$

where u is fluid velocity.

The surface specific dissolution rate G is evaluated by normalising Equation (2-39) by granule surface area ($4\pi r_p^2$), which results to

$$G = 0.635C_s D^{2/3}u^{1/3}r_p^{-2/3} \tag{2-40}$$

The importance of Equation (2-40) is that the surface specific dissolution rate depends on surface curvature. For the same particle surface area, bigger particle sizes have lower dissolution rates.

Chen et al., [62] showed that although the expressions are different, this conclusion qualitatively confirms the single spherical particle diffusion controlled model developed by Wang and Flanagan [23]. Using this expression for diffusional flux under those flow conditions it can be written as

$$W^{5/9} = W_0^{5/9} - 2.35C_s D^{2/3}u^{1/3}\rho^{-4/9}t \tag{2-41}$$

2.3.5 Single particle convective dissolution experimental studies

Convective dissolution experiments of single particles have been carried out in only a few cases, mainly in chemical engineering, but recently also in food and pharmaceutical sciences. The first paper published in 1996 by Dorozhkin [30] who investigated the effect

of flow on dissolution kinetics of phosphate rock, utilising images of single dissolving particles, and modelled the dissolution process using of the Fokker–Plank equation. Effects of dislocation acceleration of dissolution rate and random fluctuations of crystal size have been discovered. Both phenomena have been described as a micro-mechanism of dissolution.

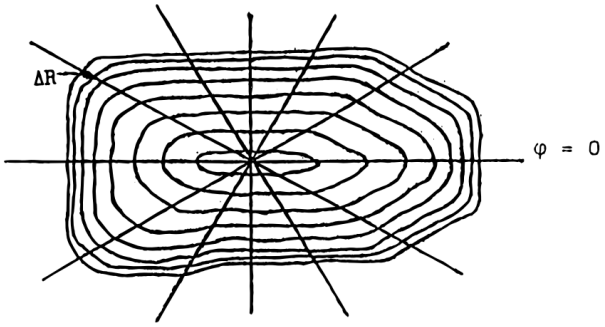

Figure 2-19 Dissolution plot of phosphate rock crystal under equal time intervals [30].

In 2002, Raghavan et al. [31] presented the dissolution kinetics of a-lactose monohydrate single crystals using a flow cell technique at various under-saturations. They obtained linear dissolution profiles as a function of time for most of the crystal phases investigated. Crystals showed high anisotropy in dissolution. Thus, granules of the same material but different shape had different dissolution profiles. They also identified the importance of lattice strain in the determination of the dissolution rates. The dissolution anisotropy phenomenon of paracetamol crystals has been investigated, the same year, by Prasad et al., [32] using a flow-cell single crystal dissolution method recording with a microscope. Results agree with the hypothesis that integral strain increases the solubility and the dissolution rate of the material. Eleven years later, Börjesson et al. [33] used a custom-made flow cell to investigate the dissolution kinetics of individual spray dried sodium caseinate particles using optical microscopy. They preferentially oriented the granules by squeezing them between two glass slides and considering a cylindrical morphology in

their calculations. Results showed that dissolution rate is a function of the flow rate of the dissolving medium. Also, they observed a significant variation in particle morphology and microstructure, which was assumed to cause the wide variation of dissolution rate between granules.

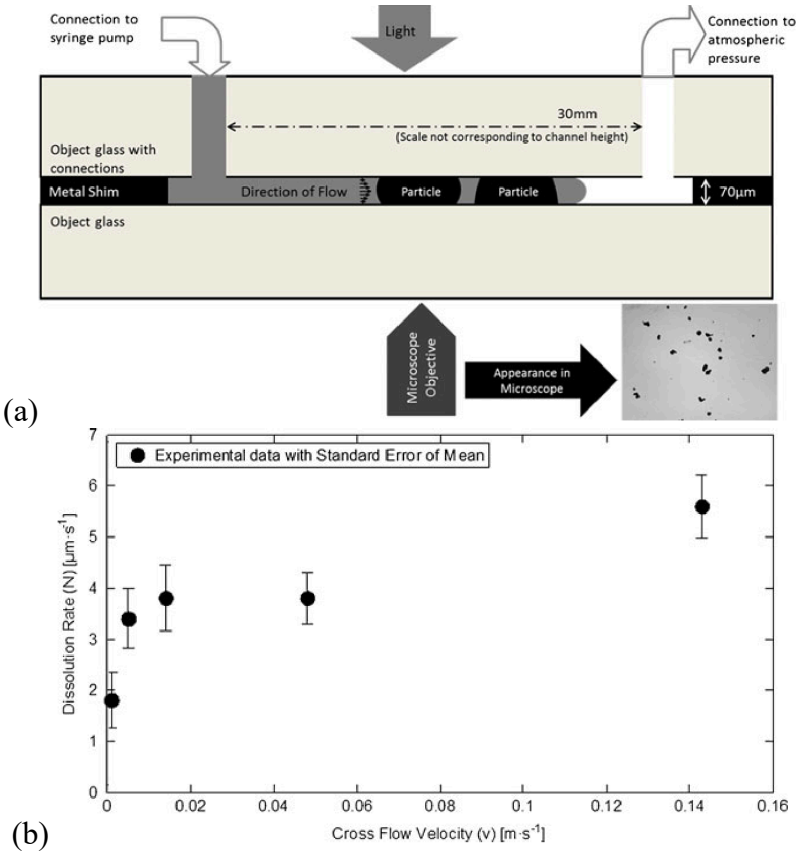

Figure 2-20 (a) Schematic representation of the single sodium caseinate particles convective dissolution experimental setup; (b) the relationship between mean particle dissolution rate and fluid velocity [33].

In 2015, Svanbäck et al., [34] developed a single particle flow cell based on Einstein's teacup principles (see Figure 2-21) for the real-time determination of intrinsic dissolution rates of individual drug compounds. The changes of the surface area of the compounds were measured using a 3D particle projection algorithm. The last convective single particle dissolution study conducted in 2016 by Smrčka et al., [35] measured the dissolution and disintegration kinetics of drug particles with the use of a flow-through

measurement cuvette and a combination of UV-Vis and light scattering. They have unveiled various mechanisms (see Figure 2-22) that cannot be revealed from the bulk measurements or common dissolution tests. Their research has demonstrated that there can be particles within a single batch that have different dissolution kinetics, "weak" granules that disintegrate during dissolution (followed by an alteration particle size), or "strong" granules that retain their particle size and from that the active compound is slowly released.

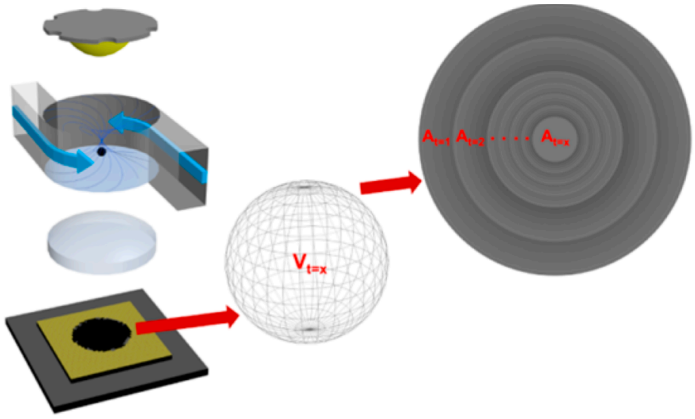

Figure 2-21 Schematic overview of the modified Einstein's teacup method developed by Svanbäck et al., [34].

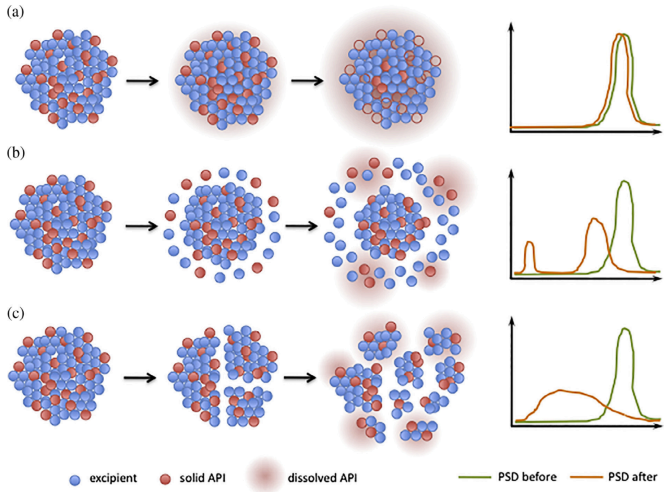

Figure 2-22 Schematic representation of the three main disintegration mechanisms in single particle dissolution (a) leaching, (b) surface erosion and (c) break-up, followed by a change in particle size distribution [35].

2.3.6 Single particle convective dissolution simulation studies

One of the biggest challenges of simulation of particle dissolution are the moving boundaries. The complication of pursuing the movement of the interface is due to the discontinuity of concentration in this section.

To simulate effectively the dissolution process researchers developed different mathematical models by generating their own codes.

Hodges et al., [110] combined first-order kinetics with the appropriate mass transfer equations to simulate the dissolution of lactose. Three different regions identified depended on lactose concentration, a) saturated lactose solutions b) concentrations between α-lactose solubility and saturated solutions and c) concentrations below a-lactose solubility. Based on that three differential equations developed to describe the dissolution process. Results compared with experimental data and showed good fitting for the first two regions. Five years later, Lowe et al., [111] published a paper suggesting that the lack of fit in the third region is due to the surface reaction rate at which the lactose molecules are dissociated from the crystal surface. They developed a surface reaction model. Data showed good agreement with numerical values.

In 1999, a dynamic partial differential equation was developed by Koiranen et al., [112], to predict convective dissolution of sucrose crystals using as parameters crystal size distribution experimental measurements.

František Štêpánek has extensively studied the modelling of the particle dissolution through the years. First [87], in 2004, he generated a three-dimensional virtual particle model with different microstructure parameters (porosity and binder). The model is based on a vector method, using a surface mesh to introduce particle dimensions and computational fluid dynamics (CFD) to evaluate the flow. Then conducted virtual particle

dissolution experiments with and without flow, using a convective-diffusion equation for each ingredient of the particle in the surrounding fluid phase, by gradually removing material. He found correlations between granule structure, formulation ingredient properties and the dissolution half-time.

Following this study, four years later, Štêpánek and Ansari [113] modified the dimensional virtual particle model by importing two different particle design techniques, Stochastic design technique and variational design technique to manufacture complex microstructures. Then compared simulated and experimental results showed that regardless of the effect of granule size, distribution of ingredients within the particle and particle formulation and porosity, granules composed of primary particles bonded together with binders dissolve slower than particles directly exposed to the solution.

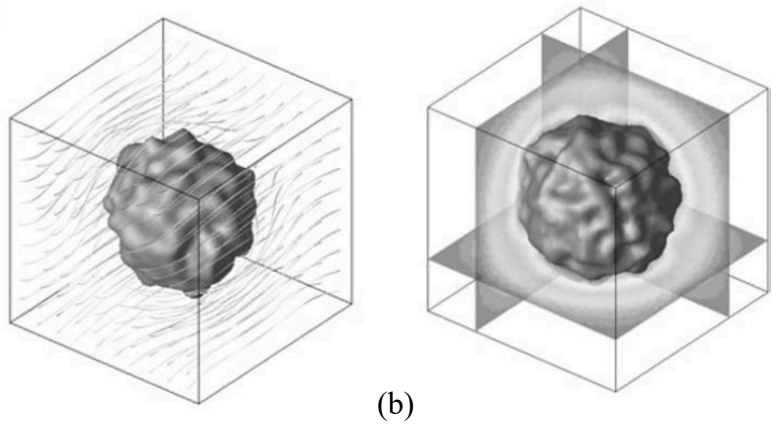

(a) (b)

Figure 2-23 Dissolution of a virtual particle. (a) Streamlines presenting the velocity profile around a partially dissolved particle; (b) Concentration profile of a main compound around a partially dissolved particle [87].

Jia et al., [79] use X-ray Micro tomography (XRT) and Lattice-Boltzmann method (LBM) to generate the code called “DigiDiss” which can simulate dissolution of granules by introducing XRT particle microstructure to LBM. The structure can be implemented in LBM because is expressed in lattice grid. The finite difference technique can be used to

solve the convective diffusion model (2-11) and the Noyes-Whitney equation (2-2) for the solid-liquid interface.

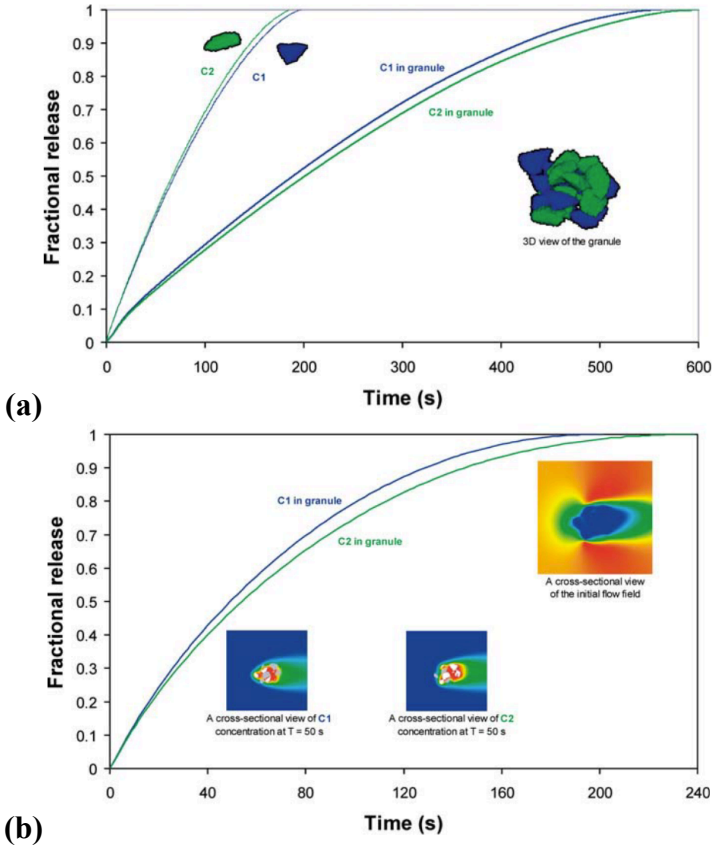

Figure 2-24 Simulation dissolution profiles of (a) standalone component particles and their agglomerate under diffusion-only conditions and (b) components of the same agglomerate under flow conditions [79].

Finally Cao et al., [114], in 2016, linked CFD simulation and Noyes-Whitney equation to build a model that connects energy input of the mixing system with the dissolution process. Non-porous sodium carbonate particles and multi-compound granule have used to validate the model. Good correlation between experimental and simulation results at different agitation speeds and temperatures has been noticed. Therefore, the model can be applied for the prediction of bulk dissolution on turbulent conditions where all the granules are well distributed in the dissolution vessel.

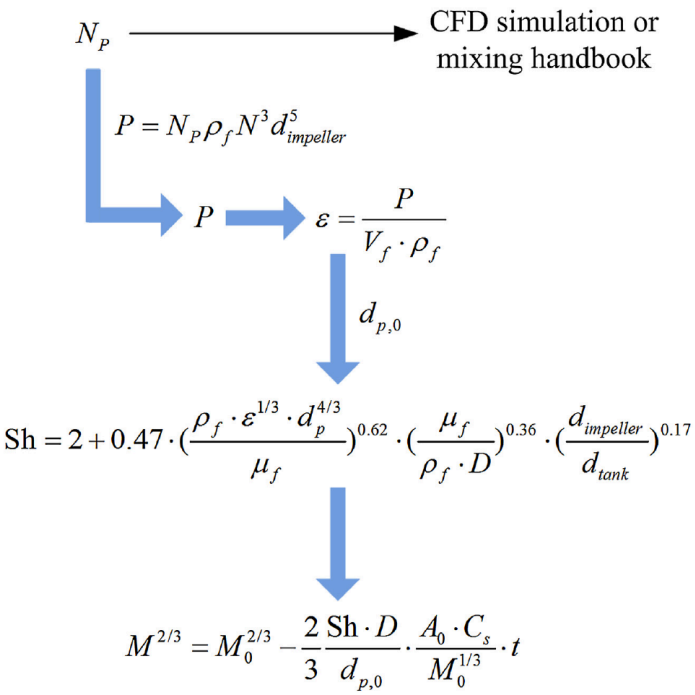

Figure 2-25 Structure of the model for linking energy input of the mixing system with the dissolution of particles [114].

2.4 Bulk particle dissolution

An extensive and wide-experimental examination has been performed in the understanding of dissolution mechanisms of commercial powders (primarily pharmaceutical and food) [1]. In the past, common techniques are frequently applied, that consider the evaluation of dissolution kinetics using a USP (U.S. Pharmacopeia) dissolution apparatus and various chemical analytical techniques.

2.4.1 Bulk particle dissolution theory

The bulk particle dissolution theory strongly depends on the type of the particles, monodisperse or polydisperse.

For the diffusion dissolution of N monodispersed particles, Equation (2-36) becomes

$$\frac{DC_s}{\rho h}t = \left(\frac{3W_{b,0}}{4N\pi\rho}\right)^{1/3} - \left(\frac{3W_{b,t}}{4N\pi\rho}\right)^{1/3} - h\ln\frac{h + \left(\frac{3W_{b,0}}{4N\pi\rho}\right)^{1/3}}{h + \left(\frac{3W_{b,t}}{4N\pi\rho}\right)^{1/3}} \quad (2\text{-}42)$$

where $W_{b,0}$ is the initial weight of bulk particles, and $W_{b,t}$ is the weight of bulk particles at time t.

For the convective dissolution N monosized spherical particles, Equation (2-41) becomes

$$W_{b,t}^{5/9} = W_{b,0}^{5/9} - 2.35C_s D^{2/3}u^{1/3}\rho^{-4/9}N^{5/9}t \quad (2\text{-}43)$$

Classic particle dissolution theories, such as "cube-root-law", are designed only for single or monodisperse particle dissolution. Nevertheless, most of the commercial powders used consist of different sized particles. Size fractions from powders have frequently applied in dissolution studies. Using theoretical measurements, Brooke [115] stated that when considered as mono-sized powders, the calculation standard deviation can be approximately 3% for the smallest size fraction determined by the particle size distribution. For wider size fractions, the error can raise up to 6-10%. Thus, a theoretical analysis on influence of polydispersity is required even for quite narrow distributed powders.

Most detergent powders are manufactured using spray drying method, and as a consequence, tend to produce asymmetrical particle size distribution. A distribution like that can be transformed to a Gaussian by converting the x-axis to logarithmic. Such a distribution is log-normal. A common hypothesis, in most theoretical studies on polydisperse particle dissolution, is that particle size distribution is log-normal.

Higuchi et al., [116] conducted a dissolution study on polydisperse pharmaceutical powder considering a log-normal distribution. By implementing the particle size distribution values to the "two-thirds-root-law", they managed to evaluate the bulk

particle dissolution profile. Moreover, the theory developed was validated by experimental results.

On the other hand, Brooke [117] determined a similar theory for log-normal distributed powder dissolution using the "cube-root-law"

$$\begin{aligned} W_\tau = re^{3(\mu+3\sigma^2/2)}\left(1-F\left[\frac{\ln(\tau)-(\mu+3\sigma^2)}{\sigma}\right]\right) \\ -3r\tau e^{2(\mu+\sigma^2)}\left(1-F\left[\frac{\ln(\tau)-(\mu+3\sigma^2)}{\sigma}\right]\right) \\ +3r\tau^2 e^{(\mu+\sigma^2/2)}\left(1-F\left[\frac{\ln(\tau)-(\mu+\sigma^2)}{\sigma}\right]\right) \\ -r\tau^3\left(1-F\left[\frac{\ln(\tau)-\mu}{\sigma}\right]\right) \end{aligned} \tag{2-44}$$

where

$$F(x)=\frac{\sqrt{2}}{2\pi}\int_{-\infty}^{\chi} e^{-x^2/2}dx$$

and

$$\tau=\frac{2kC_s}{\rho t}$$

where W_τ is the undissolved weight, μ is the mean particle diameter, σ is its standard deviation, $r=\pi\rho N_{particles}/6$ ($N_{particles}$ = number of particles), k is a constant.

Moreover, Brooke [118] showed that particle size distribution of many powders is truncated. Thus, using a non-truncated distribution or ideal log-normal distribution, high deviations will be caused. If the same equation, was used for a truncated distribution, the result will be falsely adding some larger or smaller particles than the existed ones. However, the error caused by the addition of larger granules is more significant than for smaller. This is due to that, for a similar number of granules, the total mass of the smaller

granules is significantly lower than that for bigger granules. Brooke then determined an approach for truncated log-normal distributed powder dissolution which can be applied before the moment that the smallest particles fully dissolve.

With faster computational methods, there is not a significant need for a model that will be able to combine a classic particle dissolution theory with a particle size distribution function to predict bulk particle dissolution profile. If the particle size distribution is known, the bulk particle dissolution process can be measured by using each size cut independently and then summarising them together. The benefit of this method is that the size of granule does not have to obey a precise distribution. Researchers [119]–[121] have shown that sufficient data can be produced using this approach.

A critical assumption that each particle dissolves by itself, has been taken in all the above dissolution studies. This might not be correct under certain experimental conditions as the dissolution of each granule is affected by the dissolution of others due to aggregation. Therefore, the above bulk particle dissolution theories cannot apply to such conditions.

2.4.2 Bulk particle dissolution studies

Dissolution rates are usually acquired, from the different formulation industries, by compressing the powder into tablets, and then conducting rotating disc dissolution experiments. In 1983 Nicklasson et al., [9] used rotating disc experiments to determine the dissolution rates of Sulfamethizole at different concentrations applying an extrapolation procedure. More recently Kaunisto et al., [11] evaluated the rotating disc method for dissolution rate measurements comparing experimental results and CFD model, using aspirin and benzoic acid. On the other hand, a specific amount of powder could be dissolved in a stirred fluid, and the concentration increases as a function of time. Carstensen et al., [122] used Hixon-Crowell cube root law to extract mass transfer

dissolution rate constants of polydisperse powders dissolving in a dissolution apparatus. Kravtchenko et al., [13] used a modified rotational viscometer to record the dissolution kinetics in order to overcome the lump formation of pectin powders during dissolution and their stickiness in the stirrer. Results shown that grains dissolve individually under dispersing conditions, while under non-dispersing formation of lumps is high. Parker et al., [123] point out that although Kravtchenko et al., method gives reproducible results their attempts at measuring viscosity vs time led to highly inconsistent results due to the high variation of lump formation. So, they developed a dissolution model independent of this phenomenon. A flow-through cell dissolution apparatus has been used by Bhattachar et al., [10] to test a soluble drug compound. Different approaches of loading the pharmaceutical powder and their influence on dissolution performance were tested. A suspension form of the sample found to be the most compatible. An extensive research on the effect of particle size, concentration and molecular weight on dissolution kinetics of guar gum powders have been performed by Wang et al., [15], [16] using a mixing jar. At intermediate concentrations, the dissolution rate increased as concentration increased while at high concentrations by increasing the concentration the rate decreased. The molecular weight had a reverse connection with the dissolution rate. Larsen et al., [17] developed a method for the evaluation of dissolution kinetics of alginate powders using a rheometer. The shear stress value has been used as an indication for viscosity to calculate the dissolution curves. Then the dissolution profiles were fitted to an exponential function to obtain dissolution rate constant. Increasing the concentration and the particle size the dissolution rate decreased. Research on the investigation of dissolution kinetics using calorimetry has been presented by Marabi et al., [18]. A decrease in the moisture content leads to a high exothermic response and a faster

dissolution. A conductivity meter has been used by Gianfrancesco et al., [12] to examine physical characteristics and the dissolution behavior of protein-based powders. They showed that lactose as a binder delays crystallisation and results to a faster dissolution performance.

2.4.3 Chemical release of bulk particles ingredients

Spray dried detergent particles can be treated as a big particle formed from smaller particles bonded together with the use of a binder. Today's detergent powder is a multi-ingredient product that contains three primary ingredients which are surfactant (∼20 wt%), builders (∼25 wt%) and fillers (∼40 wt%) [124], [125]. The most common surfactant is the linear alkyl benzene sulfonate (LAS). As a builder, usually sodium tripolyphosphate (STPP), citric acid and sodium citrate, zeolites and sodium layered silicate are selected, and as a filler, sodium sulphate or sodium chloride is often used.

Particles differ between them due to the different microstructure that they exhibit. A possible structure could be that builders are the core and the rest compounds act as a surrounding layer which covers it. From a different view, the structure of a particle might possibly be a mix of all compounds. When a particle is immersed in a liquid medium, the soluble ingredients dissolve from the inner structure as well as the surface. Their dissolution process depends on particle microstructure, particle size, water filling rate of porous and the dissolution of each compound and their interactions. Nevertheless, the understanding of the chemical release of the particle ingredients and how to control it is still considered as a key target. Therefore, many industries are highly interested in the examination of these parameters as they will enhance product performance and quality.

However, a limited amount of studies, mainly in the pharmaceutical sector, have been conducted in this area. Sergei Kazarian from Imperial College London focused his

research on understanding of release of active pharmaceutical ingredients. He used FTIR spectroscopic imaging in combination with flow through cells for attenuated total reflection (ATR) [126], [127]. This approach was characterised as "chemical photography" method. With this method was able to study pharmaceutical tablet dissolution and drug release [128]–[130]. The data produced can reveal the concentration distribution of a compound within the imaging area. He developed two custom-made dissolution experimental set-ups. The first one was a dissolution cell which allowed to compress the powder on the detecting surface of the ATR-FTIR imaging area. The other one was a transparent flow chamber that could attach to the ATR-FTIR imaging modules. The benefit of these approaches was that at the same time visual images of drug dissolution and ATR-FTIR could be captured [131].

Wray et al., [132] compared dissolution profiles obtained from dissolution turgs experiments with ATR-FTIR spectroscopic imaging with UV detection of dissolved pharmaceutical. They found that the UV release profiles correlate well with those from the dissolution vessel.

One year later, Wray et al., [133] presented that NIR chemical imaging can be used for dissolution experiments by implementing a flow-through dissolution cell to compress a tablet.

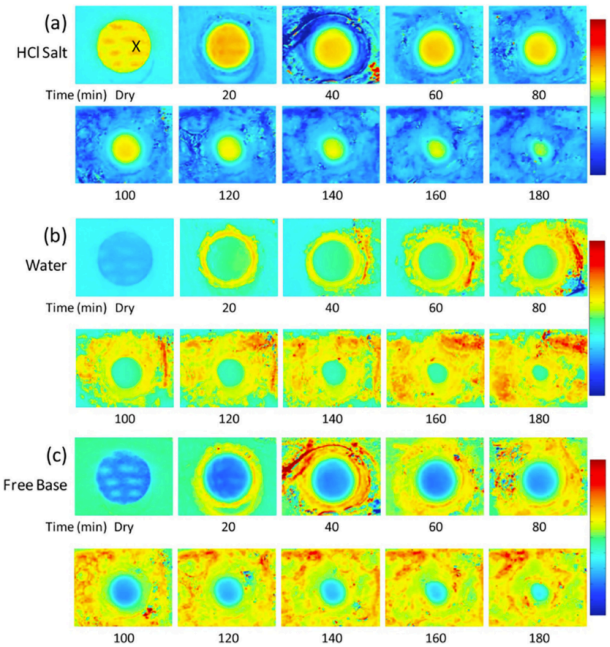

Figure 2-26 NIR images for the distribution of (a) ionised HCl salt form, (b) water and (c) free based on a pharmaceutical tablet dissolution [134].

In 2017 Punčochová et al., [135] examined the dissolution process of spray-dried multi-component drug formulations via three spectroscopic imaging methods: MRI, ATR-FTIR imaging and Raman mapping. The dissolution profiles were obtained using dissolution turgs. The comparison of the different methods was able to develop a hypothesis and determine the mechanism of pharmaceutical crystallisation using dissolution.

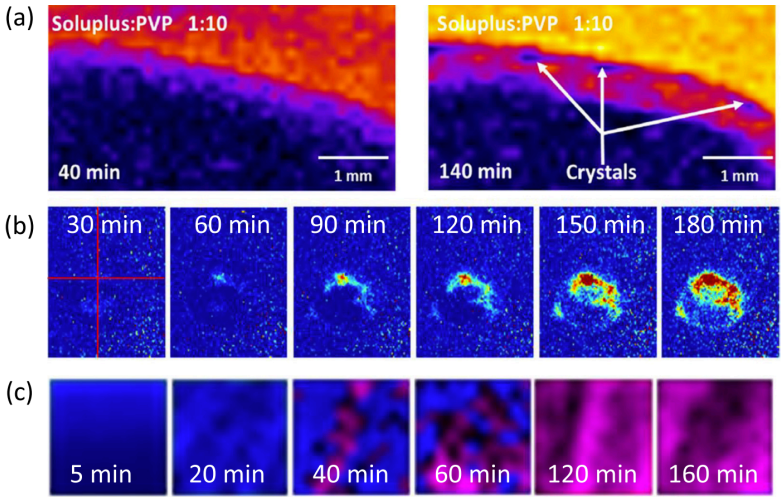

Figure 2-27 Dissolution of multi-compound pharmaceutical formulation using three different spectroscopic imaging methods. (a) MRI images of the interface of the tablet, (b) ATR-FTIR images and (c) Raman maps of the crystalline compound [134].

From the detergents point of view, Pan et al., [136] combined a UV-Vis spectrophotometer and a conductivity meter to study the dissolution of NaLAS and Na_2CO_3 granules respectively.

2.5 Dissolution measurement techniques

In the previous decades, the dissolution experimental setup has commercialized. Two main methods have been developed for conducting dissolution experiments, the stirred beaker technique and the flow through procedure as well as some other non-standard apparatus.

The most frequently applied worldwide dissolution apparatus are the rotating basket method and the paddle method.

2.5.1 Rotating basket method (USP Apparatus 1)

The apparatus, shown schematically in Figure 2-28(a), contain a covered vessel of specific shape and dimensions and capacity of 1000 mL (smaller volume vessels are used in certain occasions), a metallic shaft one end of which attaches to a motor, and a cylindrical metallic mesh basket that attaches to the opposite end of the shaft. The sample is placed inside the basket, and the basket assembly is immersed in the dissolution vessel containing dissolution medium and rotated at a specified speed. In 1970, it was confirmed as the official dissolution method by the United States Pharmacopoeia (USP) and characterised as the rotating basket method, USP Apparatus 1 [137].

2.5.2 Paddle method (USP Apparatus 2)

The paddle method was approved by USP as an official dissolution method a few years later than USP Apparatus 1 and presented as USP Apparatus 2. It is currently the most commonly used apparatus for solid samples. The dissolution vessel used for this method is the same as for the rotating basket method. Nevertheless, the basket assembly is

replaced by a specific dimension paddle as it is presented in Figure 2-28(b). With this approach, the solid sample is dropped into the dissolution vessel containing the solvent and allowed to sink into the bottom. The paddle is then rotated at a certain speed. The paddle can be immersed in the vessel before dropping the solid sample, but the rotation of the paddle should not start until the sample has been dropped. This is the usual industry procedure [137].

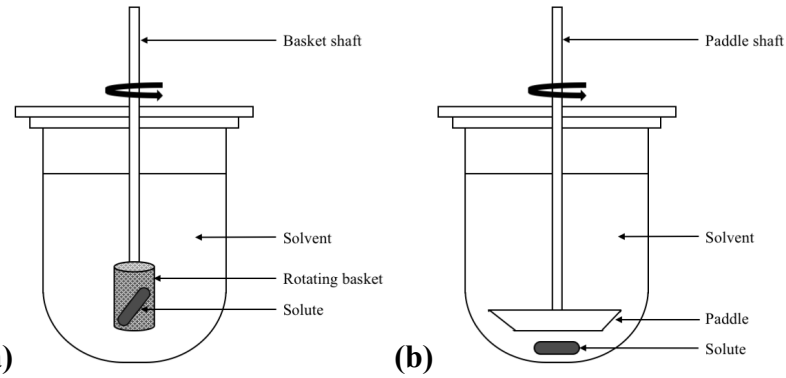

Figure 2-28 Schematic representation of (a) Rotating basket method (USP Apparatus 1); (b) Paddle method (USP Apparatus 2).

Both USP Apparatus1 and 2 are easy to operate and robust and are in most cases adaptable to a range of dissolution experiments for different structured products. Therefore, USP Apparatus 1 and 2 are suggested for dissolution testing.

A characteristic dissolution tergotometer is presented in Figure 2-29 . The machine can be configured for use with rotating baskets (USP Apparatus 1) or paddles (USP Apparatus 2) and can accommodate 1000 mL dissolution vessels.

Figure 2-29 6+6 position vessel dissolution tergotometer [138].

2.5.3 Reciprocating cylinder apparatus (USP Apparatus 3)

The United States Pharmacopeia incorporated the USP Apparatus 3 in 1991 as a different approach to rotating basket (USP Apparatus 1) and paddle method (USP Apparatus 2). The reciprocating cylinder apparatus was developed to overcome the difficulties of shaft wobble, location, centring and coning of USP Apparatus 1 and 2 [139]. The geometry is based on the disintegration tester as shown in Figure 2-30. This method can be used for extended release samples and for solids which are mostly non-disintegrating. The limitations of this method lie on the foam generation of surfactant and of the limited volume of dissolution medium [140].

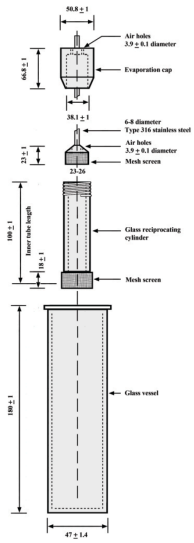

Figure 2-30 Schematic representation of reciprocating cylinder apparatus (USP Apparatus 3) [140].

2.5.4 Flow-through cell apparatus (USP Apparatus 4)

The flow-through cell method for conducting dissolution experiments was first presented in 1957 by the U.S. Food and Drug Administration (FDA). More recently in the 1990s was also adopted by the USP as an official dissolution testing method. The apparatus contains a reservoir which includes the solvent, a pump that moves the solvent upwards via the vertically placed flow cell and a water bath to monitor the temperature at the cell

as shown in Figure 2-31. Different categories of cells are used for different products. This method is commonly used for drug products like solids, semi-solids and liquids. The difficulties of this method base on the pump precision and the limited volume of dissolution medium [141].

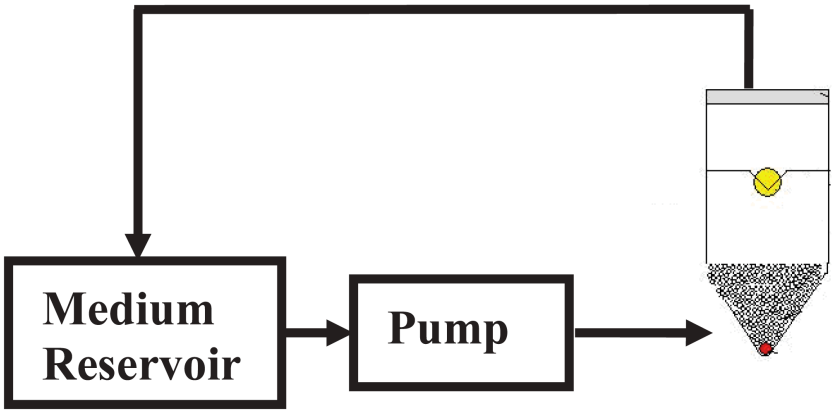

Figure 2-31 Schematic representation of flow through cell apparatus (USP Apparatus 4) [141].

2.5.5 Other USP dissolution apparatus

Other dissolution apparatus approved by USP include the paddle over disk apparatus (USP Apparatus 5), the cylinder apparatus (USP Apparatus 6) and the reciprocating holder apparatus (USP Apparatus 7). These methods were developed and primarily operated for the analysis of transdermal delivery systems.

2.5.6 Small-scale dissolution methods

Over the years, the official USP dissolution apparatus methods have been an important setup for the evaluation of the instant properties of a product. The idea of small-scale dissolution appears from the need to understand and evaluate the dissolution kinetics of low concentration of active ingredient samples mainly in the pharmaceutical sector [142]. However, small-scale dissolution studies for new product development are not too many. The reason for this could be the lack of suitable technological equipment [143]. So, there is an increasing need for new small-scale methods that will reduce the experimental time,

the amount of sample and the operation cost. The aim of the new small-scale dissolution methods should be the production of high-quality measurements. Furthermore, the efficiency, the delicacy, the precision and the replicability of the new techniques need to be maintained.

USP dissolution apparatus require volumes of the dissolution medium of 100 mL to 4000 mL and solid sample portions of 100 mg to 1000 mg and are therefore not suitable for small-scale experiments.

During product formulation, the aim is usually to scale down the physicochemical characterisation techniques. However, in most cases, the small-scale dissolution experiments have focused on reducing the volume of the official USP dissolution apparatus [144]. The aim of these "mini-paddle" and "mini-basket" dissolution apparatus (Figure 2-32) is to generate identical experimental conditions e.g. hydrodynamics as the USP apparatus. This is logical since the focus of these methods is to provide results for primary formulations that will be in good agreement with USP apparatus measurements [145]. Nevertheless, they are not the best approach to follow in the development of new small-scale dissolution methods.

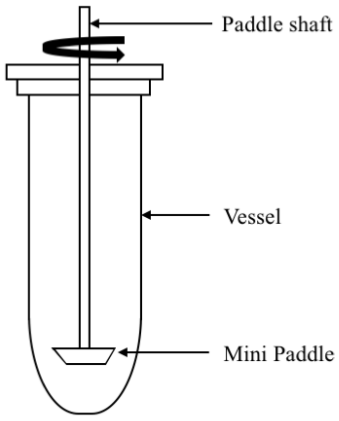

Figure 2-32 Schematic representation of a "mini-paddle" apparatus.

There are also some commercially available small-scale dissolution techniques that demand only millilitre volumes and examine the samples by in situ fibre-optic probes [142]. One approach is the micro dissolution apparatus "μdiss method" developed by Avdeef [146] which uses 2 mL of dissolution medium and 10-100 mg of sample. This method is currently used for gaining solubilities. In 2012 Hulse et al., [20] presented a small-scale method using a flow-through dissolution apparatus and UV area imaging for the determination of dissolution of 3-10 mg drug samples.

2.5.7 The use of optical microscopy as a dissolution method

Between all the previous studies on single particle dissolution, the most commonly used analytical method was the optical microscopy [1], [26], [28], [31]–[34]. The recent technological achievements in computing and image processing have allowed optical microscopy to be used as an analytical tool for the acquisition of high accuracy particle morphology measurements [147].

According to Allen [24], optical microscopy can be used to evaluate the size of granules from 3 μm to 150 μm, with a minimum resolution at 0.2 μm. Nevertheless, the ring of diffraction of the light is inversely proportional to the particle size. Therefore, the ring will be higher for smaller particle sizes. Consequently, the over-evaluation of the size of the granule decreases with increasing the particle size and becomes critical for granules less than 3 μm. Due to this fact, a sensible threshold limit for the estimation of the particle size is the 0.8 μm. Another disadvantage of optical microscopy is the narrowed depth of focus. So, the surface area of big granules or of different particle size multi-particle systems, cannot be in focus in the same image. For the examination of the single particles the limitation on focus implies that the granule either should be placed or fixed at a certain distance from the lens.

Regardless all these disadvantages, there are many benefits of performing dissolution experiments using optical microscopy compared to the chemical techniques. Chemical methods like UV-Vis spectrophotometry, Conductivity and High-Performance Liquid Chromatography (HPLC) require chemical calibration to determine the dissolved compound. In contrast, the analysis of the particle size or the particle surface area from images does not need any chemical calibration. So, it can be used for the dissolution testing of new product formulations where the chemical properties or of some ingredients might be unknown or the concentration very low.

Furthermore, the surface area of particle accommodates more precise data than in situ analytical methods that evaluate the concentration at a specific region of the solvent. As the concentration will not be homogeneously distributed in the solvent, there will be regions with higher or lower concentration and the orientation of the chemical probe will be a cause of an error. Moreover, image analysis does not request any sample collection or preparation which can cause additional errors and need to be verified. Also, the higher the amount of the sample treatment stages between the collection and the analysis, the greater the possibility of error due to sample loss. The sensitivity and the precision of chemical techniques are proportional to the level of complexity of the solvent. Finally, the absence of complication of image acquisition and image processing forms a highly automated, real-time analytical technique.

2.5.8 Image processing on single particle dissolution

Optical images contain several squares named picture elements or pixels [148]. The images need to be converted into 8-bit monochrome (grayscale) images, to be evaluated and processed [24], [148]. The pixels of grayscale images are expressed by a numerical value between 0 and 255. The intensity is defined by this value and depends on the

brightness and the hue of each pixel, where 0 symbolises a black pixel and 255 a white [24]. Then the grayscale image is additionally treated e.g. by eliminating the noise of background and transforming the grayscale image into a black and white image, via threshold. Threshold symbolizes a value on the grayscale, below which all the numerical values get the value of 0 (black) and above get the value of 255 (white). So, a black and white binary image is generated. This process, in which the particle to be evaluated needs to be separated from the background is named segmentation [149].

On the occasion that the quality of the raw image is poor, the segmentation of the binary granule will be insufficient so the binary image will need additional improvement [149]. The biggest challenge of the image analysis of single particle dissolution is the separation of the granule from the formatted bubbles which surrounding it. Using the image processing method, we can only extract as many information possible, and we are not able to implement data that were not present in the raw image. Thus, the quality of the original image defines the level of accuracy of the image processing measurements.

Optical microscopy is a method that is commonly conducted only from one side, so the position of the granule when the image is obtained defines its two-dimensional projection [24], [150]. For some shapes like spheres, the position that the granule is examined is not crucial because they present identical two-dimensional projection in every orientation. On the other hand, the image analysis of irregularly shaped particles needs to consider that they have a preferred position at which they are lying on the dissolution medium surface [150]. Therefore, for the analysis of irregularly shaped particles, an equivalent diameter conversion is commonly used. This conversion hypothesises that the measured volume of the granule is like the volume of a sphere. The diameter of the two-dimensional

projected surface area of the granule can be used for the evaluation of the equivalent volume of the sphere.

2.5.9 Concluding Remarks

The above literature review demonstrates that the most common method of studying dissolution rates of small sample amounts is via a bulk approach [1]. Numerous studies have been published on the investigation of dissolution kinetics of multi-particle systems with the use of a dissolution apparatus and chemical analytical techniques [9], [10], [19], [11]–[18].

However, single particle diffusion [1], [25]–[29] and convective [30]–[35] dissolution experiments have been carried out in limited cases. All previous single-particle studies were focused on solid structured granules and no understanding on the dissolution phenomena/kinetics of porous particles has been developed. Furthermore, no link of the single particle understanding to the bulk has been performed.

This project focuses on studying dissolution kinetics of highly porous detergent powders at the individual granule's level. Therefore, it will make a valuable contribution to the knowledge base in this particular area, since systematic studies and data at this level are extremely rare.

CHAPTER 3 MATERIALS AND CHARACTERISATION

3.1 Introduction

The characterisation of the powders is crucial for the understanding of their dissolution behaviour in different conditions. Different particle structure causes different dissolution phenomena. In general, spray dried powders have hollow or semi-hollow structures consisting shell or film regions with different physical and chemical properties and a large central void space [151]. In this section, details of the prototypes have been presented with composition information from the industrial provider. Physical properties such as sample solubility, size distribution, surface morphology and internal structure have been characterised as it has been requested by Procter & Gamble, Newcastle Innovation Centre (NIC). The results are compared with sample manufacturing conditions to show the presence of binder on particle morphology and microstructure.

3.2 Materials

Spray drying is a process of producing dry powder from a feed in a liquid or slurry condition by atomising the feed into either co-current or counter-current hot drying gas [152]. About 50%-60% detergent powders are produced by this process world widely. Today's spray-dried detergent powder has multi ingredients containing surfactant, polymer, silicates, carbonate and sulphate. Each of them impacts a different cleaning function of the product [3].

- the key ingredient of detergent powders is surfactant. These are usually anionic and non-ionic surfactants and their combinations. The main anionic surfactant is the linear alkyl benzene sulphonate (LAS). The surfactants are the main cleaning agent, because they efficiently remove grease/body soils.
- builders are used to remove water hardness ions (e.g. calcium, magnesium), to improve cleaning efficiency and end-use application properties. The most common

builders are sodium tripolyphosphate (STPP), citric acid, sodium citrate, zeolites and sodium layered silicate.

- sodium carbonate and sodium silicate as buffers provide right alkaline conditions to the cleaning process. They also provide the 'right environment' for the other detergent ingredients to work effectively.
- electrolytes such as sodium carbonate and sodium sulphate can maintain the appropriate ionic strength.
- fillers include sodium sulphate, sodium chloride, clays and calcite.
- other organic additives such as polymers can stop stains redepositing, boost the surfactant, protect the fabric and are very good dispersants. Brighteners change the color of fabrics by absorbing UV light and re-emitting colored light (green/blue), which gives fabric the blue whiteness that makes them appear 'whiter than white'. Bleach and bleach activators are for changing stains color and improving the whiteness. Enzymes can help break down soils.
- perfumes provide a pleasant smell, which makes clothes seem cleaner and fresher.

The new trend in the detergent industry is to develop a highly porous detergent powder containing as less ingredients as possible without losing function to improve profit margin. As illustrating in Figure 3-1, it will only contain sodium sulphate, a surfactant and a binder. Hence, the type of the binder will play a significant role in the physical properties of the detergent powder [3], [124].

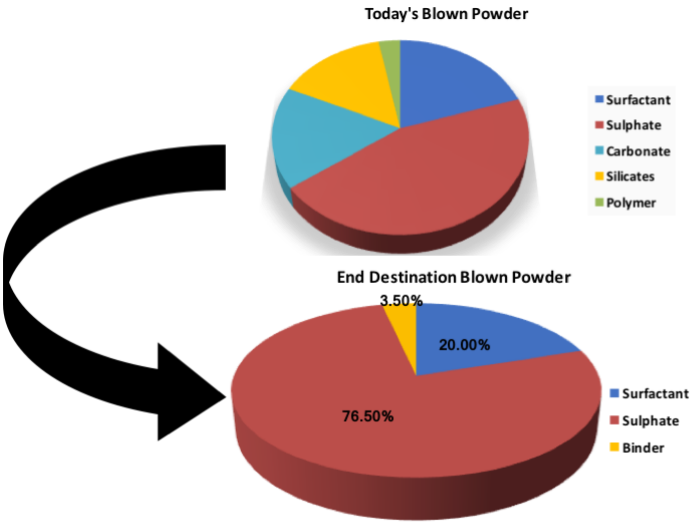

Figure 3-1 The transition from the Today's Blown Powder to the Future Simple Blown Powder.

In this study, a binary set of blown powders has been manufactured to study binder effects on their dissolution performance. The sample ingredients are listed in Table 3.2. Sample1 and 2 contain sodium sulphate (Na_2SO_4) and linear alkyl benzene sulfonate (LAS, a surfactant) with no binder, while Sample3-5 contain different binders. Sample1 was produced with a low slurry mix moisture content (LSMM), 35%, while Sample2 was produced with a high slurry mix moisture (HSMM), 62%. Sample3 and 4 were manufactured by adding in the low water content slurry Sodium Silicate, on two different molar ratios SiO_2:Na_2O 1.6 and 2.35 respectively. Sample 5 contains a mixture of three ingredients, namely zeolite, magnesium sulphate and Citric Acid as a binder and has 30.24% slurry mix moisture. Citric Acid except balancing slurry pH values to control slurry viscosity also works as a disintegrant [153]. Disintegrants are ingredients added to the powder formulations to enhance the breakup of the powder granules into small fragments in an aqueous solution [154]. All samples were provided by Procter & Gamble NIC (see Table 3.1).

Table 3.1 Batch codes of the five spray dried powder samples provided by Procter and Gamble, Newcastle Innovation Centre.

Samples	Batch Code
Sample1	IM-14-000848
Sample2	IM-14-000849
Sample3	IM-14-000860
Sample4	IM-14-000847
Sample5	PRC 16-00047

Table 3.2 Overview of the chemical composition of the spray dried detergent powder samples.

Samples	Composition in dry powder									
	Na_2SO_4 (%)	LAS (%)	Silicate 1.6R (%)	Silicate 2.35R (%)	$MgSO_4$ (%)	Citric Acid (%)	Zeolite (%)	Na_2CO_3 (%)	Water (%)	Others (%)
Sample1 (LSMM)	77.06	19.5	-	-	-	-	-	-	1	1.3
Sample2 (LSMM)	77.06	19.5	-	-	-	-	-	-	1	1.3
Sample3	64.31	19.5	11.23	-	-	-	-	1.14	2.5	1.3
Sample4	61.71	19.5	-	14.35	-	-	-	1.14	2	1.3
Sample5	63.77	20.4	-	-	4.18	6.97	3.13	-	-	1.6

3.3 Fluid related properties

3.3.1 Density of the fluid

The density of deionised (D.I.) water ρ_{water} was measured using a density meter DMA 4500 M (Anton Paar, United Kingdom) at 20dC, 40dC and 60dC. Results are presented in Table 3.3.

Table 3.3 Density of D. I. water ρ_{water} (kg/m^3) at 20dC, 40dC and 60dC.

Physical property	Temperature (dC)		
	20	**40**	**60**
ρ_{water} **(kg/m^3)**	998.2	992.2	983.2

3.3.2 Viscosity of the fluid

The dynamic and kinematic viscosity of D.I water, μ_{water} and v_{water}, were evaluated using an AR G2 Rheometer (TA Instruments, United Kingdom) at 20dC, 40dC and 60C. The dynamic viscosity of water μ_{water} is the tangential force per area needed to move one horizontal plane with regards to another horizontal plane when sustaining a specific distance apart in the water. On the other hand, kinematic viscosity of water v_{water} is the ratio of dynamic viscosity μ_{water} to the density of water ρ_{water}. Results are presented in Table 3.4.

Table 3.4 Dynamic viscosity of D.I water μ_{water} (kg/sm) and kinematic viscosity of water v_{water} (m^2/s) at 20dC, 40dC and 60dC.

Physical property	Temperature (dC)		
	20	**40**	**60**
μ_{water} **(10^{-3} kg/sm)**	1.002	0.653	0.467
v_{water} **(10^{-6} m^2/s)**	1.004	0.658	0.474

3.4 Characterization of the samples

3.4.1 Solubility

As mentioned previously in Section 2.2.1 of the Literature, solubility can be described as the feature of a solute to dissolve in a specific solvent. Solubility depends on the physicochemical properties of the sample and the solvent as well as the temperature, pressure and pH value of the solution. To evaluate solubility, saturated concentration is commonly used, and, in some occasions, the equilibrium solubility is surpassed to reach a supersaturated solution.

The solubility of the samples was measured by adding 2 g of powder into 100 mL of water each time and measuring the conductivity of the solution (JENWAY 4520 Bench Conductivity meter) as a function of powder mass until the conductivity stops changing with mass. The solubility of the samples was evaluated at 20dC, 40dC and 60dC.

Figure 3-2 shows conductivity results as a function of different powder sample mass.

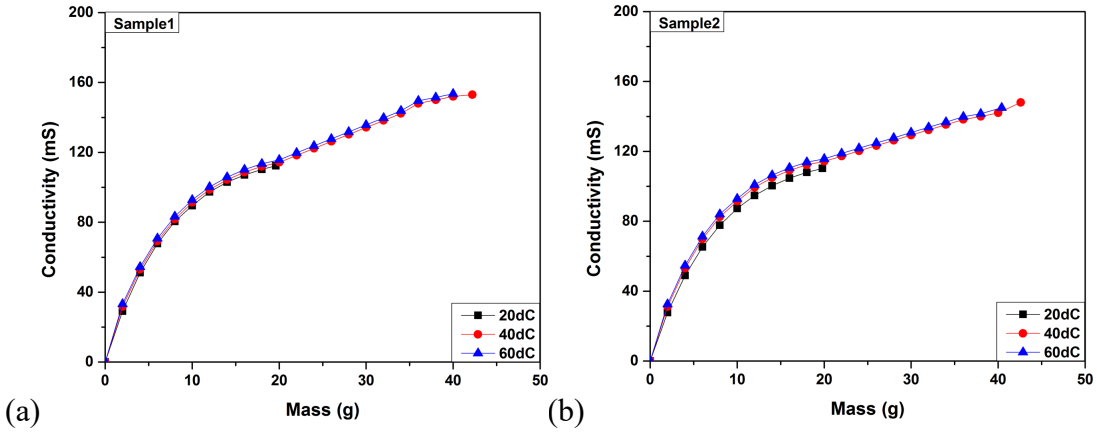

(a) (b)

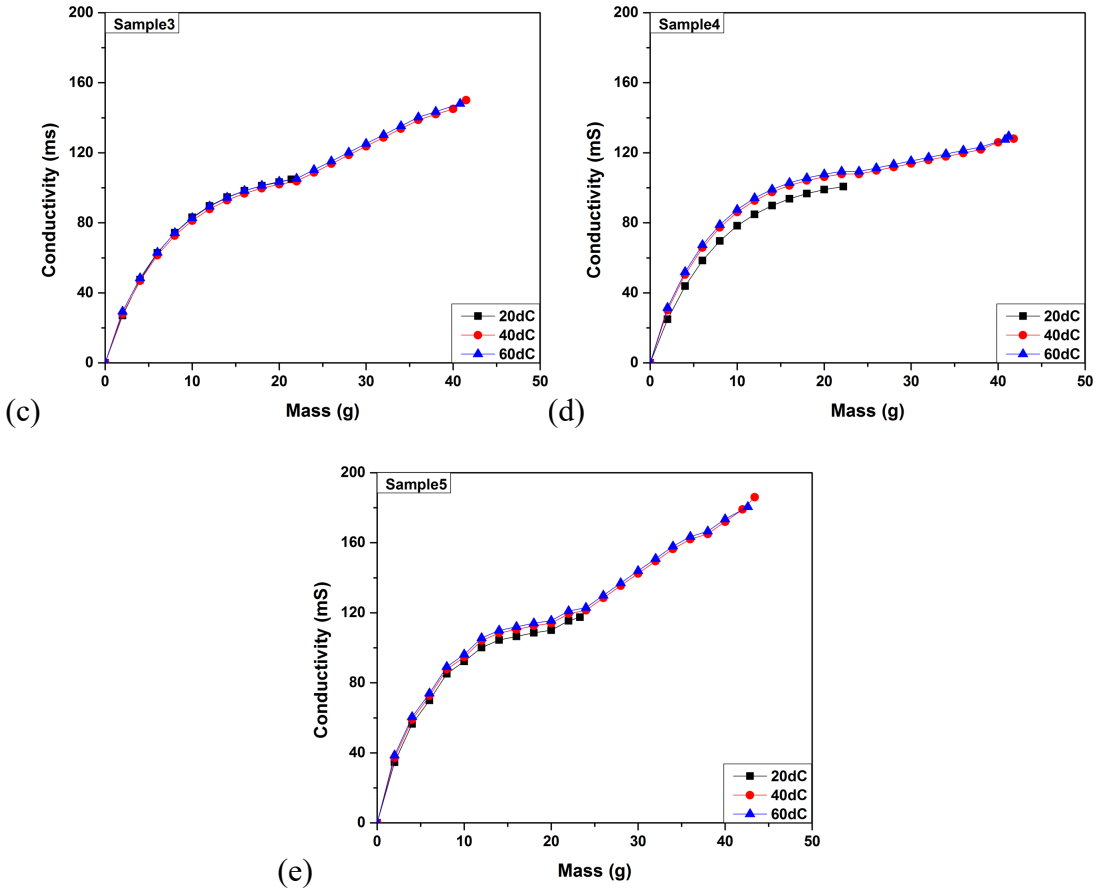

Figure 3-2 Solubility test of (a) Sample1, (b) Sample2, (c) Sample3, (d) Sample4 and (e) Sample5 at different temperatures in 100 mL of water.

The comparison of the solubilities of the five samples at 20dC, 40dC and 60dC is presented in Figure 3-3. Results show that across the samples the solubility is increases significantly from 20dC to 40dC and decreases slightly from 40dC to 60dC. This is because the solubility of the main compound of the samples which is sodium sulphate decreases from 478.2 kg/m^3 to 447.2 kg/m^3 at this temperature range [155]. Among the samples, Sample5 presents the highest solubility in the different temperatures.

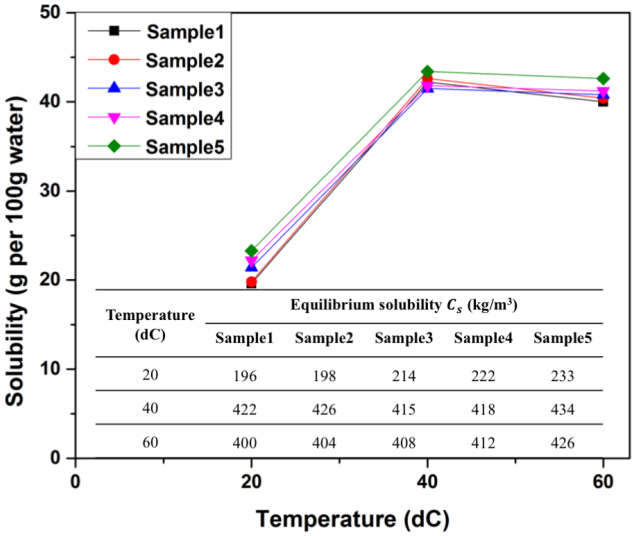

Temperature (dC)	Equilibrium solubility C_s (kg/m³)				
	Sample1	Sample2	Sample3	Sample4	Sample5
20	196	198	214	222	233
40	422	426	415	418	434
60	400	404	408	412	426

Figure 3-3 Comparison of solubilities of the five samples at 20dC, 40dC and 60dC.

3.4.2 Diffusivity

The diffusivity of the samples in water at different temperatures was evaluated from Equation (2-10) and Table 2.1 and is presented in Figure 3-4. Results show that the diffusivity increases with the temperature. Sample1 and Sample2 that contain the highest portion of sodium sulphate (highest diffusivity among the ingredients) show the highest diffusivity across the samples.

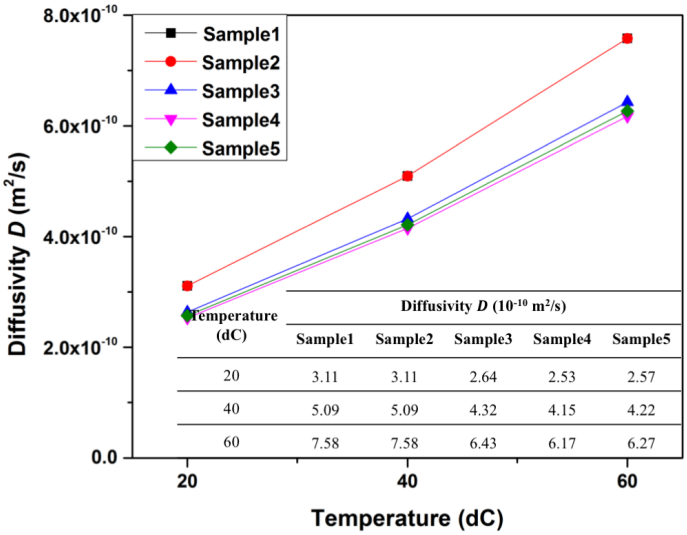

Temperature (dC)	Diffusivity D (10^{-10} m²/s)				
	Sample1	Sample2	Sample3	Sample4	Sample5
20	3.11	3.11	2.64	2.53	2.57
40	5.09	5.09	4.32	4.15	4.22
60	7.58	7.58	6.43	6.17	6.27

Figure 3-4 Diffusivity *D* of the spray dried powder samples at 20dC, 40dC and 60dC.

3.4.3 Particle Size Distribution (PSD)

Particle size has a significant effect on its dissolution behaviour (see Section 2.2.1 in the Literature) [22], [84].

The particle size distribution was characterised by a gravity disperse connected with the vibratory feeder and a dynamic image analysis sensor in the measuring area (Sympatec GmbH, Germany). The measuring range of the system is 200 – 10,000 µm. The particles were accelerated in the gravity field and gently dispersed through particle to particle and particle to wall collision in the impact plate cascade. The fall shaft provides smooth dispersion and control and homogenises the speed of the granules presented to the laser beam. This method provides results that are in good agreement with those of the traditional sieving method [156]. A schematic representation of the system is shown in Figure 3-5. For each powder, 5 g sample was used, and 10 replicates was performed, to obtain the mean values and the standard deviations. The particle size distribution results were presented by means of various statistics, including x10, x50, x90 VMD and SMD. VMD is the mean diameter based on the volume of the particles, while SMD is the mean diameter based on the surface of the particles (usually referred as the "Sauter diameter").

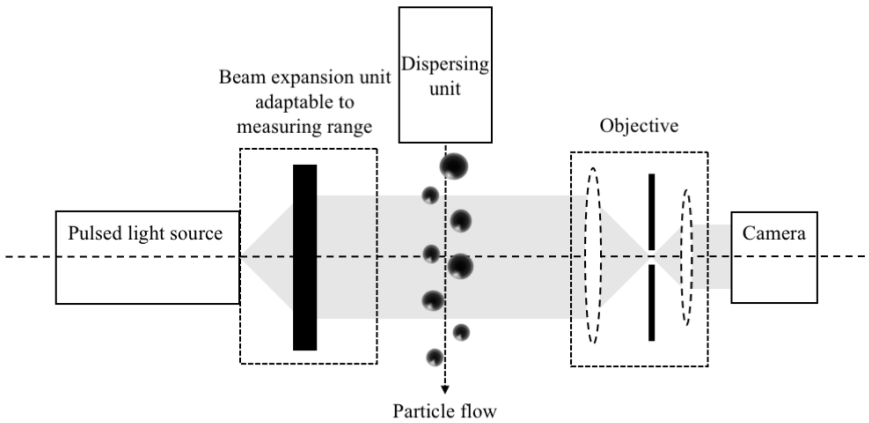

Figure 3-5 Schematic representation of dynamic image analysis optical setup for the measurement of particle size distribution [156].

Particle size distributions of the samples are shown in Figure 3-6. The comparison of the results shows that powder samples containing binder Sample3, 4 and 5 have wider distribution and higher degree of agglomeration comparing to no binder samples, Sample1 and 2. The particle size ranges from 64.21 µm to 2580.23 µm, 2124.39 µm, 3133.89 µm, 2580.23 µm and 2124.39 µm for Sample1, 2, 3, 4 and 5 respectively. It can be observed (see Table 3.5) that the characteristic particle size lies from 250 µm to 600 µm. The VMD of nil binder samples is narrower than Sample3,4 and 5. However, no significant difference can be noticed for the SMD. Based on the particle size distribution measurements the spray dried powder samples were manually sieved. Five stainless steel (outer diameter = 200 mm) sieves with woven wire mesh (Fisherbrand, Fisher Scientific, UK) were used to sieve the particles into four different size fractions below 250 µm, 250 to 500 µm, 500 to 710 µm and 710 µm to 1 mm.

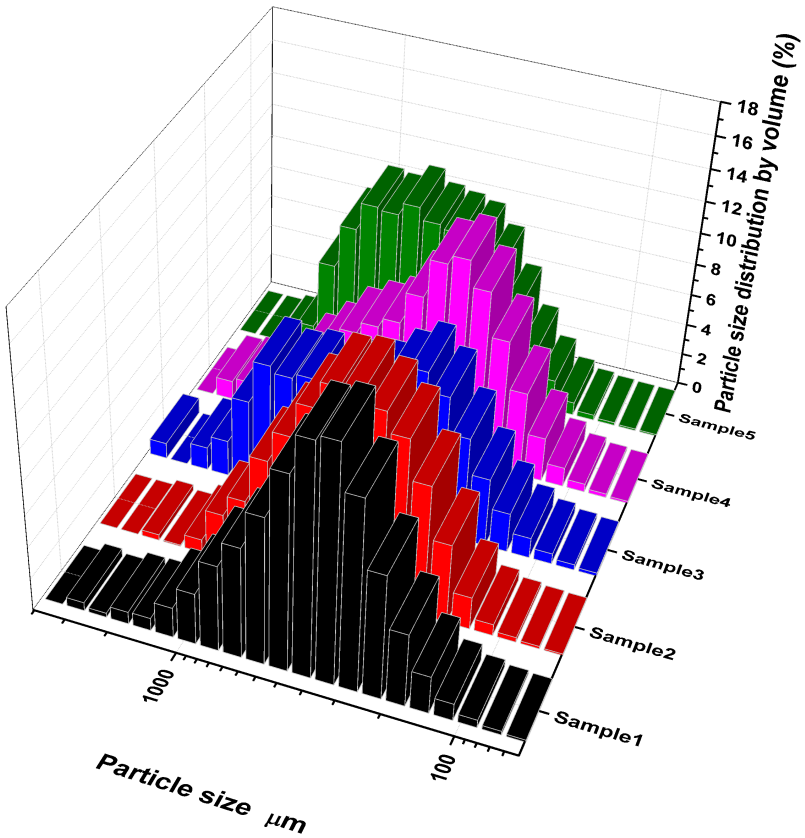

Figure 3-6 Characterisation of the particle size distribution for all the spray dried powder samples utilised in this study.

Table 3.5 Main parameters of particle size distribution of the samples.

Physical Property	Samples				
	Sample1	**Sample2**	**Sample3**	**Sample4**	**Sample5**
X10 (µm)	173.76 ± 4.07	179.46 ± 8.54	173.09 ± 7.84	167.68 ± 6.24	226.95 ± 18.20
X50 (µm)	331.11 ± 18.52	365.46 ± 26.48	434.86 ± 56.51	345.13 ± 17.82	532.49 ± 65.94
X90 (µm)	723.53 ± 56.35	774.94 ± 48.16	1170.75 ± 108.24	979.71 ± 110.92	1115.73 ± 117.76
VMD (µm)	408.707 ± 37.53	430.35 ± 21.75	560.54 ± 46.50	476.27 ± 73.61	610.44 ± 66.01
SMD (µm)	294.17± 15.3	313.92 ± 17.71	337.39 ± 24.89	302.22 ± 14.02	417.35 ± 41.23

3.4.4 Bulk Density & Porosity

Bulk density and porosity are vital measurements for the quality control in powder industry. These two parameters can have a significant effect in the dispensing, packaging

and transport consumption [3], and they are related to the physicochemical properties of the compound and the structural and morphological characteristics of the individual granules.

The bulk density of a powder can be defined as $W_{powder}/V_{container}$ when a powder covers a container of known volume $V_{container}$, and the mass of the powder is W_{powder}. In case that the container is tapped, the powder will settle, and additional powder needs to be imputed to reach the initial volume as the bulk density has elevated. The bulk voidage or porosity is directly connected to bulk density. Bulk density ρ_b is the mass of granules that covers a volume of a unit. On the other hand, Porosity ε_p is the volume of voids in-between the unit divided by the volume of the unit [84].

The two parameters are linked with the following mass balance:

$$\rho_b = \rho_s(1 - \varepsilon_p) + \rho_a \varepsilon_p \tag{3-1}$$

where ρ_s is particle density and ρ_a is the density of air. As the air density is much smaller compared to bulk density, it can be neglected. Therefore, the porosity of the powder can be evaluated as:

$$\varepsilon_b = \frac{\rho_s - \rho_b}{\rho_s} \tag{3-2}$$

The bulk density is different from the particle density as it considers the voids between the particles in the examined volume.

The porosity ε_b (%) and the bulk density ρ_b (kg/m^3) of the samples were measured using a Mercury Porosimeter Autopore IV (Micromeritics, Norcross, GA). 5 g of each powder sample was loaded in a penetrometer (see Figure 3-7) and placed inside the instrument. The penetrometer is made of glass. It has a cylindrical glass sample holder on one end

(the bulb) and is sealed when the sample is loaded. The other end of the cylinder extends into a glass stem which is coated with a metallic fill.

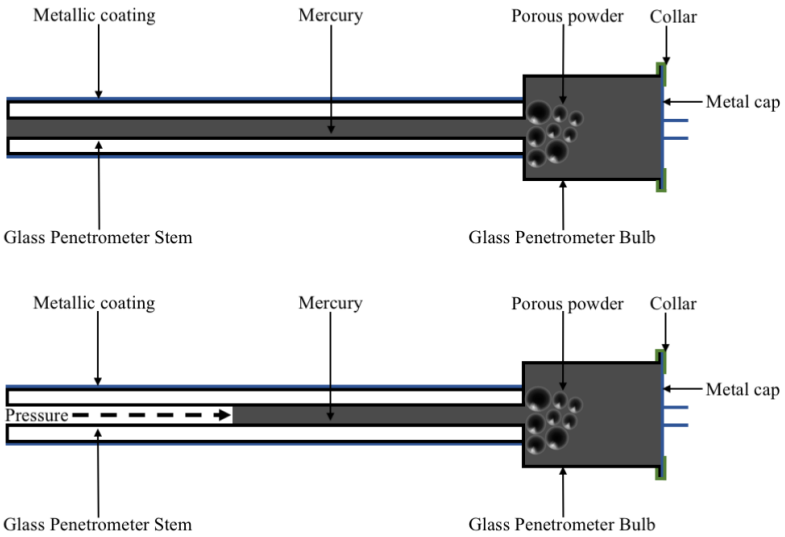

Figure 3-7 Cross section of a penetrometer (up) filled with mercury (down) which pressure has forced some mercury into the pores of the powder and almost 50% of the stem capacity has been used.

At the beginning of the analysis the penetrometer was evacuated below 0.001 psi and then was backfilled with mercury. So, at the start of the analysis, the sample was enveloped with mercury while the bulb and the stem were filled with mercury. The volume of mercury held in the stem becomes a reservoir for intruding into sample pores at when pressurised. As the applied pressure was increased, mercury intruded into pores. This movement of mercury along stem was measured by changes in electrical capacitance. To intrude into pores of 3 nm, the smallest pore size measured by this instrument, 60,000 psi was generated and applied [157].

The results of bulk density ρ_b and porosity ε_b are shown in Table 3.6. Porosities of Samples 1 and 2, are higher than the Samples 3-5. Sample1 has a porosity of 78 ± 2 %, Sample2 85 ± 3 %, Sample3 68 ± 3 %, Sample4 65 ± 4 % and Sample5 73 ± 3 %. The amount of binder in granules affect their porosity [19]. High slurry mix moisture resulted in an increase of particle porosity after spray drying process. Therefore, Sample2 has a

higher porosity than Sample1. On the other hand, the porosity of samples with Silicate binder is lower than Sample5 which contains Citric Acid as the main ingredient of its binder. This is due to the function of Citric Acid as disintegrant to enhance the porosity of the powder [154]. The bulk densities of Sample3 and Sample4 are nearly twice the value of Sample1 and 2. This is mainly due to the effect of binder on bulk properties [158], [159].

Table 3.6 Initial bulk density ρ_b (kg/m^3) and porosity ε_b (%) for the five powder samples.

Physical property	Samples				
	Sample1	**Sample2**	**Sample3**	**Sample4**	**Sample5**
Bulk density (kg/m^3)	383 ± 8	277 ± 8	627 ± 19	631 ± 25	535 ± 16
Porosity (%)	78 ± 2	85 ± 3	68 ± 3	65 ± 4	73 ± 3

3.4.5 Particle Density

A porous particle has a different description of density, including the absolute particle density, the apparent particle density and the envelope particle density.

Absolute particle density $\rho_{absolute}$ is the density of the solid compounds of which the granule is produced excluding the volume of open and closed pores.

Apparent particle density $\rho_{apparent}$ is the density of the solid compounds of which the granules is produced excluding only the volume of the open pores.

Envelope particle density $\rho_{envelope}$ is the density of the solid compounds of which the granule is produced including the volume of open and closed pores.

The above particle densities differ from bulk density as they exclude the inter-particle voids.

The absolute density of the samples $\rho_{absolute}$ (kg/m^3) was measured using a Helium Pycnometer AccuPyc II 1340 (Micromeritics, Norcross, GA). The instrument uses the ideal gas law equation and the gas displacement technique. Sample volume was measured from the observed pressure change that helium faced when was expanded from one chamber which contains the sample to another empty chamber. The instrument consists of two chambers (a sample chamber and an expansion chamber), a pressure measuring transducer and three valves (see Figure 3-8).

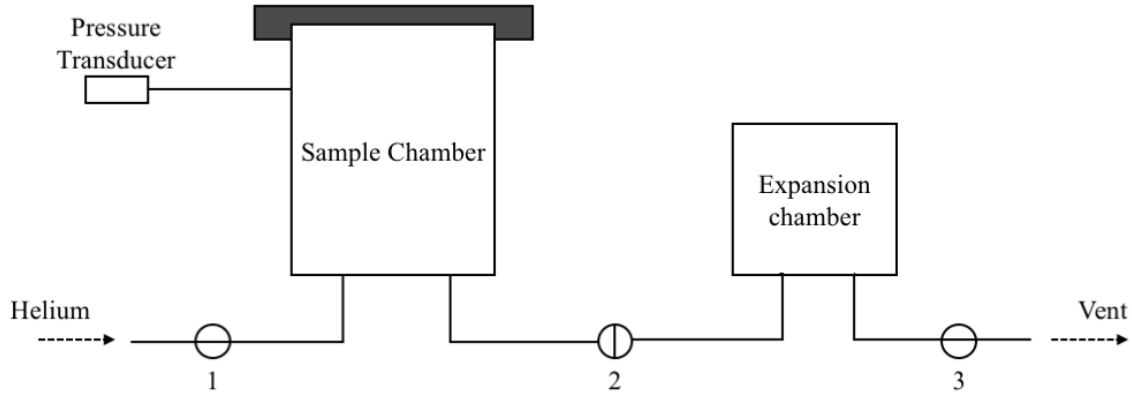

Figure 3-8 Schematic representation of a gas pycnometer [160].

0.1 g of powder samples were placed in the sample chamber which then was pressurised with gas from a helium tank set at 19.5 psig. The equilibrium rate was set at 0.02 psig/min. This was achieved with a series of purges. Purging was accomplished by opening valve 1 and leaving valve 2 and 3 close. Then when the sample chamber was filled with gas, valve 1 closed and valves 2 and 3 opened, letting helium to release. This procedure was replicated five times to remove all unwanted gases. After that, the pressure covering the sample was evaluated. Valve 3 then opened, and the helium was released to the atmosphere. The cycle was repeated five times to get accurate measurements of sample volume. Finally, the sample volume was divided into sample mass to estimate absolute density. A summary report of the sample was then generated [160].

As shown in Figure 3-9, for the samples that contain binder, Sample3, 4 and 5 and for Sample1 which has low slurry mix moisture absolute density presents a linear relationship with porosity. So, as we increase the porosity from 65 to 78 % the absolute density increases as well. However, Sample2 which is the sample with the high slurry mix moisture and the highest porosity does not follow the same trend as it has the lowest value of $\rho_{absolute}$, 1965 kg/m^3 between the samples. A better understanding of this significant difference we will be able to get from the characterisation of the microstructure of the samples as particle density is linked to open and closed pores.

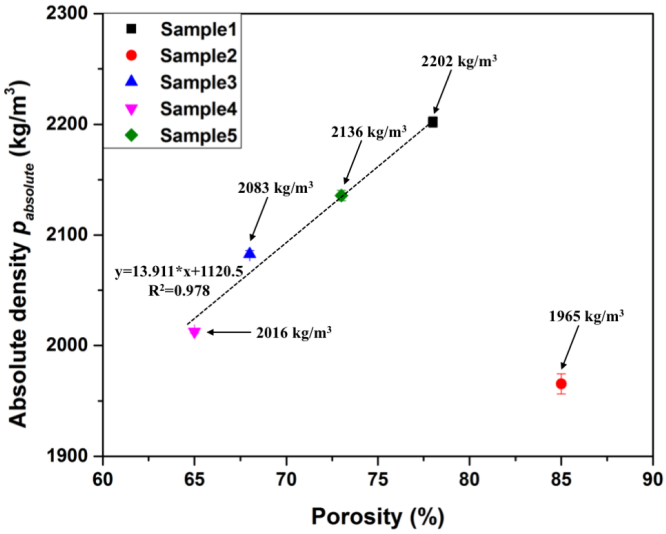

Figure 3-9 Absolute density $\rho_{absolute}$ as a function of porosity.

For a porous granule, the porosity $\varepsilon_{particle}$ can be determined as:

$$\varepsilon_{particle} = \frac{V_{pore}}{V_{particle}} = 1 - \frac{\rho_{envelope}}{\rho_{absolute}} \tag{3-3}$$

where V_{pore} is the volume of pores, $V_{particle}$ is the volume of the particle, $\rho_{envelope}$ is envelope particle density and $\rho_{absolute}$ is absolute particle density.

Considering $\varepsilon_{particle}$ equal to ε_b, the acquired information from Mercury Porosimetry and Helium Pycnometer can be implemented in Equation (3-3) to calculate the particle envelope density $\rho_{envelope}$, of the samples.

Figure 3-10 shows that envelope density $\rho_{envelope}$ decreases with the increasement of porosity from 65 to 85 % in a linear trend. However, this relationship is not ideal considering the effect of particle ingredients in envelope density. Sample4 with 65% porosity has the highest $\rho_{envelope}$ 704 kg/m^3, while Sample2 with 20% higher porosity than Sample4 has the lowest 295 kg/m^3.

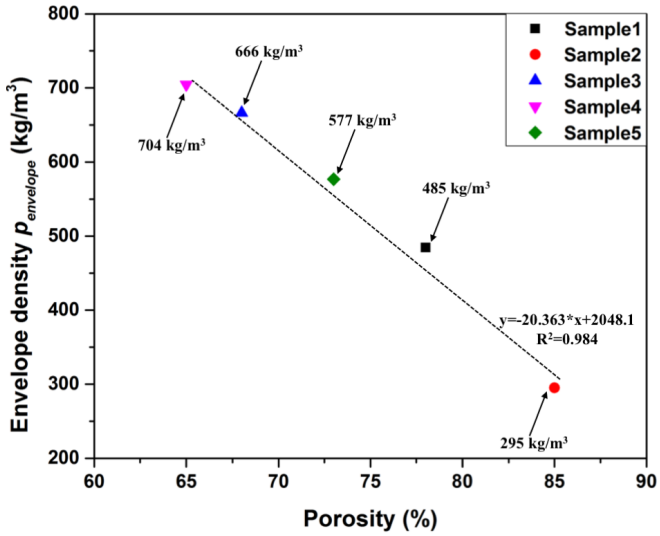

Figure 3-10 Particle envelope density $\rho_{envelope}$ as a function of porosity.

3.4.6 Surface morphology

Surface morphology of the samples was observed using a scanning electron microscope (TM3030, Hitachi High Technologies America, Inc., U.S.A).

The equipment was operated at 15 kV in low vacuum mode and equipped with a backscatter detector. Prior to observation, a small amount of the samples from both the bulk and each size cut were put on the holder coated with carbon conductive. Two magnifications were used for the bulk, x50 and x200. For each size fraction, the magnification was set at x200. Then EDX analysis on an individual particle was conducted with the use of QUANTAX 75 software (Bruker Co., Massachusetts, U.S.A.) to map the chemical components of each sample. The scanning time of EDX analysis was set at 180 s to gain high precision results.

In general, spray dried powders have hollow or semi-hollow structures consisting of shell or film regions with different physical and chemical properties and a large central void space [151]. In Figure 3-11, one can see SEM images of the five different detergent powder samples at x50 (low) and x200 (high) magnification for the bulk and x200 magnification for each size fraction. SEM images of the bulk demonstrate that all the samples have a wide particle size distribution, from tens of micrometres to hundreds of micrometres which correlates well with the PSD results (see Figure 3-6). For Sample1 and 2 particles over 200 μm are often agglomerates of smaller ones; this is a typical size range when spray dried powder start to agglomerate [151]. However, for the samples with the binder, Sample3, 4 and 5, agglomeration appears across the size range. The size distribution of the particles forming the agglomerates ranges from 40 μm (on <250 μm) to 120 μm (on 710 μm to 1 mm). Representative examples of agglomeration are presented in the figure with the red line. Different sized holes appear on particle surfaces from several micrometres to up to 200 μm. Examples of holes are illustrated with the green line. The samples with the absence of sodium silicate were found to tend to be more spherical and smoother. Sample1 shows a smoother surface comparing to Sample2. The magnified SEM images of the bulk show that various small spherical particles (<100 μm) attaching on the surface of Sample2, whereas significant less of them on Sample1.

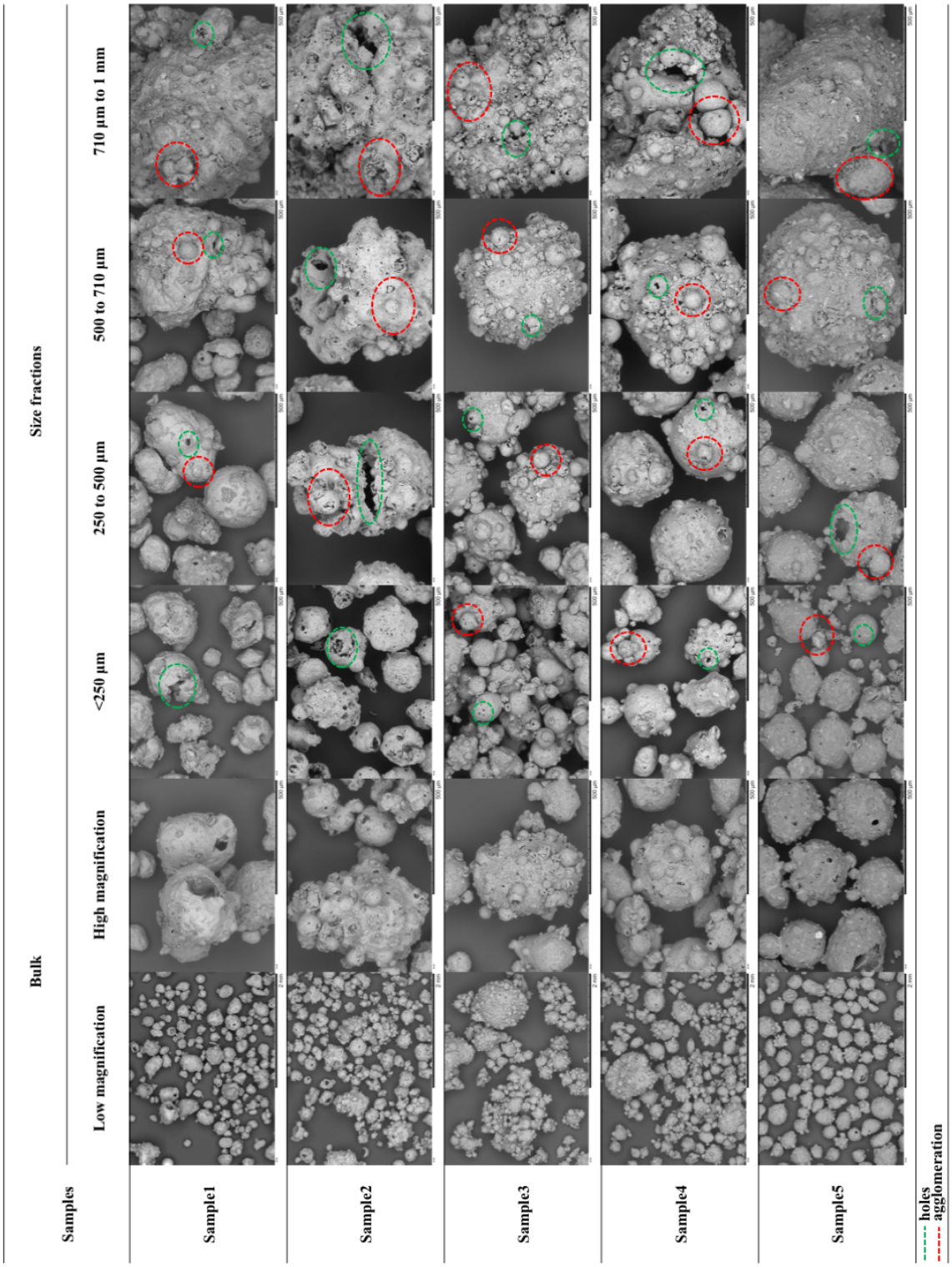

Figure 3-11 SEM images of the bulk, at low and high magnification, and each size fraction for the five detergent powder samples. The green line represents characteristic holes, while the red line shows typical agglomerates.

Figure 3-12 presents the stages of the EDX analysis. The first column shows an individual granule that has been chosen from the bulk of each sample to be observed at x180 magnification. Then the scanning area was selected in the software, and the EDX analysis was performed for 180 s. The distribution of the chemical components of each spray dried powder was mapped with a different colour. Sample1 and 2 which contain only two ingredients LAS and Na_2SO_4 were found to consist of sodium, Na, (red colour) and sulphur, S (blue colour). Sample3 and 4 with the sodium silicate as binder also contained silicon, Si, (turquoise colour), while Sample5 that has a mix of Magnesium sulphate, Citric Acid and Zeolites as binder consisting of magnesium, Mg, (green colour).

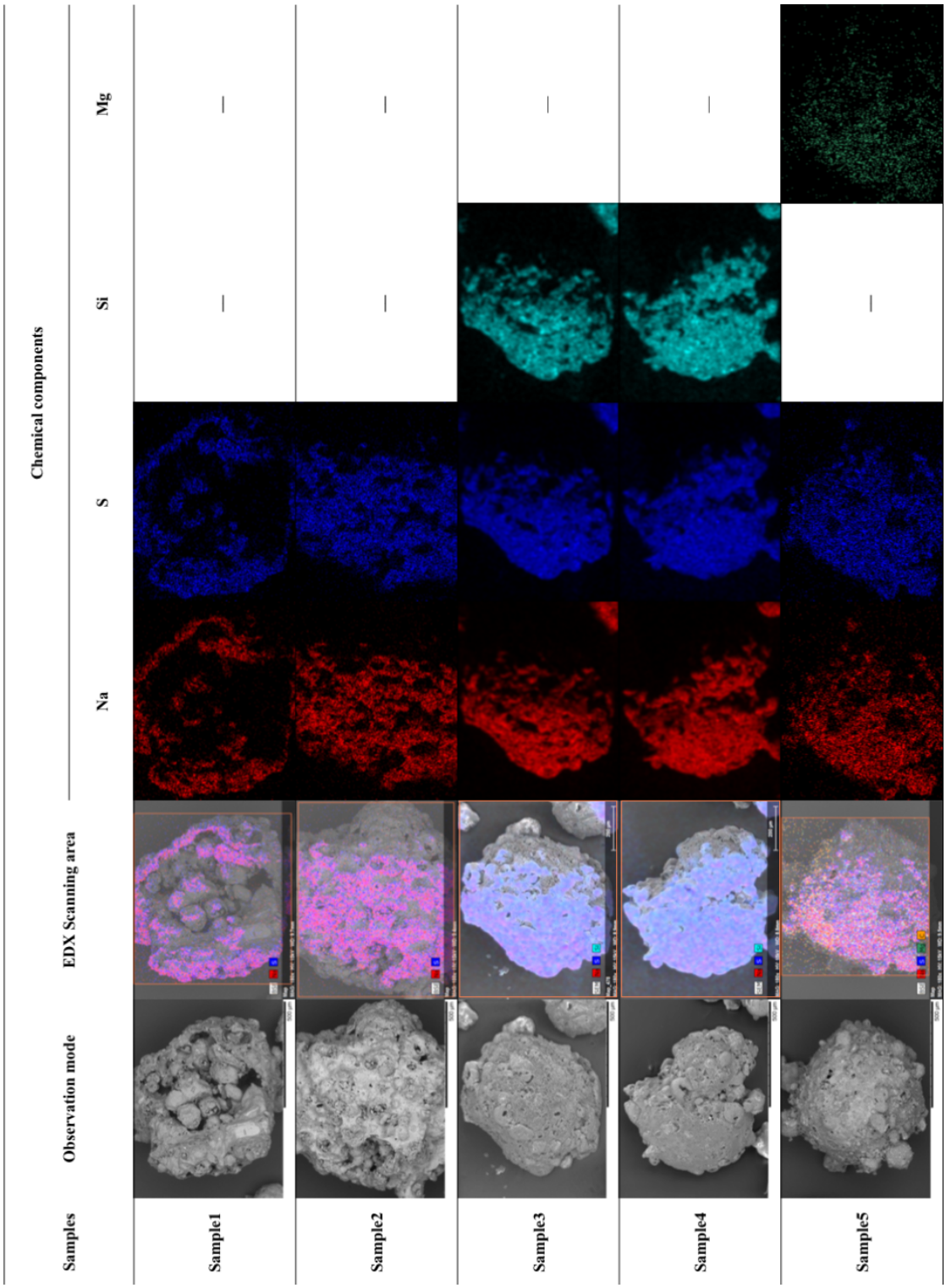

Figure 3-12 EDX analysis of singles particles for each powder sample.

3.4.7 Microstructure analysis

X-ray microtomography (XRT) is a method to non-invasively characterise the three-dimensional (3D) microstructure of powders at a spatial resolution of 1 – 6 μm [161]. This technique has been used to evaluate the microstructure of the spray dried powder samples due to its high resolution and the capability to perform 3D analysis [162]. XRT data give the possibility to extract information regarding particle packing [162], porosity, pore size distribution and crystal size distribution [161], [163].

The XRT uses a mixture of X-ray microscopy and tomographic algorithms. The contrast of X-ray images produced by the differences in X-ray beam intensity is the base of those algorithms. X-ray beam intensity is associated with differences in the density and the atomic number of the ingredients consisting the sample as well as the beam energy [164]. The X-rays are going through a sample which rotates to be scanned. The detector calculates the beam intensity of X-rays passing through the sample [165]. Then, 2D projected images are stacked to reconstruct the 3D image of the sample. A schematic representation of XRT scanning device is given in Figure 3-13.

The X-ray beam intensity is significantly affected by the differential thickness and the absorption coefficient of the sample.

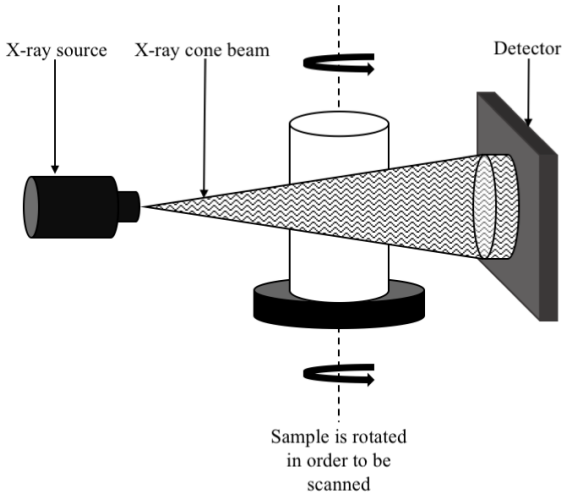

Figure 3-13 Schematic representation of XRT scanning instrument [163].

A connection lies between the densities of the sample components and the calculated from XRT absorption coefficients. The absorption coefficient is connected to the grey value which is between 0 and 255 in 8-bit grayscale images [165].

In this study, X-ray microtomography was performed using a Skyscan 1275 (Bruker microCT, Belgium). First 0.3 g of each spray dried powder was placed in a cylindrical container and scanned (see Figure 3-14). Then, single particles of each size fraction of every sample were scanned (see Figure 3-15). The X-ray parameters, such as voltage, filter and exposure time, were optimised regarding the samples analysed to get the best image contrast. The XRT settings are presented in Table 3.7.

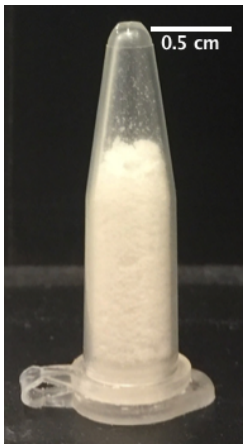

Figure 3-14 Sample holder for XRT scan using 0.3 g of each powder sample.

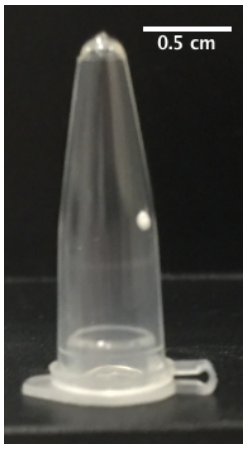

Figure 3-15 Sample holder for XRT scan using a single particle of each size fraction of every powder sample.

Table 3.7 XRT settings of the bulk and the individual granule.

X-ray parameters	Bulk powder	Single particle
Voltage (kV)	44	50
Current (µA)	100	
Camera pixel size (µm)	6.76	1.56
Rotation step (deg.)	0.30	
Rotation (deg.)	360	
Averaging (frames)	6	

The acquired projection images (4,000 x 2,064 pixels) were reconstructed using the N-Recon software provided by Skyscan. The reconstruction algorithm is based on a filtered back projection procedure for fan beam geometry with specific noise reduction collection [166]. When a set of images is uploaded, the default value of different reconstruction parameters is presented. Those parameters include post-alignment, beam-hardening correction, ring-artifacts reduction and smoothing.

Post-alignment: it is a critical parameter as the wrong alignment can cause tails, doubling or blurring in the reconstructed image.

Beam-hardening reduction: the beam hardening effect is reduced by linear conversion in the software. The correction value ranges from 0 to 100 according to the density of the sample.

Ring-artifacts reduction: it is applied in projection images before any other reconstruction step. The level of correction lies from 1 to 20 to reduce the effect of ring-artifacts to a minimum.

Smoothing: it reduces the noise but may introduce blurring for delicate structures. The smoothing level ranges between 1 and 10.

The modification of the above parameters varies between the different samples. In our study, during the image reconstruction process, the post-alignment was set at 3.5, the beam hardening reduction at 98, the ring artifacts reduction at 13 and the smoothing at 0. These reconstruction parameters were remaining the same across the different scans. At the end of the topographical reconstruction process, a number of flat cross-sections were acquired.

Parameters such as porosity, pore size distribution and crystal size distribution were then evaluated using the CTAn software provided by Skyscan. A region of interest (ROI)was first selected, then the images were segmented by threshold at different levels each time, and the region of interest of each image was shrinked to the boundary of the binary image. Finally, a 3D analysis was conducted for both bulk powders and single particles to measure the above parameters. Porosity was evaluated as the area of the fully enclosed spaces of a segmented sample as a percent of the total area of the segmented sample. The study of pore size distribution and crystal size distribution were conducted by measuring the structure thickness of the sample. The measurement of this parameter involves two stages. Firstly, a "skeletonisation" is performed to reveal the medial axis of all structures. Secondly, a "sphere fitting" model is applied for all the voxels lying across the axis. Structure thickness for a spot in solid is described as the diameter of the largest sphere that contains the spot and is totally enclosed with the solid surfaces [167]. A 3D model of each different sized single particle of each powder sample was also built using the CTVox software.

Figure 3-16 presents the scanning area of the bulk particles. Characteristic images of the particles are shown in Figure 3-17, in which white colour (255 in grayscale value) represents solid (high density), and black colour (0 in grayscale value) represents the air

(low density). The cross-sections were cleaned up with ImageJ (US National Institutes of Health) [168] setting the threshold at 24. Figure 3-17 (a) shows a cross-section image of bulk Sample1, and Figure 3-17 (b), (c) and (d) are different cross-section images of the particle dash circled in (a). The cross-section image of bulk Sample2 is shown in Figure 3-17 (e), and the different cross-section images of the particle dash circled in (e) are presented in Figure 3-17 (f), (g) and (i). Figure 3-17 (j) presents a cross-section of Sample3 in bulk, and Figure 3-17 (k), (l), (m) are different cross-section images of the particle dash in (j). The bulk cross-section image of Sample4 is shown in Figure 3-17 (n) and Figure 3-17 (o), (p) and (q) are different cross-section images of the particle dash in (n). The cross-section of the bulk Sample5 is presented in Figure 3-17 (r), and the different cross-section images of the particle dash in (r) are shown in Figure 3-17 (s), (t) and (u).

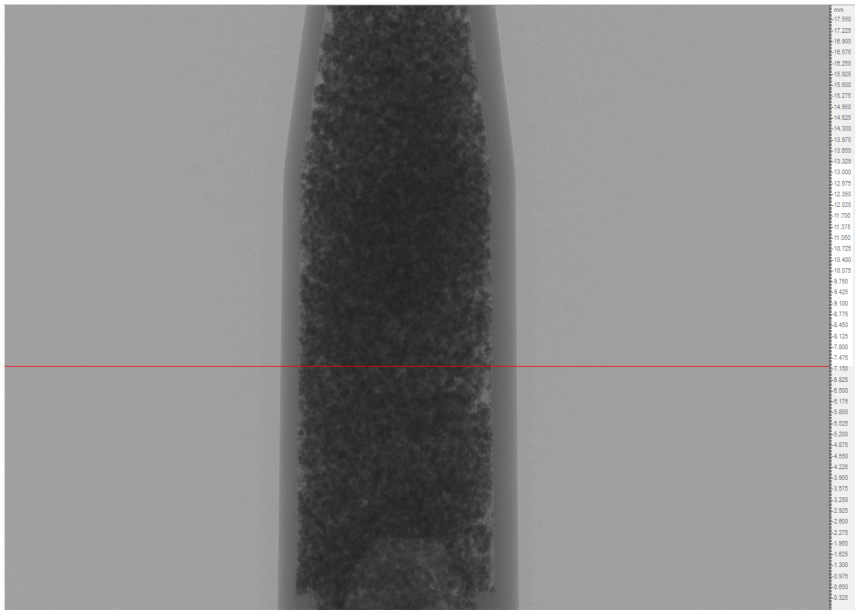

Figure 3-16 XRT scanning area of bulk particles (red line presents one cross-section).

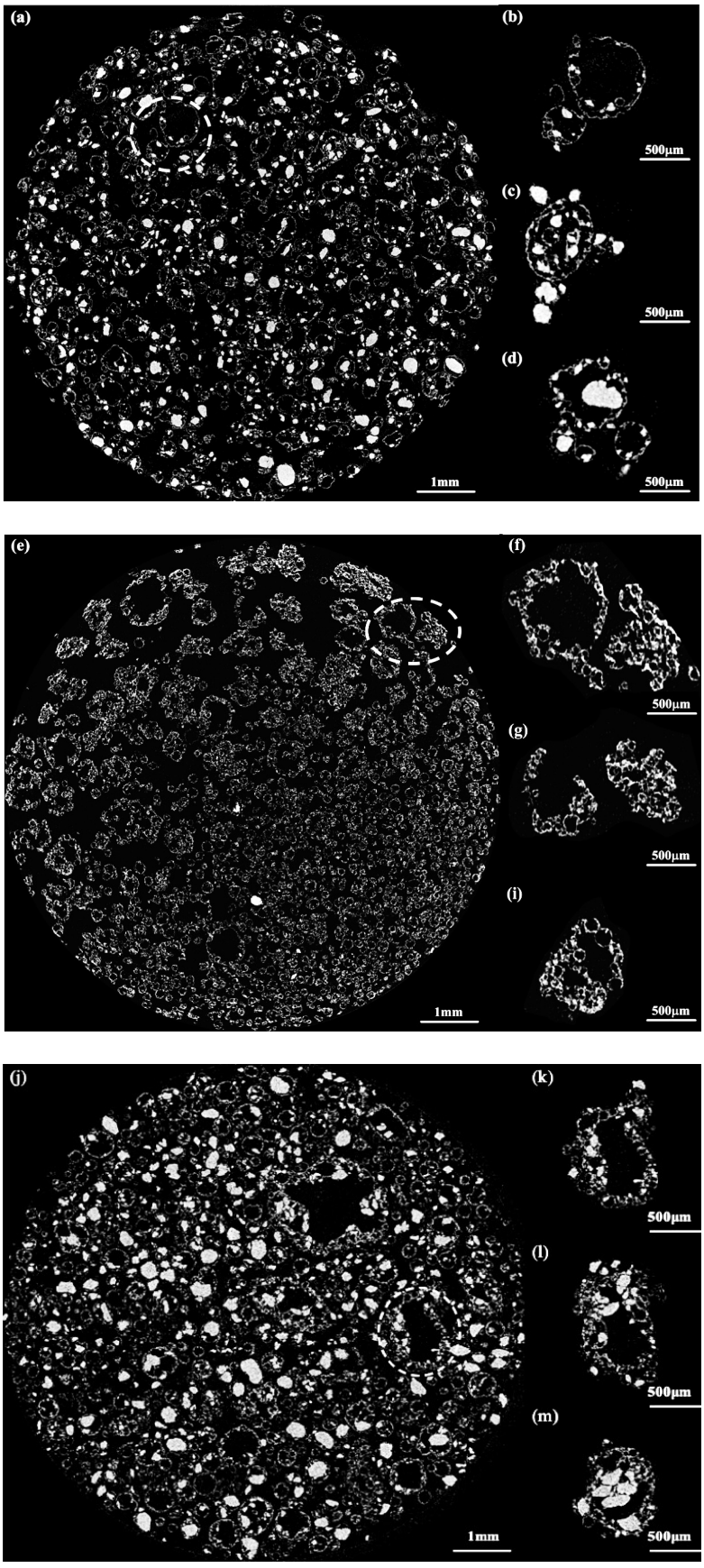
(a)
(b)
500µm
(c)
500µm
(d)
1mm
500µm
(e)
(f)
500µm
(g)
500µm
(i)
1mm
500µm
(j)
(k)
500µm
(l)
500µm
(m)
1mm
500µm

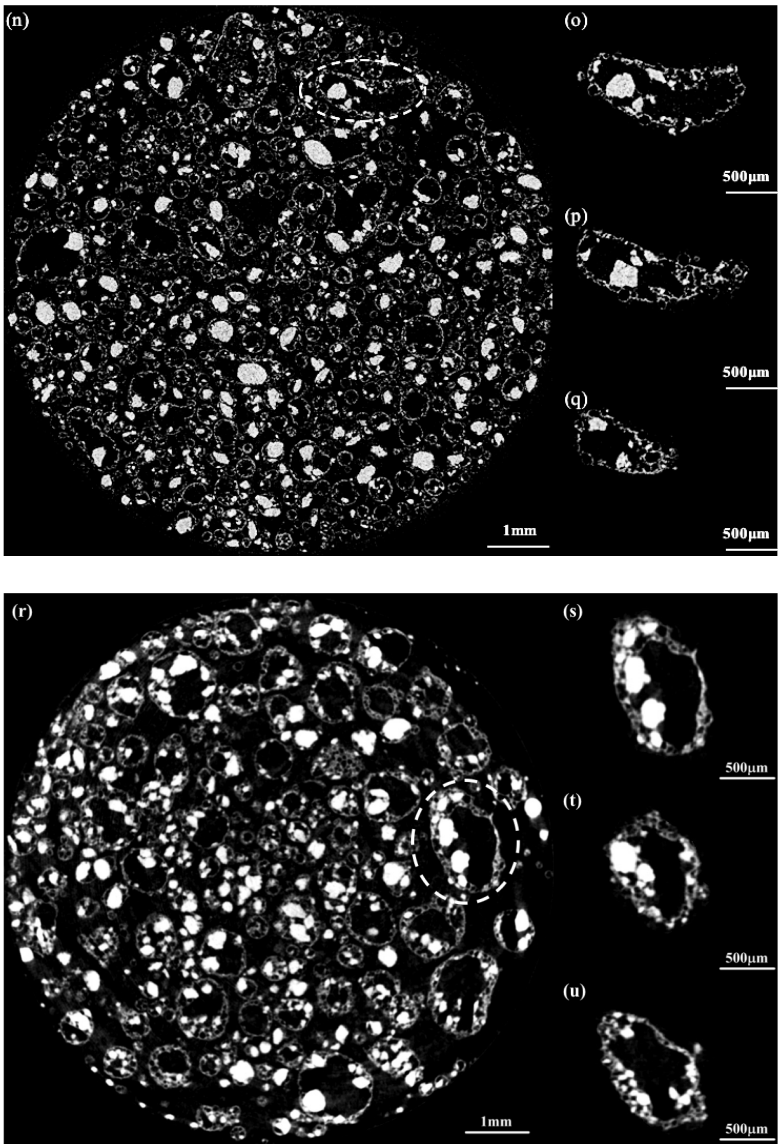

Figure 3-17 XRT images of Sample1 (a) to (d), Sample2 (e) to (i), Sample3 (j) to (m), Sample4 (n) to (q) and Sample5 (r) to (u). (a) is cross-section of bulk particles at one position, (b) (c) (d) are cross sections of the particle dash circled in (a). Same as (e) to (i), (j) to (m), (n) to (q) and (r) to (u).

The cross-section images of the bulk particles confirm that the particles have a shell structure with a thickness of about 10 μm to 100μm, and an internal hole opening towards inside and outside of the particles about several micrometres to 1 mm. Strong proof of the shell structure of particles with high internal void space has been observed from the cross-sectional images of particles in all the samples, which also agrees with literature [151]. In Sample1, high intensity pebble looking shapes have been detected inside

particles, surrounded by a thin layer about 10 to 50 μm low intensity shell. The samples with the binder Sample3, 4 and 5 following the same trend as Sample1. However, Sample2 has different features than the rest samples. A shell structure (about 10 to 100 μm) with high internal void space has been detected. As Table 3.8 shows, only small amounts of undissolved salt, 0.6%, exist in the hollow part compared to 15.4%, 10.7%, 9.7% and 10% of Sample1, 3, 4 and 5 respectively.

3D analysis results (see Table 3.8) present that Sample1, 2, 3, 4 and 5 have porosities of 75%, 81.5%, 69.4%, 62.1% and 71.6% accordingly. These results are in good agreement with Mercury Porosimetry results (see Table 3.6). Combining the results of SEM and XRT, it is not difficult to conclude that the main difference between Sample1 and 2 in terms of structure is caused by water concentration in slurry formation. Sample2 has high moisture content (62%) comparing to Sample1 (35%), which indicates that before slurry reaching spray-drying tower, there is more water in Sample2 slurry, and most of the salt is fully dissolved. While for Sample1, with lower water concentration in slurry, salt cannot be fully dissolved, and these undissolved salt remains in particles after spray-drying process. Water concentration in slurry does not only contribute to salt morphology, but also changes particle porosity. After being injected into spray-drying tower, the droplet with higher moisture evaporates more water and forms higher porosity in particle. This is confirmed by XRT results showing that Sample2 has less salt but more void space inside shell structure. The lower moisture in slurry is also the main reason for low porosity of Sample3 and 4. Sample5 has slightly lower slurry mix moisture, 30.24% comparing to Sample1, 35%, hence slightly lower porosity 71.6% to 75%.

Table 3.8 The effect of slurry water concentration on undissolved Na_2SO_4 (%) and porosity (%) results evaluated from XRT 3D analysis of bulk.

Samples	Slurry water concentration (%)	Undissolved Na_2SO_4 (%)	Porosity (%)
Sample1	35	15.4	75
Sample2	62	0.6	81.5
Sample3	28.2	10.7	69.4
Sample4	26	9.7	62.1
Sample5	30.24	10	71.6

The pore size and crystal size distribution of the 3D analysis of the bulk are presented in Figure 3-18. The comparison of the pore size distribution results shows that Sample1(low water content) and Sample3, 4 and 5 (low water content + binder) have wider distribution of pores compared to high water content and nil binder Sample2 (see Figure 3-18 (a)). The pore size of these samples ranges from 7-<20 μm to 277-<291 μm while for Sample2 is narrower from 7-<20 μm to 196-<210 μm. However, the primary percentage of pores across the samples lies between 50μm and 115 μm.

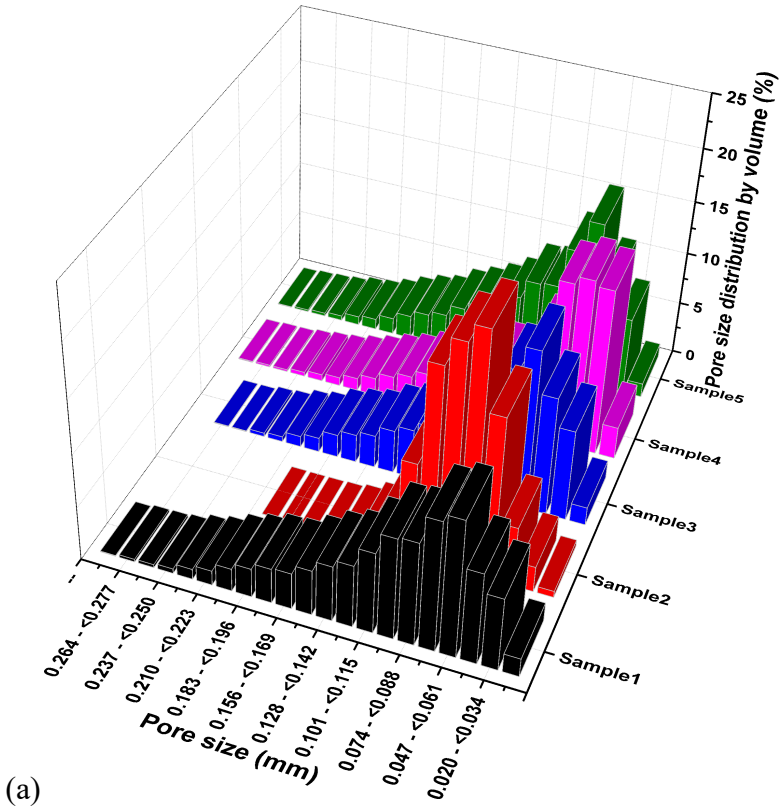

(a)

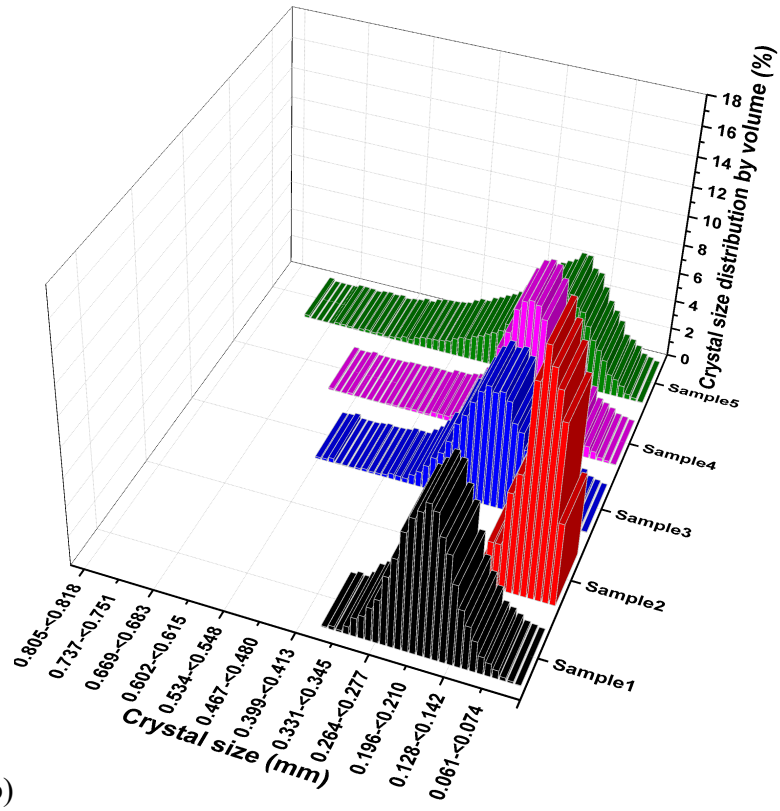

(b)

Figure 3-18 (a) Pore size distribution by volume (%) and (b) Crystal size distribution by volume (%) based on XRT 3D analysis of bulk.

The graph of crystal size distribution shows a similar trend to pore size distribution. Sample2 reveals a narrow crystal size range in contrast with the rest samples that show a more extensive profile and most of their crystals are between 0.142 - <0.156 mm and 0.237-<0.250 mm. The narrow distribution of Sample2 is probably due to the high-water portion of the slurry which dissolves most of the sodium sulphate, leaving a limited amount of small-sized crystals [151].

Figure 3-19 shows the images of the XRT analysis of individual particles from the five spray dried powder samples. Each column represents each size fraction while the rows symbolise the XRT scanning area, the XRT cross-sectional area and a random orientation of the 3D model. Single particle XRT cross-sectional area results confirm the hypothesis of the bulk that the spray dried particles have a shell structure. Furthermore, the internal structure of the particles from low water content slurries (Sample1, 3, 4 and 5), in size range of 250 to 500 μm, was found to be either hollow or semi-solid. Most of the particles contain a large a central vacuole accompanied by small-sized vacuoles distributed throughout the wall. However, the presence of small voids and/or some degree of vacuolization on the particle wall are more particularly prevalent among spray dried particles containing high slurry mix moisture, Sample2. It has also been observed a large number of non-homogenously distributed undissolved sodium sulphate around the central vacuole that occupies most of the internal space for Sample3 and 4.

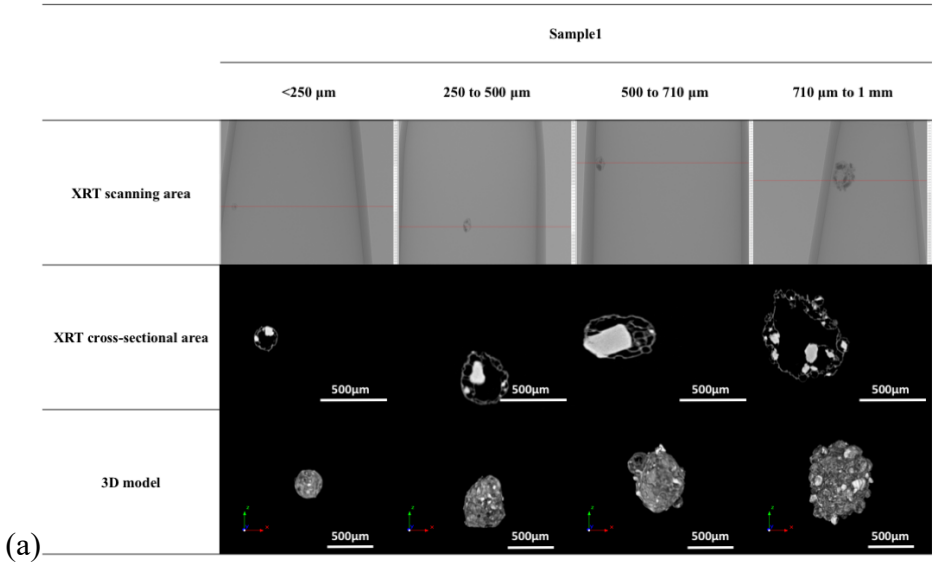
Sample1
<250 µm
250 to 500 µm
500 to 710 µm
710 µm to 1 mm
XRT scanning area
XRT cross-sectional area
3D model
500µm

(a)

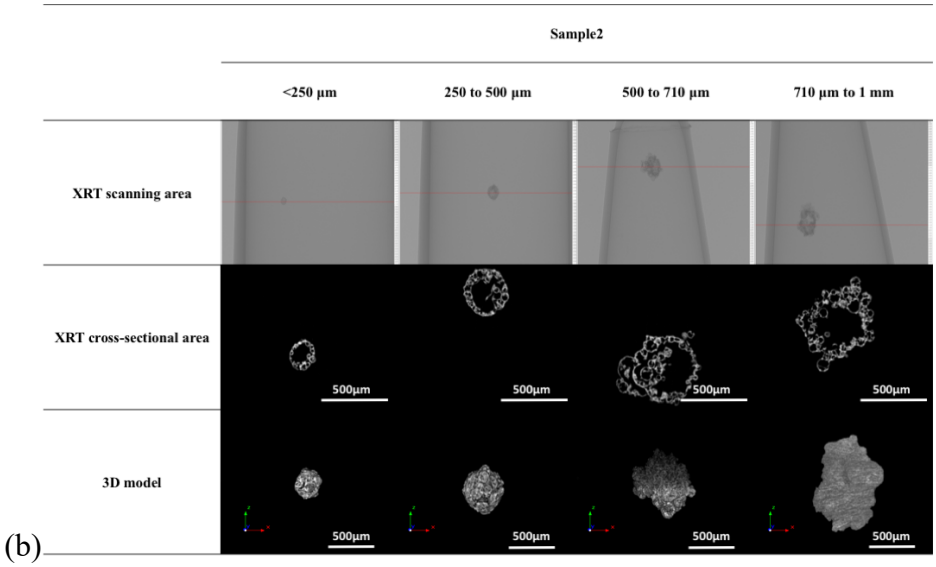
Sample2
<250 µm
250 to 500 µm
500 to 710 µm
710 µm to 1 mm
XRT scanning area
XRT cross-sectional area
3D model
500µm

(b)

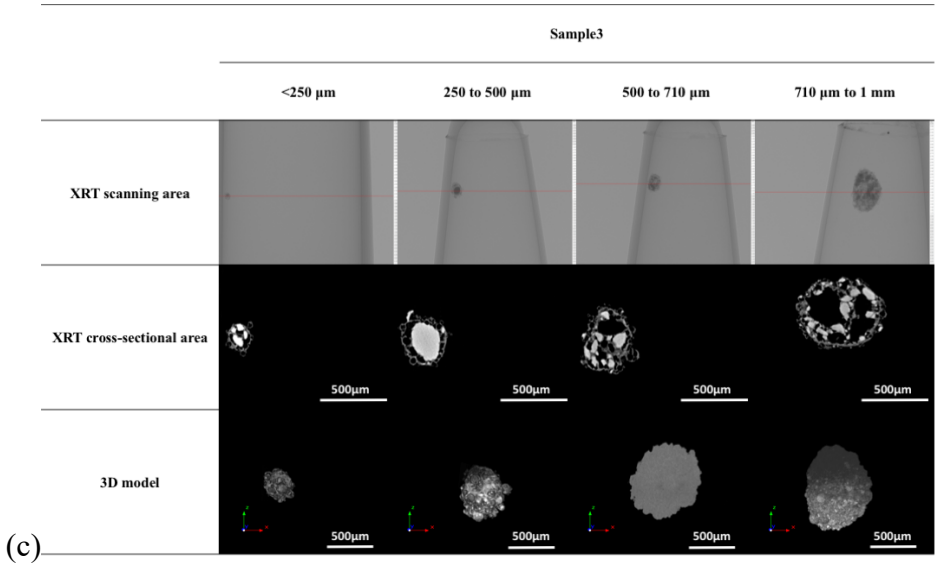
Sample3
<250 µm
250 to 500 µm
500 to 710 µm
710 µm to 1 mm
XRT scanning area
XRT cross-sectional area
3D model
500µm

(c)

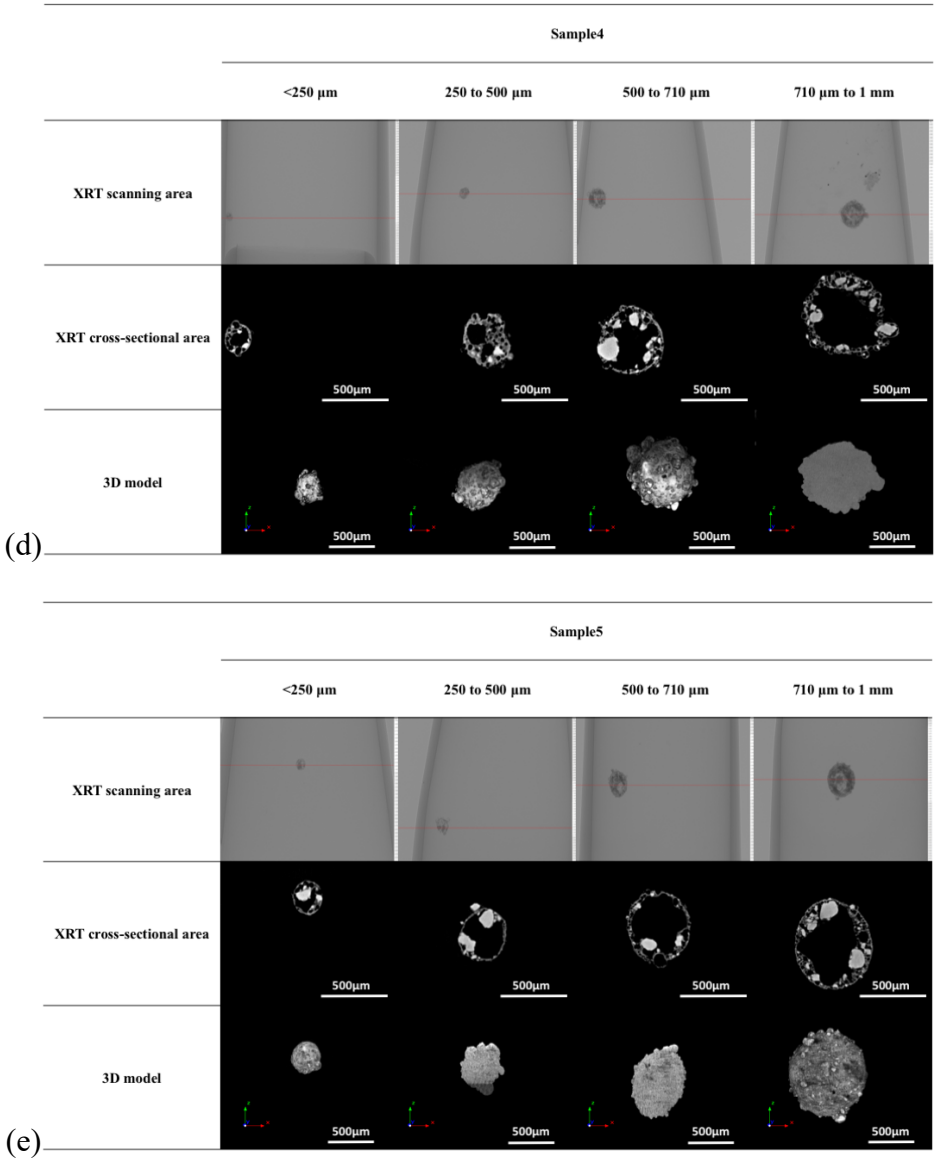

Figure 3-19 XRT images of different sized individual granules of (a) Sample1, (b) Sample2, (c) Sample3, (d) Sample4 and (e) Sample5.

The pore and crystal size distributions of the 3D analysis of different sized individual particles are presented in Figure 3-20 and Figure 3-21 respectively. The results of the single particles agree with the data obtained from the bulk analysis (see Figure 3-18 (a)) and has explained thoroughly above. In summary, the pore size distributions of Figure 3-20 show that the low water content samples (Sample1, 3, 4 and 5) have a wider distribution than high slurry mix moisture and no binder Sample2 and the main pore size of the particles is between 11 and 48 µm. Similarly, the measurements of crystal size

distribution (see Figure 3-21) agree with the bulk measurements (see Figure 3-18 (b)). It should be noticed that the results of the 3D single particle analysis cannot represent the whole of each size fraction due to the high level of diversity between the particles even of the same sample. However, they can be used as an indication of each size category that they represent.

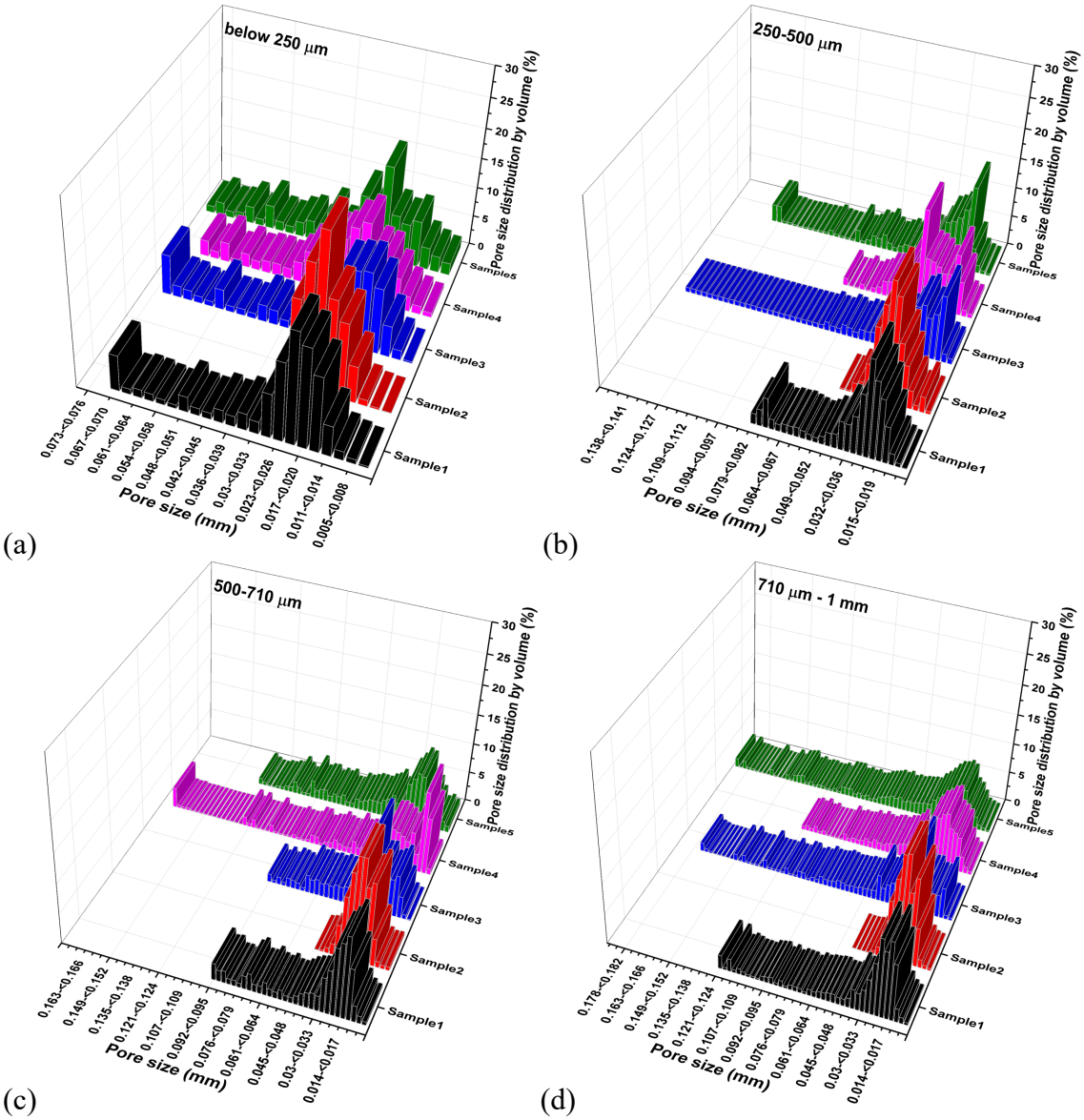

Figure 3-20 Pore size distribution by volume (%) based on XRT 3D analysis of (a) below 250 µm, (b) 250 to 500 µm, (c) 500 to 710 µm and (d) 710 µm to 1 mm single particles.

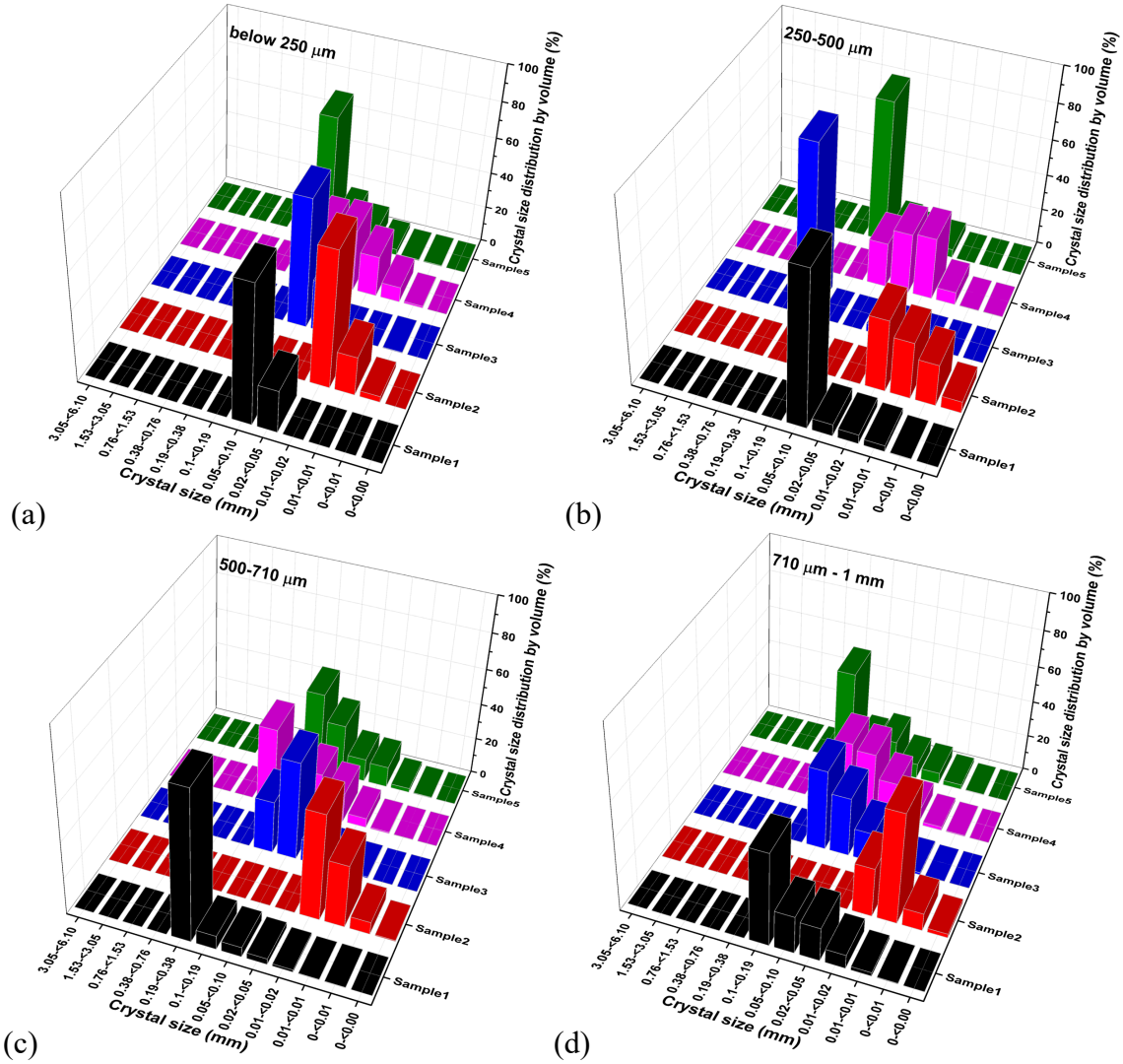

Figure 3-21 Crystal size distribution by volume (%) based on XRT 3D analysis of (a) below 250 µm, (b) 250 to 500 µm, (c) 500 to 710 µm and (d) 710 µm to 1 mm single particles.

3.5 Conclusions

In the above sections, a detailed analysis of the manufacturing process and the ingredients of the spray-dried detergent powders used in this study was presented. Characterization approaches including particle solubility, diffusivity, particle size distribution, porosity, morphology and microstructure of the five different powder samples was given. The surface morphology from SEM images and microstructure from XRT cross-section images shows that the detergent powder samples are highly porous particles which

confirmed the Mercury Porosimetry results. These particles have a shell structure with high internal void space and a large number of undissolved sodium sulphate non-homogenously distributed around the central vacuole. High slurry mix moisture results in much less amount of undissolved salt and a narrower distribution of it compared to the samples with lower slurry mix moisture. The amount of water in the slurry process affects significantly not only the particle structure but also their porosity. The effect of binder on bulk density and porosity is also crucial as it was expected based on the literature. Furthermore, the morphological properties of the particles depended on the addition of the binder. Particles with more spherical and smooth characteristics were found with the absence of binder while with its presence in the formulation a high degree of agglomeration was observed which agrees with the literature [151], [159].

The characterisation results of the spray-dried detergent powders obtained on Chapter 2 will be used to understand their dissolution performance in the following chapters.

CHAPTER 4 SINGLE PARTICLE DIFFUSION DISSOLUTION

Abstract

Particle dissolution is a commonly occurring step in many industries, e.g. in Home & Personal Care, Powders. Typical dissolution studies being used for this purpose involve several particles. However, the bulk approach cannot reveal the several phenomena taking place and the complexity of the dissolution process that the single particle dissolution studies can provide. The presented work aimed to understand the fundamental diffusion dissolution mechanisms by developing a single particle approach, to investigate the effect of porosity, particle size, binder and air on dissolution performance and to link the single particle understanding to the bulk. Dissolution of individual spray dried porous particles from below 250 μm to 1 mm in diameter was observed using a microscope with Peltier stage to control solvent temperature. The results showed a large variation in dissolution phenomena between particles and within the dissolution process of an individual granule due to the difference in particle morphology and structure. High slurry mix moisture results in up to 68% faster dissolution performance. The release rates of single particles, obtained by Image Processing, were used to predict bulk particles dissolution profiles via Nernst-Brunner equation and a Monte Carlo analysis. The comparison between experimental data and chemical measurements showed a good agreement for the samples without binder. In the presence of binder, the results did not correlate well as the polymerisation of Silicate is a strong parameter of the process.

4.1 Introduction

Dissolution kinetics of powders have been investigated for more than a century and are crucially important in various fast moving consumer goods, such as food, pharmaceutical and household products [1]. The control of the dissolution process is crucial to achieving the required properties of these products. Spray dried detergent powders account per 60-70% of the commercially available detergent washing powders and are the most common detergent powders sold globally [2]. These powders normally have porous microstructures and multi compounds [3]. Therefore, analytically studying dissolution of these powders is challenging compared to one ingredient solid powders because gas (porosity), liquid or soft solid (detergent) and solid (primary particles) phases are all involved in this process [4].

Researchers [1], [5]–[8] proposed, the following sequential stages regarding the dissolution process of a structured particle (see Figure 2-11): i) wetting of granules i) penetration of liquid into pores due to capillary forces depends on if the particle has porous structure or not, ii) immersion of granule in the liquid, iii) dispersion of the primary particles within the liquid and iv) the dissolution of soluble primary particles. In these steps, the kinetics of the dissolution mechanisms are influenced not only by the physical but also the chemical characteristics of the liquid medium (e.g. surface tension, viscosity, density, temperature) and those of the powder itself (e.g., particle size, density, porosity, chemical composition).

The fundamental equations often used to describe the dissolution process are based on Fick's laws of diffusion [61], [62], such as the Noyes and Whitney [36] and Nernst and Brunner [38], [42] equations and the Hixson and Crowell cube root model [43]. Other relevant models describe the dissolution process including zero and first-order kinetics

and those developed by Niebergall et al. [64] and Higuchi and Hiestand [65] are summarised in Table 2.2 of Literature.

In general, the investigation of dissolution rates of small amounts has been conducted via bulk dissolution methods [1]. The most common method for conducting dissolution experiments is a USP (U.S. Pharmacopeia) dissolution apparatus. Several studies on pharmaceutical and food powders have been published based on this method, quantifying the dissolution process with the use of UV spectrophotometer [9]–[11], conductivity meter [12], viscometer [13]–[16], rheometer [17], calorimeter [18], rheometrics fluid spectrometer [14], [15] and an immersion refractometer [19].

However, dissolution of bulk-particles is very challenging and complex to understand precisely [20]. This is due to critical parameters influencing the dissolution rate of powders such as the particle size and shape, degree of aggregation and agglomeration and the interactions between the particles are difficult to explain accurately [21]–[23]. The difficulty is enhanced if we consider the dynamic change of these parameters through the dissolution. Therefore, the accuracy of the measurements obtained from bulk particles relies on the efficiency of the statistical predictions [24]. This obstacle can be avoided by assessing the dissolution rate from single particles. By examining single granules, the cohesive interactions between particles can be ignored and the particle shape and size may be exactly observed. Therefore, the single-particle theory can minimise the hypothesis considering parameters affecting the dissolution behaviour, and the results can be considered as more trustworthy.

Nevertheless, dissolution experiments of single particles have been carried out in limited cases. The first papers published by Raghavan et al. [31] and Prasad et al. [32] who studied the effect of different faces of a-lactose monohydrate and paracetamol single

crystals on dissolution kinetics respectively. Bhandari and Roos [26] investigated the effect of temperature and concentration on the dissolution of sucrose crystals. A research on single sucrose particle dissolution kinetics has been conducted by Marabi et al., [1], who measured the impact of liquid viscosity and enthalpy of dissolution. In 2011, Ostergaard et al. [100] investigated the effect of pH in the dissolution of sodium naproxenate. Borjesson et al. [33] showed that dissolution of sodium caseinate particles is related to the flow rate of the dissolving medium. Recently Smrcka et al., [35] presented that dissolution is sensitive to the granulation process conditions.

In all previous single-particle studies no link of the single particle understanding to the bulk has been performed, and no investigation on the effect of air on the dissolution of spray dried powders has been examined. In the present study, two different approaches have been used to link single particle diffusion dissolution understanding to the bulk based on different sized single particle dissolution analysis experimental data, a Nernst-Brunner approach and a Monte Carlo analysis. To evaluate this approach chemical analysis data of the same bulk powder samples has been used. The comparison of these methods will allow us to understand the effect of interactions developed between the particles and their significance on bulk dissolution performance that the standard analytical methods cannot reveal. The possible use of this approach would give significant benefits compared to the current bulk particle dissolution methods.

4.2 Materials and Methods

4.2.1 Materials

Five spray-dried detergent powder samples, Sample1, 2, 3, 4 and 5 have been used for the single particle diffusion dissolution experiments. The composition of the samples has been discussed thoroughly in Section 3.2 of Chapter 3.

4.2.2 Diffusion dissolution experimental setup

A new dissolution method was developed to obtain kinetics of single particle diffusion dissolution using an optical microscope. The schematic of the dissolution experimental setup is shown in Figure 4-1. An inverted light microscope Leica Z16 AP0 coupled to a monochromatic digital CCD camera (Leica Microsystems GmbH, Germany) was used to monitor and record the dissolution process. Image resolution was set at 1376x1038 pixels (406.3890 pixels/mm) for all the experiments. Images were recorded at 5 frames per second by the open source software µManager (US National Institutes of Health) [169]. 50 individual particles from each size fraction (below 250 µm, 250-500 µm, 500-710 µm and 710 µm to 1 mm) were put in the cavity of a microscope slide, which contains 140 µL of deionised (DI) water. The microscope slide was placed on a Peltier stage LTS120 (Linkam Scientific Instruments Ltd., United Kingdom) to control water temperature at 20dC. To enhance the contrast of the image, a black hardboard was placed underneath the glass slide.

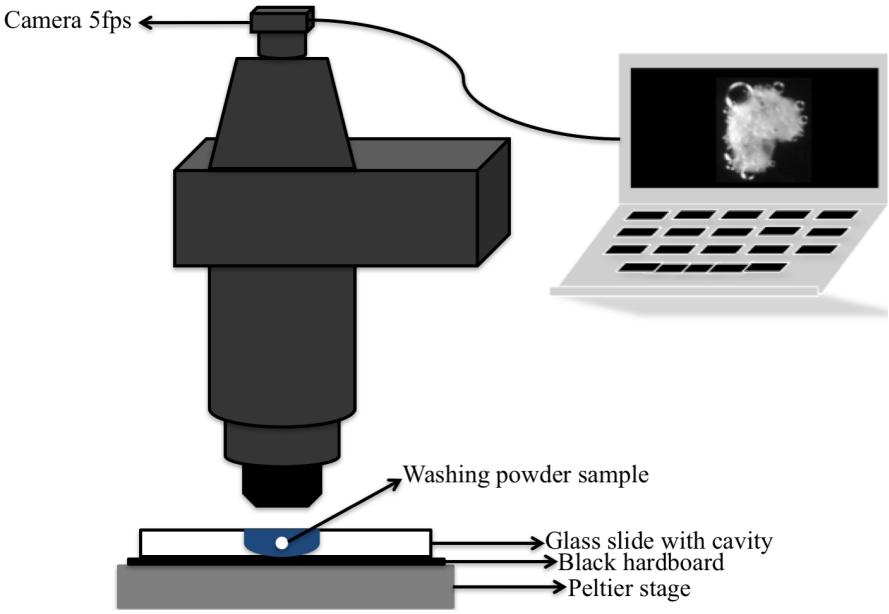

Figure 4-1 Schematic of single particle diffusion dissolution experimental setup.

4.2.3 Image Processing

The recorded images were analysed with ImageJ (US National Institutes of Health) [168], and dissolution profiles obtained based on the extracted surface area. Bubbles appearing in the perimeter or the surface of the granules during the dissolution process were removed using a custom-developed by myself algorithm in Java language. The algorithm first requests for the input folder, which is the folder with the raw images, and the output folder, which is the folder where the generated processed images will be saved after the process. Then, duplicates the initial raw image and applies grayscale morphology plugin (mathematical morphology on grayscale images), auto thresholds and coverts the image to black and white and finally subtracts the duplicated processed image from the initial. Two images produced one with the particle without the bubbles and one with the removed bubbles. They were both saved in the output folder. The surface area of the particles is then estimated from the processed images. A detailed overview of the custom-developed algorithm is given in APPENDIX A.

4.3 Results and Discussion

4.3.1 Dissolution phenomena

In an attempt to understand the mechanism behind diffusion dissolution, experiments were conducted on 50 individual particles at four size ranges to observe the process using an optical microscope at 20dC.

The stages of dissolution process of active ingredients of a porous particle are shown in Figure 4-2: i) the Wetting, where water intrudes into the pore system of the granule due to capillary forces, ii) Early Disintegration, as water fills the pores of the granule, an amount of trapped air is trying to escape by breaking granule's initial structure, iii) Shrinking where granule mass reduces gradually due to diffusion, iv) the dissolution of

the solid bridges between the main particles resulted in the Later Disintegration of the main particles within the liquid and v) Dissolution of soluble main particles. It is critical to mention that in bulk dissolution these stages are difficult to be entirely isolated. These steps might occur simultaneously rather than sequentially depending on physicochemical properties of powder and dissolving liquid. Thus, evaluation and simulation of these processes remain a challenge [6]. The presented dissolution phenomena are similar to the phenomena described in the literature [7], [8]. The first line shows the raw images and the second the images after the Image Processing treatment. The comparison of the raw and processed images can reveal the high accuracy of the custom-developed algorithm that was used.

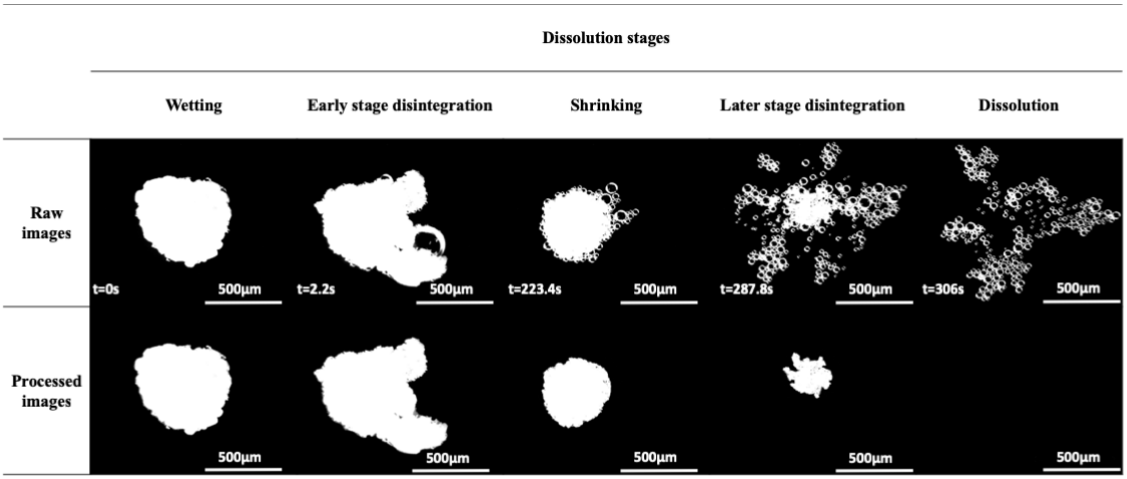

Figure 4-2 Overview of the dissolution stages (first line: raw images; second line: images after image processing).

Different dissolution behaviours of single and multiple particles according to the different types of binder that the powder samples contain were summarized in Figure 4-3. First line in Figure 4-3 shows the characteristic dissolution process of a single particle without the presence of binder (Sample1 and 2). The particle breaks after wetting in 2.2 s due to capillary forces and trapped air into the pores, followed by a period of shrinking and then disintegrated very fast in less than 18 s. The third line in Figure 4-3 presents the

characteristic dissolution process of a single particle with Silicate binder (Sample3 and 4). The dissolution behaviour is different than the one described above. The particle breaks in 42.2 s after wetting and the transparent solution starts to become cloudier forming a gel. This is due to the polymerization of silicate. In mildly acidic to basic conditions it is established that silica polymerization starts with the condensation of monosilicic acid into cyclic oligomers, which elevates to three dimensional polymer particles [170]. The polymerization rate of Silicate is affected by the pH, silicate concentration, temperature and concentration of the divalent cations [171]. That cloudiness thickens as gel develops in shrinking stage. The particle is slowly released as the gel layer blocks the dissolution. Dissolution finished after 422 s where the bubbles remained inside the gel. The fifth line in Figure 4-3 presents the characteristic dissolution behaviour of a single particle containing a mix binder of Citric Acid, $MgSO_4$ and Zeolite (Sample 5). Although it was expected the dissolution performance to have similarities to single particle with Silicate binder, it looks comparable to the single particle without binder dissolution of the first line. This is due to the presence of Citric Acid in the formulation which works as disintegrant and its role is to enhance the breakup of the granule [154]. The particle breaks in 4 s after the wetting due to water penetration through capillary action, then a long period of reducing the size follows and finally disintegrates instantly. The second, fourth and sixth line in Figure 4-3 represents the dissolution of multiple particles without binder, with Silicate binder and with mix binder respectively. The dissolution performance of multiple particles across the different type of samples is similar. Especially for the particles with Silicate binder, it was expected that the cloudy gel layer to increase due to the number of particles however this did not happen. One of the particles break in 5.6 s and then the shrinking stage started earlier than on the single

particles. The total dissolution lasts 166.2 s while one of the three particles has already been dissolved previously. In comparison, the dissolution of the multiple particles with Silicate binder was significant faster than the dissolution of single particle with Silicate binder and equivalent to the dissolution time of the particles without binder and with mix binder. The absence of polymerized Silicate formation is probably due to increase of concentration of sodium sulphate in the solution. According to literature [170] there is a critical coagulation concentration (ccc) of salt that determines the Silicate flocculation rate. The main theory by which salt affecting the polymerization of Silicate is through an additional short-range repulsive force. Two are the hypothesis concerning the nature of this additional repulsive force. Several researchers [172]–[174] consider that the Silicate particles are well bound to water molecules and the additional repulsive force is a hydration force derived from the disorientation of the arranged water layer requires for the particles to come in contact and aggregate. The second hypothesis assumes that the repulsive force is a steric force derived from the presence of "silica hairs" coming through the Silicate surface [175], [176]. These hairs, which are silanol or silicilic acid groups, can fall apart at higher ionic strength, presenting less steric resistance [177]. A second theory by which salt affecting the polymerization of Silicate can be the impact of specific ionic effects on the chemical bonding among aggregated Silicate particles. Addition of salt to an alkaline solution (pH ≈ 10) leads in lower pH, charge screening and reducing the dielectric constant of the aqueous phase, which decreases gelation time [171].

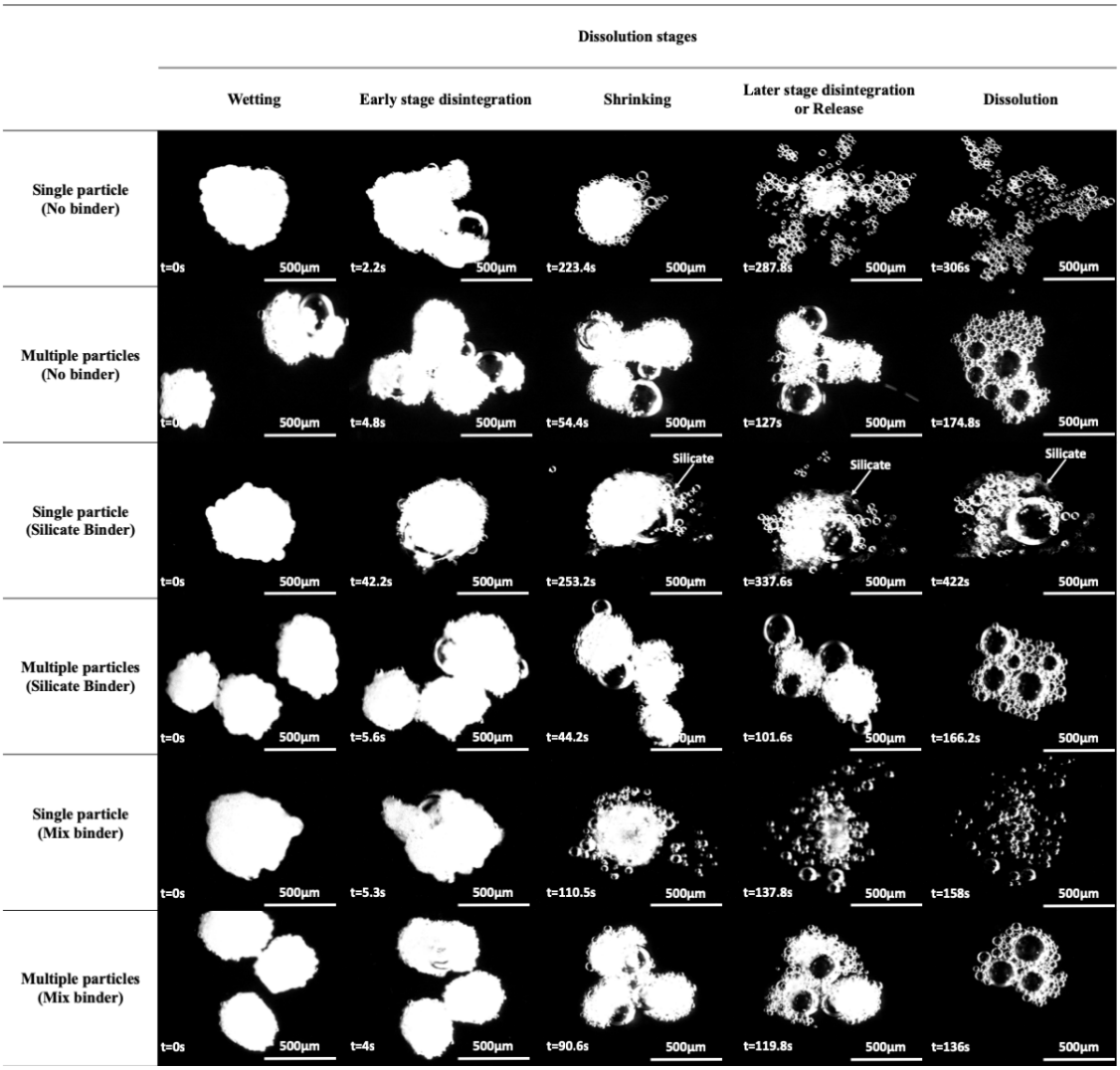

Figure 4-3 Different dissolution behaviour: the first and second line represent the dissolution of single and multiple particles without binder respectively; the third and fourth line show the dissolution of single and multiple particles with Silicate binder respectively; and the fifth and sixth line present the dissolution of single and multiple particles with mix binder (Citric Acid + $MgSO_4$ + Zeolite).

4.3.2 Disintegration phenomenon

Four different types of dissolution process have been observed, as shown in Figure 4-4. Each row represents one particle dissolution process. The first three rows are type I. In this type, particle broke up in a very short time after immersing in water, 3, 1.4 and 2.2 s from A → B, I → II and (1) → (2) respectively. Meanwhile, big bubbles (bubble size is bigger than one fourth of particle size) appeared on all of the three particles, seeing images

B, II and (2) on each row. Then, particles dissolved, size decreased and eventually all solid part disappeared, dissolution finished. In this case, disintegration occurred abruptly in the early stage with big bubble appearance. The fourth row is the type II dissolution process. Big bubble also appeared in dissolution but did not break particle (image (b)). The rest of the process was similar to type I, particle dissolved, size decreased, and solid part disappeared. No disintegration was observed. The fifth row is type III dissolution process. From image (i) to (ii), particle slightly swelled. No big bubble appeared at early stage. As particle continuously dissolved, size decreased, a big bubble appeared in the middle of the solid part (image (iv)) until particle fully dissolved. No disintegration was observed. The bottom row in Figure 6 are images from type IV dissolution process. In this type, neither big bubbles nor disintegration was observed. Particle shrank to smaller size until all the solid part disappeared. In summary, it appears that disintegration is strongly related to the existence of big bubbles. They are located either in the middle of the particle or beside the particle. Some of them appeared in the early stage accompanied with obvious particle disintegration. Some of them appeared later accompanied with particle swelling. However, when there was no big bubble in the process, no disintegration happened either. These phenomena lead to a hypothesis that the force breaking these particles comes from the compressed air inside them. Once contacting with water, due to the high surface tension, water invades inside porous powder due to the capillary pressure. The resident air is compressed, resulting in particles being stressed by the air pressure. Meanwhile, the solid bridges between the primary particles weaken continuously, as a result, particle breaks, and disintegration happens.

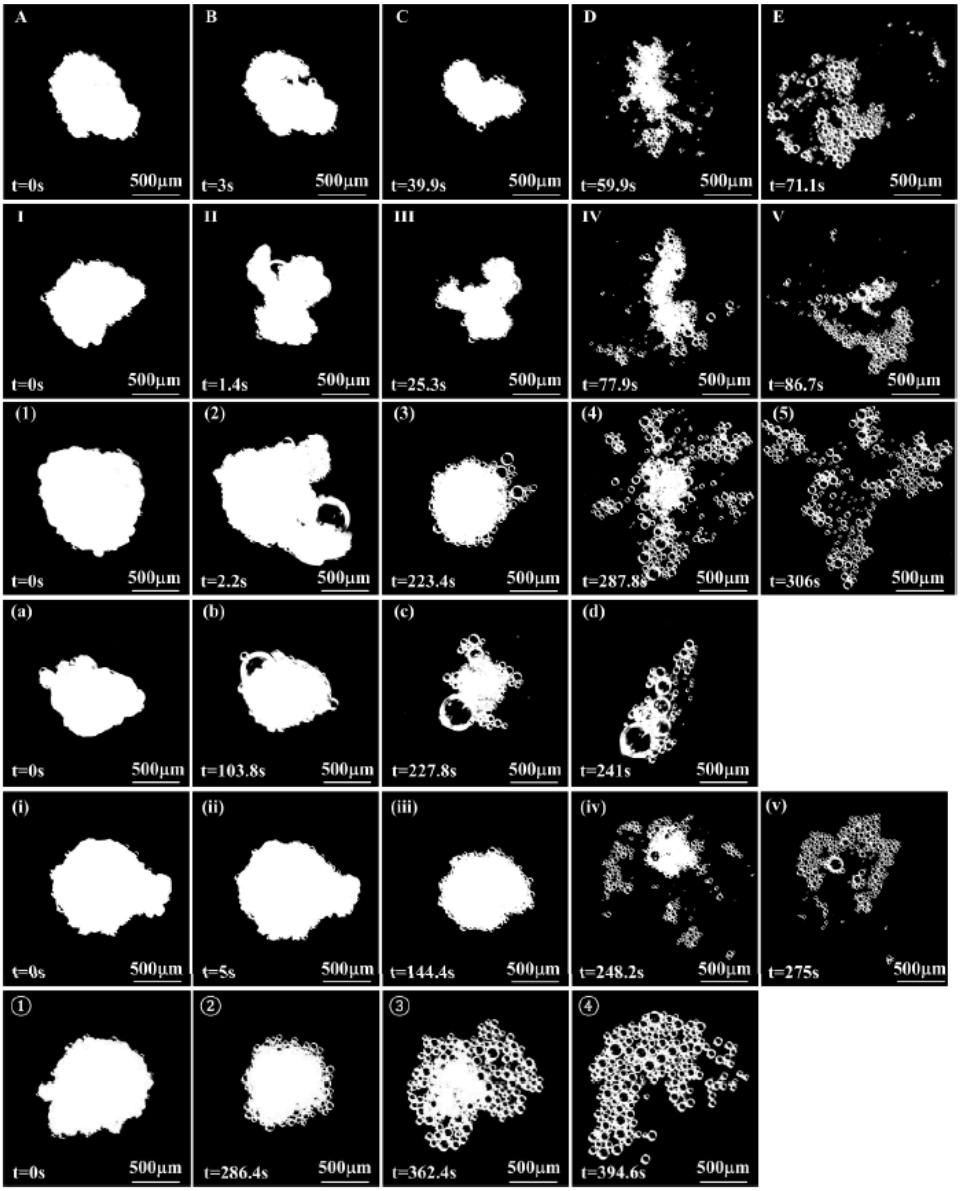

Figure 4-4 Typical different dissolution phenomena summarized in image sequences of which particles dissolve in water at 20dC: first row A~E represent a granule dissolves in water and disintegration happens at 3 s, second row I~V particle dissolves and disintegration happens at 1.4 s, third row (1)~(5) represents particle dissolution and disintegration happens at 2.2 s, fourth row (a)~(d) are granule dissolving and no disintegration happens, fifth row (i)~(v) particle swells (not significantly) instead of disintegrates, and last row ①~④ particle dissolving and no disintegration happens.

Observing the phenomena occurring during dissolution via the analysis of 1250 dissolution videos, a map of the dissolution behaviour of the powders was created (see Figure 4-5). Each phenomenon is presented with the probability (%) to occur during a

single particle diffusion dissolution of one of the five spray dried powder samples. Green arrows represent the flowline which shows the order of procedure, while red arrows represent the choice of flowline if the previous phenomenon does not take place. The subcategories of a phenomenon are presented with the dashed line. Big bubbles have been defined the bubbles with size equal or above of 100 μm and fast disintegration is the disintegration which happens in less than 2 s.

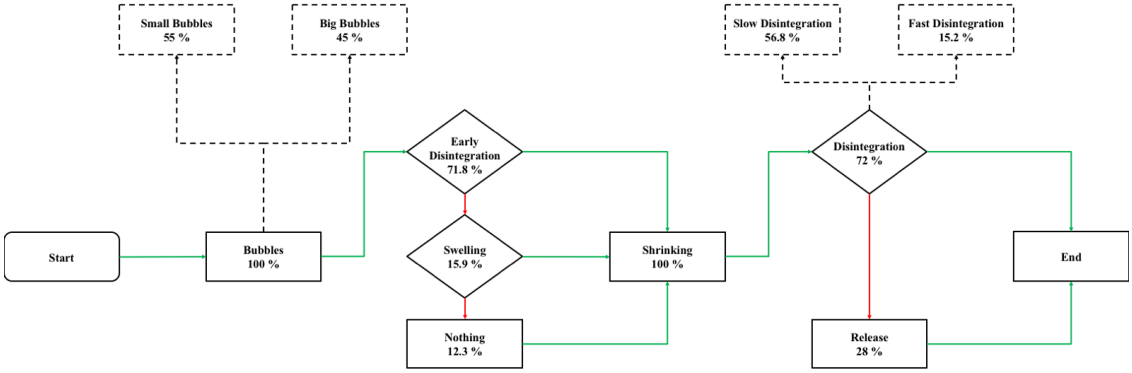

Figure 4-5 Flowchart of single spray dried particle diffusion dissolution phenomena.

4.3.3 Effect of particle size and microstructure on dissolution times

The total dissolution time t_f (s) as a function of particle size (μm) is plotted in Figure 4-6 (a). A significant effect of particle size and porosity on dissolution time has been revealed. Particularly it can be observed that increasing the size of the particles. The dissolution time increases linearly for all the powder samples. For below 250 μm Sample 2 and Sample 5 dissolves significantly faster, in 17.24 ± 5.47 s and in 22.5 ± 7.16 s respectively, than Sample1 60.10 ± 33.74 s, Sample 3 63.17 ± 33.85 s and Sample4 94.54 ± 34.64 s. The same trend follows the rest size fractions. However, as the particle size increases higher than 250 μm the dissolution time of Sample5 is faster than Sample2. Boerefijn et al., [3] commented that the surface area of the granule is affecting the dissolution time but is not determining it. Because surface roughness and asperities are dissolved away quickly, therefore the particle size is one of the main factors determining it. Another factor

is particle porosity which can alter the dissolution time, as the higher the particle porosity, the smaller the relative volume to dissolve per granule and hence, the faster dissolution. In this study, the effect of porosity is strongly correlated to formulation as the increased slurry mix moisture leads to less undissolved Sodium Sulphate and as a consequence higher levels of porosity. For Sample3 and 4 which are generally slower than Sample1 and 2 except the slurry mix moisture, Silicate binder affects the porosity, the dissolution behaviour of the particle through the polymerisation of Silicate (as described in the previous Section 4.3.1 and as a result dissolution time. However, it is interesting that Sample5 that contains a different type of binder (mix of Citric Acid + $MgSO_4$ + Zeolite) and 73% of porosity is slightly faster than Sample2 which has 85% of porosity and no binder. It seems that the Citric Acid which is a disintegrant through the enhancement of the breakup of the particle increases the available surface area and the fast release of the powder [153], [154]. Ansari et al., [19] noticed that porosity should decrease linearly as the volume of binder is increased, due to the increased fraction of the inter-particle void space which would be filled by the binder. This correlates well with Stepanek [87] who has shown in the simulations of particle dissolution that depending on the binder, porosity can have an effect on dissolution time, as lower porosity leads to slower dissolution.

In addition to this, disintegration is a different method to influence dissolution time and a particle will disintegrate when the binding components between the primary particles are either dissolved or broken. The dissolution time of a washing powder particle has been described as:

$$t_{dissolution} = t_{disintegration} + t_{dissolution\ of\ disintegration\ products}$$

where $t_{disintegration}$ is the time needed for the disintegration process, and $t_{dissolution\ of\ disintegration\ products}$ is the time needed to dissolve the primary particles

generated via disintegration [3]. In this research, the critical disintegration phenomena times: early stage disintegration time t_b(s) and later stage disintegration time t_d (s) were measured by Image Processing. Figure 4-6 (b) and (c) shows the relationship between the early and late disintegration with the dissolution time, t_b/t_f and t_d/t_f versus powder porosity (%). All powders present early and late disintegration when total dissolution process reaches the 15% and the 70% respectively. The t_b/t_f, decays exponentially with the increasement of porosity from 65 % to 85% as more trapped air is located inside the granule, higher internal forces generated after water intrusion and the particle breaks faster. On the other hand, as the particle size increases the t_b/t_f decreases due to the longer dissolution times of bigger particles. Sample1 and 2 show early stage disintegration only for particles above 250 μm compared to Sample3, 4 and 5 which particles break across the size range. This is because as SEM results indicated (see Figure 3-11) that the agglomeration of Sample1 and 2 starts at above 200 μm. Furthermore, Sample3 and 4 break later on the dissolution process. This is probably due to the polymerisation of Silicate which slows down the dissolution phenomena. The later stage disintegration does not show any significant relationship between the particle size, the powder porosity and the time that it happens across the samples.

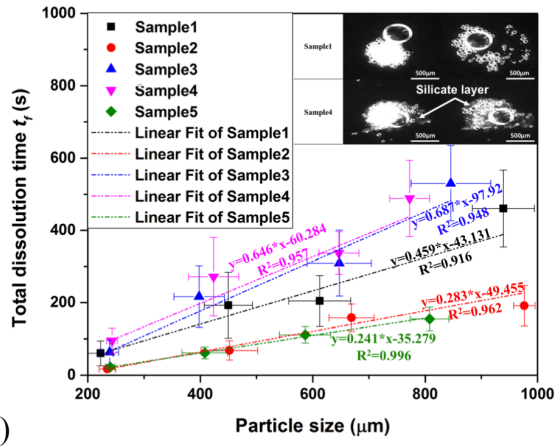

(a)

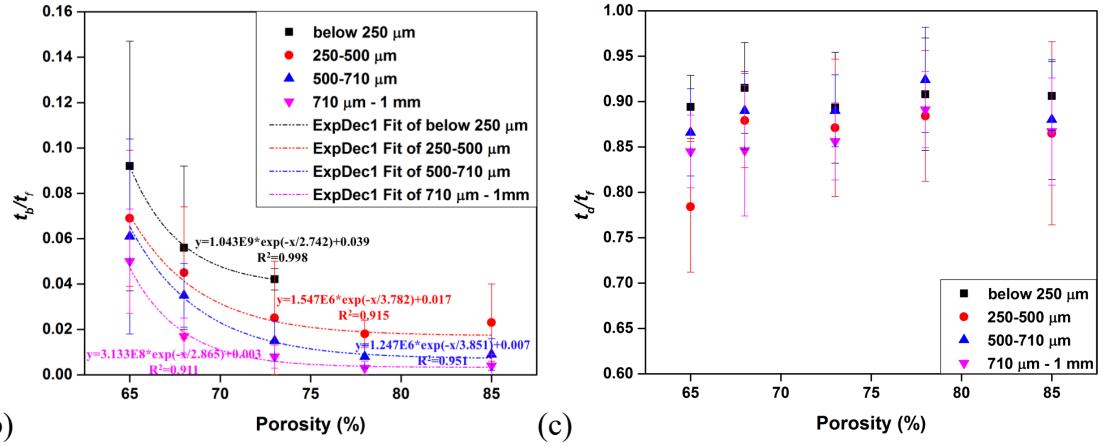

Figure 4-6 (a) Total dissolution time t_f (s) versus particle size (μm) of the samples for each size fraction, (b) the ratio between the early stage disintegration time t_b and t_f (t_b/t_f) versus powder porosity (%), (c) the ratio between the later stage disintegration time t_d and t_f (t_d/t_f) versus powder porosity (%).

4.3.4 Dissolution profiles

The release profiles of the particles based on the changes of the surface area of the particle, A_p (mm^2) were evaluated using Equation (4-1) and are shown in Figure 4-7.

$$dissolved_t = \left(1 - \frac{A_{p,t}}{A_p}\right) 100 \tag{4-1}$$

where $A_{p,t}$ is the projected surface area of the granule at time t.

All the powders have unique dissolution profiles, different from the results obtained from other dissolution measurements [178], and high standard deviations. This is because each particle is unique, irregular shaped with different dissolution behaviour. In general, the dissolution starts more progressively, then slows down and finally finishes very fast in the last 30% of the dissolution when the disintegration moment begins. For particle size, less than 500 μm the sample with no binder and high slurry mix moisture, Sample2, and the sample with the disintegrant Citric Acid in the binder mixture, Sample5, show the faster dissolution behaviour, while above 500 μm Sample5 is the fastest dissolving. Throughout the different sizes Sample2 shows faster dissolution performance from the

beginning and for the biggest part of dissolution the compared to the rest of the samples. On the other hand, Sample5 starts dissolving slowly until it reaches the disintegration point where its progressing very fast until its fully dissolved. The samples that contain the Silicate binder, Sample3 and 4, are the slowest dissolving across the size cut, which is due to the polymerization of Silicate that slows down dissolution phenomena. Negative released surface area values have been detected which is mainly due to early-stage disintegration. Since the initial particle surface area was used as the initial value when early stage disintegration happens, particle break up, the surface area increases hence the negative value. The unique advantage of this experimental approach is to show clearly the disintegration of our samples. Across the size range Sample1 and 2 started showing negative values (early stage disintegration) when the particle is above 250 μm while Sample3, 4 and 5 started from the smallest size cut. It appears that, Sample3 and 4 disintegrate for a longer period than Sample1,2 and 5. This is mainly due to the appearance of Silicate binder, in the formulation. Comparing Sample3 and 4 the result implies that the higher the Silicate binder concentration, the longer the disintegration period will be. However, since Silicate polymerises in the solution and forms a layer structure around the particle even if disintegration happen the dissolution will not be accelerated [158], [159]. In contrast, for Sample5, the disintegrant Citric Acid in the binder composition enhances the early disintegration phenomenon and via the increasement of the available surface area speeds up the total dissolution process [154].

The characteristic particles illustrated in Figure 3-11 and Figure 3-17 demonstrate that the particle morphology and microstructure differ significantly between granules from the same sample, resulting in different dissolution profiles between the particles, hence the variation of the results. As seen in Figure 3-11 and Figure 3-17, the particle porosity,

as well as the smoothness of the particles, varies greatly between the granules. Both these parameters will influence the dissolution behaviour of the granule. Nevertheless, the smoothness of the surface of the particle is possible to affect only the initial stage since the rapid swelling of the particle is expected to smooth out any irregularities at the particle surface, leaving the differences in particle porosity as the main cause for the variation in dissolution profiles (between particles) [33]. Also, the level of agglomeration influences the dissolution behaviour as according to de Villers [179] the presence of agglomerates slows down the dissolution of the powders. Smrcka et al. [35] indicated that the dissolution mechanism is sensitive to the granulation process conditions, and can change from the disintegration to the leaching mechanism for the same formulation with the same bulk properties (particle size, bulk density).

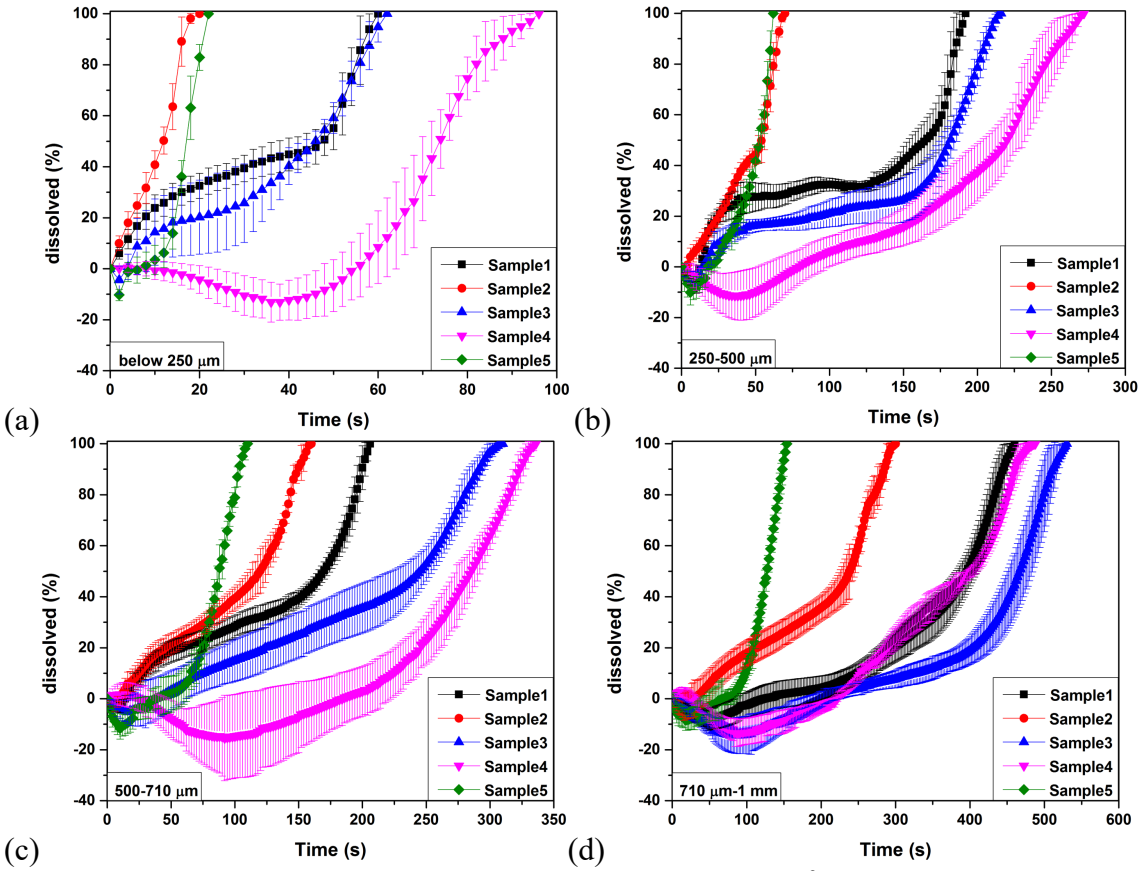

Figure 4-7 Dissolution profiles based on surface area (mm^2) versus time (s) for (a) below 250 µm, (b) 250-500 µm, (c) 500-710 µm and (d) 710 µm-1 mm.

4.3.5 Effect of particle size on dissolution rate

Dissolution rates are commonly acquired by bulk measurements, either using rotating disc method [9], [180] or a stirred dissolution medium [12], [19]. However, particles might have a different interior structure compared to the surface [181], resulting in time-dependent rates of dissolution. Such differences are difficult to measure using bulk methods since the dissolution rate will be averaged between all the particles and often also over time. The phenomena are on the scale of individual particles. It is often preferable to express the dissolution rate as a function of a surface specific value. This can be achieved either by exposing a constant surface area of the solid to the dissolving liquid or by continuously measuring the change in surface area, as a function of time.

In this study, the dissolution rates for the particles of each size fraction were obtained using two different approaches.

In the first approach, the dissolution rate dW/dt per mm^2 was obtained by differentiating the changes in weight during time and dividing it with the surface area of the particle at that time $A_{p,t}$ (see Figure 4-8). The weight of the particle at each time interval $W_{p,t}$ was evaluated by multiplying the initial weight of the granule W_p with the amount dissolved at that moment

$$W_{p,t} = W_p dissolved_t \tag{4-2}$$

The value of the dW/dt per mm^2 during the 4/5 of the total dissolution process does not change significantly for the different particle sizes and it varies between 0 mg/smm^2 and 10 mg/smm^2. This part includes the wetting, early disintegration and shrinking stage. When the particle breaks at the first moments of the dissolution, the surface area increases as previously explained in Section 4.3.4 and the dissolution rate slightly drops (negative values). During the shrinking stage the dissolution rate, does not change significantly

because the changes on the surface area between the time intervals are not big. The dissolution rate accelerates and takes the highest value at the final stage of the dissolution when the disintegration starts. At that moment, the dissolution rate increases from 40 % to 90 % for Sample1, from 20% to 90% for Sample2, from 50% to 280 % for Sample3, from 50% to 300 % for Sample 4 and from 50% to 120 % for Sample 5 at each size respectively. It seems that the dispersion of the agglomerated in smaller parts results in an increase of the dissolution rate. This is due to the decrease of the diffusion layer thickness around each particle [64], [73] and also by the increasement of the interfacial surface area [36], [38], [42]. According to equation (2-4) the higher the effective surface area is, the greater the contact between the surface of the solute and the solvent and thus the faster the dissolution process becomes. The difference in the maximum value of dW/dt per mm^2 for each particle is due to the difference of particle mass and the bulk density between the samples. Sample2 shows the lowest value as it has the lowest bulk density across the samples. However, Sample2 and Sample5 have the highest dissolution rate dW/dt for all the size cuts due to their fast dissolution behaviour and the short early disintegration period (see dW/dt (kg/s) versus time (s) in Figure 4-8). Negative values of dissolution rate as well as fluctuations have been detected. The negative values are mainly due to early-stage disintegration as it has been explained in the previous Section 4.3.4 . On the other hand, the fluctuations are a result of the variation of the morphology and microstructure (density and porosity) within the particles.

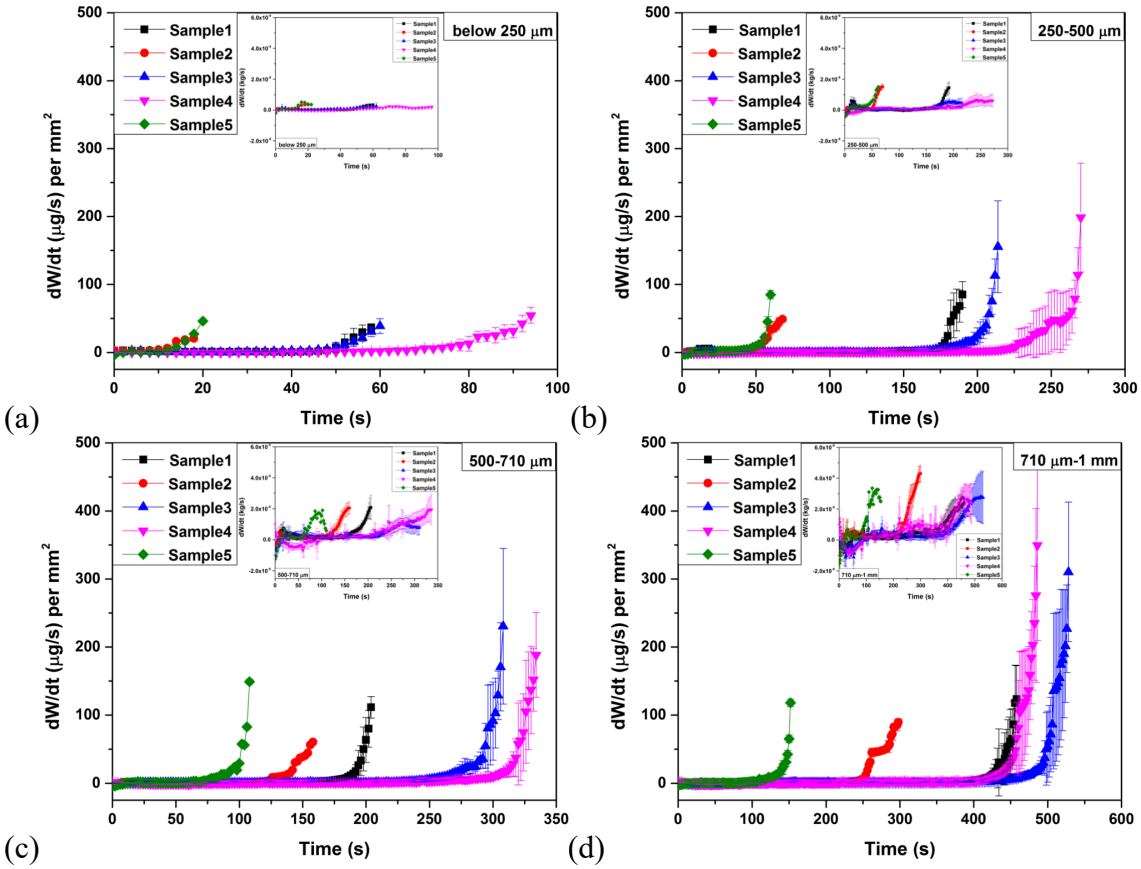

Figure 4-8 Dissolution rate dW/dt (µg/s) per mm² versus time (s) for (a) below 250 µm, (b) 250-500 µm, (c) 500-710 µm and (d) 710 µm-1 mm. The dissolution rate dW/dt (kg/s) versus time (s) is embedded in each graph.

The second approach follows the theory developed by Nyström et al., [81] for the surface specific dissolution rate G, also mentioned as the intrinsic dissolution rate. The evaluation of G was conducted using the Equation (2-26). Figure 4-9 shows the effect of particle size on the surface specific dissolution rate G. Data of G starts from negative values due to early disintegration, then progresses slowly as it passes through the shrinking stage and when disintegration happens it increases slightly. Sample5 exhibits the highest G for all the particle sizes as it is the fastest dissolving sample. However, results (order of magnitude) did not correlate well with the dW/dt per mm² (see Figure 4-8). This is because an important assumption of this approach is that the particle shape does not change during the dissolution [22]. In our case, the particles of the powder samples are

highly agglomerated, and irregular shaped as SEM and XRT results revealed (see Sections 3.4.6 and 3.4.7). Therefore, the changes of the effective surface area occurred by the dissolution phenomena cannot be taken into account with this method. As the particle size range increases the value of the dissolution rate decreases because the particle is considered throughout the dissolution process as one piece.

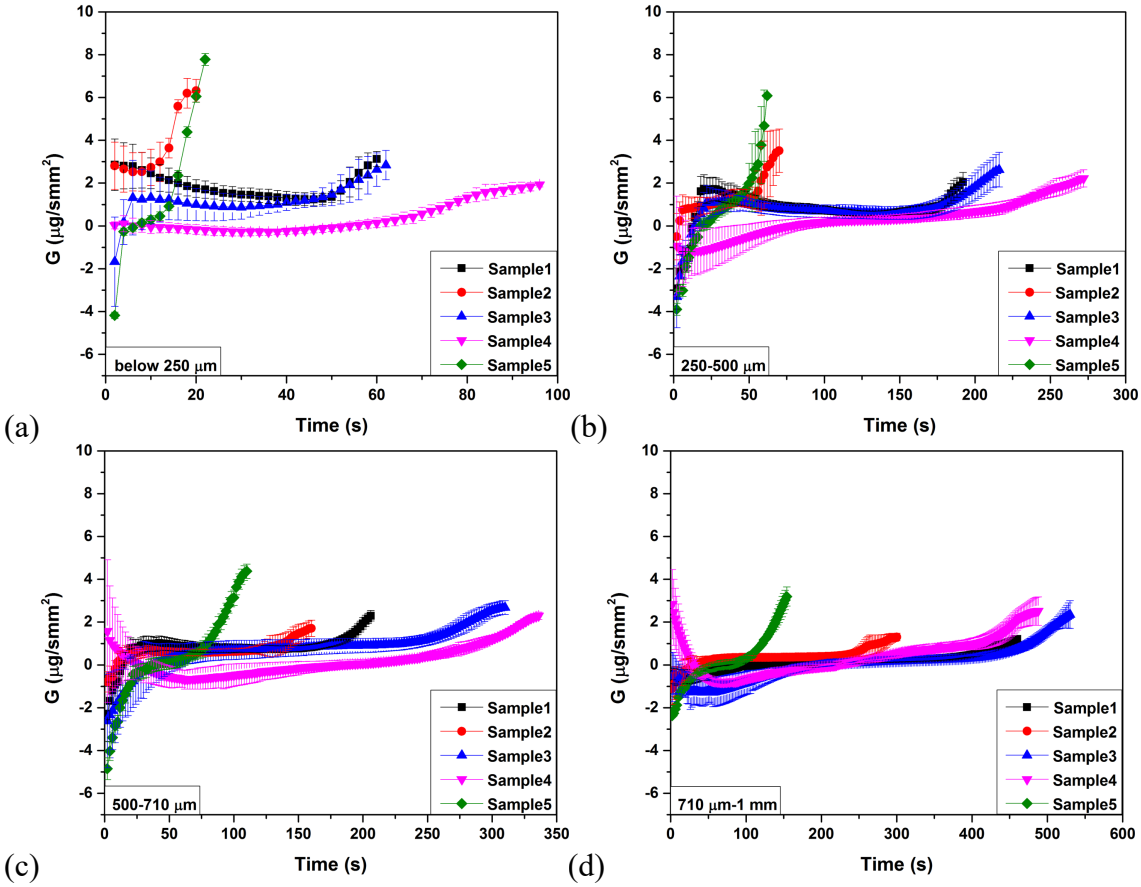

Figure 4-9 Surface specific dissolution rate *G* (µg/smm^2) versus time (s) for (a) below 250 µm, (b) 250-500 µm, (c) 500-710 µm and (d) 710 µm-1 mm.

4.3.6 Effect of particle size on dissolution rate constant *k*

The macroscopic phase differences acquired form the dissolution profiles of the samples were fitted in the classic Nernst-Brunner equation [38], [42] (see Equation (2-4)) solving for dissolution rate constant *k*

$$k = \frac{dW}{dt}\frac{1}{A_{p,t}(C_s - C_{p,t})} \quad (4\text{-}3)$$

where the $\frac{dW}{dtA_{p,t}}$ acquired from Figure 4-8 and solubility results (see Figure 3-3) for C_s at 20dC. The concentration of the particle at time t, $C_{p,t}$, was evaluated by multiplying the initial concentration of the granule C_p with the amount dissolved (%) at that moment

$$C_{p,t} = C_p dissolved_t = \frac{W_p}{V_p} dissolved_t \quad (4\text{-}4)$$

where V_p is the volume of the granule and was calculated using the equation for the volume of a sphere

$$V_p = \frac{4}{3}\pi r_p^3 \quad (4\text{-}5)$$

Figure 4-10 presents the dissolution rate constant k changes as a function of time for each size fraction. Order of magnitude of k (10^{-6} to 10^{-3}) for all samples correlates well with literature results [182]. It seems that across the size range and the different powder samples, the value of k follow the same trend as dW/dt per mm^2 where for the longest period of dissolution remains constant and when disintegration occurs accelerates. At this point, the increasement of k is more than two orders. Samples that contain Silicate binder, Sample3 and 4 show the highest k for all the particle sizes as a result of long early disintegration stage of the samples and the fast performance that required to overcome it at this size range (see Figure 4-7). The variation of k especially at the final moments of dissolution is due to the differences in dissolution behaviour between particles of the same batch. The dissolution rate constant increases with the particle size as a result of the increasement of the dW/dt per mm^2 which is proportional. Negative values of k have been detected during the early disintegration due to an increasement of the exposed surface area as it has been discussed thoroughly in Section 4.3.4 .

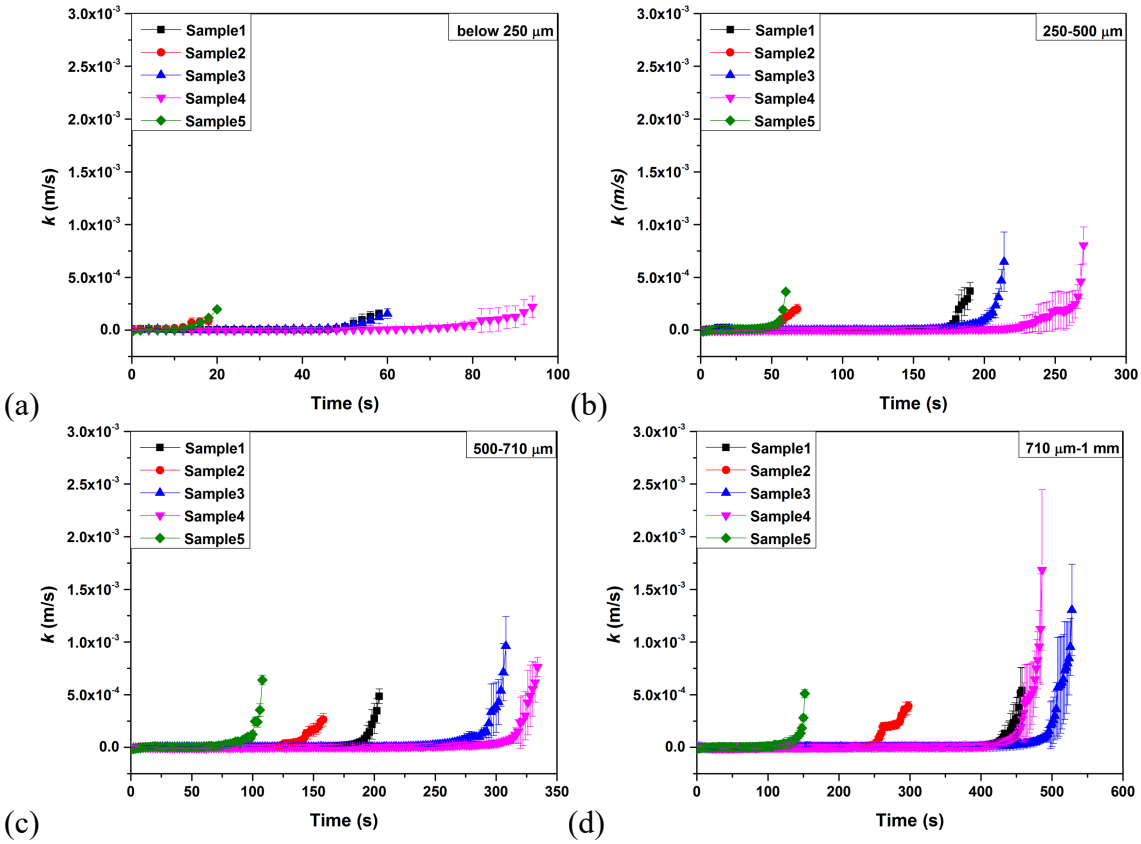

Figure 4-10 Dissolution rate constant *k* (m/s) versus time (s) for (a) below 250 µm, (b) 250-500 µm, (c) 500-710 µm and (d) 710 µm-1 mm.

4.3.7 From single particle dissolution to bulk dissolution

It can be expected that in a powder sample, all dissolution mechanisms (see Figure 4-2) may be present simultaneously to a varying extent during different stages of the dissolution process. So, there can be particles in the bulk powder that are more exposed to one or other mechanism [35]. The overall observed dissolution curve would then be a sum of dissolution curves from individual particles that form the population [183]. Taking that into account we aim to predict bulk dissolution behaviour for the five different samples based on the dissolution understanding obtained from single particle experiments. Two different approaches were used for this purpose.

The first approach uses the dissolution rate constant *k* of the powder samples for the different particle sizes (see Figure 4-10) and the results of the Particle Size Distribution

for each powder (see Figure 3-6) to solve the classic Nernst-Brunner equation [38], [42] (see Equation (2-4)) for dW. More precisely assuming the weight of the bulk powder used as W_{bulk}, the weight that lies on each particle size category of the distribution $W_{sizefraction}$can be written as

$$W_{sizefraction} = \%PSDW_{bulk} \tag{4-6}$$

where $\%PSD$ is the % mass distribution of each size category obtained from the Particle Size Distribution technique.

Using the Equation (4-5) for the particle volume V_p and the results of $\rho_{envelope}$ (see Figure 3-10), the W_p that represents the weight of a particle of each size category of the PSD was acquired by

$$W_p = V_p\rho_{envelope} = \frac{4\pi r_p^3 \rho_{envelope}}{3} \tag{4-7}$$

Then the number of particles $N_{particles}$ that represent each particle size category of the distribution on the W_{bulk} can be acquired by dividing Equation (4-7) from Equation (4-6)

$$N_{particles} = \frac{W_{sizefraction}}{W_p} \tag{4-8}$$

So, the area of the $N_{particles}$ of the particle size category of the distribution, $A_{particles,size}$ can be written as

$$A_{particles,size} = A_p N_{particles} = 4\pi r_p^2 N_{particles} \tag{4-9}$$

Substituting Equation (2-4) with Equation (4-9) and assuming that $C_t = dW_{sizefraction}/V_{water}$, $dW_{sizefraction}$ of the particle size category of the PSD can be expressed as

$$dW_{sizefraction} = \frac{kA_{particles,size}C_s dt}{1 + \frac{kA_{particles,size}dt}{V_{water}}} \quad (4\text{-}10)$$

where V_{water} is the volume of water used.

Therefore, the dW can be considered as a sum of each $dW_{sizefraction}$

$$dW = \sum_{i=1}^{n} dW_{sizefraction,i} \quad (4\text{-}11)$$

By integrating Equation (4-11), the release profiles of the bulk dissolution can be obtained by

$$dissolved_t = \left(1 - \frac{W_{bulk,t}}{W_{bulk}}\right) \quad (4\text{-}12)$$

The predictive curves of this approach have been compared with conductivity (Orion Star A212, Thermo Fischer Scientific U.S.A.) measurements of 1g of each sample dissolving in a USP Apparatus 2 dissolution tergotometer (see Figure 2-29) in two different concentrations, low and high. Low and high concentration defined as

$$LowC = \frac{W_{avgsize(<250\mu m)}}{V_{water}} \; and \; HighC = \frac{W_{avgsize(710\mu m-1mm)}}{V_{water}} \quad (4\text{-}13)$$

where $W_{avgsize(<250\mu m)}$ and $W_{avgsize(710\mu m-1mm)}$ is the mass of the average size for particles of size fraction below 250 μm and 710μm – 1 mm respectively. The experimental conditions are presented in Table 4.1.

Table 4.1 Experimental conditions of Low and High concentration (ppm) of bulk dissolution testing for each powder sample.

Samples	Low Concentration (ppm)	High Concentration (ppm)
Sample1	200	1200
Sample2	155	880
Sample3	350	1225

Sample4	410	1035
Sample5	300	1138

For the second approach a model has been developed using the Monte Carlo statistical method (Matlab R2017a, The MathWorks Inc., Natick, MA, 2017). All the single particle dissolution profiles and particle size distribution of each powder sample were first implemented. The model first evaluates the maximum amount of mass being used in single particle studies. Then takes random particles of different size subjected to the particle size distribution and interpolate between them. After that it checks the two closest particle sizes from the single particle dissolution experiments, one above, one below and interpolate between with the particle size required. Then, the predictive dissolution results of this approach were compared with conductivity (Orion Star A212, Thermo Fischer Scientific U.S.A.) measurements of 1g of each sample dissolving in 800 mL of water in a USP Apparatus 2 dissolution tergotometer (see Figure 2-29). The parameters mean squared error (MSE) and sum of squares due to error (SSE) have been calculated. The overview of the model is presented in APPENDIX B.

The comparison of the dissolution profiles obtained with the first approach and dissolution curves from conductivity data on two concentrations, low and high is presented in Figure 4-11. A relatively good agreement has been observed between experimental and numerical data for the samples without binder, Sample1, 2, and for the sample with the new binder, Sample5, if we take into consideration the fact that in the numerical approach the concentration of the solution is in-between the two experimental concentrations. A lack of fit appears on Sample3 and 4, which is due to the slow and unique dissolution behaviour that the polymerisation of Silicate causes, and which affects the dissolution rate constant k. Results indicate that the developed framework has

potential to be used as a tool for the prediction of the bulk particle dissolution of multi-component spray dried powders based on the dissolution knowledge of single particle.

On the other hand, results obtained from the Monte Carlo approach (see Figure 4-12) confirm the first approach. Physical (Monte Carlo) data comply with the chemical data for Sample1, 2 and 5 ($MSE_{Sample1}$ = 0.0161, $MSE_{Sample2}$ = 0.0048 and $MSE_{Sample5}$ = 0.0023) but they do not seem to correlate very well for the samples containing Silicate as binder Sample3 and 4 ($MSE_{Sample3}$ = 0.0764, $MSE_{Sample4}$ = 0.0737). There is a hypothesis concerning this. As we have previously presented in Figure 4-3, although on the dissolution of single particles with binder we face polymerisation of Silicate, on three particle dissolution this phenomenon disappears. Bulk dissolution experiments are a scale-up of the three-particle dissolution that we conducted. The cohesive interactions between the particles in bulk dissolution accelerate the chemical release of polymerised silicate (see Figure 4-2). This is because the polymerisation rate decreases as the salt (Na_2SO4) concentration increases in the multi-particle systems[170]. Particle interactions in multi-particle systems have been described by a fluid-averaged isotropic Derjaguin-Landau-Verwey-Overbeek (DLVO) [184], [185] pair-interaction potential of mean force. The DLVO pair-interaction potential between particles consists of both attractive van der Waals forces, and repulsive electrostatic forces [186]. In contrast in single particle approach that particle interactions do not exist, we have detected a thick cloudy layer of polymerised Silicate that slows down the dissolution performance (see Figure 4-2). Therefore, the comparison of Monte Carlo method which is based on single particle experiments and conductivity measurements can reveal how significant affect the cohesive forces the dissolution performance.

This is the main difference between the two approaches where the Monte Carlo approach via the implementation of the single particle dissolution profiles into the model can reveal the complexity of the dissolution phenomena taking place. Thus, the discontinuities. While the first method based on the use of a single parameter, the dissolution rate constant k can not. However, this approach can be used by the industry to accurately predict bulk dissolution profiles using single particles.

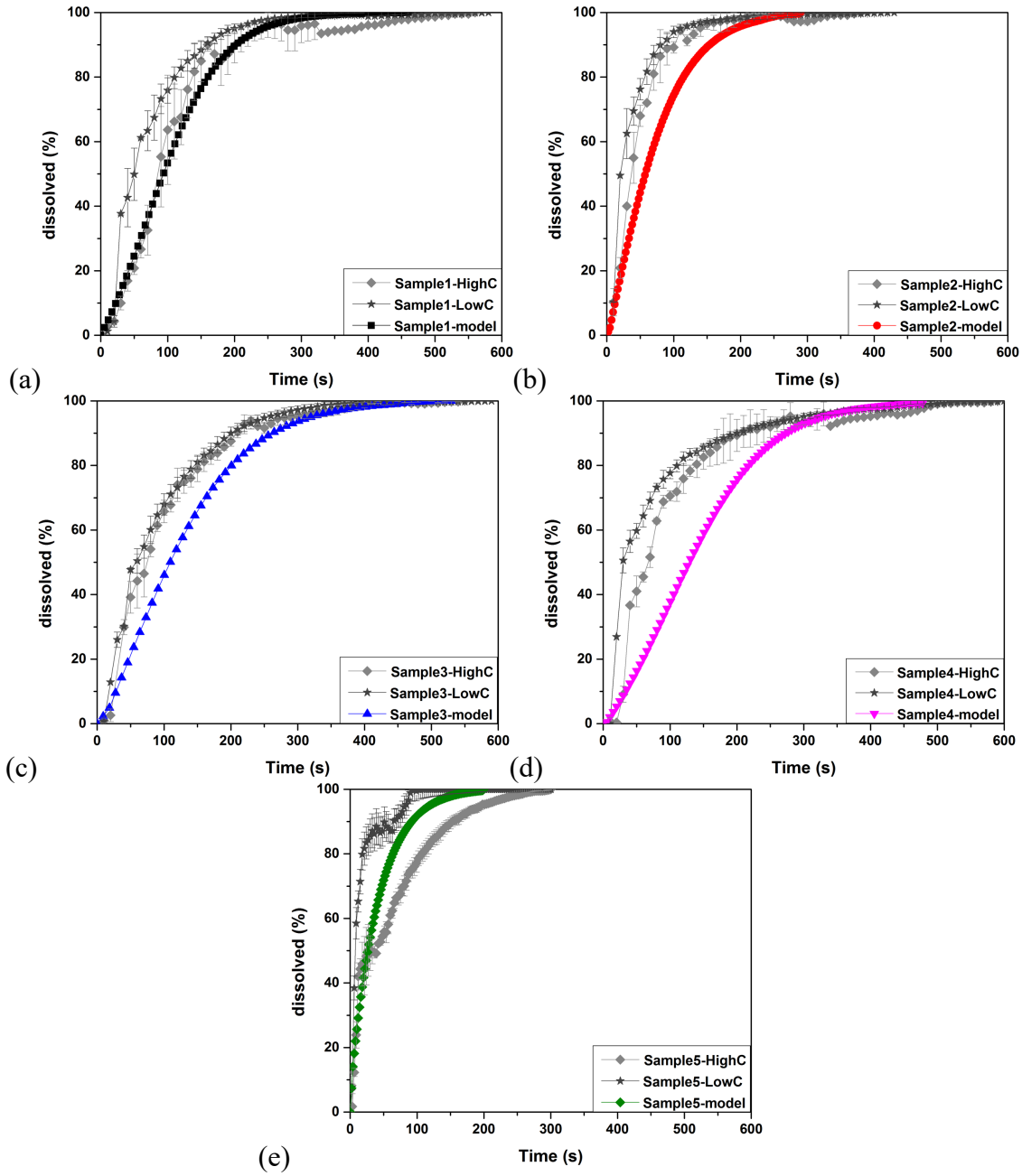

Figure 4-11 Comparison of dissolution profiles of 1g of (a) Sample1, (b) Sample2, (c) Sample3, (d) Sample4 and (e) Sample5 using Equation (4-11) with conductivity data.

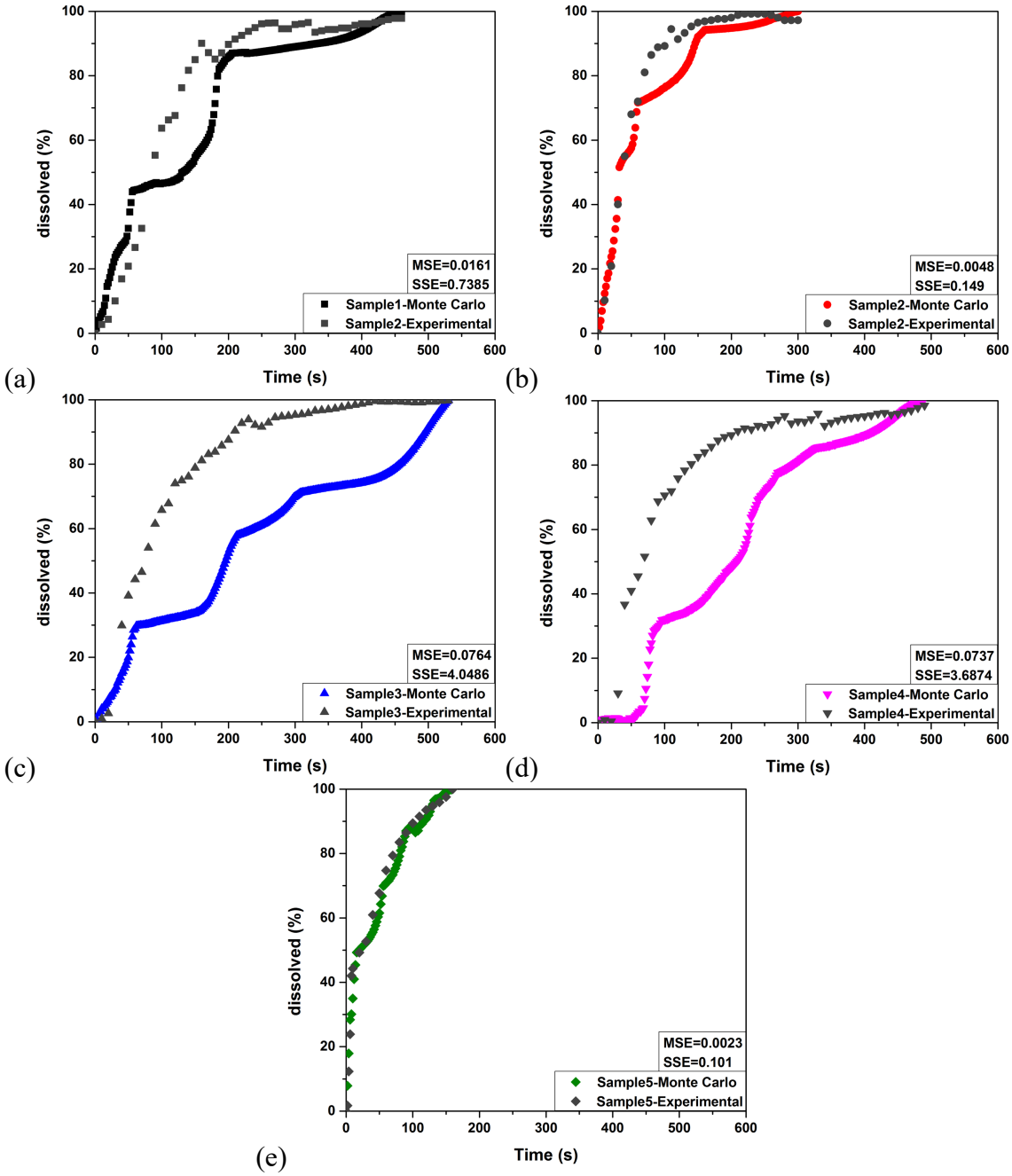

Figure 4-12 Comparison of Monte Carlo analysis single to bulk approach for (a) Sample1, (b) Sample2, (c) Sample3 and (d) Sample4 with conductivity data.

4.4 Conclusions

In this present study, an optical methodology has been applied to understand single particle diffusion dissolution mechanisms, to provide information for the explanation of the discrepancy between diffusion dissolution performance of spray-dried powders and

to enable us to link single particle dissolution to bulk. The method defines the dissolution behaviour of single particles and could, therefore, be used to obtain information otherwise invisible due to the averaging of a large number of particles. The results indicate a significant variance in dissolution behaviour between particles and within the dissolution process of a single particle. This is explained by a vast diversity in particle morphology and microstructure (see Section 3.4.6 and 3.4.7), between particles of the same powder. As Mercury Porosimetry (see Table 3.6), SEM (see Figure 3-11) and XRT (see Figure 3-17) results shown more water in the slurry increase the porosity and affects the morphology and the structure of the particles. This has a significant impact on the dissolution performance cause the powder sample with high slurry mix moisture dissolves smoother, faster and more controllable than the low slurry mix moisture samples. The effect of the binder also plays a significant role. Silicate binder due to polymerisation slows down the dissolution while Citric Acid in the binder formulation enhances disintegration and as a result dissolution. Single particle dissolution profiles acquired by Image Processing linked to bulk particle release profiles via Nernst-Brunner equation and Monte Carlo method. It was shown that data obtained from the Nernst-Brunner approach correlate well with conductivity measurements, for dissolving bulk particles of multi-compound spray-dried powders. On the other hand, the comparison of Monte Carlo approach and chemical data will allow us to understand the effect of interactions developed between the particles and their significance on bulk dissolution performance that the standard analytical methods cannot reveal.

This work allows supplying reliable results for the evaluation of image analysis not only as an applicable analytical method for single particle dissolution understanding but also

as a tool for predicting bulk particle dissolution from the dissolution knowledge of one granule.

CHAPTER 5 SINGLE PARTICLE CONVECTIVE DISSOLUTION

Abstract

Dissolution of particles is a ubiquitous process in formulation industries. Scientific challenges remain unsolved due to the complex of interfacial properties and physical interactions between solid, liquid and gas phases. If more knowledge regarding the phenomena dominating the dissolution process could be acquired, powder dissolution could be optimised. This requires examination of the process at the scale of individual granules. In this study, a novel microfluidic dissolution testing device is presented for the investigation of single spray-dried particle convective dissolution under various experimental conditions (flow rate, temperature). The microfluidic device was first optimised comparing experimental and simulation data. The dissolution process was recorded using an optical microscope and the analysis of the data conducted using Image Processing. Then, a new dissolution model which combines Noyes-Whitney dissolution equation and experimentally calculated particle velocity is proposed. The results showed that the addition of flow rate and temperature into the system enhances the dissolution process of the particles. Especially for the powder samples containing Silicate binder dissolution time reduces by more than 55% for particle size 250 to 500 μm. Comparison of experimental and predicted single particle dissolution profiles showed a 93.5 ± 3.1 % confidence level for the new dissolution model proposed.

5.1 Introduction

Building an ideal particle is the ultimate goal which industry has been pursuit for a long time. With cost in mind, the ideal particle, for instance, our research object spray-dried detergent powder, needs to bear the best performance regarding washing, handling, transporting etc. Different performance is ruled by different particle properties as well as the mechanisms behind it. From the dissolution point of view, with complex formulation nowadays, making detergent powder dissolving fast at room temperature and leaving no residues are the two of the key factors while energy consuming and environmental legislation are concerned. To achieve this, researchers have to identify and understand the fundamental factors and the rate-limiting steps affecting the dissolution process.

The main methodology of dissolution testing requires a specific amount of the powder immersed in a predefined volume of dissolution medium. The concentration of the released powder in solvent is evaluated at different time intervals, leading to time-dependent dissolution profiles. The unit accommodating the dissolution of the powder is usually a vessel or chamber containing a paddle. The dissolution medium is poured or pumped through this unit at a constant flow rate, and the solute concentration is the solvent is evaluated with conductivity or UV-Vis Spectrophotometer. As we have seen in Chapter 4, the spray dried powder can undergo changes in its solid phase during dissolution which can have considerable effects on the dissolution kinetics.

These effects cannot be explained with concentration analysis alone, and this would have a significant impact on industry to develop new formulations that will enhance dissolution performance. Historically, several methodologies have been developed to simulate and study the dissolution behaviour of powders such as pharmaceutical drugs [9]–[11], [19], food [12]–[16], [18] and chemical [17] powders. However, these methodologies are

limited to provide information on dissolution, and they do not give any indicators to the dissolution phenomena involved in realistic systems as all the mechanisms involved in the dissolution process are lumped into a single collective process. Indeed, there is currently no suitable dissolution testing device for single granules, which enables the simultaneous visualisation of the particles and measures the dissolution profiles. Thus, there is a strong demand for a dissolution testing device that will accommodate these functions.

Given some limitations of above methods, a novel microfluidic dissolution testing device was developed which enables the convective dissolution of individual granules to be studied under laminar flow and different temperatures. This approach aims to provide an understanding of the dissolution properties of spray-dried detergent powders within a "micro wash environment" under standard conditions and to define the dispersion and dissolution mechanisms taking place. The optimisation of the microfluidic device was carried out by comparing Ghost Particle Velocimetry with COMSOL simulation data. Particle's velocity during different dissolution conditions was evaluated and implemented in a dissolution model based on Noyes-Whitney Equation to predict single particle convective dissolution.

5.2 Materials and Methods

5.2.1 Materials

Five spray-dried detergent powder samples, Sample1, 2, 3, 4 and 5 have been used for the single particle convective dissolution experiments. The composition of the samples has been discussed thoroughly in Section 3.2 of Chapter 3.

5.2.2 Convective dissolution experimental setup

A novel microfluidic approach was developed to obtain kinetics of single particle convective dissolution as a function of water flow and temperature. The schematic of the dissolution experimental setup is shown in Figure 5-1. The microfluidic device was fabricated in polydimethylsiloxane (PDMS) (Sylgard 184, Dow Corning). The manufacturing procedure is described below in Section 5.2.3 . A diagram and the top view of the chamber are shown in Figure 5-2. 10 individual particles from the characteristic particle size fraction below 250 μm and 250-500 μm were tested for each experimental condition. The granules were placed in the centre of the bottom of the channel with a cross-sectional area of 1 mm^2, 2 cm ahead of the inlet to allow the flow to be completely developed when it reaches the particle. The length of the channel was 100 cm. At the chosen flow rates 0.2, 0.4, 0.6, 0.8 and 1 μL/s the deionised water flow was generated with the use of a 60-mL syringe (BD Plastipack, United Kingdom) mounted on a syringe pump Legato 110 (KD Scientific Inc., USA) with accuracy ±0.5%. Polyvinylchloride (PVC) tubing with an internal diameter of 1.8 mm has been used to connect the syringe to the inlet of the microfluidic device. To maintain the temperature of the water in the syringe stable at 20dC, 40dC and 60dC a syringe warmer with a temperature controller (Harvard Apparatus, USA). The temperature was monitored throughout the experiment with an Infrared Thermometer (Cole-Palmer, United Kingdom). The outlet of the device was directed via PVC tubing to a beaker for a once-through operation. Observation and recording of the dissolution process were carried out using an inverted light microscope Leica Z16 AP0 coupled to a monochromatic digital CCD camera (Leica Microsystems GmbH, Germany). Image resolution was set at 1376x1038 pixels (406.3890 pixels/mm) for all the experiments. Images were recorded

at 5 frames per second by the open source software μManager (US National Institutes of Health) [169]. To enhance the contrast of the image, black tape was placed underneath the microfluidic device.

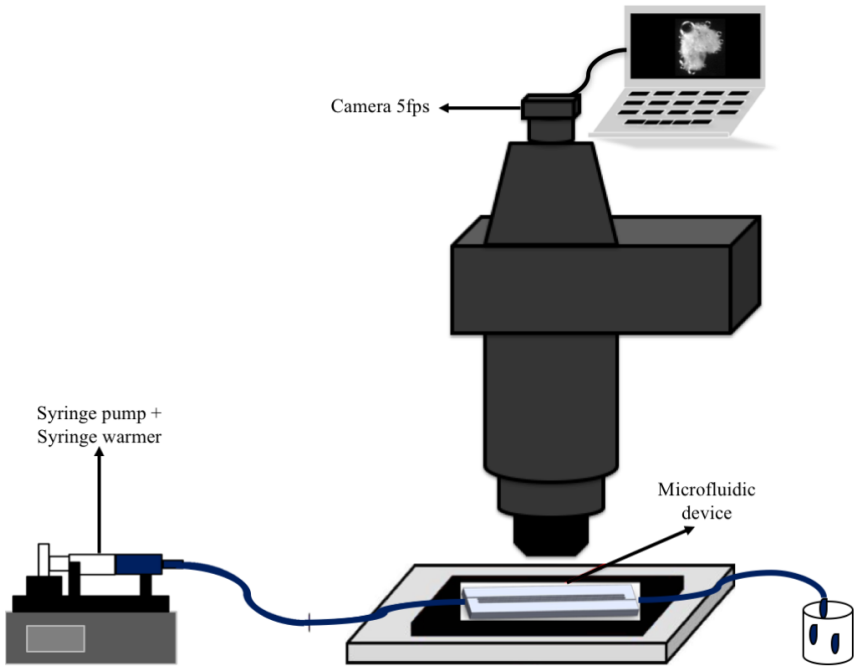

Figure 5-1 Schematic of single particle convective dissolution experimental setup.

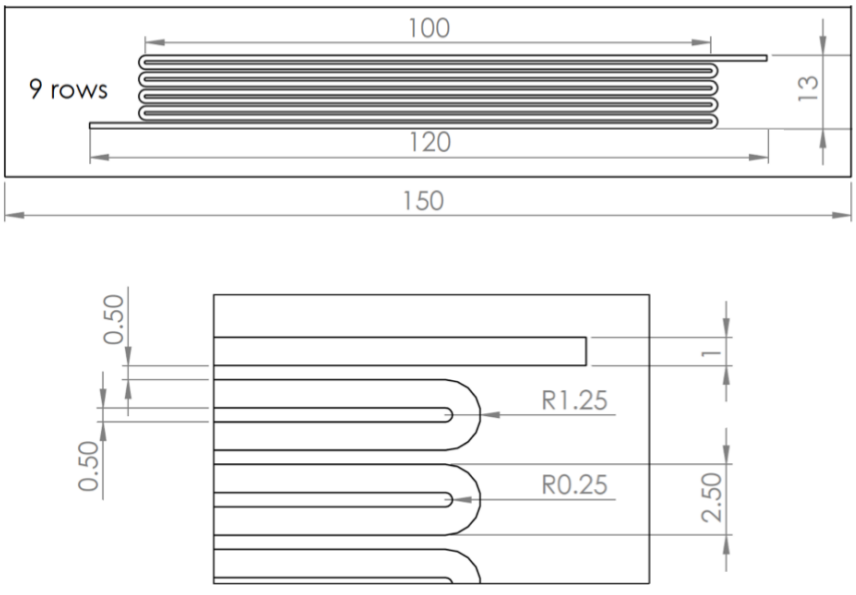

(a)

(b) 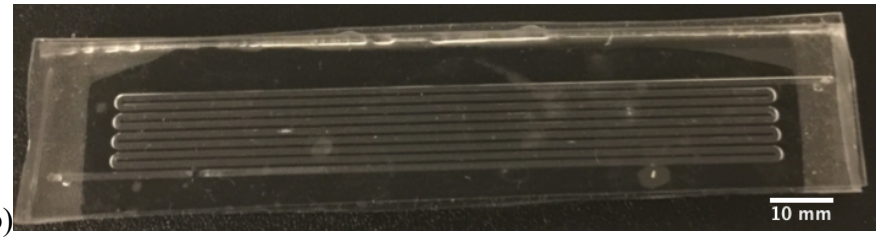

Figure 5-2 (a)Diagram and (b)Top view of the microfluidic device used in experiments.

5.2.3 Manufacturing protocol of the microfluidic device

Due to the large dimensions of the microfluidic device standard soft lithographic methods could not be used for its fabrication. For this purpose, an aluminium mould (see Figure 5-3) was first manufactured from 3D drawings using AutoCAD software (AutoDesk Inc., Canada) by Wunderlichips GmbH, Switzerland. The channel was decided to be 1 mm, double the size of biggest particle (500 μm), to reduce the effect of wall shear stress, while the gap is 0.25 mm after taking into consideration the pressure drop. The device contains 9 channels as it was designed based on the dissolution times of the single particle diffusion dissolution experiments of the previous chapter 4.3.3 . However only the first channel was finally used, due to the faster dissolution behaviour of the granules under convection.

The protocol in brief is given in APPENDIX C.

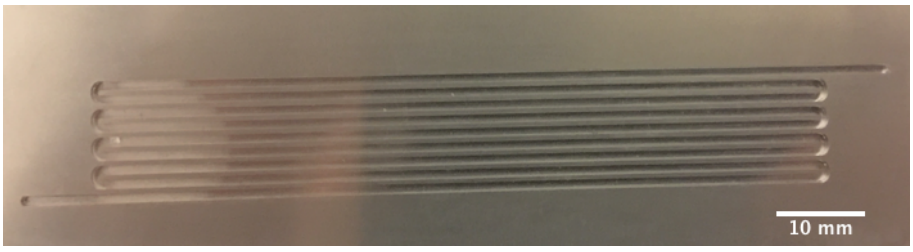

Figure 5-3 The aluminium mould of the microfluidic device.

5.2.4 Image Processing

The recorded images were analyzed with ImageJ (US National Institutes of Health) [168]. A detailed overview of the process is given in Section 4.2.3 .

5.2.5 Ghost Particle Velocimetry (GPV)

Ghost Particle Velocimetry (GPV) is a flow visualisation method which is capable of reconstructing a planar component flow velocity fields [187]. The GPV utilises a standard bright field microscope to illuminate a sample containing submicron sized tracer particles. By controlling the numerical aperture of the condenser lens and by subtracting out the median of several successive frames as the background static contribution it is possible to record the speckle pattern generated by the interference of light scattered by the suspended tracers [188]. The experimental setup includes a standard inverted bright field microscope Nikon Ti-E (Nikon, Japan), white light illumination and a high-speed camera FASTCAM Mini UX 100 (Photron Inc., USA). Glass beads of 250 μm and 500 μm (Sigma Aldrich Inc., USA) were glued with PDMS in the centre of the bottom of the channel. The flow field of a 2D plane (1.5 mm X 1mm) the microchannel with and without the glass beads was evaluated using deionised water flow seeded with 200 nm polystyrene particles, concentration 0.2% by weight (Thermo Fisher Scientific, Molecular Probes Fluospheres, USA) moving from right to left at 10 μL/s. The numerical aperture of the condenser was set to 0.15. A 20X objective was used to satisfy the requirement that the size of a single speckle must be bigger than 2 pixels to be distinguishable from the camera noise. The movies were recorded at 3200 fps, using an exposure time of 100 μs. The open source PIVLab 1.4 Matlab toolbox (Matlab R2017a, The MathWorks Inc., Natick, MA, 2017) was used to cross-correlate particle movement using speckle patterns from two successive images by considering a displacement, from frame to frame, equal to 50% of the ROI's size and thus extract the associated velocity profile [189]. To increase the resolution of the velocimetry measurements, a three-pass technique was employed (and implemented in PIVlab software), where each step employs

a ROI smaller than the previous one. The results obtained with each pass are used as first input for the second iteration.

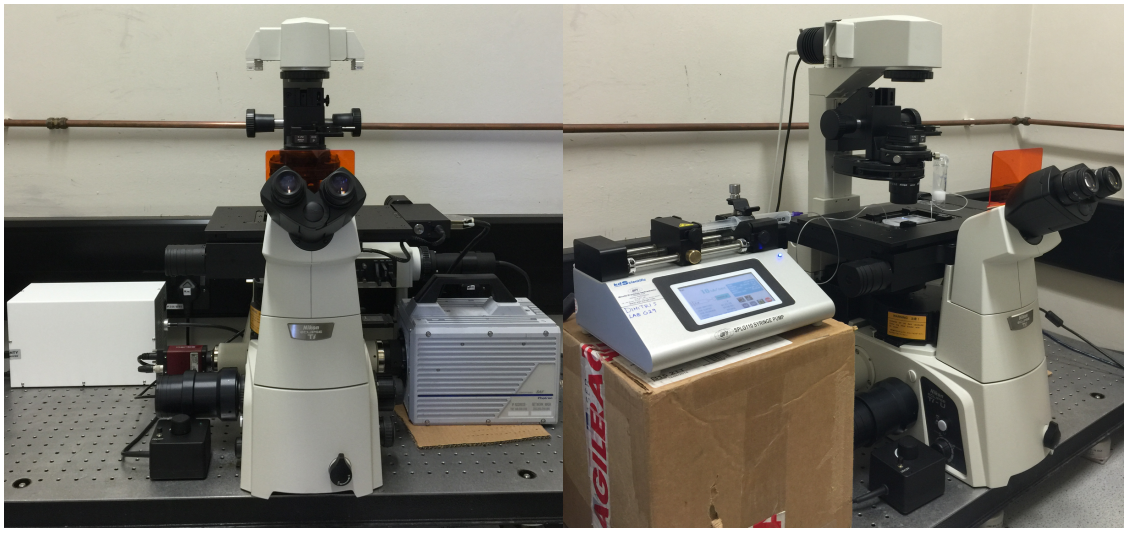

Figure 5-4 GPV experimental setup.

5.2.6 COMSOL simulation

A 3D model was developed in COMSOL Multiphysics 5.2 (COMSOL, Massachusetts, USA) to simulate the GPV experimental conditions using laminar single-phase flow application mode. We performed a 3D CFD simulation to explore the flow velocity of a part of the microfluidic channel (2 mm X 1 mm X 1 mm) with and without the glass beads (250 µm and 500 µm). The geometry of the model is presented in Figure 5-5. The density and viscosity were set to those of water at 20dC, and flow was fully developed at the inlet with the boundaries (channel and sphere walls) set to the no-slip boundary condition. The flow was allowed to exit passively at the outlet via null pressure condition, i.e. $P = 0$. Mesh size between 0.036 mm and 0.2 mm.

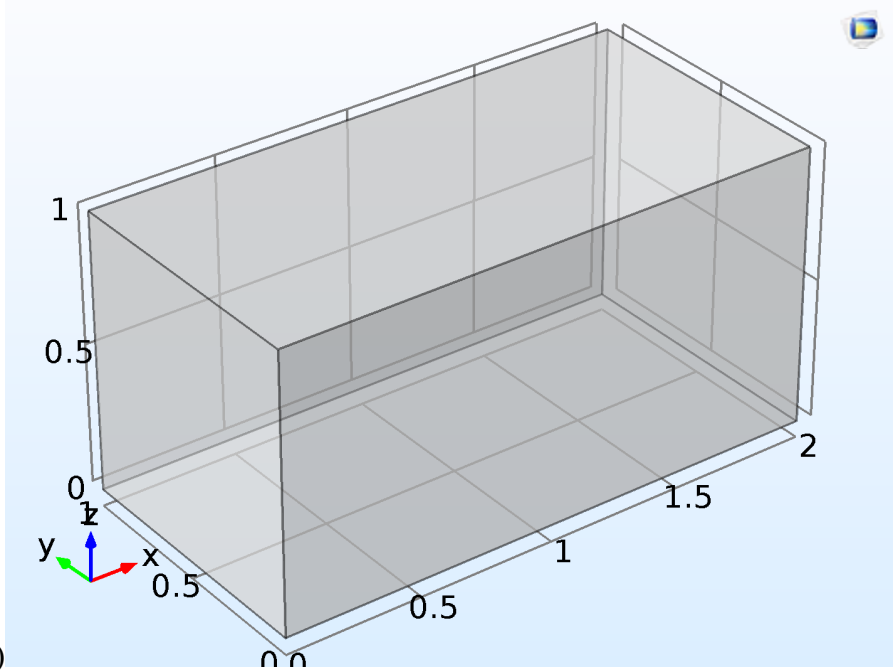

(a)

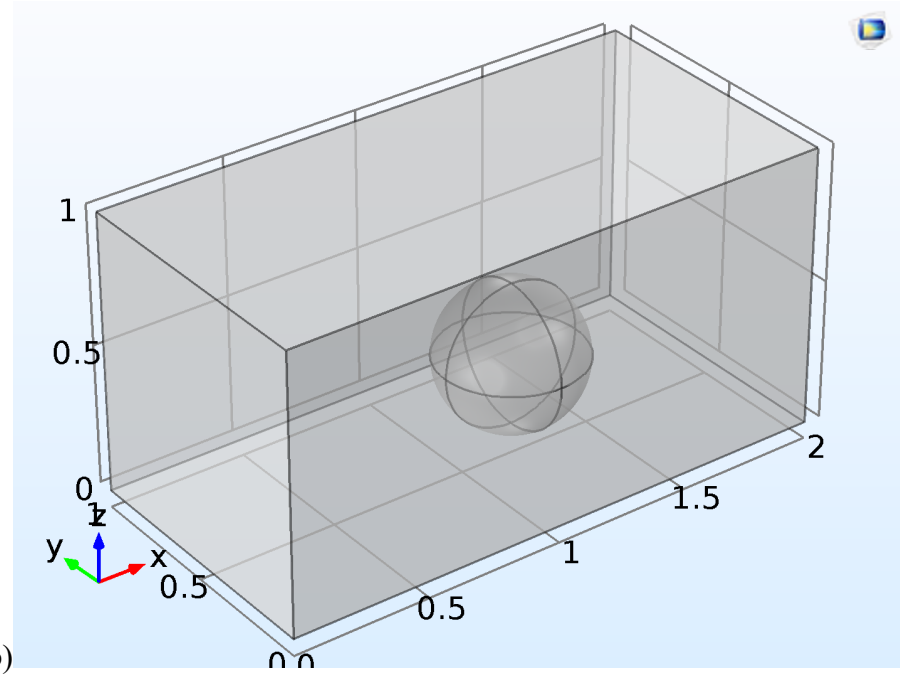

(b)

Figure 5-5 The geometry of the model (a) without and (b) with the sphere.

5.3 Results and Discussion

5.3.1 Theoretical analysis of the system

Flow past a spherical particle has been extensively investigated for a long time, due to its fundamental importance in many physical processes and industrial applications as well

as its academic value [190]. This section presents a comprehensive analysis of the physics and fluid dynamics took place in our system. First will be presented the evaluation for flow through empty rectangular channel and then for flow past a sphere in a rectangular channel.

Flow through empty rectangular channel

Firstly, at the chosen flow rates 0.2, 0.4, 0.6, 0.8 and 1 μL/s we have to evaluate the velocity of the water u_f considering that our system consists only the empty channel of the microfluidic device, without the granule. To achieve this, we have to divide the flow rate, Q, with the cross-sectional area of the channel, $A_{channel}$

$$u_f = \frac{Q}{A_{channel}} = \frac{Q}{WH} \tag{5-1}$$

The results of the relationship between flow rate Q and velocity of the water u_{water} are presented in Figure 5-6. A linear correlation can be noticed which is due to the fact that the cross-sectional area of the channel is 1 mm^2 (width, W = 1 mm and height, H = 1 mm).

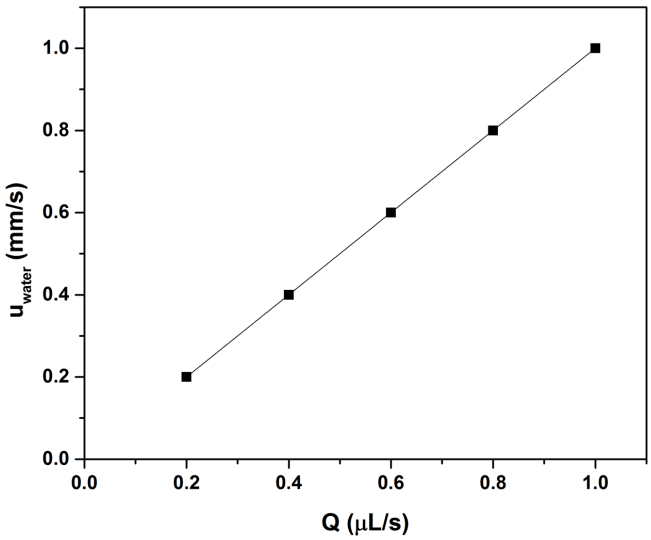

Figure 5-6 Linear relationship between flow rate Q (μL/s) and velocity of water u_{water} (mm/s).

By obtaining the u_{water} we can now evaluate the Reynolds of the flow in the channel, Re

$$Re = \frac{\rho_{water} u_{water} D_H}{\mu_{water}} \tag{5-2}$$

where ρ_{water} and μ_{water} is the density and dynamic viscosity of the water respectively, and D_H is the hydraulic diameter of the pipe and can be estimated by

$$D_H = \frac{4A_{channel}}{2P_{wet}} = \frac{4A_{channel}}{2W + 2H} \tag{5-3}$$

where P_{wet} is the wetted perimeter of the cross-section.

Using the values of Equation (5-2) we can estimate the length to fully developed velocity profile l_e for laminar flow

$$l_e = \frac{0.0575 Re}{D_H} \tag{5-4}$$

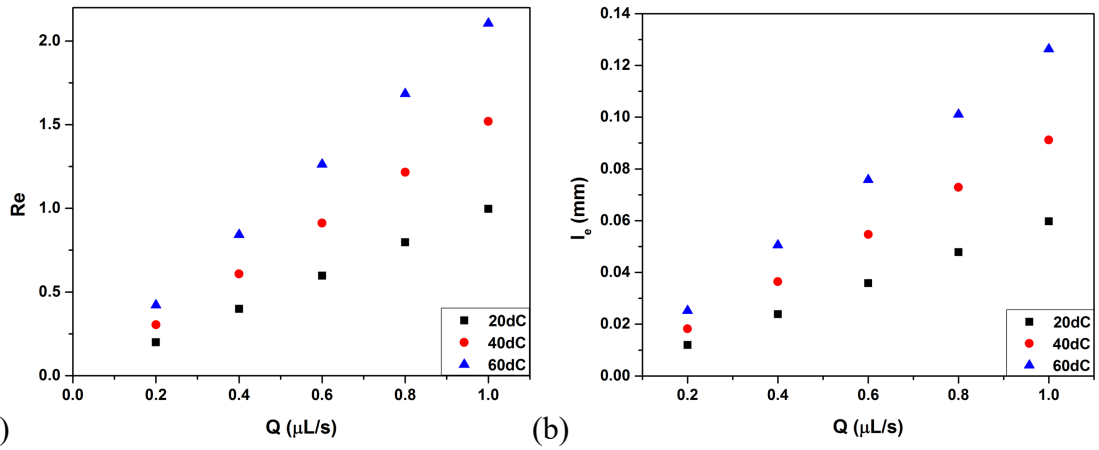

(a) (b)

Figure 5-7 (a) Reynolds number *Re* and (b) Length to fully developed velocity profile, l_e (mm) as a function of flow rate *Q* (µL/s).

Figure 5-7 shows the results of (a) Re and (b) l_e as a function of Q. The Reynolds number is very low $Re < 2300$ across the different hydrodynamic conditions, so the system exhibits laminar flow. On the other hand, the presented values of l_e (see Figure 5-7 (b)) show that flow is fully developed in less than 0.143 mm (0.126 mm for 1 µL/s at 60dC)

for the different measurements and flow rates which confirms our decision of the convective dissolution experimental setup to place the granule 2cm ahead of the inlet.

Then, Darcy's friction factor f_D for laminar flow, which is a consequence of Poiseuille's law was calculated by

$$f_D = \frac{64}{Re} \tag{5-5}$$

Figure 5-8 shows the relationship of f_D with Re. f_D decays exponentially with the increasement of Reynolds number. However, that does not mean that the energy loss due to friction forces reduces as velocity becomes higher. Actually, it happens the opposite which is confirmed by the Darcy-Weisbach equation [191], [192].

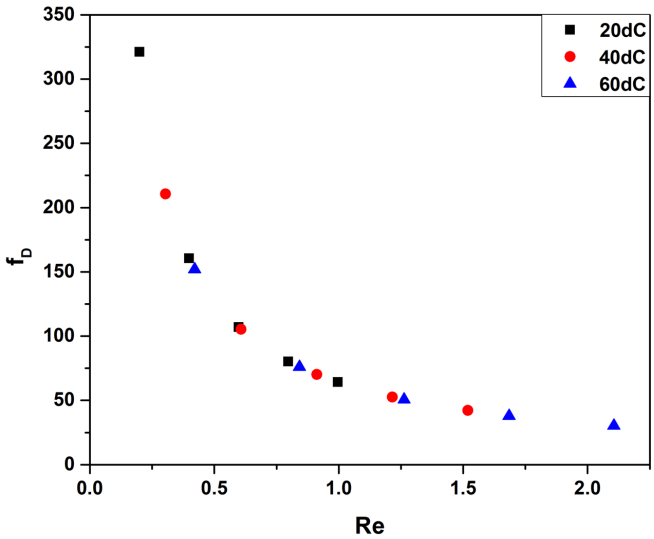

Figure 5-8 Friction factor f_D as a function of Re.

Furthermore, based on [193], [194] the pressure drop ΔP along a rectangular channel in which there are no bubbles or obstructions present it was being evaluated by

$$\Delta P = \frac{a\mu_f QL}{WH^3} \tag{5-6}$$

where L is the length of the channel and a a dimensionless parameter that depends on aspect ratio W/H and is defined by

$$a = 12\left[1 - \frac{192H}{\pi^5 W}\tanh\left(\frac{\pi W}{2H}\right)\right]^{-1} \quad (5\text{-}7)$$

Equation (5-6) is accurate to within 0.26% for any rectangular channel that has $W/H \leq 1$, given that $Re < 1000$.

Results of ΔP across the channel of the microfluidic device are presented in Figure 5-9. ΔP is higher with the increasement of flow rate and the decrease of temperature. The difference in ΔP from 0.2 µl/s to 1 µl/s for 20dC is 22.6 Pa, for 40dC is 14.8 Pa and for 60dC is 10.5 Pa. In general, in our system, the ΔP for all the hydrodynamic conditions is in a similar manner to literature results [195].

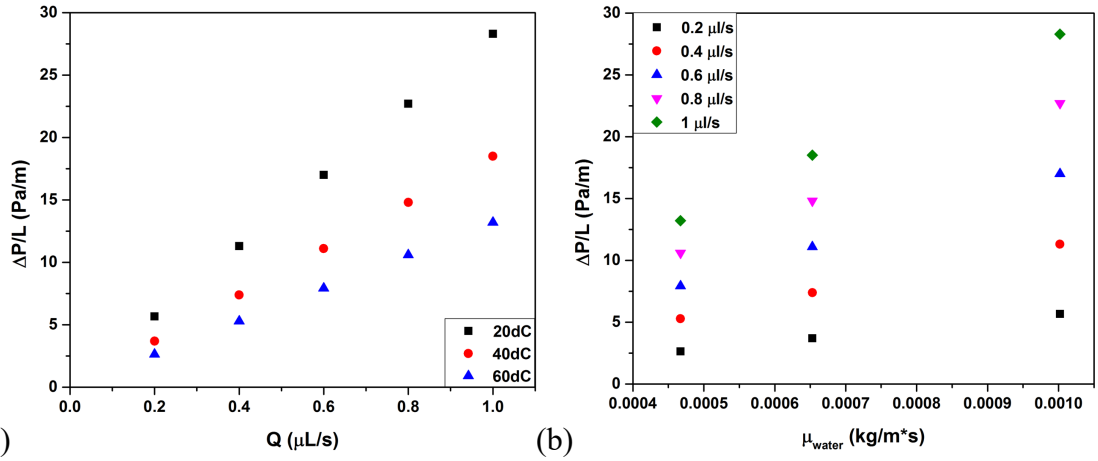

Figure 5-9 Pressure drop across the channel $\Delta P/L$ (Pa/m) as a function of (a) flow rate Q (µL/s) and (b) dynamic viscosity of the water μ_{water} (kg/m*s).

Flow past a sphere in a rectangular channel

Considering now in our system the presence of a granule as in the real case we measured the related parameters. As we have seen from the morphological and microstructural analysis (see Figure 3-11 and Figure 3-17), the spray dried powders consist of irregularly shaped granules. To implement the shape of the granules in our theoretical analysis, we related it to a known shape (cube, sphere etc.). In fluid dynamics, this correlation is based

on the ratio $l_{particle}/d_p$, where $l_{particle}$ is the length of the particle. In our case $l_{particle}/d_p \cong 1$, which means that the granules can be considered as spheres.

To understand the type of the flow that passes through the sphere we evaluated the Reynolds number of the particle, Re_p for different diameters (from 0.2 to 0.5 mm) to represent the particle size range of our granules which is from 200 to 500 µm.

$$Re_p = \frac{\rho_{water} u_p d_p}{\mu_{water}} \tag{5-8}$$

where u_p is the velocity of the sphere relative to the fluid some distance away from the sphere, such that the motion of the sphere does not disturb that reference parcel of fluid. Since we do not know the exact value of u_p, in this case, we consider it as equal to u_{water}.

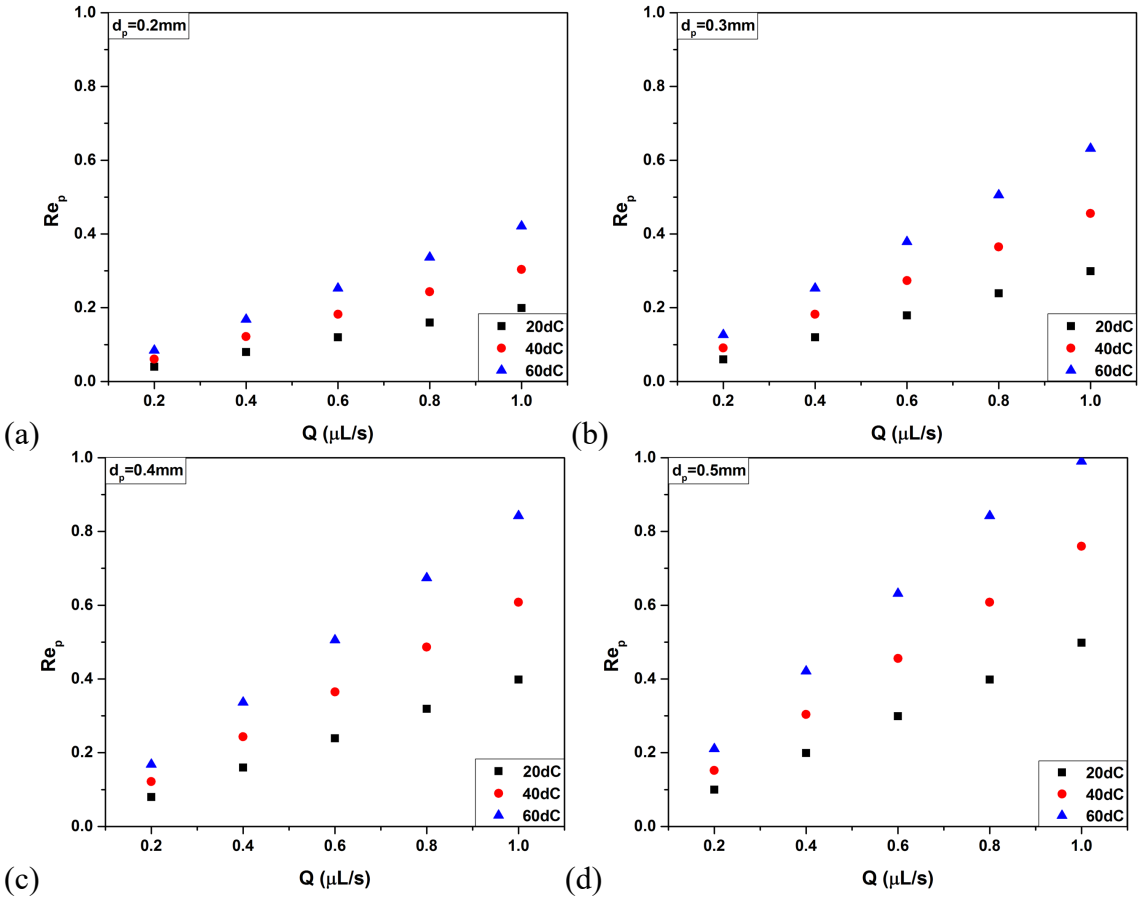

Figure 5-10 Reynolds of the particle Re_p as a function of flow rate Q (µL/s) for (a) d_p=200 µm, (b) d_p=300 µm, (c) d_p=400 µm and (d) d_p=500 µm.

The relationship of the Re_p with the Q for different particle diameter is presented in Figure 5-10. Re_p increases with temperature and flow rate. The value of Re_p is less than 1, for all the different conditions, therefore, the system exhibits creeping flow, which is a very slow flow and is also called Stokes' flow [196]. Creeping flow is a type of fluid flow where advective inertial forces are small compared to viscous forces.

The drag coefficient C_D and the total drag force on the sphere F_D were calculated using Stokes' law [196]

$$C_D = \frac{24}{Re_p} \tag{5-9}$$

and

$$F_D = 6\pi r_p \mu_{water} u_{water} \tag{5-10}$$

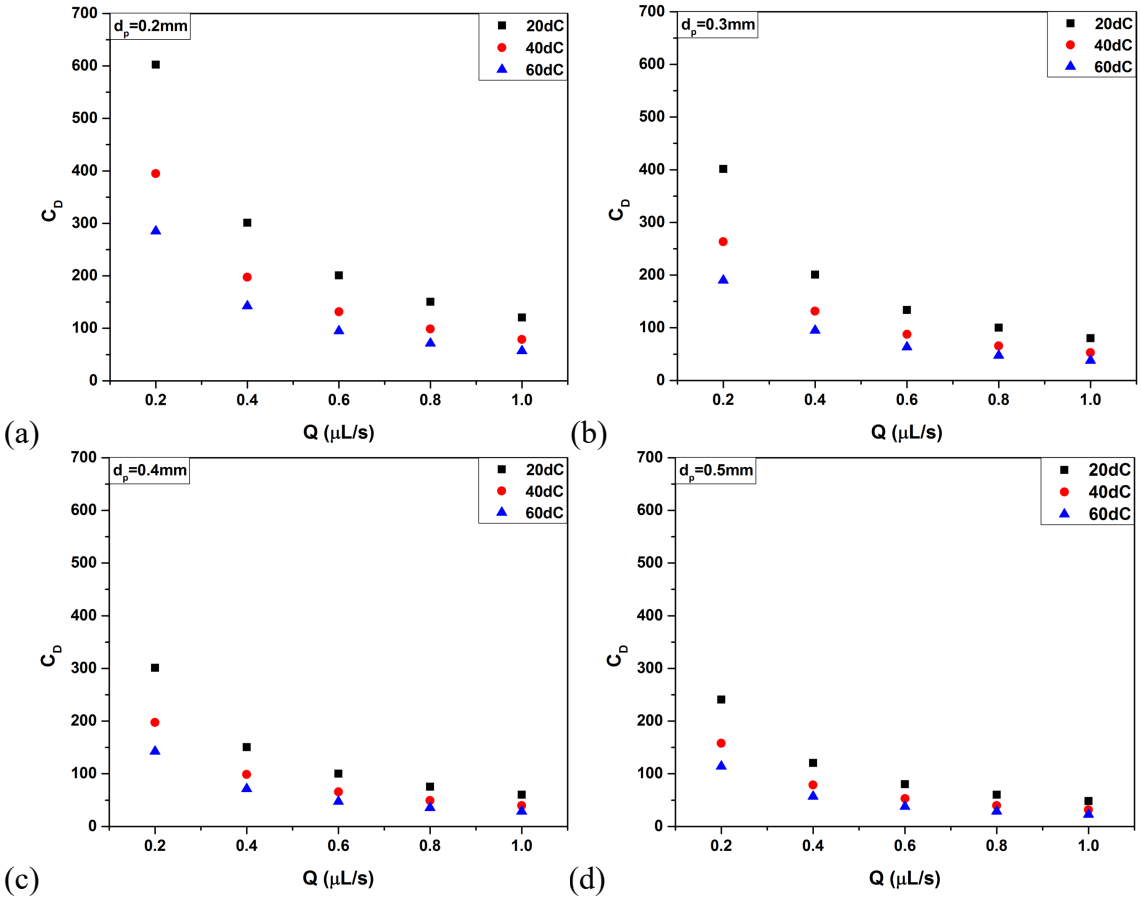

Figure 5-11 Drag coefficient C_D as a function of flow rate Q (µL/s) for (a) (a) d_p=200 µm, (b) d_p=300 µm, (c) d_p=400 µm and (d) d_p=500 µm.

Figure 5-11 and Figure 5-12 show the C_D and the F_D in relation to Q accordingly. The C_D is decreasing with the increasement of temperature and velocity of the water while the F_D increases with flow rate but decreases as temperature rises from 20dC to 60dC. In general, the total drag force on the sphere is in acceptable levels and in compliance with experimental results found in the literature [197] where for similar conditions the difference is 2E-4 µN.

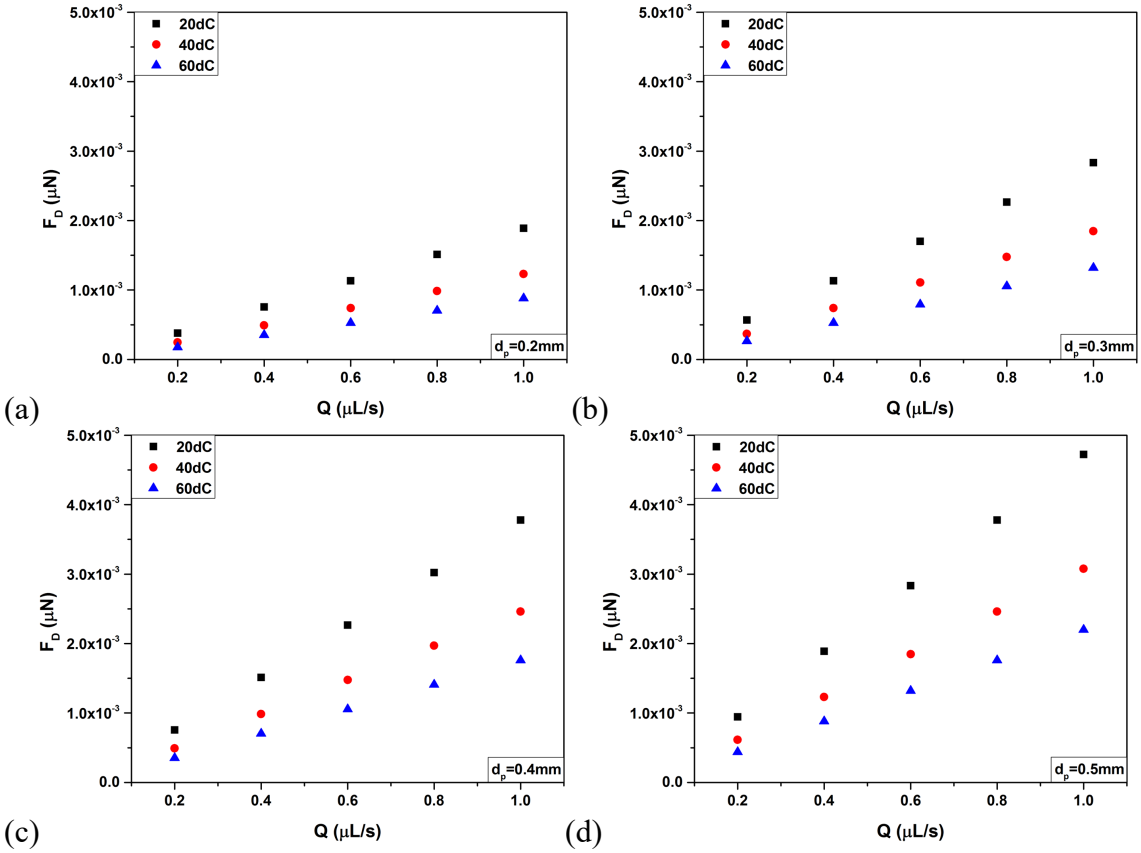

Figure 5-12 Total drag force on the sphere F_D (μN) as a function of flow rate Q (μL/s) for (a) d_p=200 μm, (b) d_p=300 μm, (c) d_p=400 μm and (d) d_p=500 μm.

5.3.2 Calibration of the microfluidic device

For the calibration of the microfluidic dissolution testing device, experimental results obtained with the GPV technique were compared with COMSOL simulation results. Figure 5-13 (a) shows a bright field image of a channel (1.5 mm wide and 1 mm high) (c) containing a glass bead of 250 μm and (e) containing a glass of 500 μm at its centre. The microfluidic device was manufactured in polydimethylsiloxane (PDMS) as described in Section 5.2.3 . A deionised water flow seeded with 200 nm polystyrene particles (0.2% by weight) moves from left to right at different flow rates (from 0.2 μL/s to 1 μL/s). The median of 30 following frames is adequate to eliminate the effects of the motionless background contribution from each frame and reveal the speckle pattern generated by the moving nanoparticles (see Figure 5-13 (b), (d) and (f)). The open-source PIVLab 1.4

Matlab toolbox was used to cross-correlate nanoparticle movement using speckle patterns from two following images and thus extract the equivalent velocity field.

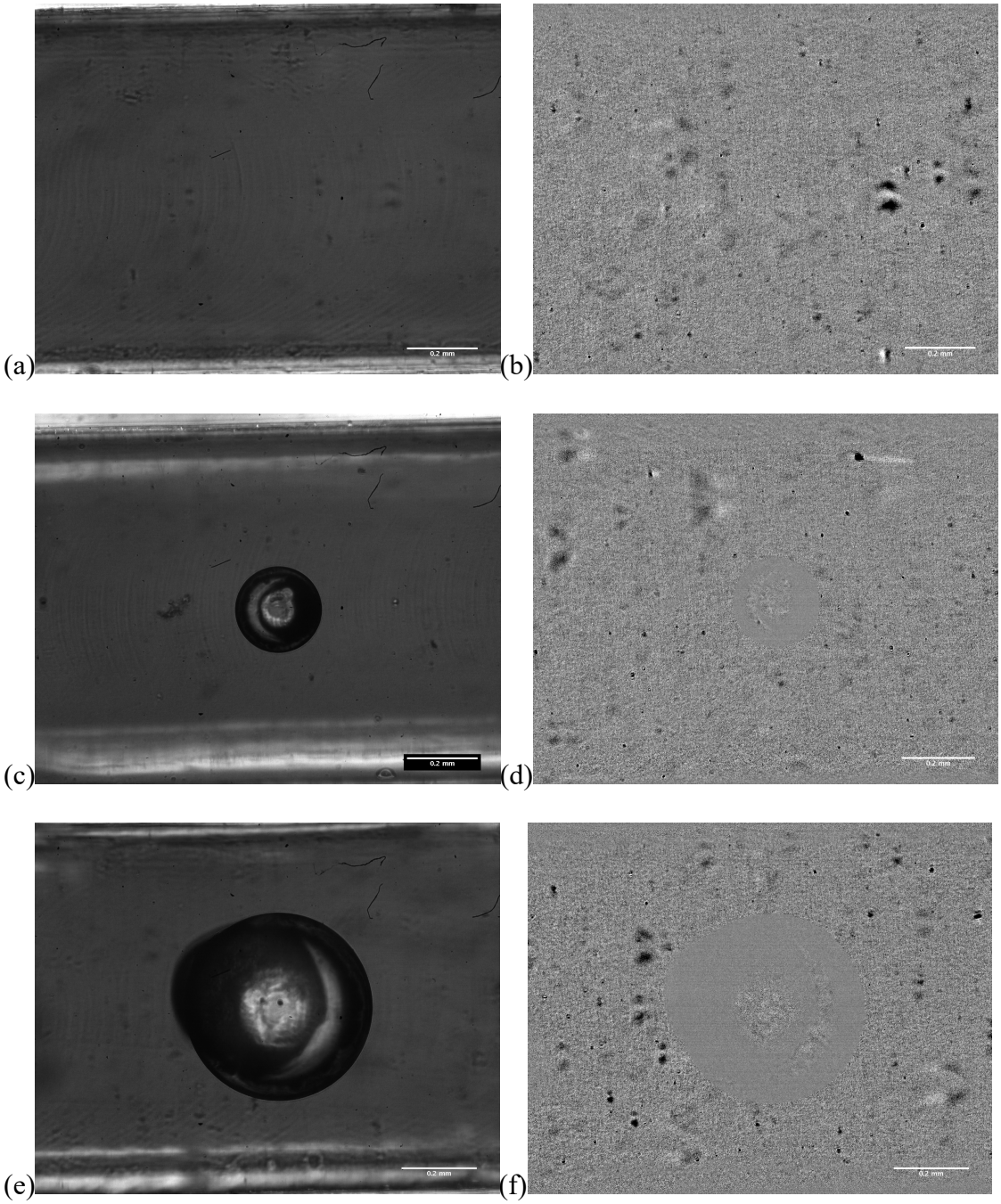

Figure 5-13 (a) Bright field image of 200 nm polystyrene particles (concentration 0.2% by weight) dispersed in deionised water flowing through a microchannel (c) containing a 250 µm glass bead and (e) containing a 500 µm glass bead. (b), (d) and (f) Speckle patterns of the bright field images (a), (c) and (e) respectively obtained by subtraction of the median image. Scale bars are 200 µm.

Figure 5-14 presents the comparison of the images between the GPV (experimentally) evaluated flow velocity distribution and COMSOL 3D simulation of the empty microchannel (see Figure 5-14 (a) (b)) and over a 250 µm and 500 µm glass bead (see Figure 5-14 (c) (d) and (e) (f) respectively). The correlation of the images illustrates the close agreement between experimental and theoretical data. This is confirmed by Figure 5-15, Figure 5-16 and Figure 5-17 which show the comparison of the velocity magnitude results for the different flow rates. Obtained from a line crossing the middle section of the chamber for the three different conditions (empty channel and 250 µm, 500 µm glass beads). GPV images over the two different sized glass beads show that the flow pattern is proportional front to back. The streamlines are straight and symmetrical in the free flow far ahead of the glass beads, but they are deflected as they move around the glass beads. Results (see Figure 5-15, Figure 5-16 and Figure 5-17) demonstrate that at the glass beads surface the velocity of the water is zero and increases gradually away of the particles. On the other hand, in the condition of the empty channel the velocity of the liquid in contact with the channel walls is approximately zero and increases steadily away of the wall. It reaches its maximum value at the centre of the channel.

(a) 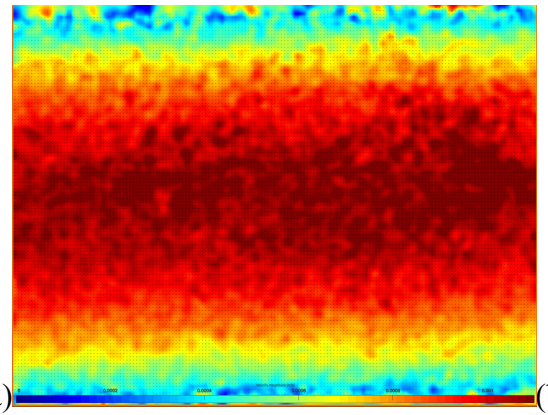 (b) 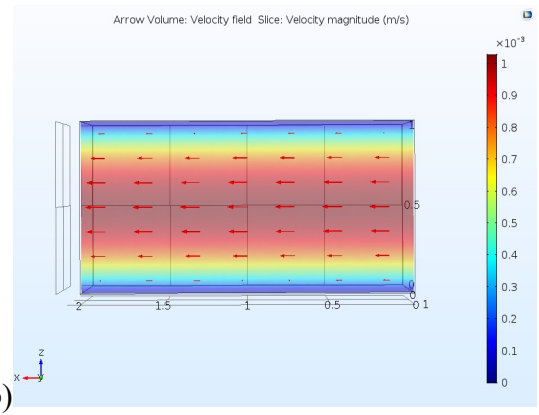

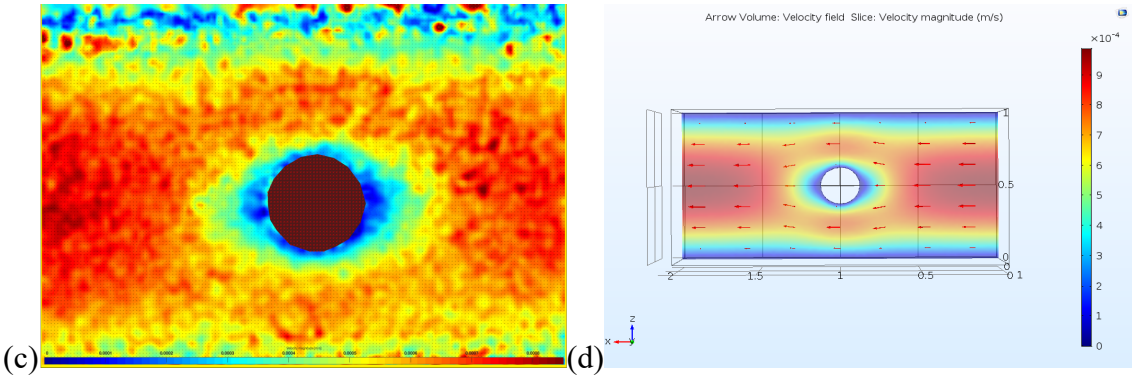

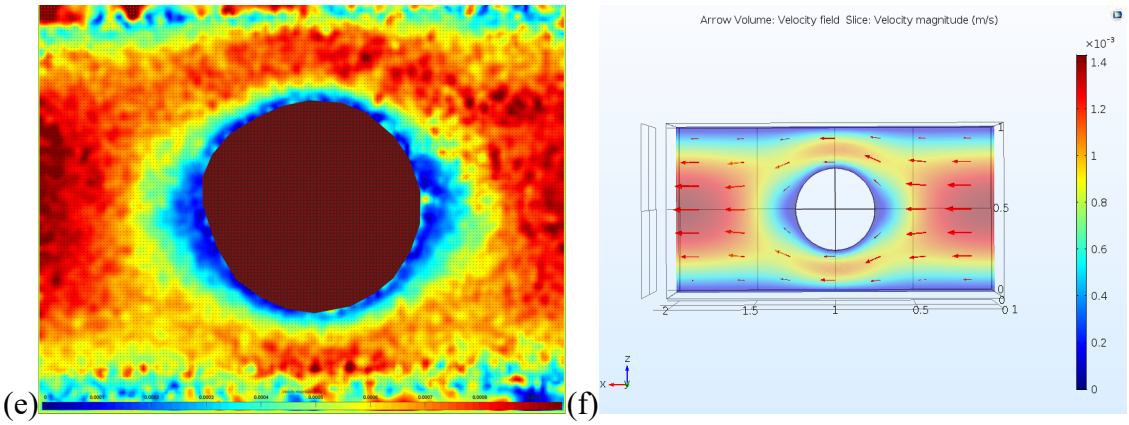

Figure 5-14 Comparison of the flow velocity field within a microchannel obtained experimentally (left column) via GPV and (right column) via COMSOL simulations for flow rate 1 µL/s for three different conditions (a) (b) empty channel, (c) (d) 250 µm and (e) (f) 500 µm.

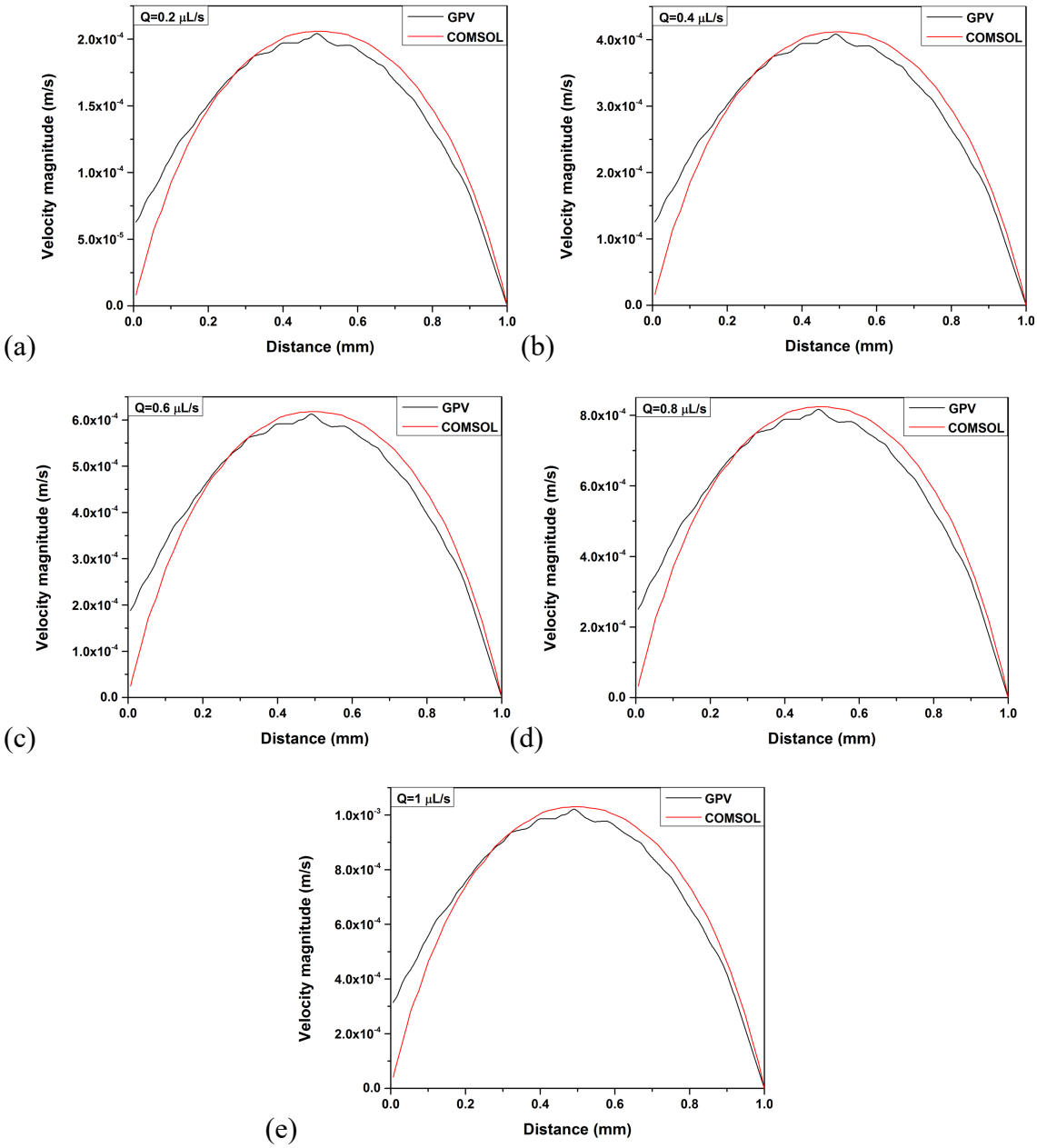

Figure 5-15 Comparison of the experimental and simulation flow velocity results for a line crossing the middle of the empty channel for a flow rate of (a) 0.2 µL/s, (b) 0.4 µL/s, (c) 0.6 µL/s, (d) 0.8 µL/s and (e) 1 µL/s.

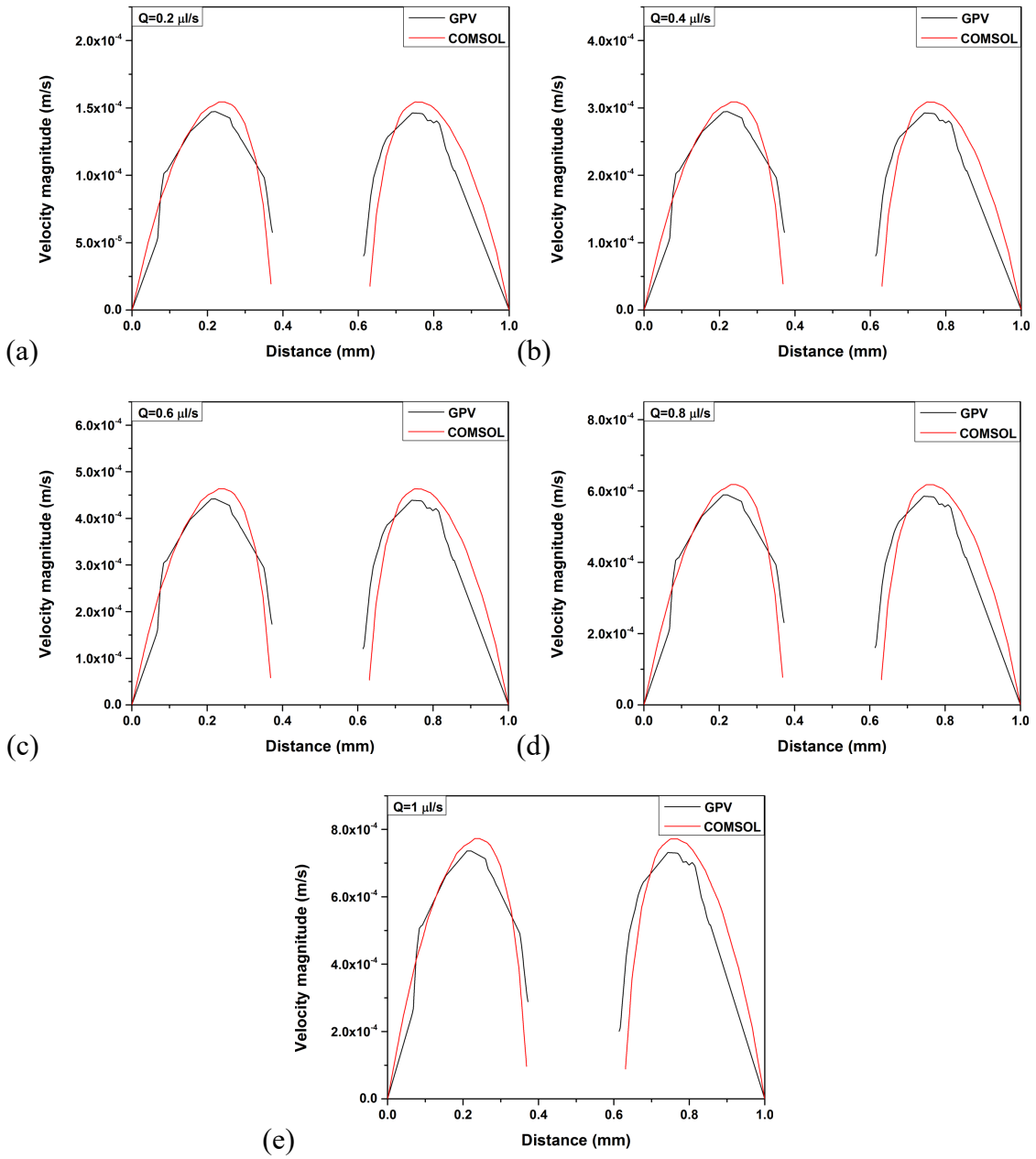

Figure 5-16 Comparison of the experimental and simulation flow velocity results for a line crossing the middle of a channel with a 250 µm glass bead for a flow rate of (a) 0.2 µL/s, (b) 0.4 µL/s, (c) 0.6 µL/s, (d) 0.8 µL/s and (e) 1 µL/s.

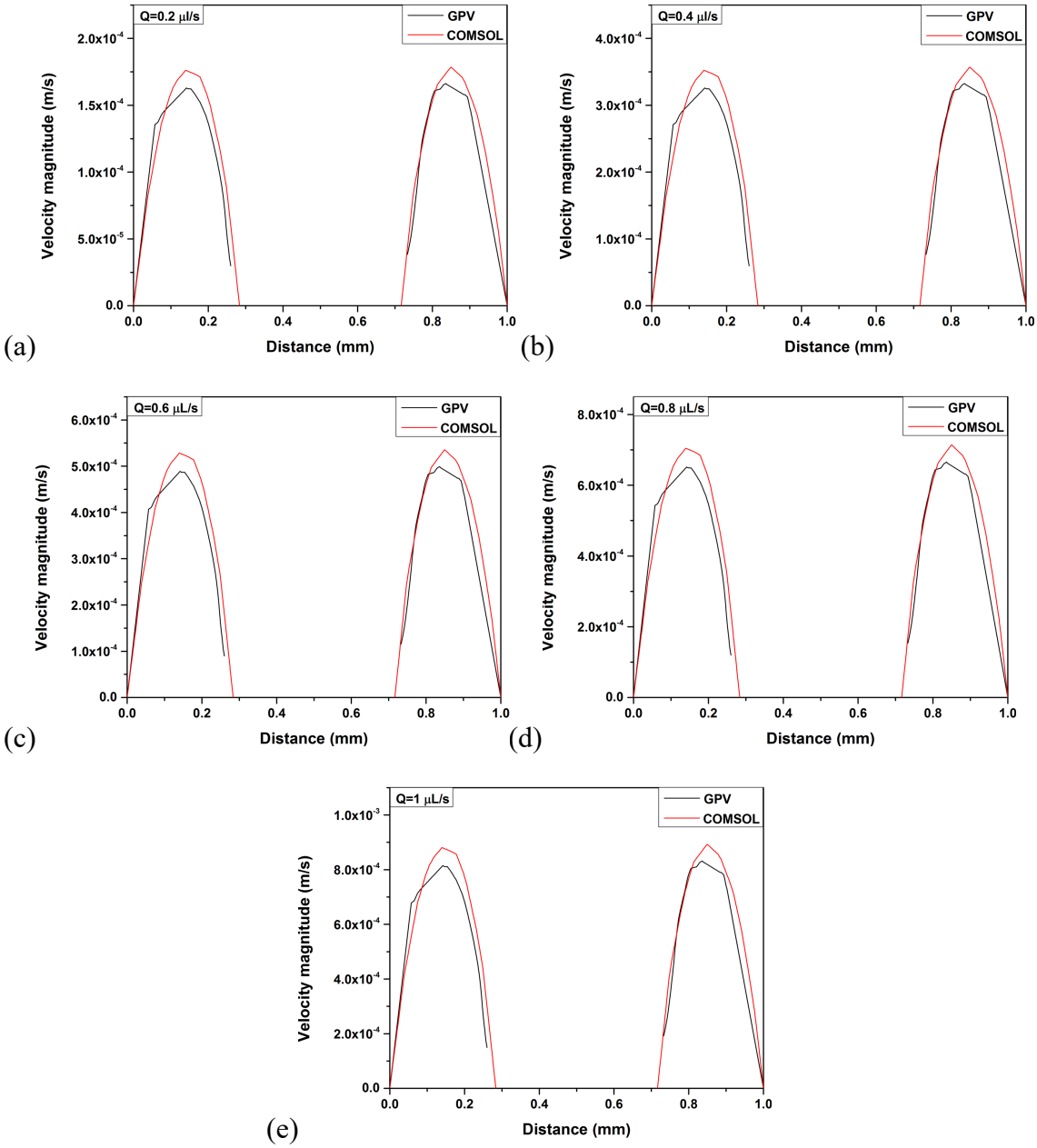

Figure 5-17 Comparison of the experimental and simulation flow velocity results for a line crossing the middle of a channel with a 500 µm glass bead for a flow rate of (a) 0.2 µL/s, (b) 0.4 µL/s, (c) 0.6 µL/s, (d) 0.8 µL/s and (e) 1 µL/s.

5.3.3 Dissolution phenomena

In an attempt to understand the phenomena, govern convective dissolution, experiments were conducted on 20 individual particles at two size ranges below 250 µm and 250 to 500 µm to observe the process using an optical microscope at 20dC, 40dC and 60dC.

Figure 5-18 shows the phenomena taking place in the convective dissolution process of active ingredients of a porous particle as these have summarized by [7], [8] as i) the wetting of the powder where water penetrates into the pore system due to capillary forces; ii) the shrinking where particle mass reduces gradually due to diffusion/convection; iii) the dissolution of the solid bridges between primary particles followed by powder disintegration; and iv) the dissolution of soluble primary particles. In comparison to the phenomena presented for single particle diffusion dissolution (see Figure 4-2) in convection, the stage where the granule breaks its initial structure as water fills the pores called early-stage disintegration is not presented, or it appears rapidly (in a range of ms) as the water flow passes through the particle and it cannot be recorded. Each row of Figure 5-18 shows a characteristic particle from Sample1 to Sample5 dissolving, at 20dC, at different flow rates between 0.2 μL/s and 1 μL/s respectively. In contrast to the different dissolution behaviours of single particles based on the type of binder (see Figure 4-3), in this study, the dissolution behaviour of the samples is similar across the different experimental conditions. The third and fourth row are representing the single particle convective dissolution of Sample3 and 4 accordingly. In diffusion dissolution, for the same samples (see Figure 4-3) we have faced the formation of cloudy, gel layer due to polymerisation of Silicate that slows down the total dissolution process [170]. However, in convection that does not seem to affect dissolution as the hydrodynamic forces does not allow this Silicate layer to be developed [171] and as a result, the dissolution time is decreased significantly. For the rest of the samples, the main difference with diffusion is that the dissolution is faster. The same trend follows as the temperature increases from 20dC to 60dC. In general, it can be commented that the dissolution mechanisms are being

accelerated and they are not affecting the overall dissolution performance as much as on diffusion conditions.

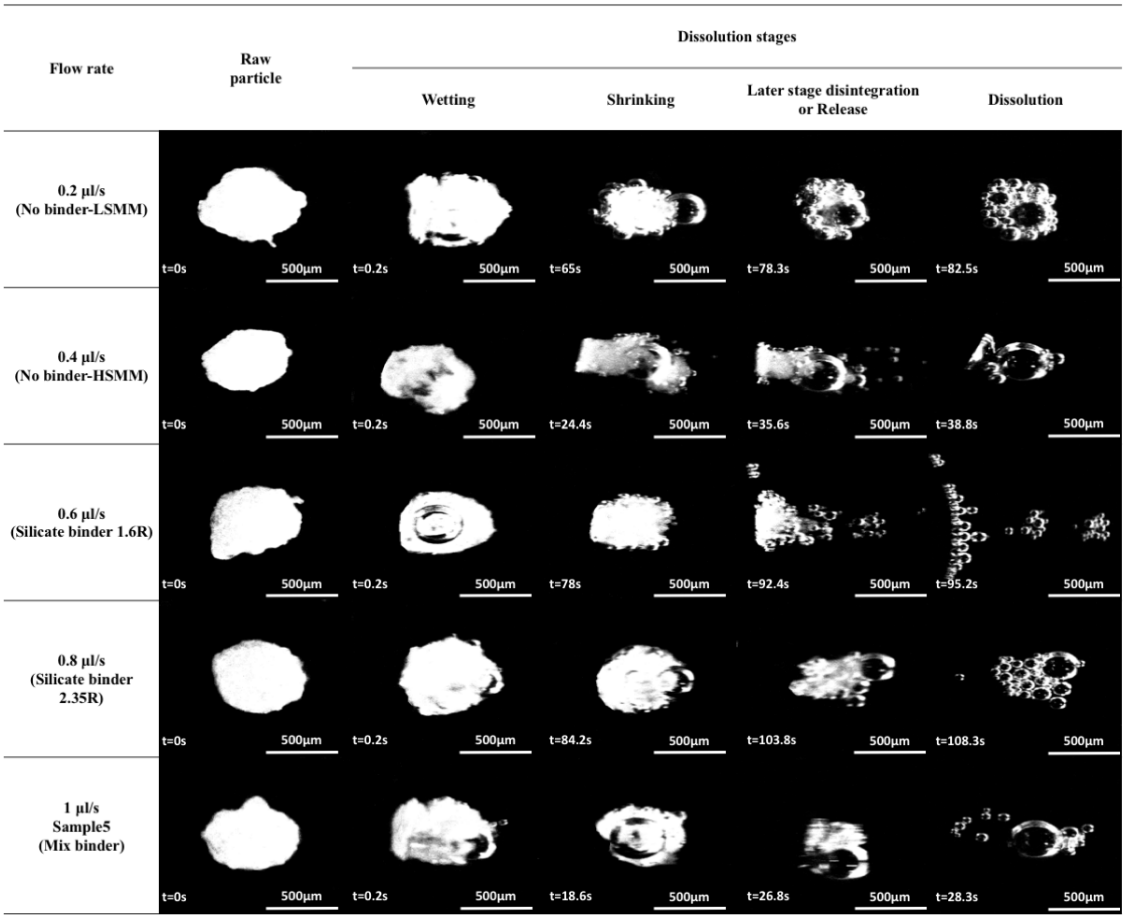

Figure 5-18 Overview of the convective dissolution stages. Each row represents the convective dissolution of a characteristic particle of each sample at a certain flow rate, from 0.2 µL/s to 1 µL/s at 20dC water temperature.

5.3.4 Effect of flow rate and temperature on dissolution times

The total dissolution time t_f (s) as a function of flow rate Q (µL/s) for particle size below 250 µm is plotted in Figure 5-19 (a), (c) and (e) while for particles between 250 and 500 µm is presented in Figure 5-20 (a), (c) and (e). The evaluation was conducted for three different temperatures 20dC, 40dC and 60dC. A significant effect of flow rate, temperature and porosity of the Samples on dissolution time has been revealed.

Specifically, it can be observed that the dissolution time decreases in a linear relationship with the increasement of the fluid velocity from 0.2 μL/s to 1 μL/s for all the powder samples. Comparing the results with the data obtained from the diffusion dissolution experiments (see Figure 4-6 (a)) it can be noticed that the dissolution time decreased significantly across the particle sizes due to the fluid related properties (flow rate and temperature). The addition of the flow rate and temperature into the system reduces the dissolution time for particle sizes below 250 μm by more than 35%, 2%, 11%, 42% and 2.2% for Sample1, 2, 3, 4 and 5 accordingly across the different temperatures tested. For size range from 250 to 500 μm this decrease is even higher as it drops down the dissolution time by more than 79%, 41%, 55%, 60% and 35% for Sample1, 2, 3, 4 and 5 respectively. These percentage decrease data reveal that the increase of flow rate and temperature affects more, samples with a slow dissolution behaviour and especially Sample3 and 4 that contain the Silicate binder rather than fast dissolving samples like Sample2 and 5. In the diffusion dissolution studies (see Section 4.3.3) we have seen that the Silicate binder affects the dissolution time in two ways. Firstly, it reduces the porosity of the sample which as Stepanek [87] has shown porosity could have an effect on dissolution time, as lower porosity leads to slower dissolution. Moreover, it has an impact via the polymerisation of Silicate that slows down the total dissolution process as it blocks the release of ingredients. However, it seems that this is not the case in convection. Although the porosity has not changed, the effect of flow rate and temperature on the second factor is critical. These two parameters does not allow the formation of the Silicate layer, [171] and as a consequence, the dissolution decreases significantly. This hypothesis correlates well with the presented dissolution phenomena in Figure 5-18. This data can reveal the main difference between single particle diffusion and convective dissolution.

In diffusion dissolution, the dominating factors are the dissolution mechanisms and the microstructure of the samples while in convection are the fluid related properties.

Furthermore, as it has been described in Section 4.3.3 , disintegration of the particle is in alternative approach to influence dissolution time as it is strongly dependent on it [3]. In this study, the later stage disintegration time t_d (s) was evaluated by Image Processing. Figure 5-19 (b), (d), (f) and Figure 5-20 (b), (d), (f) present the relationship between the later stage disintegration with the dissolution time, t_d/t_f versus flow rate Q (μL/s). All powder samples exhibit later disintegration when the dissolution process achieves at least 80%. The later stage disintegration does not show any significant relationship between the flow rate and temperature on time that it happens across the samples. In contrast to diffusion dissolution experiments early stage disintegration does not appear, or it is rapid and cannot be captured and for that reason was not possible to be measured.

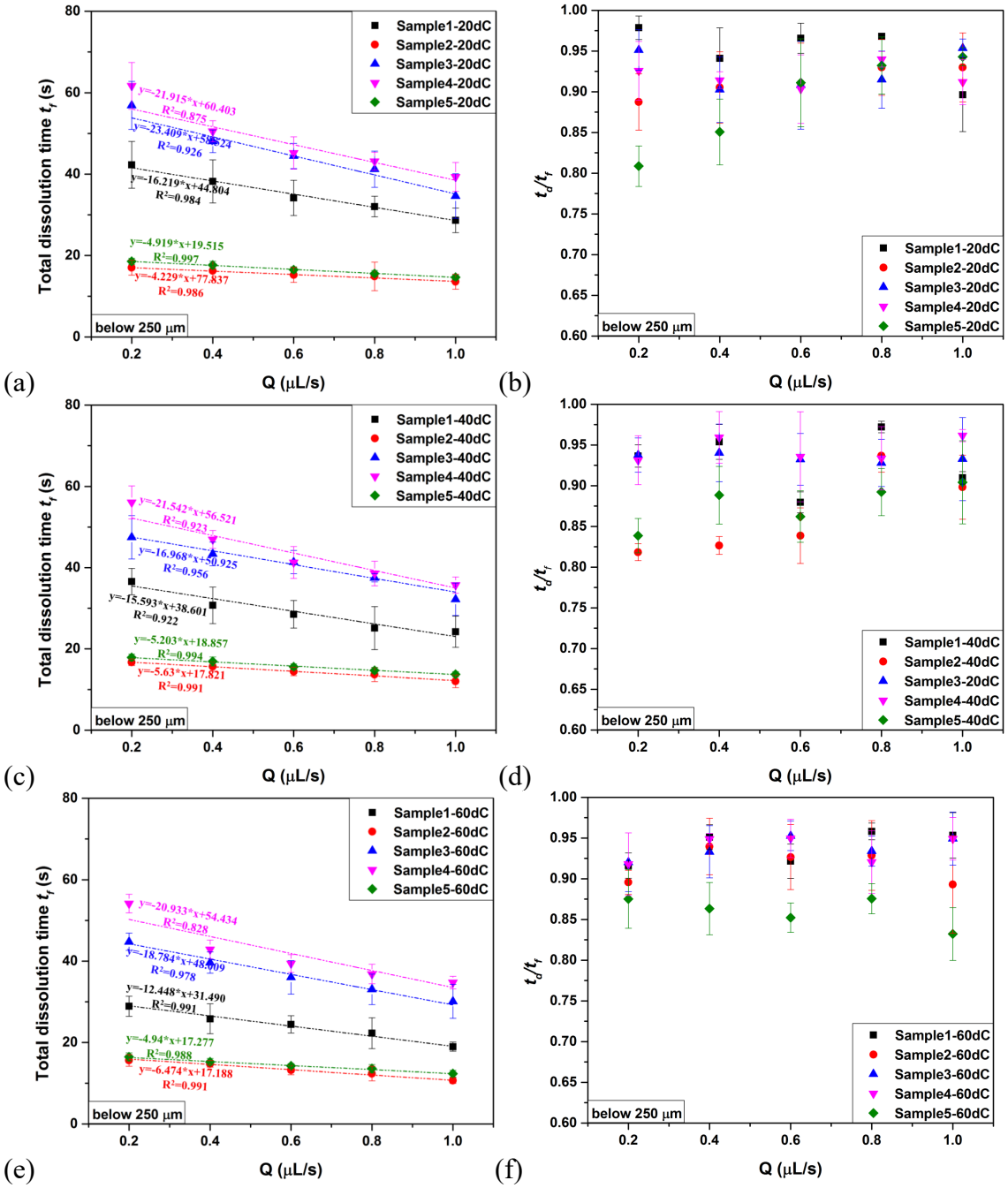

Figure 5-19 (a), (c), (e) Total dissolution time t_f (s) versus flow rate Q (μL/s) of the samples for particle size below 250 μm at 20dC, 40dC and 60dC respectively; (b), (d), (f) The ratio between the later stage disintegration time t_d and t_f (t_d/t_f) versus flow rate Q (μL/s) for particle size below 250 μm at 20dC, 40dC and 60dC respectively.

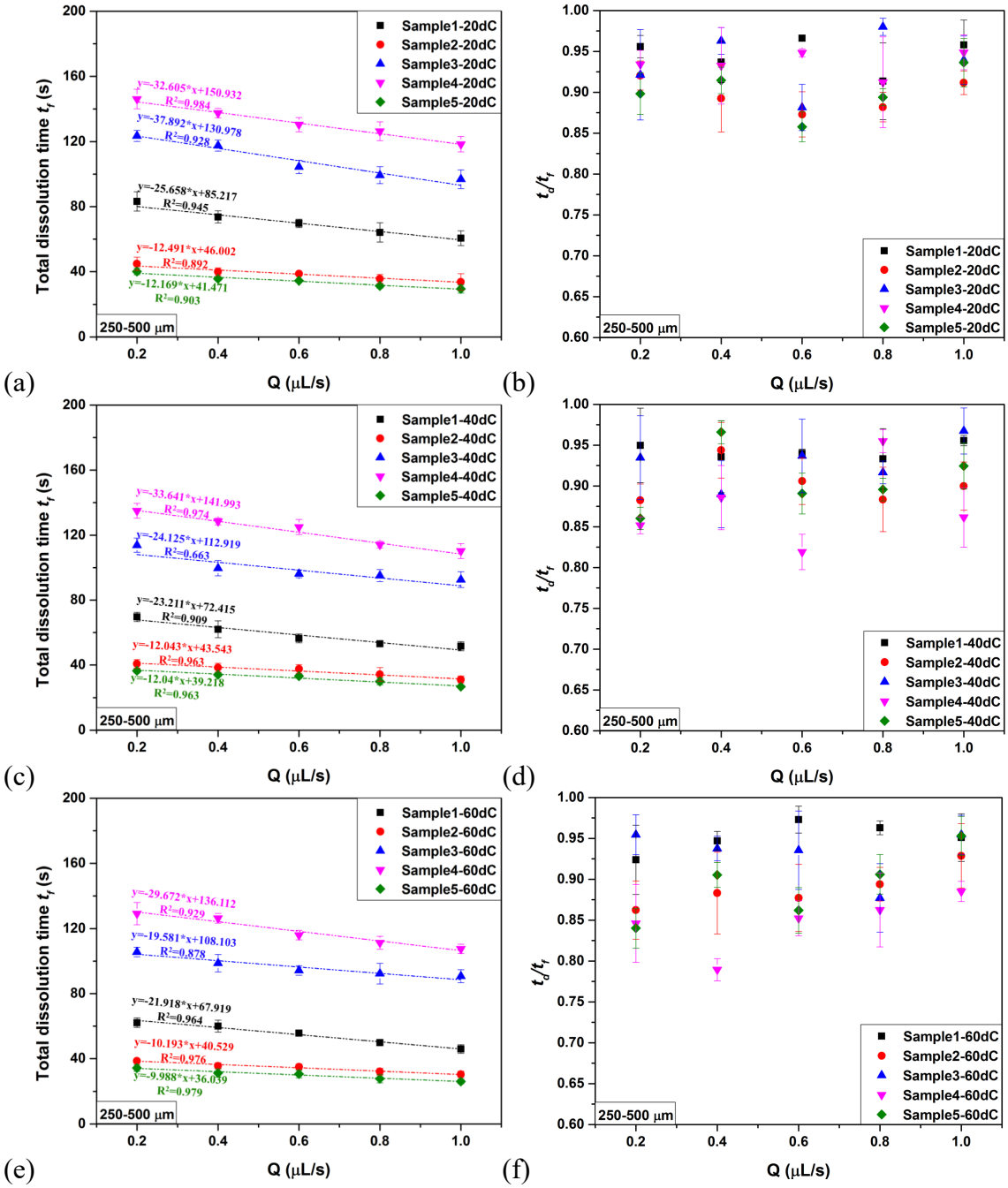

Figure 5-20 (a), (c), (e) Total dissolution time t_f (s) versus flow rate Q (μL/s) of the samples for particle size 250-500 μm at 20dC, 40dC and 60dC respectively; (b), (d), (f) The ratio between the later stage disintegration time t_d and t_f (t_d/t_f) versus flow rate Q (μL/s) for particle size 250-500 μm at 20dC, 40dC and 60dC respectively.

5.3.5 Dissolution profiles

The release profiles of below 250 μm granules based on the changes of the surface area of the particle, A_p (mm^2) at 20dC, 40dC and 60dC were evaluated using Equation (4-1)

and are presented in Figure 5-21, Figure 5-22 and Figure 5-23 respectively. For particle size 250-500 μm the dissolution profiles at the three different temperatures are given in Figure 5-24, Figure 5-25 and Figure 5-26 accordingly. As we expected from the single particle dissolution studies (see Figure 4-7), it is obvious that the powder samples have distinguished dissolution profiles, different from the results obtained from bulk dissolution measurements [178]. This is due to the unique particle morphology and microstructure that differs extensively between particles from the same batch as it has been illustrated from SEM and XRT results in Figure 3-11 and Figure 3-17 respectively. In general, the dissolution starts quite progressively where approximately the 15% of the sample has been dissolved in the first seconds, then slows down for the shrinking stage and finally finishes very fast in the last 20% of the dissolution when the disintegration moment begins. For both particle sizes the sample with no binder and high slurry mix moisture, Sample2, and the sample with the disintegrant Citric Acid in the binder mixture, Sample5, show the faster dissolution behaviour compared to the rest of the samples. This is because Sample2 has the highest porosity between the powder samples and Sample5 contains the disintegrant Citric Acid which via the increasement of the available surface area speeds up the total dissolution process [154]. The samples that contain the Silicate binder, Sample3 and 4, are the slowest dissolving across the size range, which is due to the low porosity levels and high degree of agglomeration where according to de Villers [179] slows down the dissolution of the powders. However, the early stage disintegration that govern the single particle diffusion dissolution profiles (see Figure 4-7) by extending the shrinking stage was not captured in the convective dissolution profiles and it does not be an important parameter of total convective dissolution process in contrast to the results obtained from the single particle diffusion study. Dissolution profiles show that in

convection important role play the hydrodynamic forces that speed up dissolution by reducing the time required for each stage of the process (wetting, shrinking and disintegration). Furthermore, although the particle porosity as well as the smoothness of the particle surface varies greatly between the particles (see Figure 3-11 and Figure 3-17), the dissolution profiles of the particles from each sample were quite reproducible which is evident by the small standard deviations appeared in this study. This is due to the velocity of the fluid that smooths out any irregularities between the particles [33]. As it has been already stated in the previous chapter the unique advantage of the single particle experimental approach is the clear representation of the dissolution phenomena of the samples.

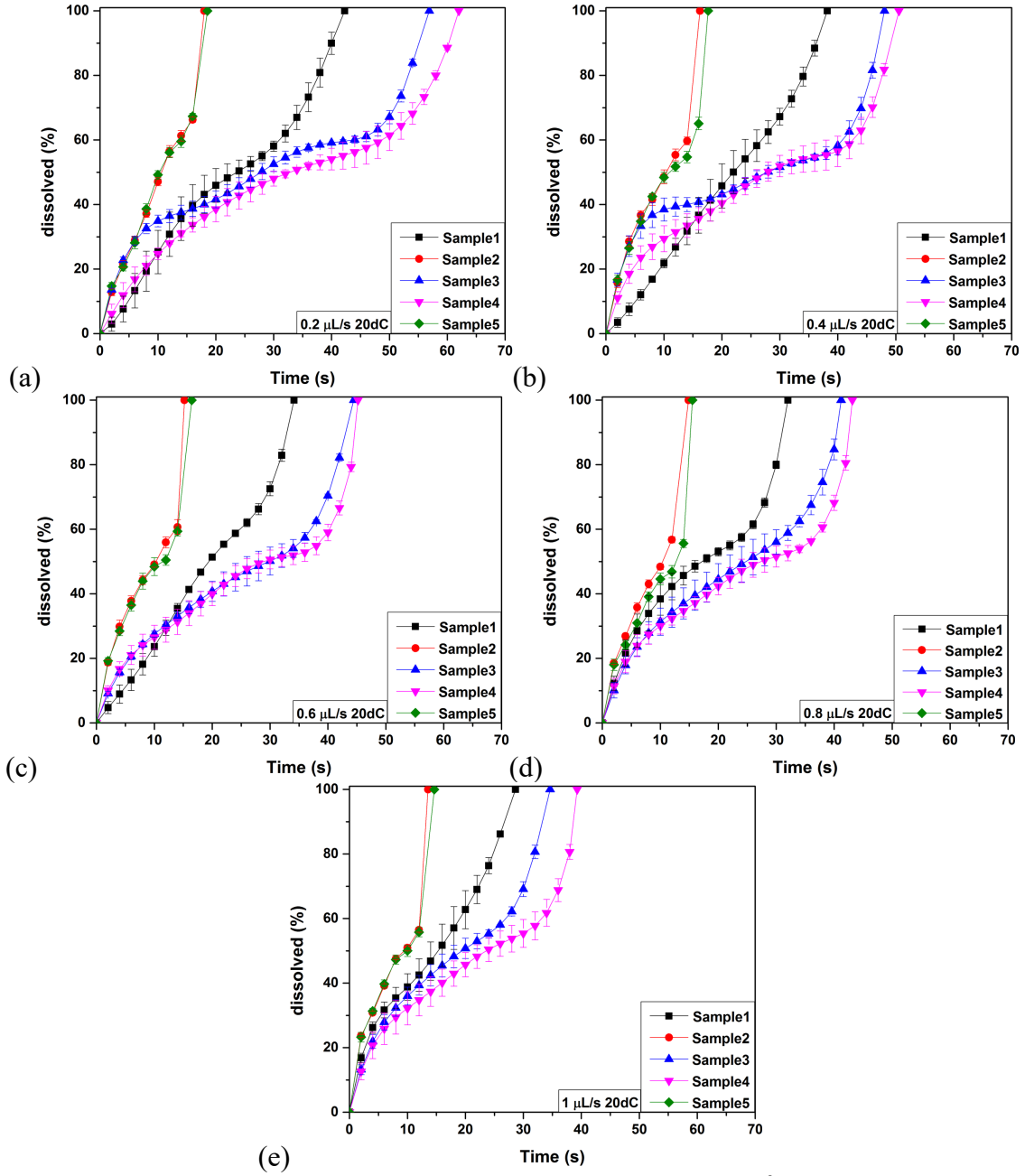

Figure 5-21 Dissolution profiles based on surface area (mm^2) versus time (s) of particle size below 250 µm for (a) 0.2 µL/s, (b) 0.4 µL/s, (c) 0.6 µL/s, (d) 0.8 µL/s and (e) 1 µL/s at 20dC.

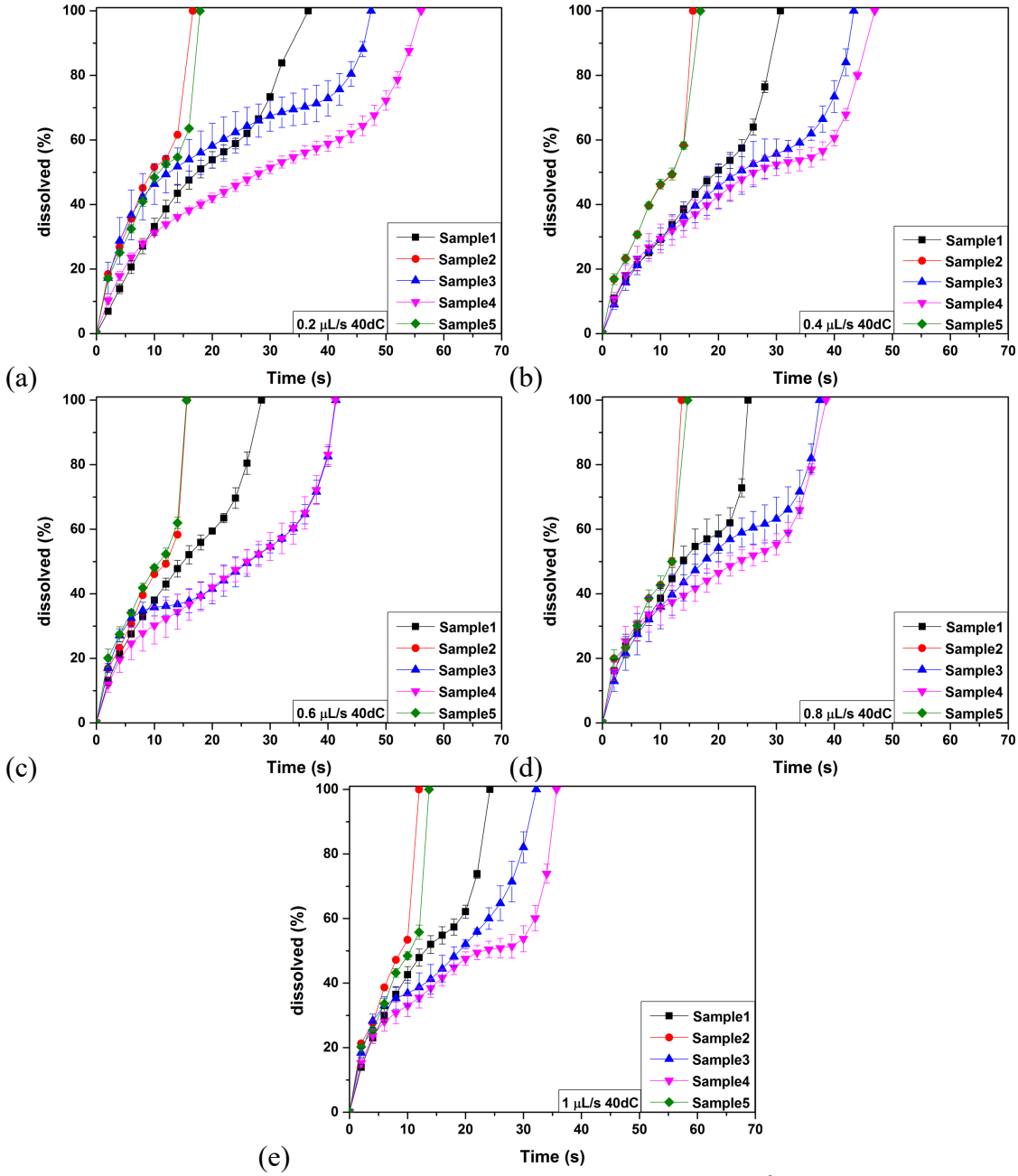

Figure 5-22 Dissolution profiles based on surface area (mm^2) versus time (s) of particle size below 250 µm for ((a) 0.2 µL/s, (b) 0.4 µL/s, (c) 0.6 µL/s, (d) 0.8 µL/s and (e) 1 µL/s at 40dC.

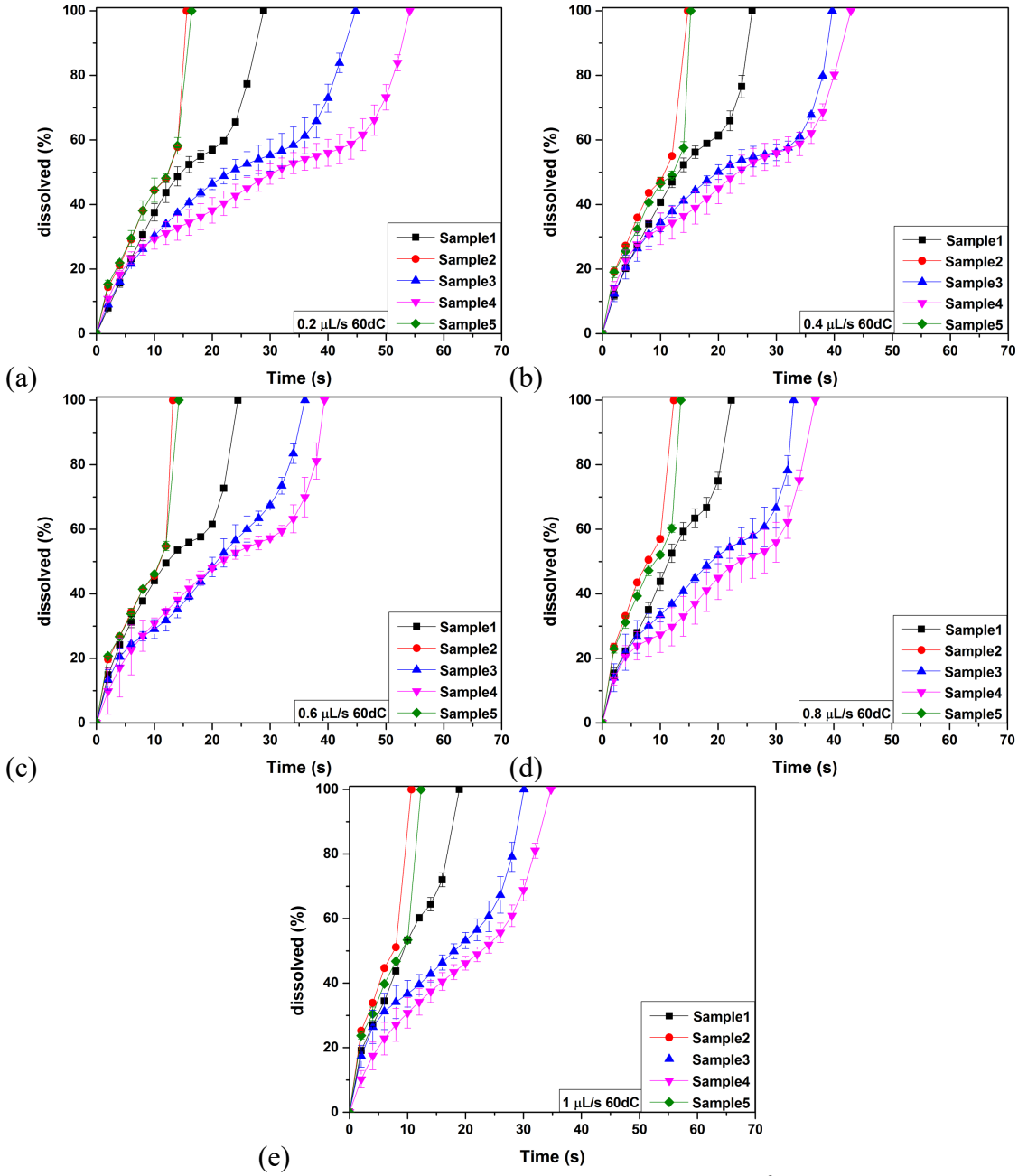

Figure 5-23 Dissolution profiles based on surface area (mm^2) versus time (s) of particle size below 250 µm for (a) 0.2 µL/s, (b) 0.4 µL/s, (c) 0.6 µL/s, (d) 0.8 µL/s and (e) 1 µL/s at 60dC.

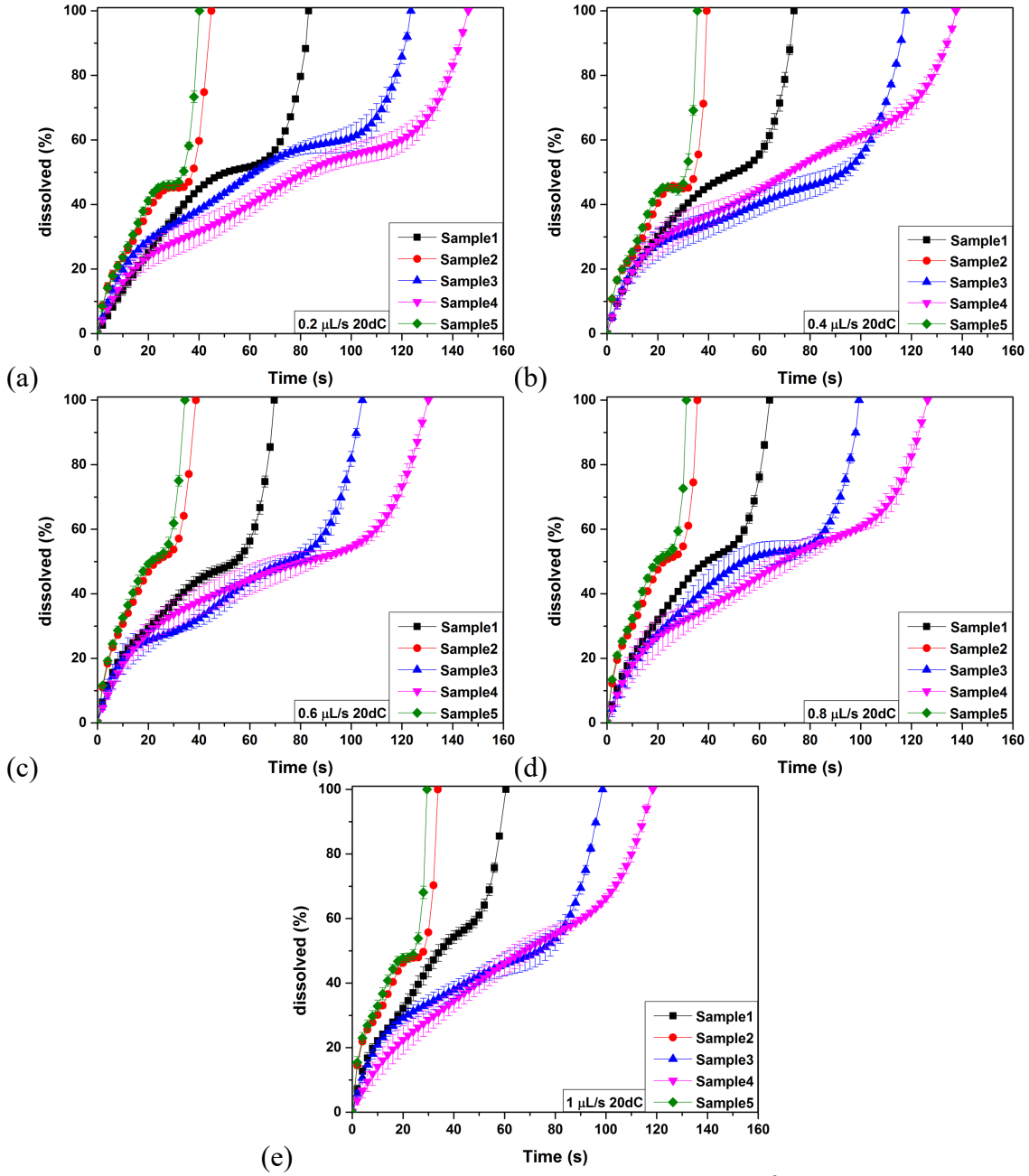

Figure 5-24 Dissolution profiles based on surface area (mm^2) versus time (s) of particle size 250-500 µm for (a) 0.2 µL/s, (b) 0.4 µL/s, (c) 0.6 µL/s, (d) 0.8 µL/s and (e) 1 µL/s at 20dC.

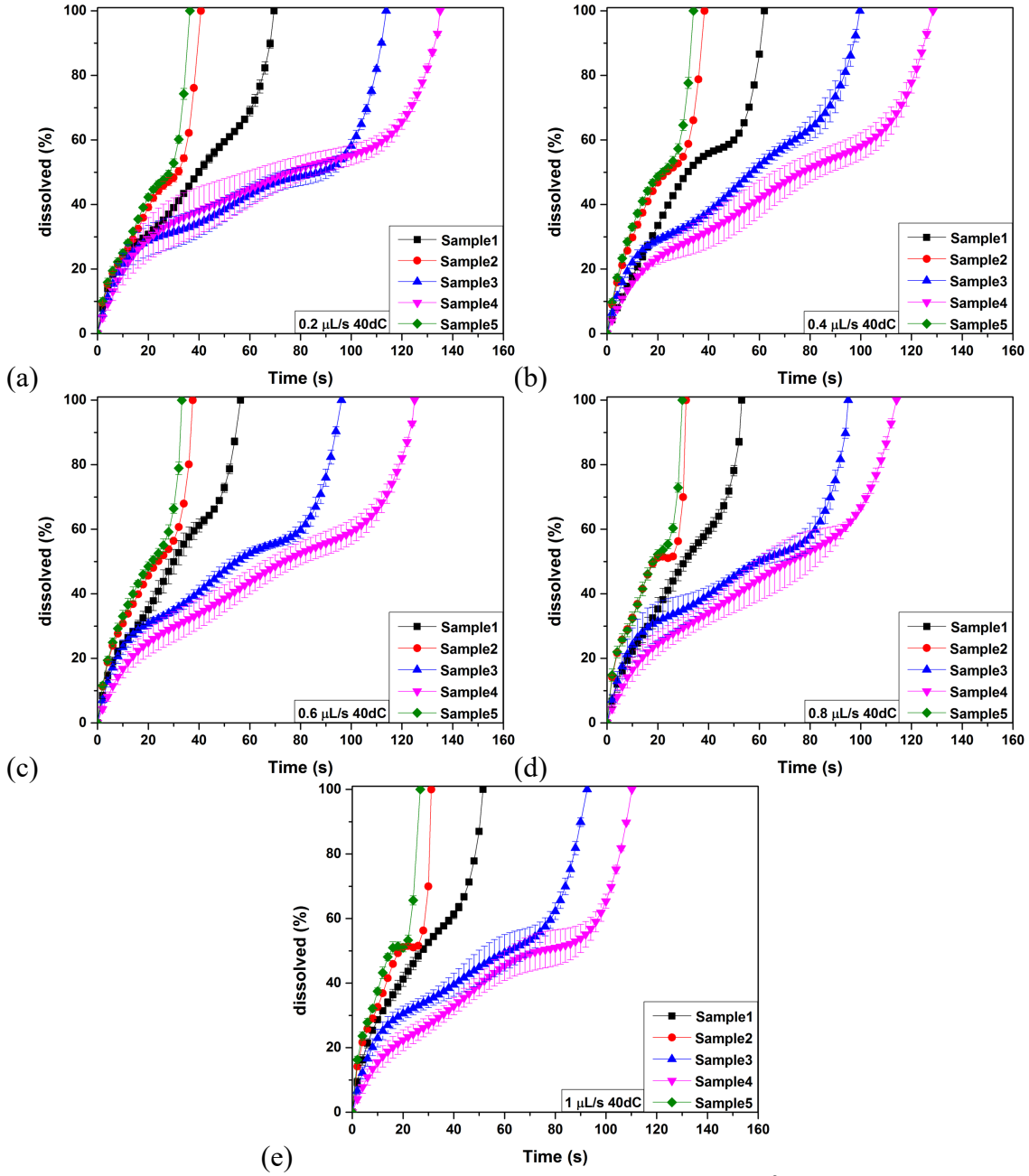

Figure 5-25 Dissolution profiles based on surface area (mm^2) versus time (s) of particle size 250-500 µm for (a) 0.2 µL/s, (b) 0.4 µL/s, (c) 0.6 µL/s, (d) 0.8 µL/s and (e) 1 µL/s at 40dC.

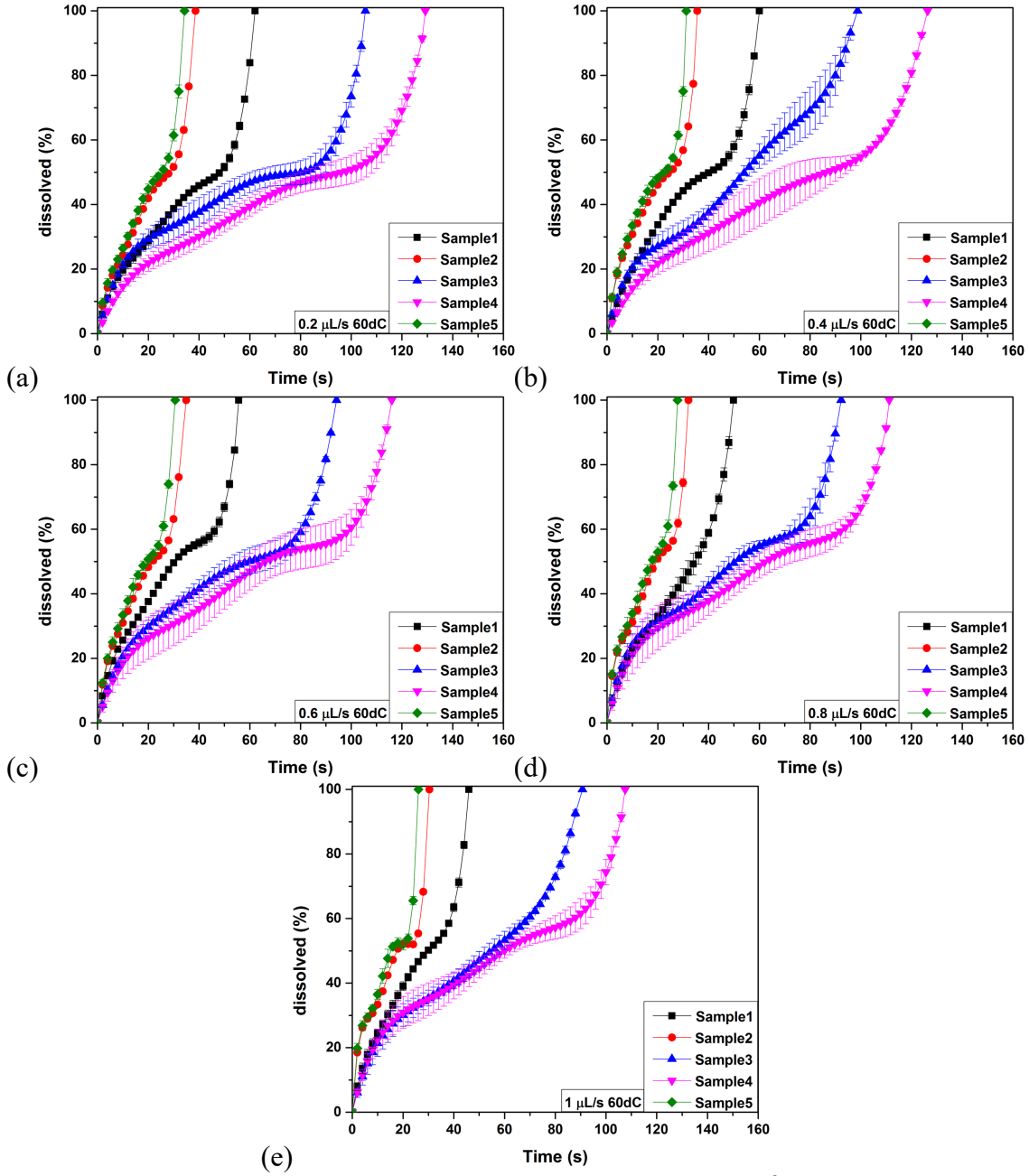

Figure 5-26 Dissolution profiles based on surface area (mm^2) versus time (s) of particle size 250-500 µm for (a) 0.2 µL/s, (b) 0.4 µL/s, (c) 0.6 µL/s, (d) 0.8 µL/s and (e) 1 µL/s at 60dC.

5.3.6 Effect of flow rate and temperature on dissolution rate

As it has been previously discussed in Section 4.3.5 the most common approach for the evaluation of dissolution rate is via bulk measurements [9], [12], [19], [180]. However, these measurements average the dissolution rate between all particles and frequently also

over time. Thus they cannot take into account the complexity of particle microstructure compared to the surface [181] and that the dissolution rate will be different among them. As the single particle diffusion (see Figure 4-3) and convective dissolution (see Figure 5-18) have shown the dissolution phenomena are on the scale of individual granules. Therefore, it is often preferred to express the dissolution rate as a function of a surface specific value, either by exposing a constant surface area of the particle to the dissolving liquid or by continuously measuring the change in surface area, as a function of time.

In this study, the dissolution rates for particles below 250 μm and 250-500 μm from 0.2 to 1 μL/s at 20, 40 and 60dC were acquired using two different approaches as described in Section 4.3.5 .

Figure 5-27 - Figure 5-32 present the dissolution rate dW/dt per mm^2 for each experimental condition. The behavior of the dW/dt per mm^2 in convective dissolution is quite similar to the diffusion one (see Figure 4-8). The dW/dt per mm^2 progresses slowly and is almost constant for the biggest part of the dissolution process as its value ranges from 1 to 10 μg/smm^2. This part includes the wetting and the shrinking stage where the changes on the surface area between the time intervals are not significant. The dissolution rate accelerates and takes the highest value at the final stage of the dissolution when the disintegration starts. For particles below 250 μm, the range of increasement of dissolution rate is from 10 up to 70 μg/smm^2, while for 250-500 μm is up to 110 μg/smm^2 depending on temperature and fluid velocity. This behavior of dW/dt per mm^2 lies on the hypothesis that as the agglomerates disintegrate in smaller pieces, the diffusion layer thickness around each particle decreases [64], [73], while the interfacial surface area increases [36], [38], [42]. The difference in the maximum value of dW/dt per mm^2 for each particle is due to the difference of particle mass and the bulk density between the

samples. Sample2 shows the lowest value as it has the lowest bulk density across the samples. However, Sample2 and Sample5 have the highest dissolution rate dW/dt for all the size cuts due to their fast dissolution behavior (see dW/dt (kg/s) versus time (s) in Figure 5-27 - Figure 5-32). In contrast to diffusion, in convective dissolution the rate of release is generally more than two times higher at each time interval due to the lack of early stage disintegration and the presence of flow rate that enhances the dissolution process. The results show that the dissolution rate is strongly dependant on the particle size and the relevant particle exposed surface area. However, they cannot reveal any specific relationship between the dW/dt per mm^2 and the flow rate and temperature.

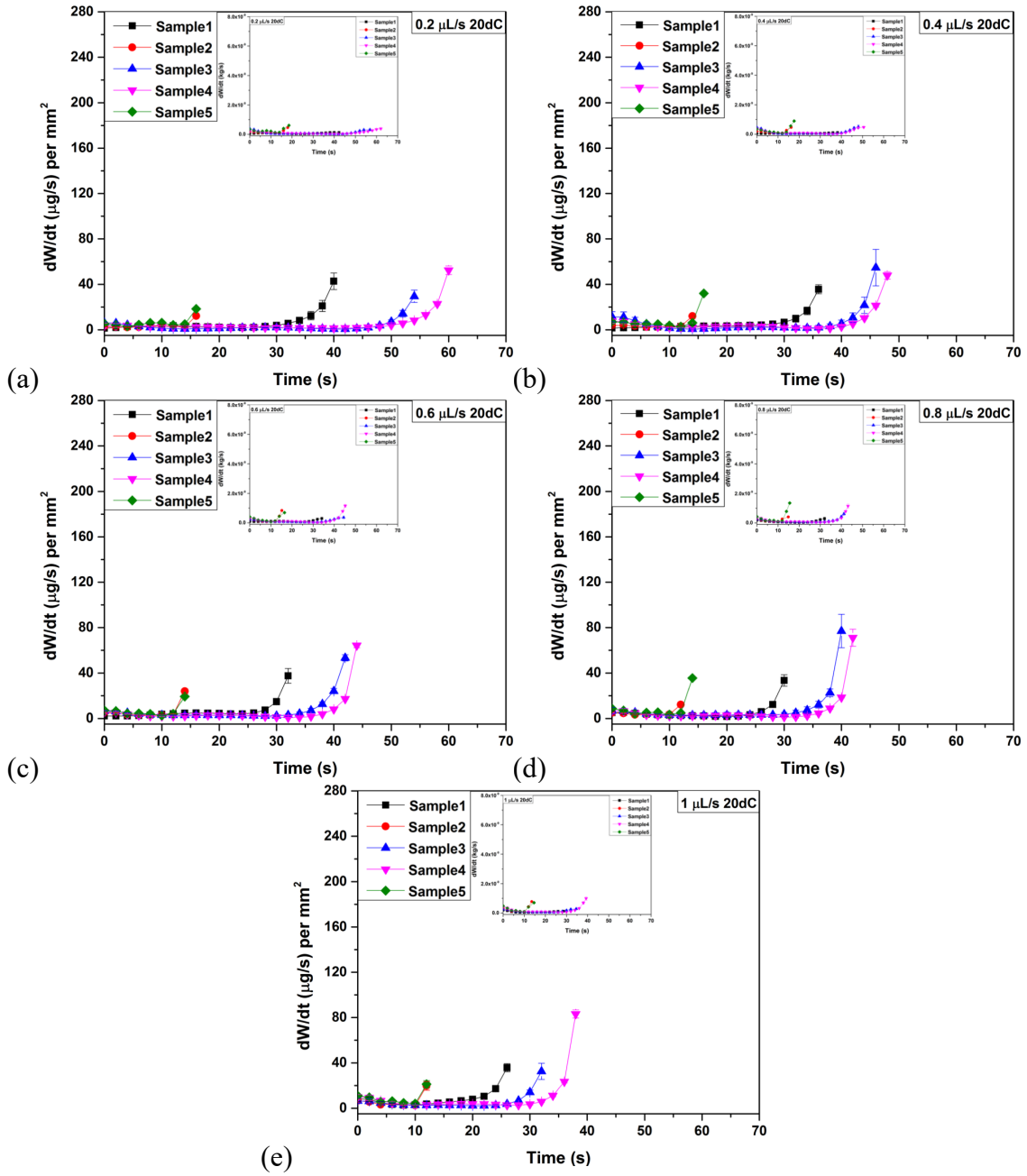

Figure 5-27 Dissolution rate dW/dt (µg/s) per mm^2 versus time (s) of particle size below 250 µm for (a) 0.2 µL/s, (b) 0.4 µL/s, (c) 0.6 µL/s, (d) 0.8 µL/s and (e) 1 µL/s at 20dC. The dissolution rate dW/dt (kg/s) versus time (s) is embedded in each graph.

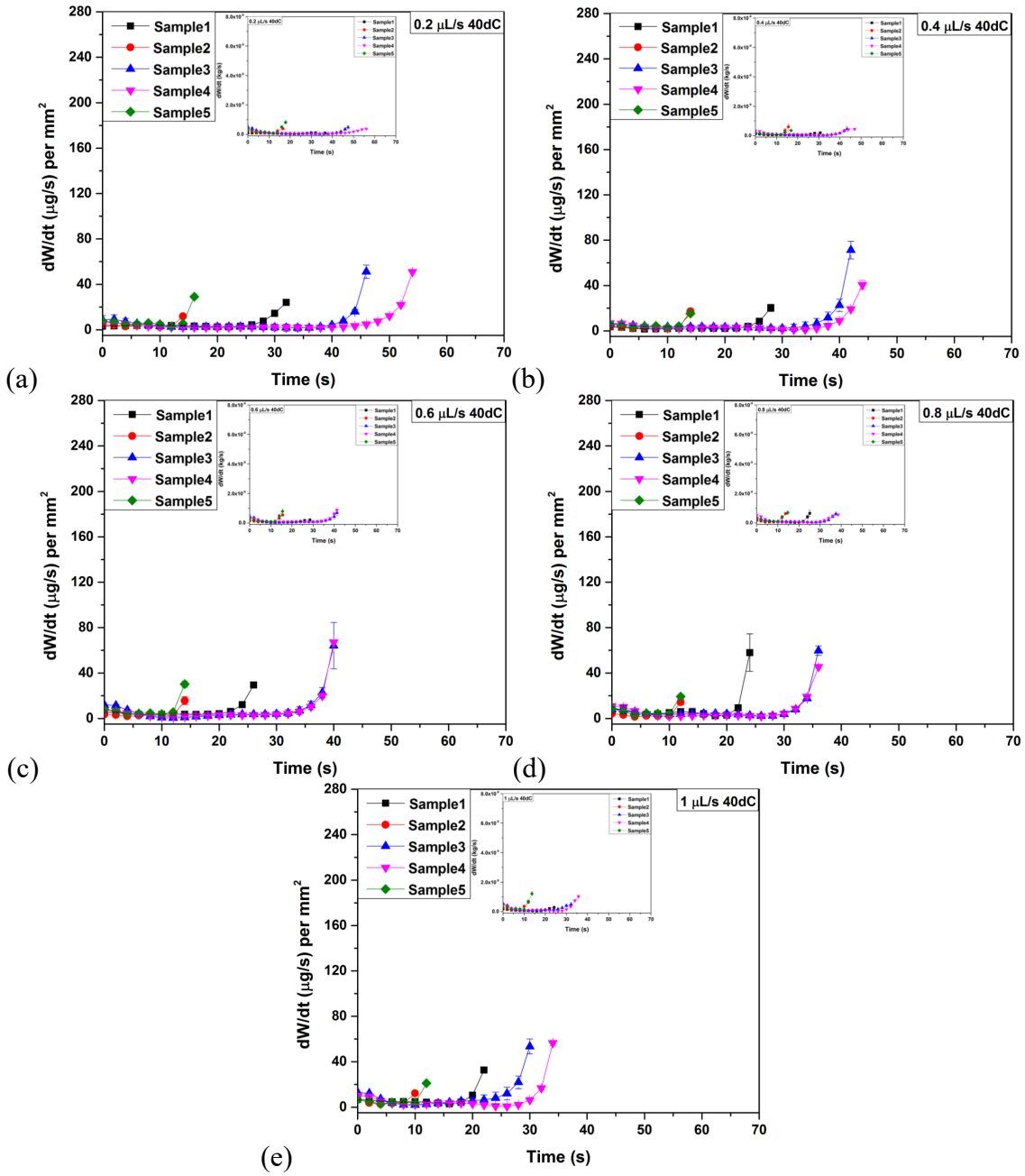

Figure 5-28 Dissolution rate dW/dt (µg/s) per mm^2 versus time (s) of particle size below 250 µm for (a) 0.2 µL/s, (b) 0.4 µL/s, (c) 0.6 µL/s, (d) 0.8 µL/s and (e) 1 µL/s at 40dC. The dissolution rate dW/dt (kg/s) versus time (s) is embedded in each graph.

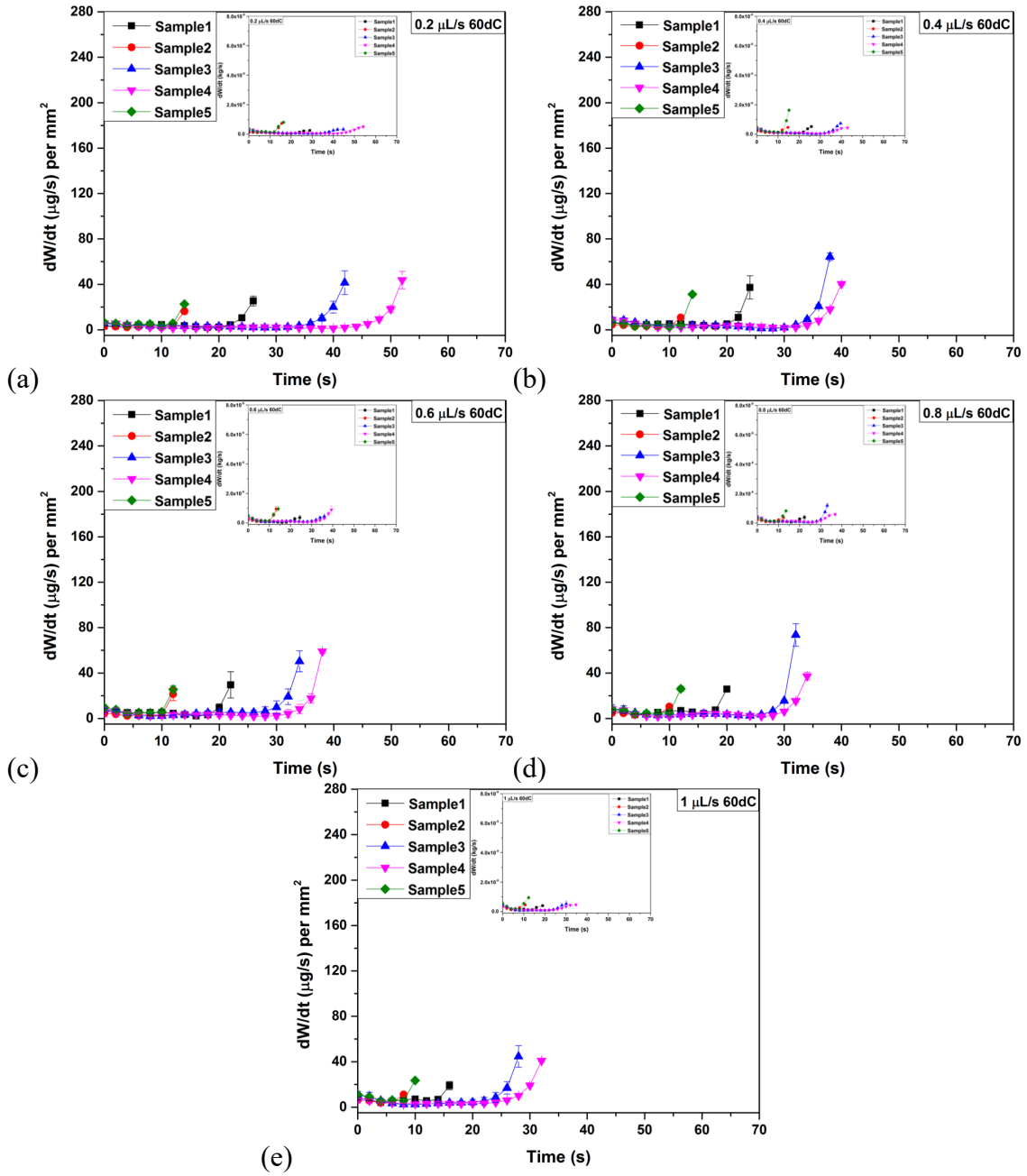

Figure 5-29 Dissolution rate dW/dt (µg/s) per mm^2 versus time (s) of particle size below 250 µm for (a) 0.2 µL/s, (b) 0.4 µL/s, (c) 0.6 µL/s, (d) 0.8 µL/s and (e) 1 µL/s at 60dC. The dissolution rate dW/dt (kg/s) versus time (s) is embedded in each graph.

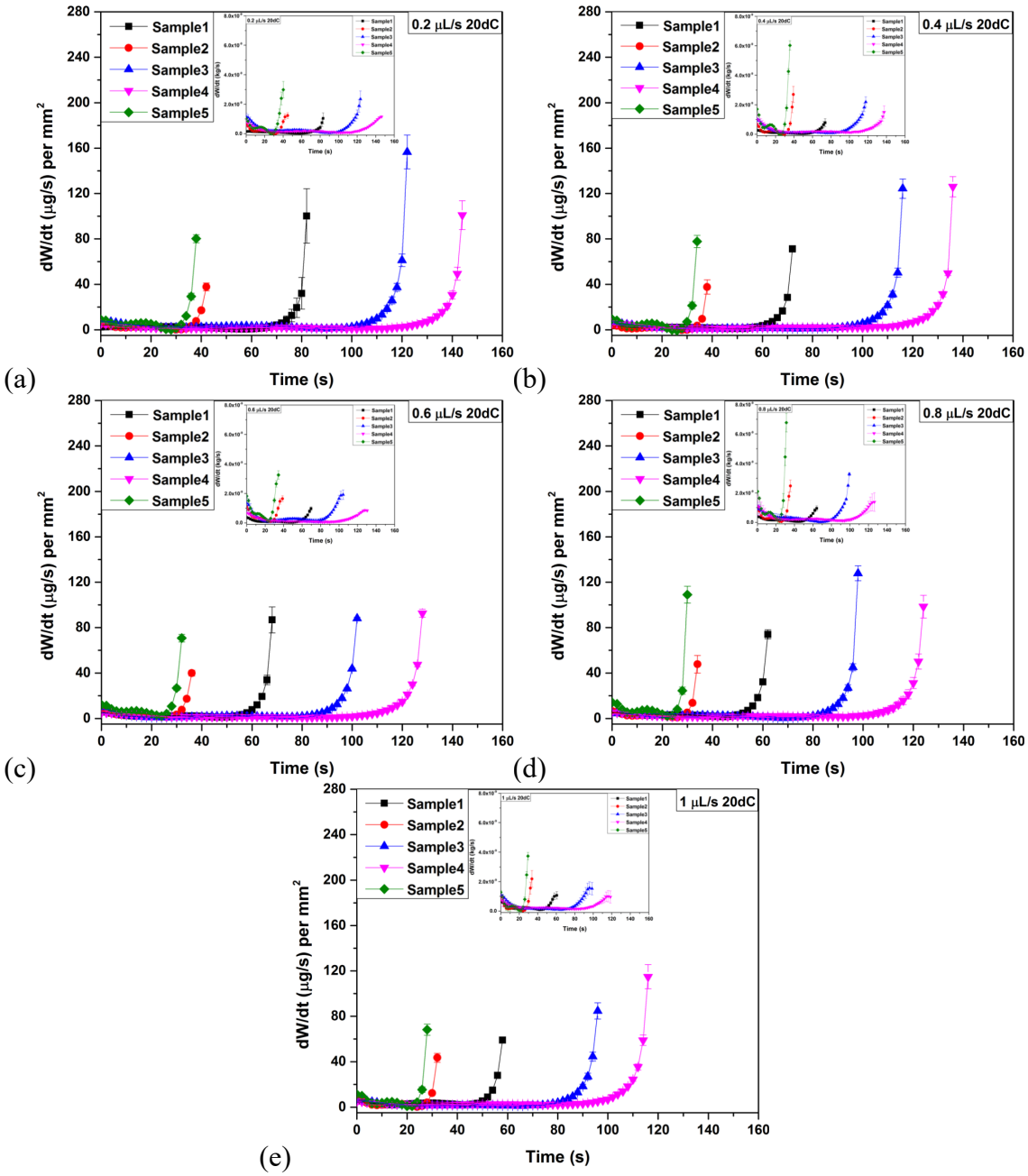

Figure 5-30 Dissolution rate dW/dt (µg/s) per mm^2 versus time (s) of particle size 250-500 µm for (a) 0.2 µL/s, (b) 0.4 µL/s, (c) 0.6 µL/s, (d) 0.8 µL/s and (e) 1 µL/s at 20dC. The dissolution rate dW/dt (kg/s) versus time (s) is embedded in each graph.

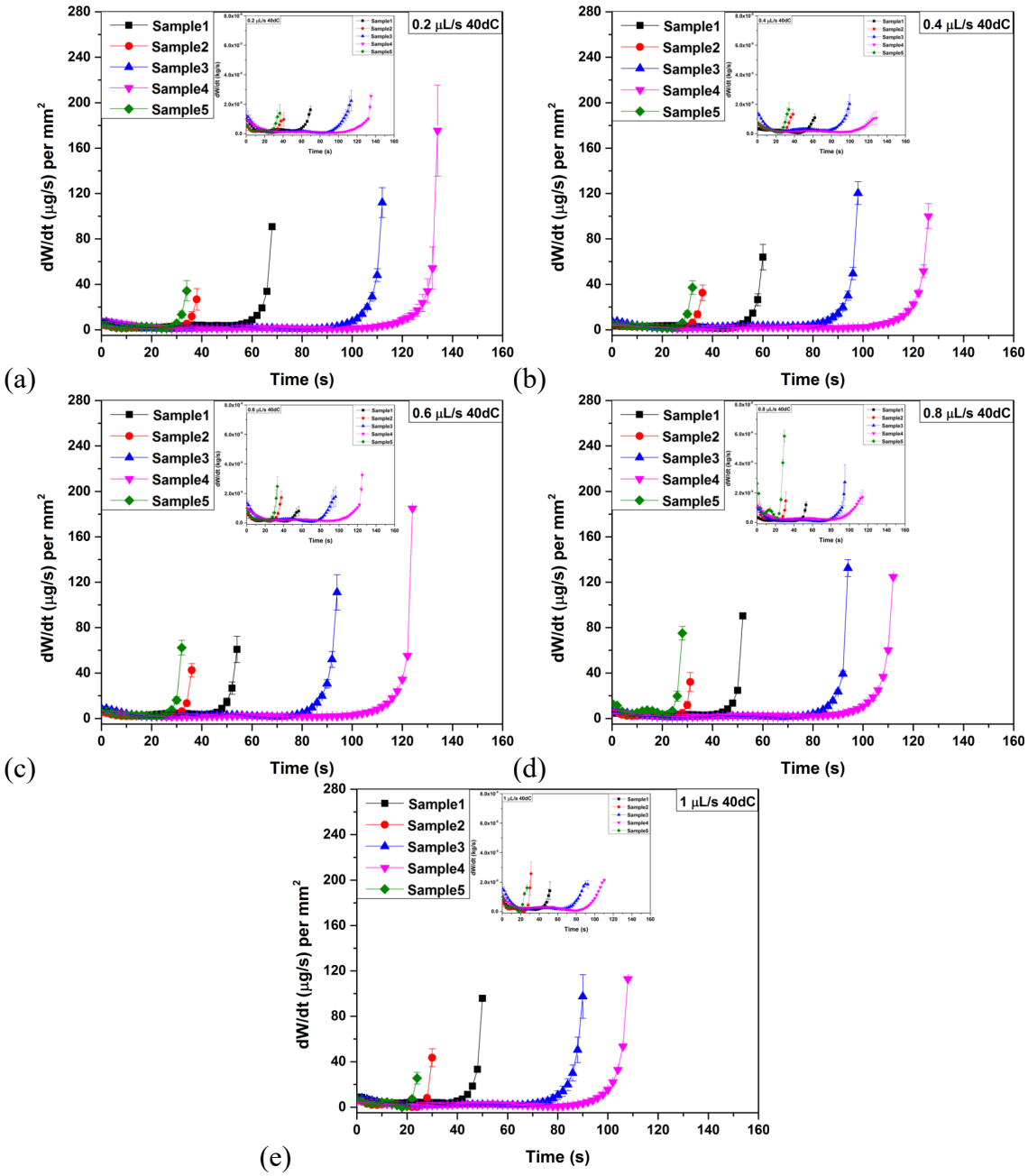

Figure 5-31 Dissolution rate dW/dt (µg/s) per mm^2 versus time (s) of particle size 250-500 µm for (a) 0.2 µL/s, (b) 0.4 µL/s, (c) 0.6 µL/s, (d) 0.8 µL/s and (e) 1 µL/s at 40dC. The dissolution rate dW/dt (kg/s) versus time (s) is embedded in each graph.

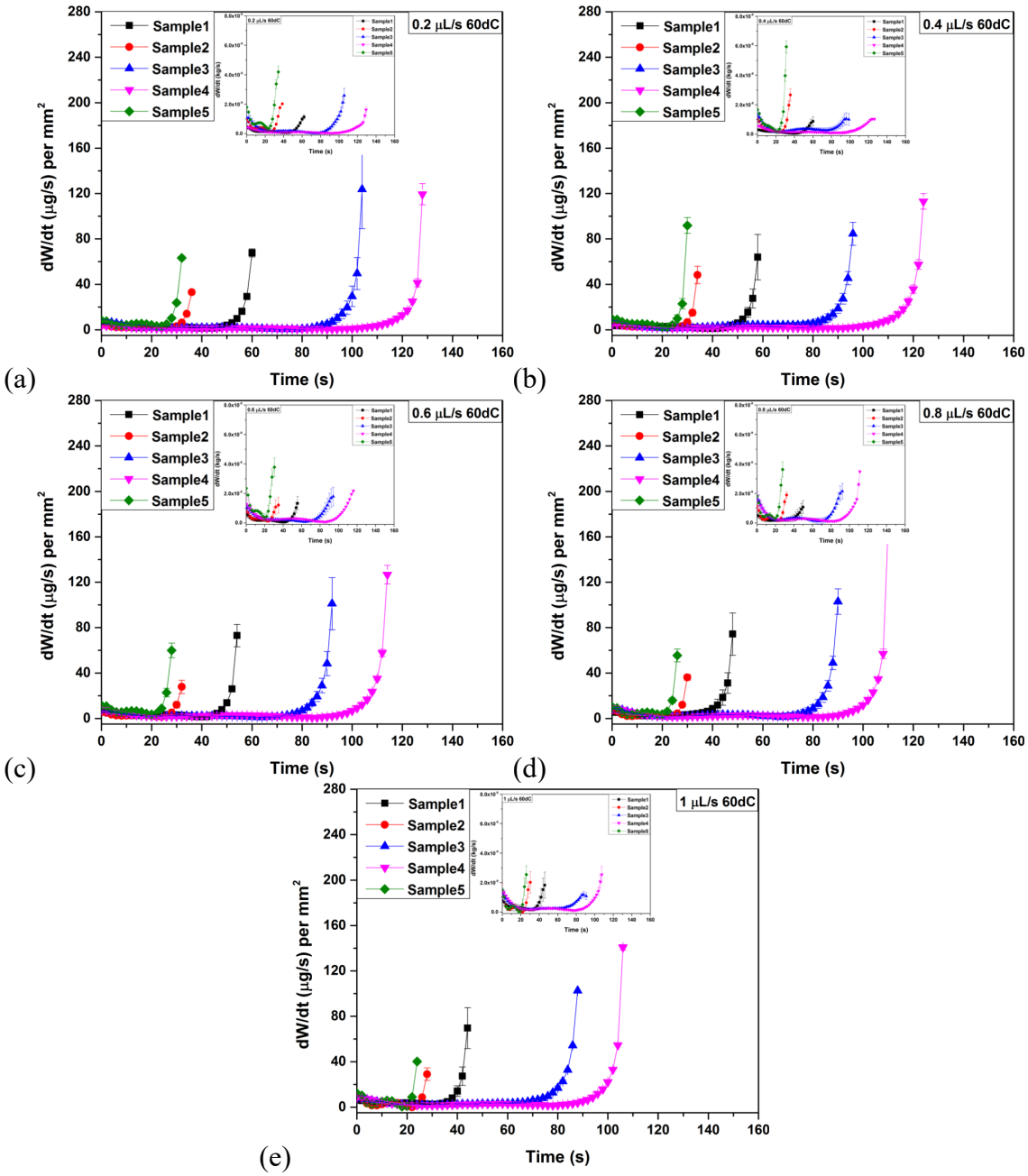

Figure 5-32 Dissolution rate dW/dt (µg/s) per mm^2 versus time (s) of particle size 250-500 µm for (a) 0.2 µL/s, (b) 0.4 µL/s, (c) 0.6 µL/s, (d) 0.8 µL/s and (e) 1 µL/s at 60dC. The dissolution rate dW/dt (kg/s) versus time (s) is embedded in each graph.

The second approach was evaluated using the Equation (2-26) and follows the theory developed by Nyström et al., [81] for the surface specific dissolution rate G. Figure 5-33-Figure 5-38 show the effect of fluid velocity and temperature on the surface specific dissolution rate G for particle size below 250 µm and 250-500 µm. Profiles of G exhibit

a different behavior than the ones observed from dW/dt per mm^2 results. G starts from high values and decreases rapidly, more than two times, with time during the shrinking stage where it reaches its lowest value. Then as dissolution process enters the disintegration period, G increases expeditiously. Sample5 exhibits the highest G across the two particle sizes and the different experimental conditions, as it is the fastest dissolving sample. However, results (order of magnitude) did not correlate well with the dW/dt per mm^2 profiles (see Figure 5-33-Figure 5-38). This is because an important assumption of this approach is that the particle shape does not change during the dissolution [22]. In our case, the particles of the powder samples are highly agglomerated and irregular shaped as SEM and XRT results revealed (see Sections 3.4.6 and 3.4.7). Therefore, the changes of the effective surface area occurred by the dissolution phenomena cannot be taken into account with this method. The main difference occurs between diffusion and convective G is that in convection the intrinsic dissolution rate is generally more than two times higher at each time interval. The same observation has been stated for the dW/dt per mm^2 results. The graphs cannot reveal any specific relationship between the G and the flow rate and temperature. However, G is affected on the particle size and the relevant particle exposed surface area.

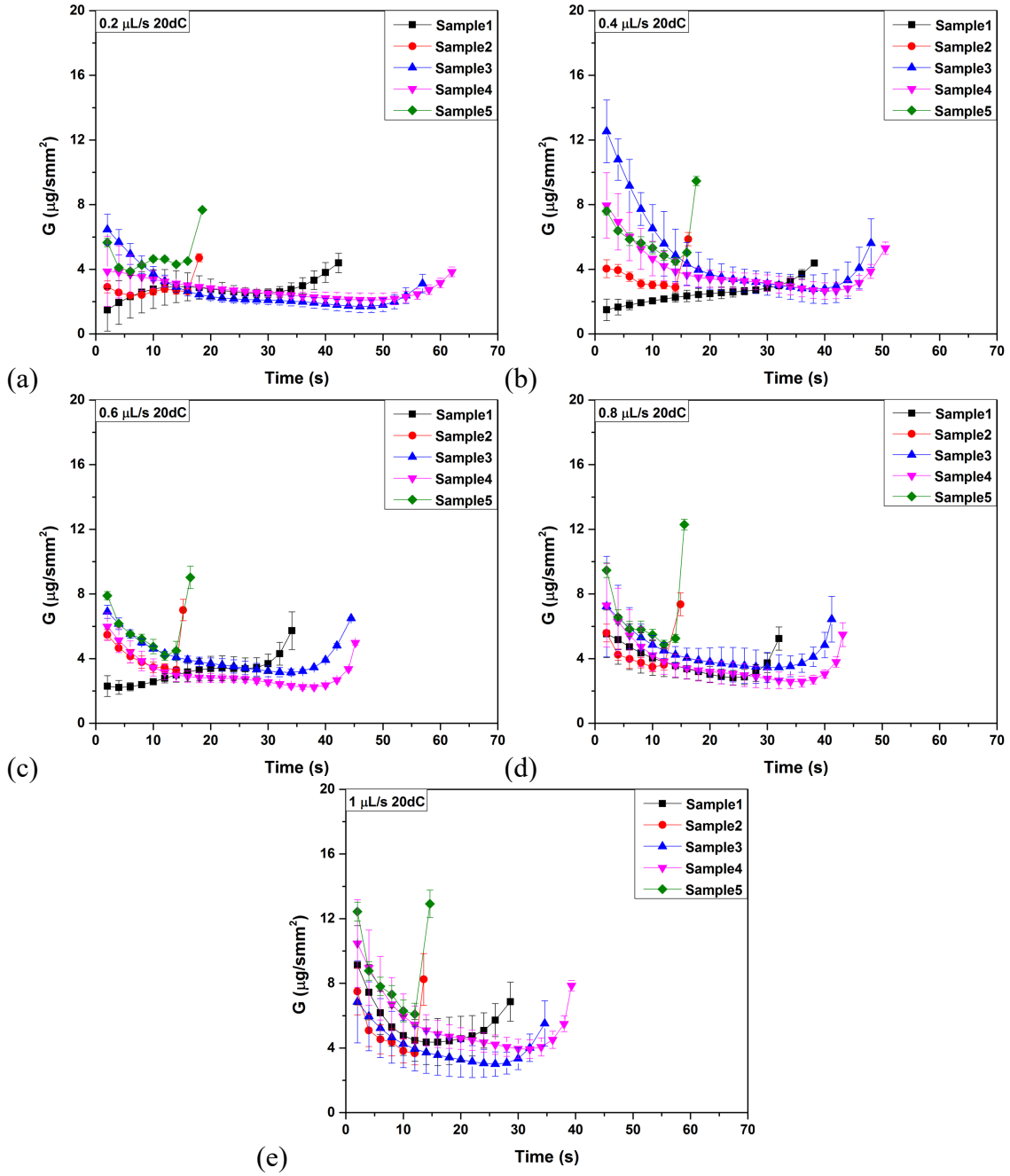

Figure 5-33 Surface specific dissolution rate *G* (µg/smm²) versus time (s) of particle size below 250 µm for (a) 0.2 µL/s, (b) 0.4 µL/s, (c) 0.6 µL/s, (d) 0.8 µL/s and (e) 1 µL/s at 20dC.

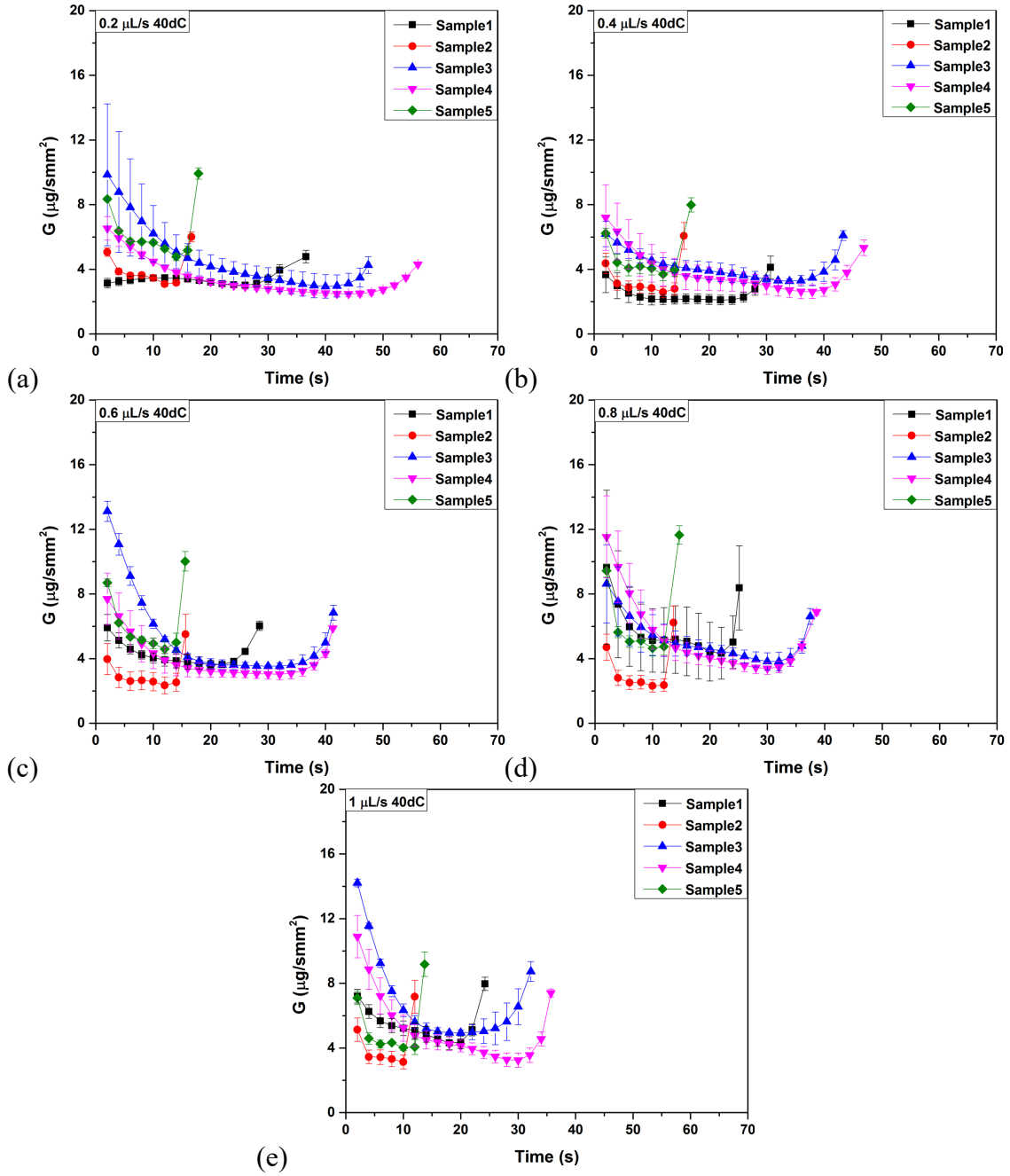

Figure 5-34 Surface specific dissolution rate *G* (µg/smm²) versus time (s) of particle size below 250 µm for (a) 0.2 µL/s, (b) 0.4 µL/s, (c) 0.6 µL/s, (d) 0.8 µL/s and (e) 1 µL/s at 40dC.

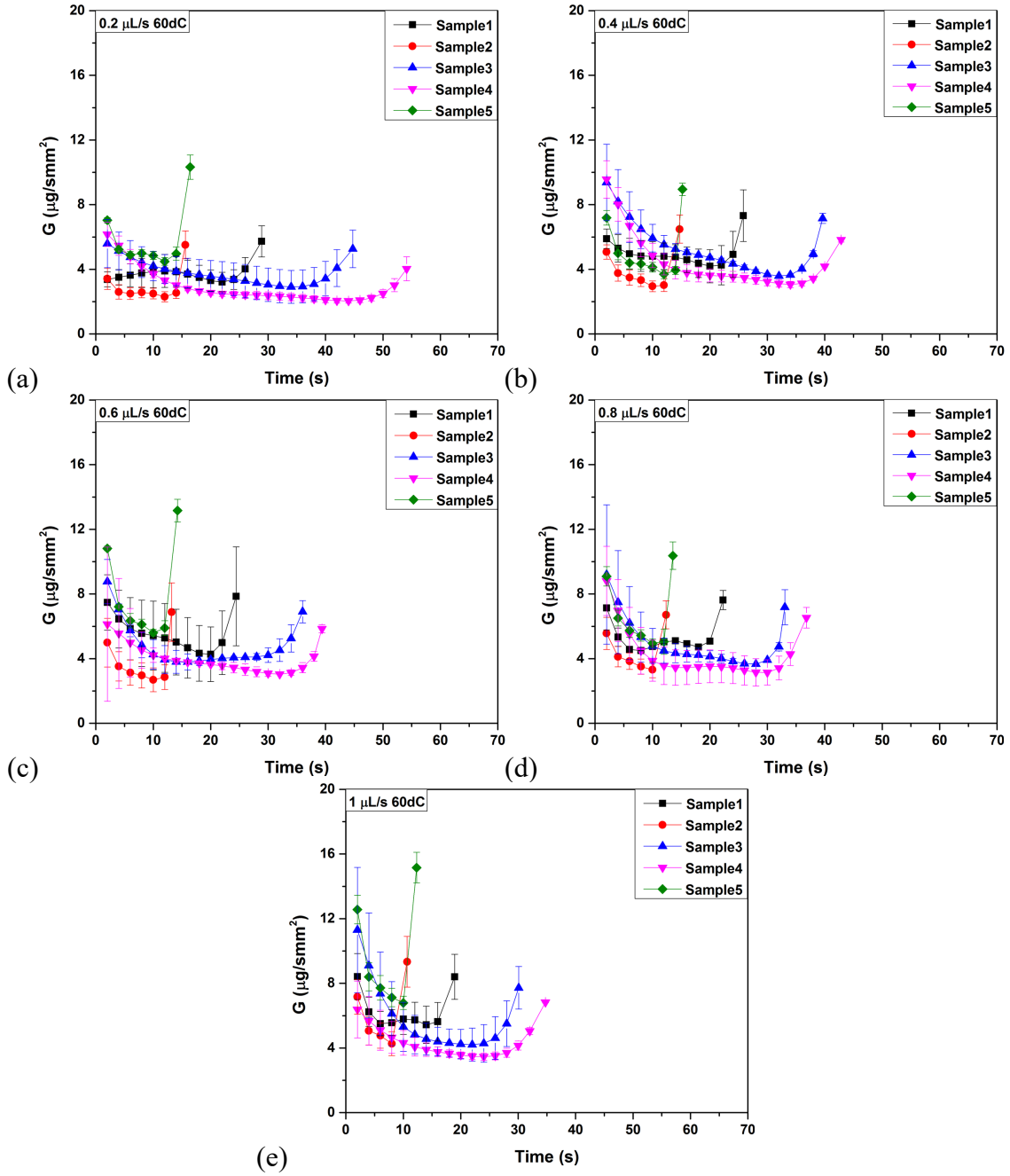

Figure 5-35 Surface specific dissolution rate *G* (µg/smm²) versus time (s) of particle size below 250 µm for (a) 0.2 µL/s, (b) 0.4 µL/s, (c) 0.6 µL/s, (d) 0.8 µL/s and (e) 1 µL/s at 60dC.

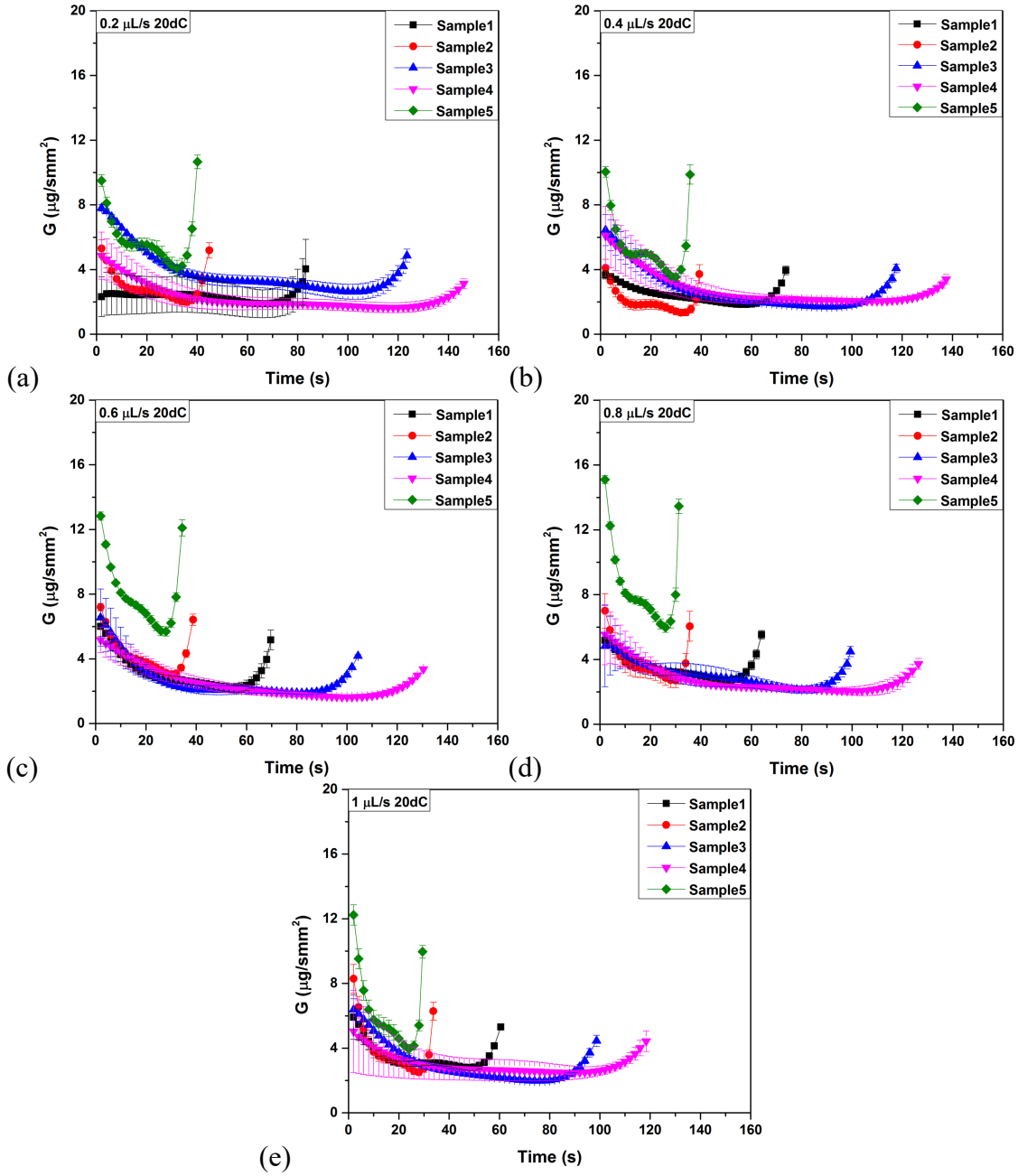

Figure 5-36 Surface specific dissolution rate *G* (µg/smm²) versus time (s) of particle size 250-500 µm for (a) 0.2 µL/s, (b) 0.4 µL/s, (c) 0.6 µL/s, (d) 0.8 µL/s and (e) 1 µL/s at 20dC.

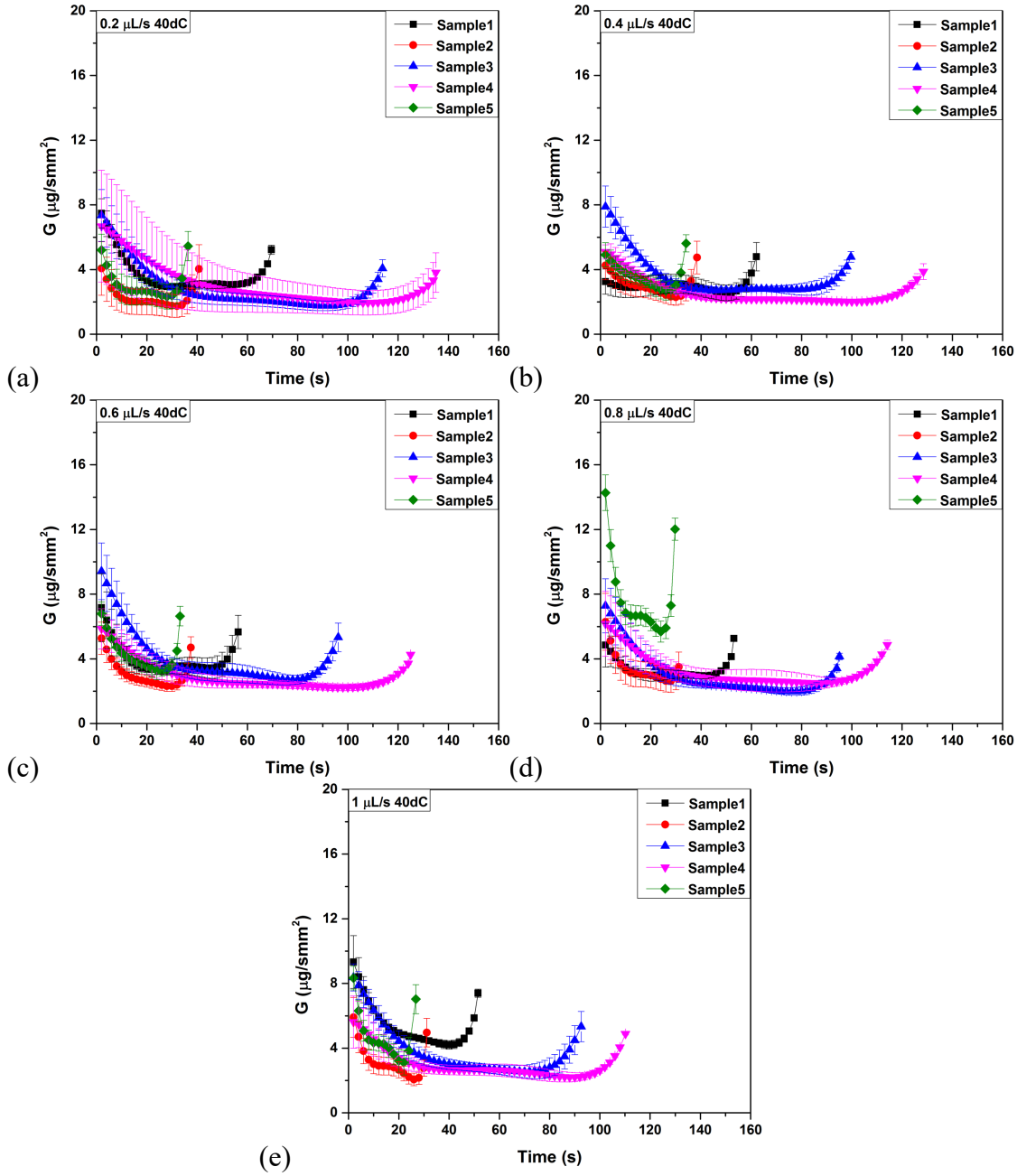

Figure 5-37 Surface specific dissolution rate *G* (µg/smm²) versus time (s) of particle size 250-500 µm for (a) 0.2 µL/s, (b) 0.4 µL/s, (c) 0.6 µL/s, (d) 0.8 µL/s and (e) 1 µL/s at 40dC.

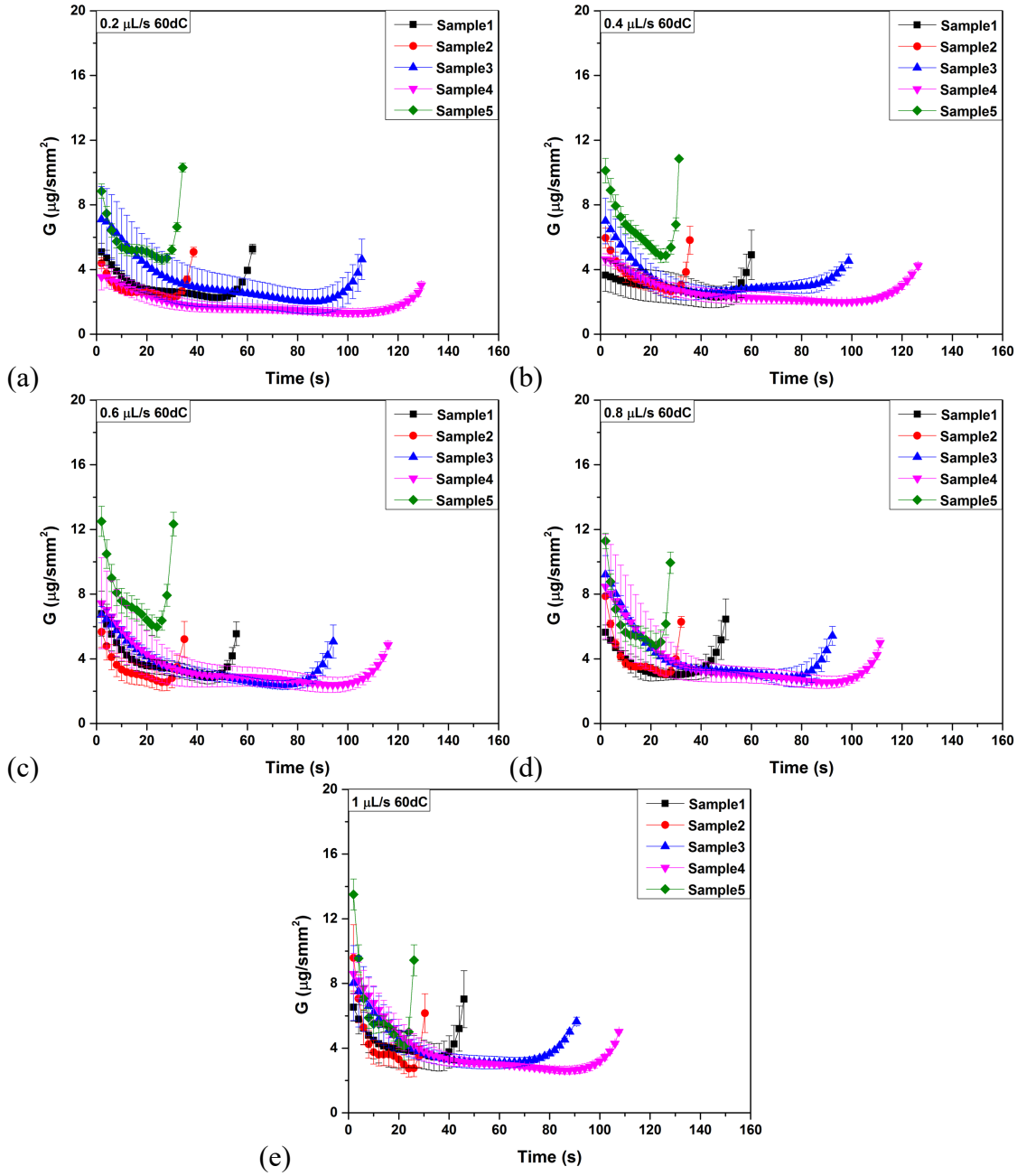

Figure 5-38 Surface specific dissolution rate *G* (µg/smm²) versus time (s) of particle size 250-500 µm for (a) 0.2 µL/s, (b) 0.4 µL/s, (c) 0.6 µL/s, (d) 0.8 µL/s and (e) 1 µL/s at 60dC.

5.3.7 Effect of flow rate and temperature on dissolution rate constant *k*

The dissolution rate constant *k* for the different experimental conditions was obtained using Equation (4-3).

Figure 5-39, Figure 5-40 and Figure 5-41 presents the dissolution rate constant k changes as a function of time for particles below 250 μm at 20dC, 40dC and 60dC respectively. For particle size 250-500 μm the results presented in Figure 5-42, Figure 5-43, Figure 5-44 accordingly. Order of magnitude of k (10^{-6} to 10^{-3}) in convective dissolution for all samples correlates well with k from diffusion dissolution experiments (see Figure 4-10) and literature results [182]. It can be noticed that across the two different size cuts of powder samples and the different experimental conditions, the value of k follow the same trend as dW/dt per mm^2 where it progresses very slowly for the longest part of dissolution process and when it reaches the disintegration stage increases rapidly. At this stage, the range of increasement of k is more than two orders. This is something that has been detected in single particle diffusion dissolution as well (see Figure 4-10). Samples that contain Silicate binder, Sample3 and 4 show the highest values of k for all the particle sizes as their dissolution process is the slowest (see Figure 5-21-Figure 5-26). The variation of k especially at the final moments of dissolution is due to the differences in dissolution behaviour between particles of the same batch. The profiles of k cannot present any relative trend between k and the velocity of fluid as it does not depend on it. However, results show that k decreases as temperature rises due to the changes in solubility. Furthermore, as we have seen in diffusion (see Figure 4-10) the dissolution rate constant increases with the particle size as a result of the increasement of the dW/dt per mm^2 which is proportional.

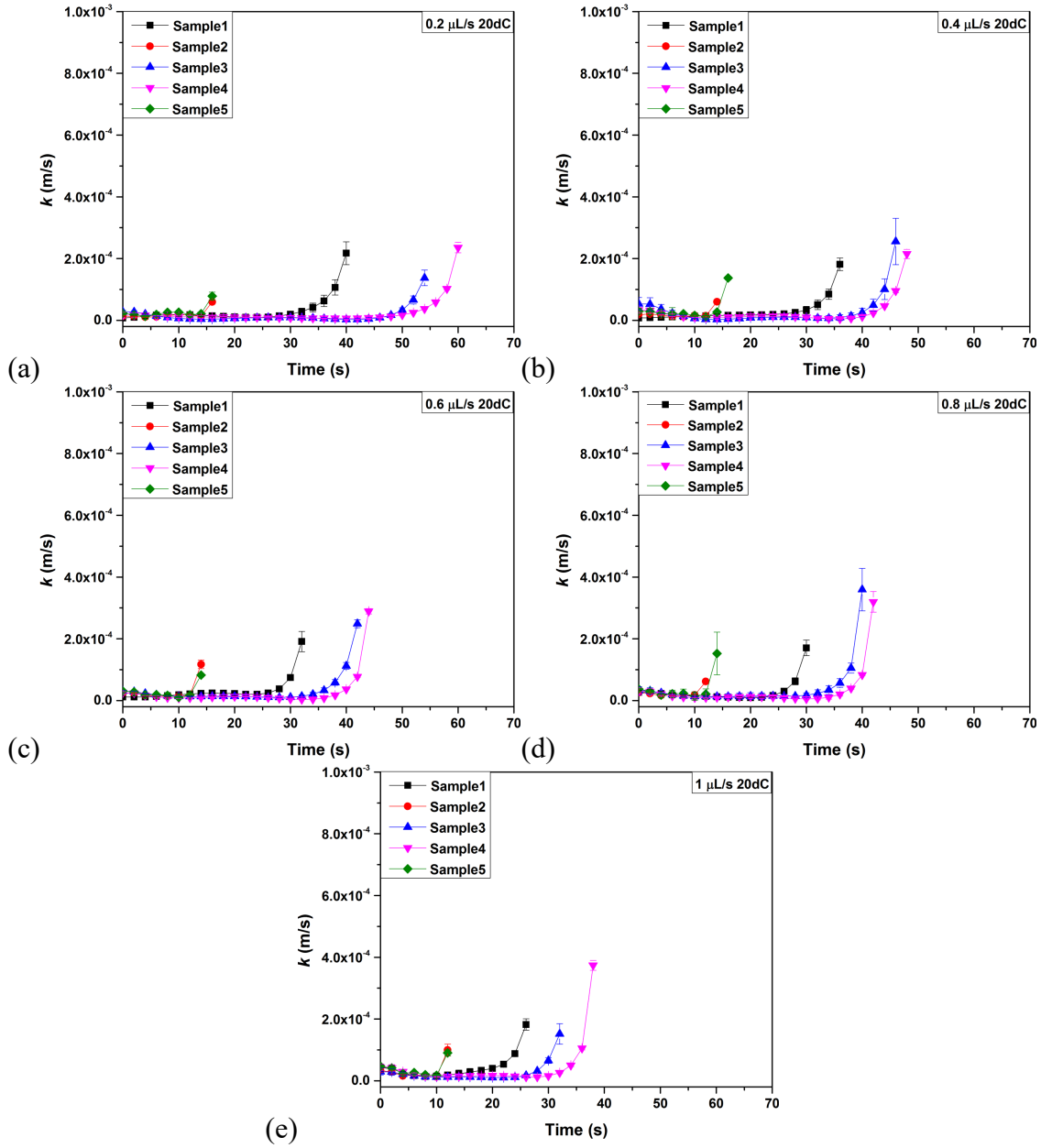

Figure 5-39 Dissolution rate constant *k* (m/s) versus time (s) of particle size below 250 µm for (a) 0.2 µL/s, (b) 0.4 µL/s, (c) 0.6 µL/s, (d) 0.8 µL/s and (e) 1 µL/s at 20dC.

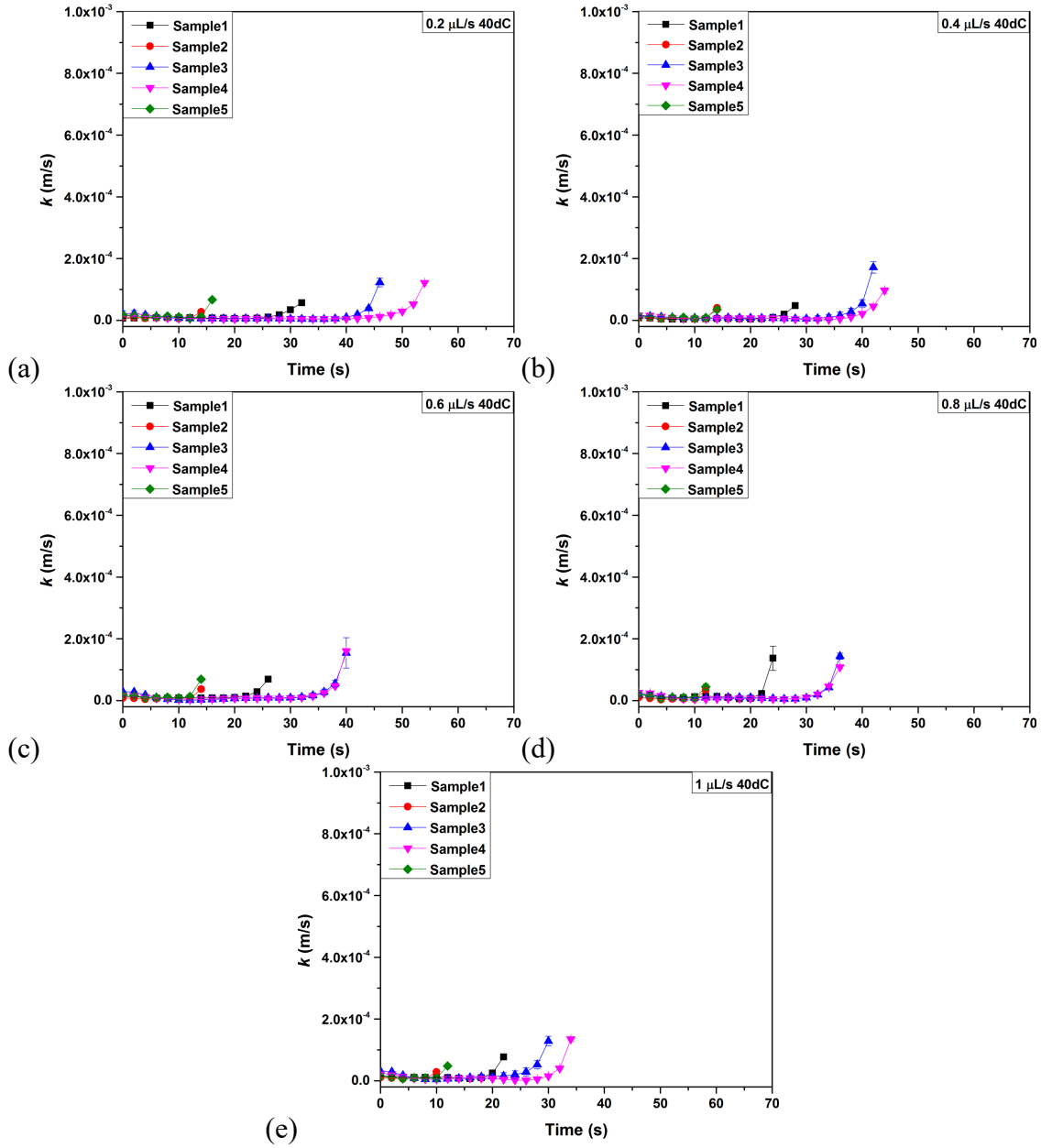

Figure 5-40 Dissolution rate constant *k* (m/s) versus time (s) of particle size below 250 µm for (a) 0.2 µL/s, (b) 0.4 µL/s, (c) 0.6 µL/s, (d) 0.8 µL/s and (e) 1 µL/s at 40dC.

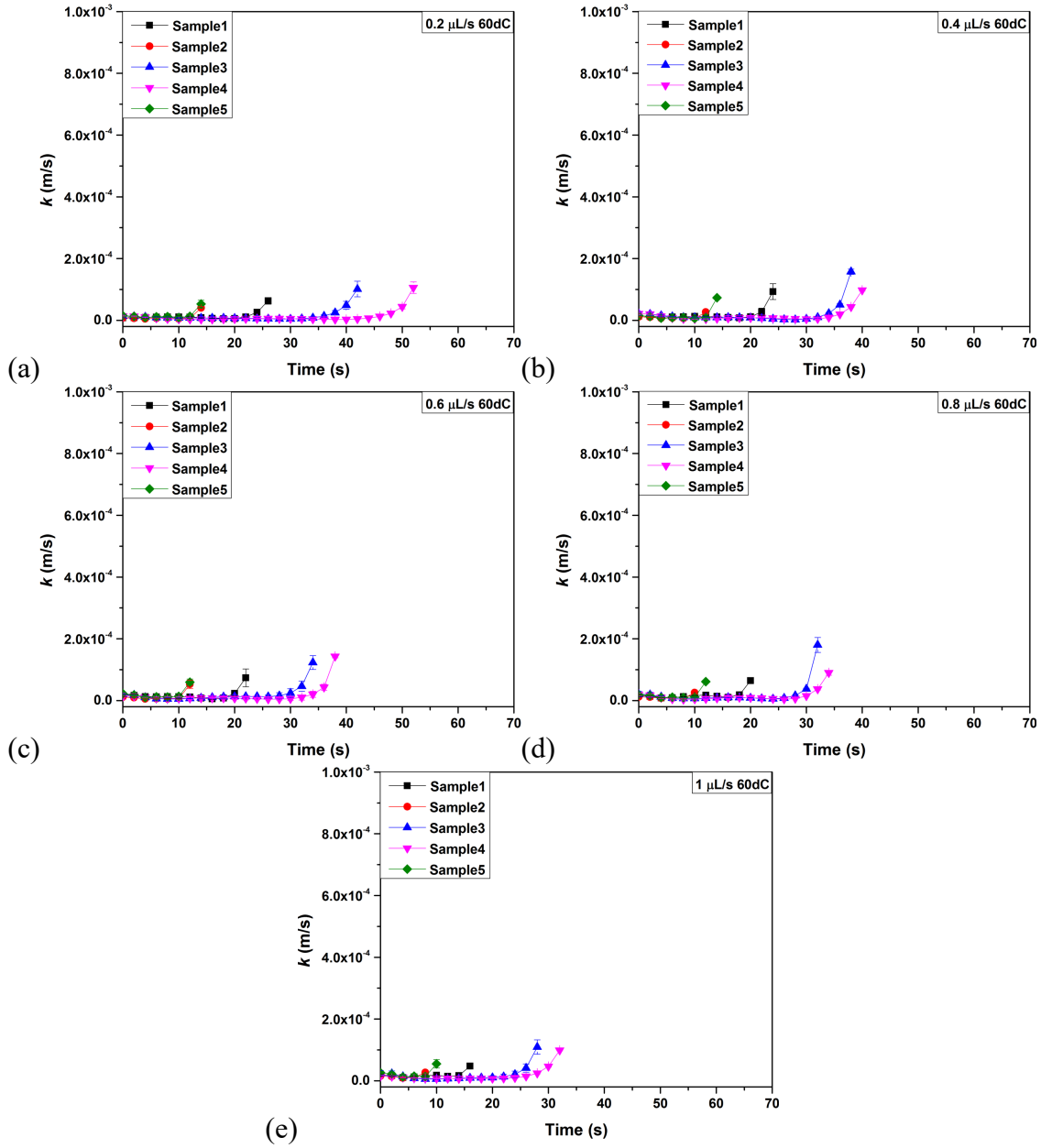

Figure 5-41 Dissolution rate constant *k* (m/s) versus time (s) of particle size below 250 µm for (a) 0.2 µL/s, (b) 0.4 µL/s, (c) 0.6 µL/s, (d) 0.8 µL/s and (e) 1 µL/s at 60dC.

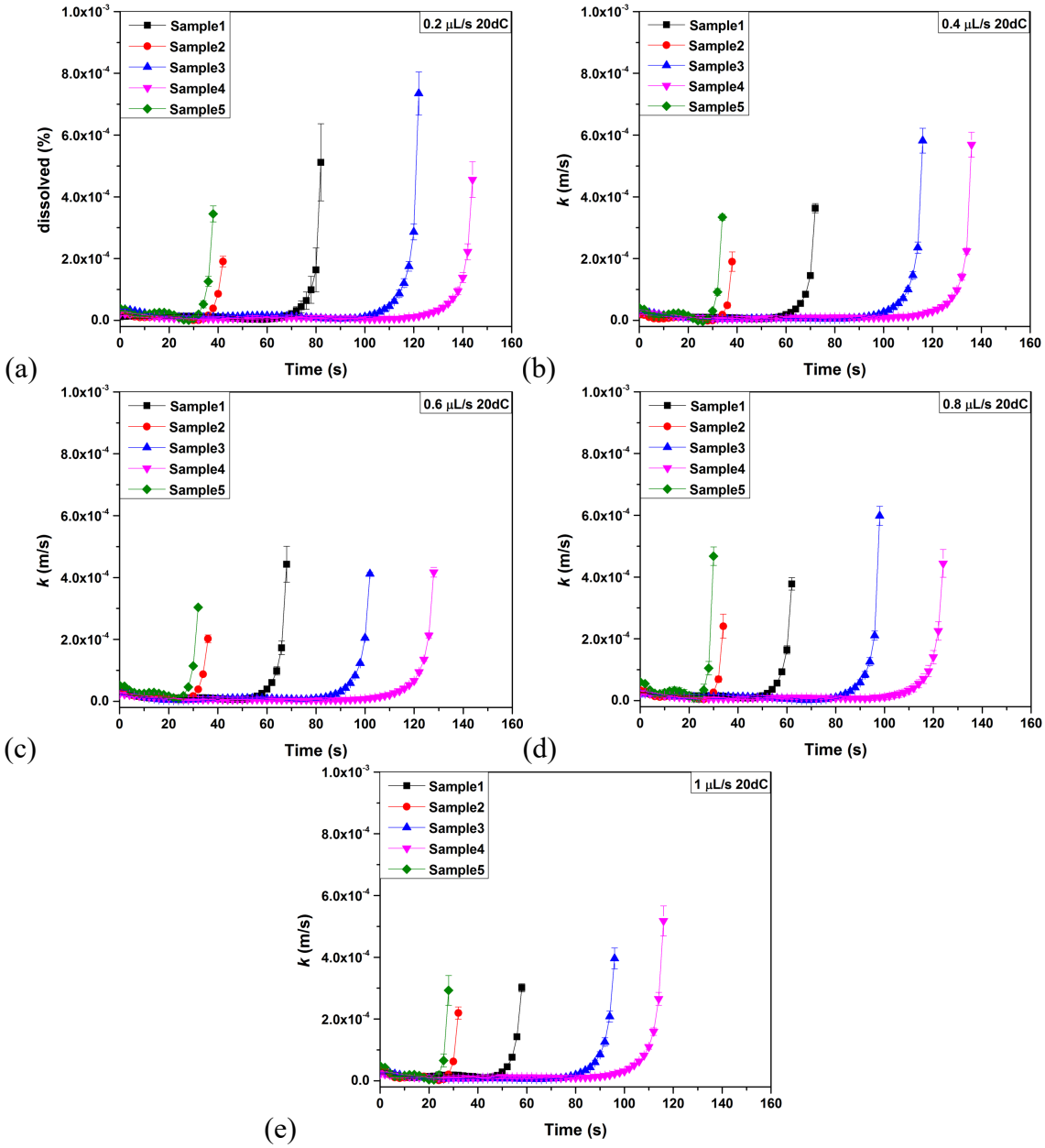

Figure 5-42 Dissolution rate constant *k* (m/s) versus time (s) of particle size 250-500 µm for (a) 0.2 µL/s, (b) 0.4 µL/s, (c) 0.6 µL/s, (d) 0.8 µL/s and (e) 1 µL/s at 20dC.

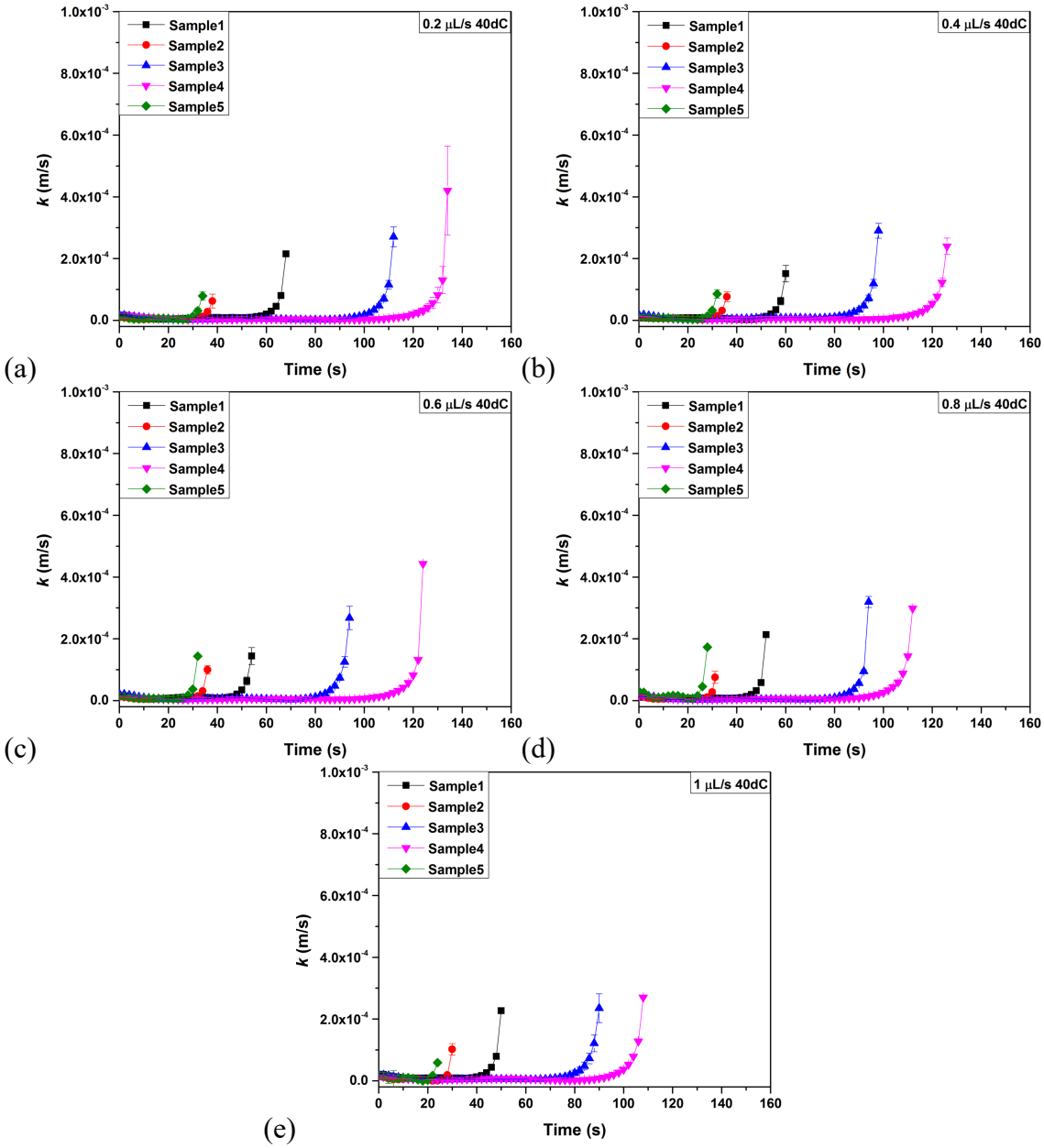

Figure 5-43 Dissolution rate constant *k* (m/s) versus time (s) of particle size 250-500 µm for (a) 0.2 µL/s, (b) 0.4 µL/s, (c) 0.6 µL/s, (d) 0.8 µL/s and (e) 1 µL/s at 40dC.

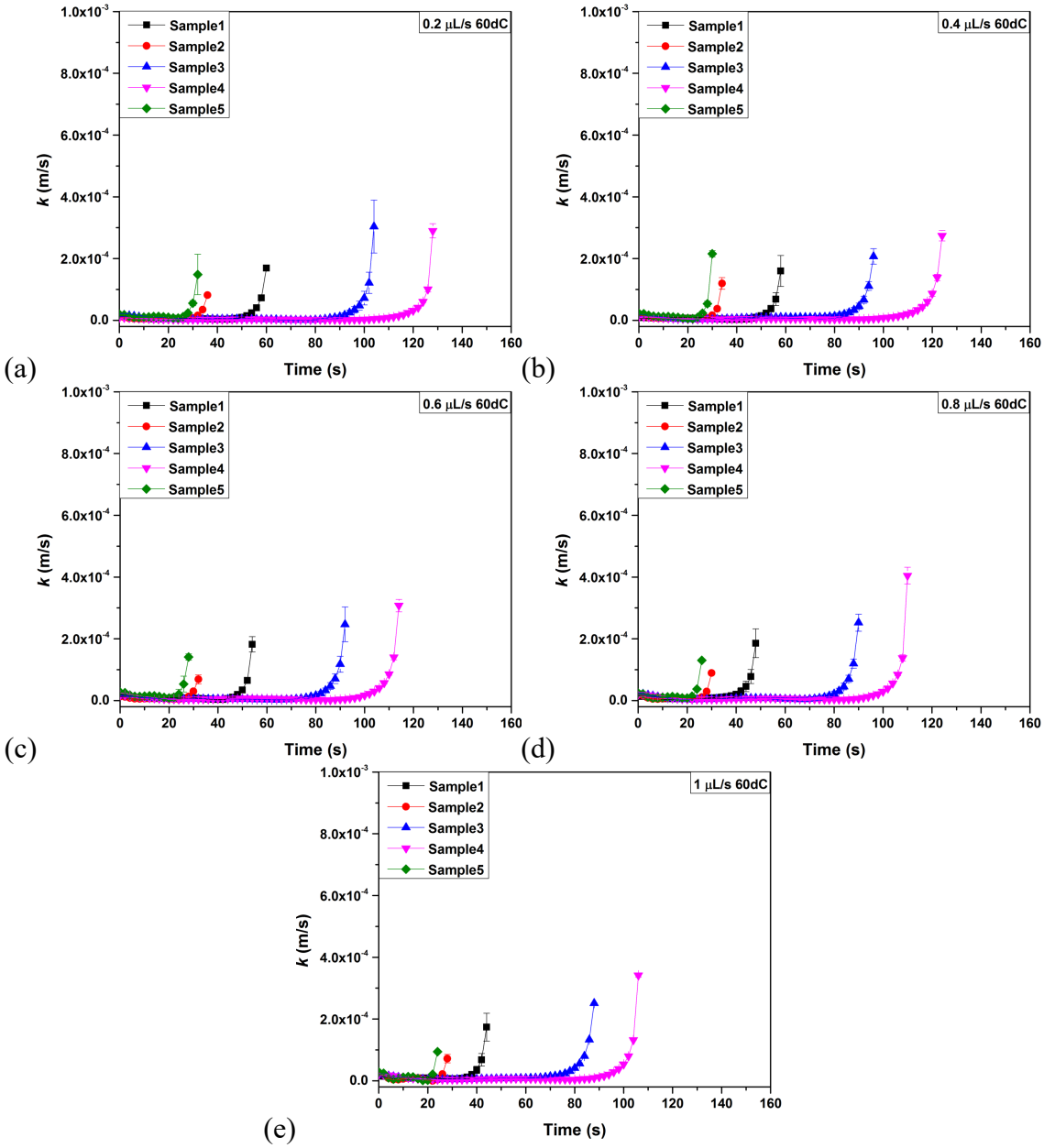

Figure 5-44 Dissolution rate constant *k* (m/s) versus time (s) of particle size 250-500 µm for (a) 0.2 µL/s, (b) 0.4 µL/s, (c) 0.6 µL/s, (d) 0.8 µL/s and (e) 1 µL/s at 60dC.

5.3.8 Derivation of single particle dissolution equation

Dissolution of particles is of critical importance on detergent washing powder performance. So far most of the particle dissolution models use average particle diameters and do not take into account the effect of particle velocity in the evaluation of mass transfer coefficient. In this section, a new model which combines Noyes-Whitney dissolution equation and experimentally calculated particle velocity is proposed. Single

particle dissolution profiles are predicted and compared with single particle convective dissolution experimental results.

As investigated in Chapter 2, when external mass transfer constraint at the granule surface boundary layer dominates the granule dissolution rate, then it can be calculated by Noyes-Whitney equation:

$$\frac{dW}{dt} = -KA(C_s - C_t) \tag{5-11}$$

where W is the remaining mass of the particles, K is the dissolution rate constant (m/s), C_t is the concentration of solution at time t, and C_s is the concentration when it is saturated.

In convective dissolution, a dimensionless number is initiated to symbolise the ratio of convective to diffusive mass transfer, called Sherwood number (Sh). It is described as

$$Sh = \frac{KL}{D} \tag{5-12}$$

The dissolution rate constant for a spherical granule can be written as

$$K = \frac{ShD}{d_p} \tag{5-13}$$

Considering that the granules are homogeneous, then the particle density ρ_p is constant. For a number of granules $N_{particles}$, their total initial weight W_0 is

$$W_0 = N_{particles}\rho_p \frac{1}{6}\pi {d_p}^3 \tag{5-14}$$

where d_p is the initial particle diameter. So $N_{particles}$ can be defined as

$$N_{particles} = \frac{6W_0}{\rho_p \pi {d_p}^3} \tag{5-15}$$

So W_t can be defined as

$$W_t = N_{particles}\rho_p \frac{1}{6}\pi {d_p}^3 = \left(\frac{6W_0}{\rho_p \pi {d_p}^3}\right)\rho_p \frac{1}{6}\pi {d_p}^3 = W_0\left(\frac{d_{p,t}}{d_p}\right)^3 \quad (5\text{-}16)$$

Therefore, $d_{p,t} = d_p\left(\frac{W_t}{W_0}\right)^{1/3}$

Consequently, the surface area of the granules $A_{particles}$ can be expressed as

$$A_{particles} = N_{particles}\pi {d_{p,t}}^2 = N_{particles}\pi {d_p}^2\left(\frac{W_t}{W_0}\right)^{2/3} = A_0\left(\frac{W_t}{W_0}\right)^{2/3} \quad (5\text{-}17)$$

where A_0 is the initial surface area of the granule.

Substituting Equation (5-11) with Equation (5-12) and Equation (5-17), and considering that $C_s \gg C_t$, Sherwood number can be implemented in Noyes-Whitney equation as

$$\frac{dW}{dt} = -\frac{ShD}{d_{p,t}}AC_s = -\frac{ShD}{d_p}A_0 C_s\left(\frac{W_t}{W_0}\right)^{1/3} \quad (5\text{-}18)$$

Considering that the Sh is a constant, by integrating Equation (5-18), mass transfer of spherical granules can be defined as

$$W_t^{2/3} = W_0^{2/3} - \frac{2}{3}\frac{ShD}{d_p}\frac{A_0 C_s}{W_0^{1/3}}t \quad (5\text{-}19)$$

During the years, a lot of different definitions of Sh for a spherical granule have been developed. The Sherwood number for a spherical particle moving into a creeping flow can be estimated by [196]

$$Sh = 2 + 0.6Re_p^{1/2}Sc^{1/3} \quad (5\text{-}20)$$

where $0 \leq Re_p < 200$ and $0 \leq Sc < 250$

Schmidt number is given by

$$Sc = \frac{\mu_{water}}{\rho_{water}D} \quad (5\text{-}21)$$

Substituting Equation (5-20) with Equation (5-21) and Equation (5-8) the Sherwood number can be expressed as

$$Sh = 2 + 0.6\left(\frac{\rho_{water} u_p d_p}{\mu_{water}}\right)^{1/2}\left(\frac{\mu_{water}}{\rho_{water} D}\right)^{1/3} \quad (5\text{-}22)$$

where u_p is the average velocity of the particle.

The velocity of the particle u_p was calculated from the convective dissolution experiments by measuring the distance that each granule covered Δx_i between two time intervals Δt_i

$$u_p = \frac{\sum_{i=1}^{n}\left(\frac{\Delta x_i}{\Delta t_i}\right)}{n_i} \quad (5\text{-}23)$$

where n_i is the total number of time intervals.

For flow rate Q from 0.2 µL/s to 1 µL/s, temperatures 20dC, 40dC and 60dC and size fraction below 250 µm and 250 to 500 µm the average values of particle velocity u_p for Sample1, 2, 3, 4 and 5 are presented in Table 5.1, Table 5.2, Table 5.3, Table 5.4 and Table 5.5 respectively. Results does not show a significant difference on u_p between the powder samples and experimental conditions.

Table 5.1 Average velocity of the particle u_p of for each flow rate, temperature and size fraction of Sample1.

Q (µL/s)	Velocity of the particle u_p (10^{-4} m/s)					
	20dC		40dC		60dC	
	< 250 µm	250-500 µm	< 250 µm	250-500 µm	< 250 µm	250-500 µm
0.2	1.93±0.13	1.93±0.14	1.93±0.12	1.90±.019	1.91±0.14	1.90±0.17
0.4	3.92±0.12	3.93±0.15	3.92±0.12	3.90±0.18	3.90±0.15	3.91±0.17
0.6	5.91±0.14	5.92±0.15	5.92±0.12	5.91±0.17	5.91±0.13	5.91±0.17
0.8	7.92±0.12	7.91±0.17	7.91±0.13	7.91±0.16	7.90±0.14	7.89±0.18
1	9.92±0.11	9.90±0.19	9.91±0.13	9.90±0.18	9.88±0.16	9.87±0.21

Table 5.2 Average velocity of the particle u_p of for each flow rate, temperature and size fraction of Sample2.

Q (µL/s)	Velocity of the particle u_p (10^{-4} m/s)					
	20dC		40dC		60dC	
	< 250 µm	250-500 µm	< 250 µm	250-500 µm	< 250 µm	250-500 µm
0.2	1.87±0.17	1.87±0.22	1.87±0.16	1.87±0.20	1.85±0.17	1.83±0.27
0.4	3.86±0.17	3.86±0.21	3.87±0.16	3.85±0.23	3.85±0.17	3.84±0.25
0.6	5.87±0.16	5.84±0.25	5.87±0.15	5.86±0.22	5.85±0.16	5.85±0.23
0.8	7.85±0.17	7.85±0.23	7.86±0.15	7.84±0.24	7.86±0.15	7.84±0.24
1	9.86±0.16	9.85±0.22	9.84±0.17	9.86±0.20	9.84±0.17	9.84±0.23

Table 5.3 Average velocity of the particle u_p of for each flow rate, temperature and size fraction of Sample3.

Q (µL/s)	Velocity of the particle u_p (10^{-4} m/s)					
	20dC		40dC		60dC	
	< 250 µm	250-500 µm	< 250 µm	250-500 µm	< 250 µm	250-500 µm
0.2	1.94±0.11	1.93±0.17	1.94±0.11	1.93±0.16	1.93±0.12	1.92±0.17
0.4	3.94±0.11	3.93±0.16	3.94±0.11	3.92±0.18.	3.92±0.13	3.92±0.18
0.6	5.93±0.12	5.92±0.18	5.93±0.11	5.92±0.17	5.92±0.13	5.92±0.18
0.8	7.93±0.12	7.92±0.18	7.93±0.12	7.93±0.15	7.92±0.13	7.91±0.19
1	9.93±0.11	9.92±0.18	9.91±0.13	9.91±0.19	9.91±0.13	9.91±0.18

Table 5.4 Average velocity of the particle u_p of for each flow rate, temperature and size fraction of Sample4.

Q (µL/s)	Velocity of the particle u_p (10^{-4} m/s)					
	20dC		40dC		60dC	
	< 250 µm	250-500 µm	< 250 µm	250-500 µm	< 250 µm	250-500 µm
0.2	1.94±0.11	1.94±0.14	1.94±0.11	1.94±0.15	1.94±0.11	1.95±0.13
0.4	3.93±0.12	3.94±0.15	3.93±0.12	3.94±0.15	3.93±0.12	3.94±0.15
0.6	5.93±0.12	5.94±0.14	5.92±0.12	5.93±0.16	5.92±0.13	5.93±0.17
0.8	7.93±0.12	7.93±0.16	7.92±0.12	7.92±0.18	7.91±0.13	7.93±0.17
1	9.92±0.13	9.93±0.16	9.92±0.13	9.92±0.17	9.91±0.14	9.93±0.17

Table 5.5 Average velocity of the particle u_p of for each flow rate, temperature and size fraction of Sample5.

Q (µL/s)	Velocity of the particle u_p (10^{-4} m/s)					
	20dC		40dC		60dC	
	< 250 µm	250-500 µm	< 250 µm	250-500 µm	< 250 µm	250-500 µm
0.2	1.87±0.17	1.85±0.23	1.88±0.15	1.87±0.19	1.85±0.17	1.81±0.28
0.4	3.88±0.16	3.88±0.13	3.93±0.06	3.93±0.06	3.86±0.16	3.83±0.26
0.6	5.87±0.16	5.89±0.12	5.96±0.03	5.93±0.06	5.93±0.05	5.87±0.14
0.8	7.91±0.08	7.88±0.12	7.96±0.03	7.81±0.27	7.92±0.07	7.89±0.12
1	9.86±0.16	9.85±0.21	9.95±0.04	9.94±0.04	9.84±0.17	9.85±0.20

Using the above u_p experimental results and Equation (5-8) and (5-22) we can estimate the actual relationship of Sherwood number Sh with the Reynolds number of the particle Re_p for each powder sample on the different experimental conditions. Results are

presented in Figure 5-45. It is obvious that the particle size, the temperature and particle velocity have an impact on the convective mass transfer coefficient. Higher Reynolds number leads to higher Sherwood number and consequently higher mass transfer rate. Moreover, Figure 5-45 show that diffusion plays an important role in the convective dissolution process cause a drop in *Sh* values is observed as the temperature rises from 20dC to 60dC.

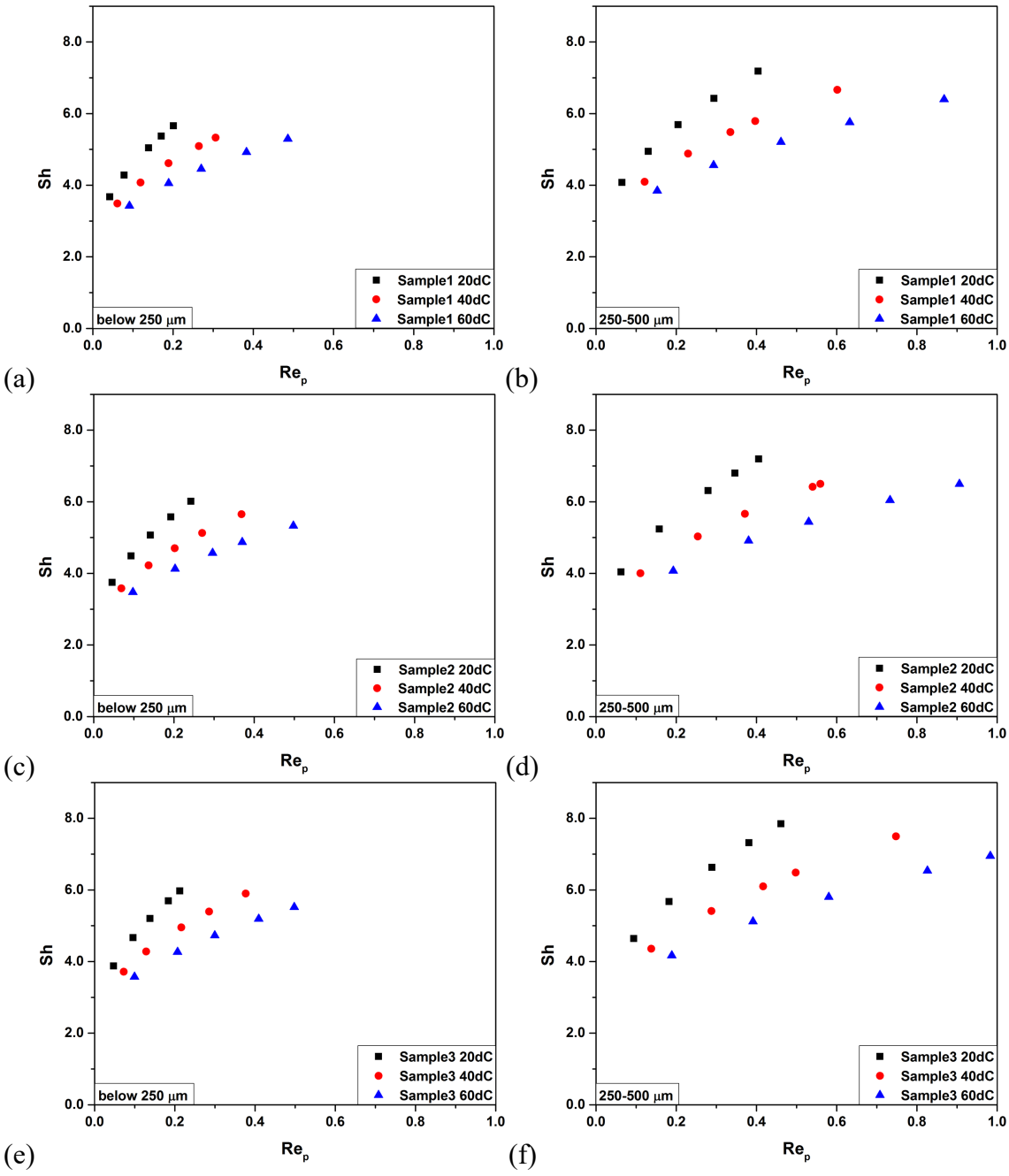

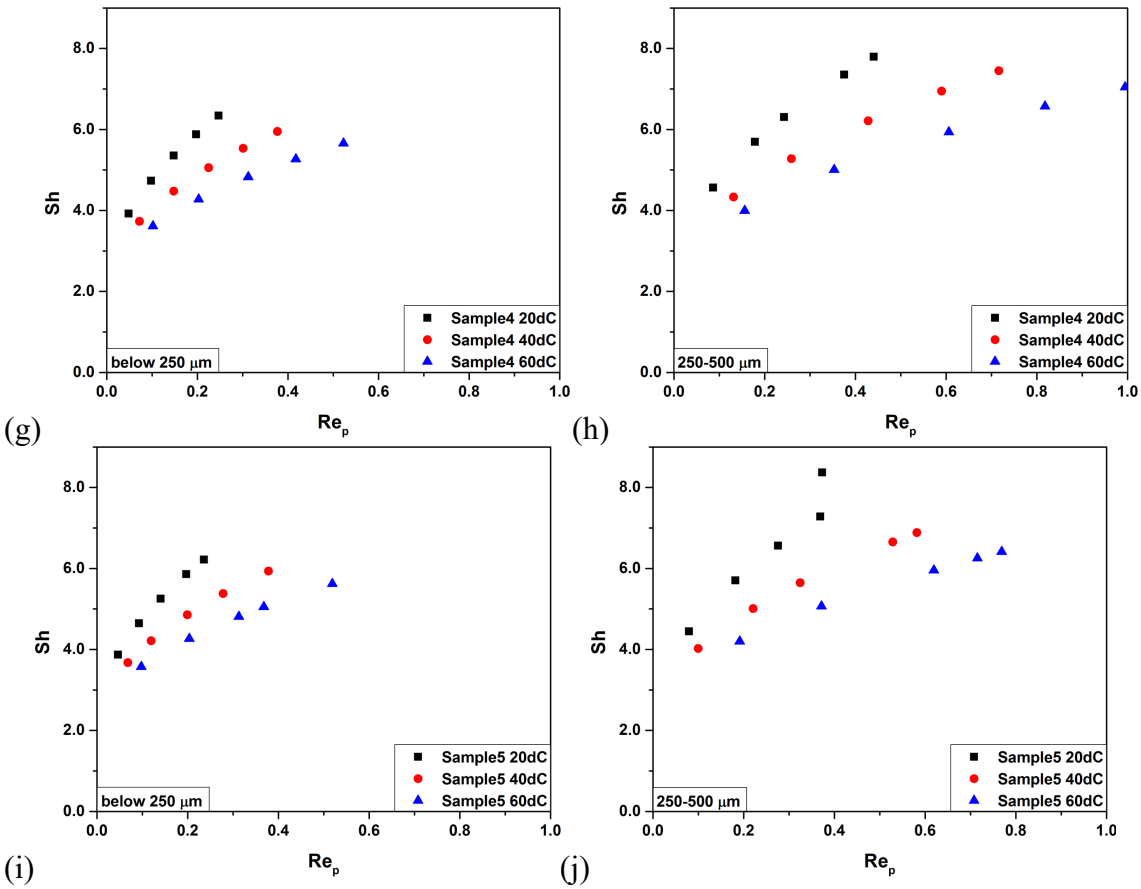

Figure 5-45 Sherwood number *Sh* as a function of Reynolds number of the particle Re_p of each powder sample. Left column represents particle size below 250 µm, while right column represents particle size 250 to 500 µm.

Using the average particle velocity, average size and mass of the particles used for the single particle convective dissolution experiments, the dissolution profiles of the particles can be predicted using Equation (5-19) and (5-22) for the different flow rates and temperatures. Figure 5-46 - Figure 5-51 show the comparison of experimental obtained and modelled dissolution profiles for each dissolution condition. The average particle velocity is used in this framework to predict granule dissolution profiles, presented as dash line in Figure 5-46 - Figure 5-51.

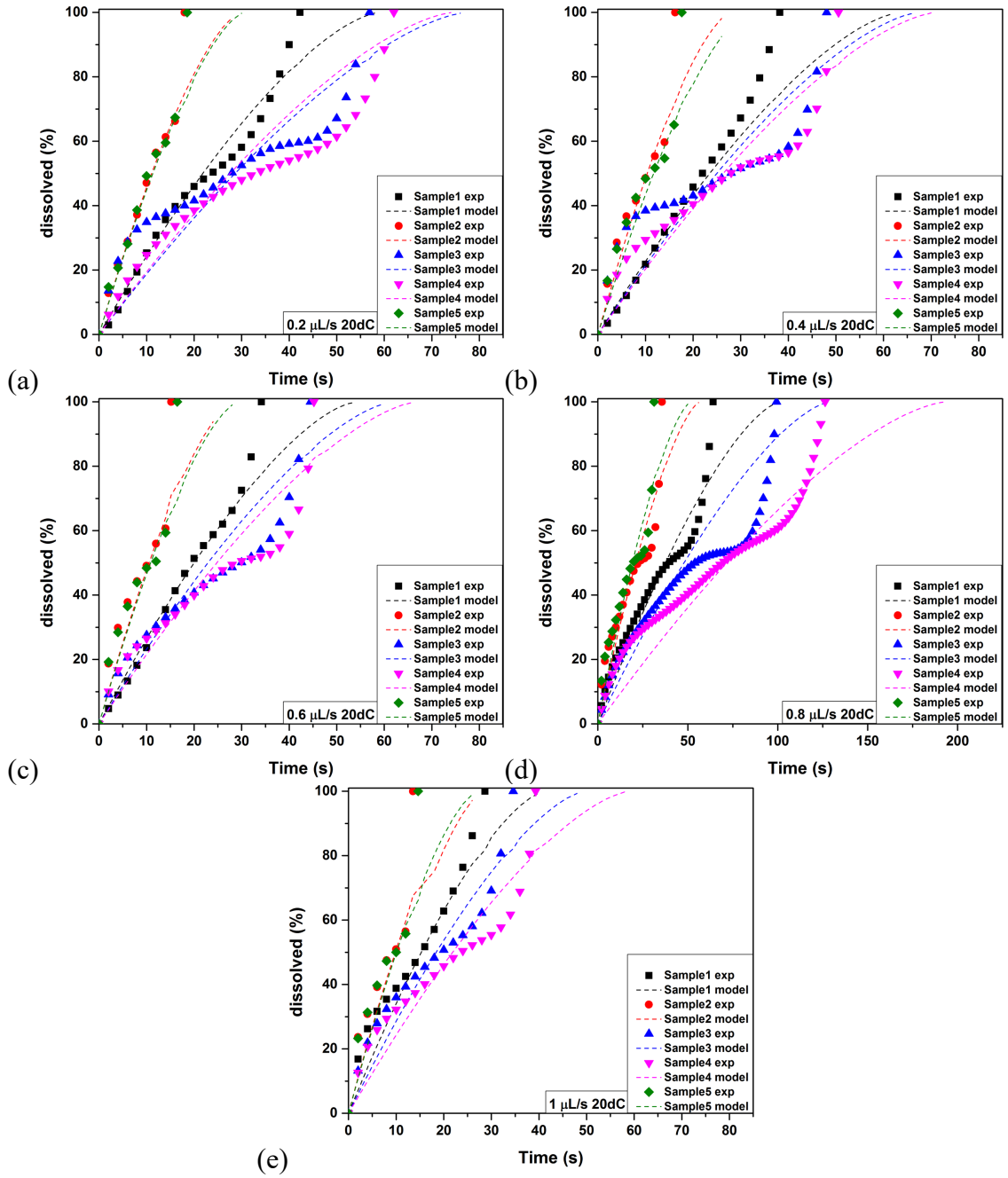

Figure 5-46 Below 250 µm dissolution profiles of experiment data vs modelling for (a) 0.2 µL/s, (b) 0.4 µL/s, (c) 0.6 µL/s, (d) 0.8 µL/s and 1 µL/s at 20dC for each powder sample.

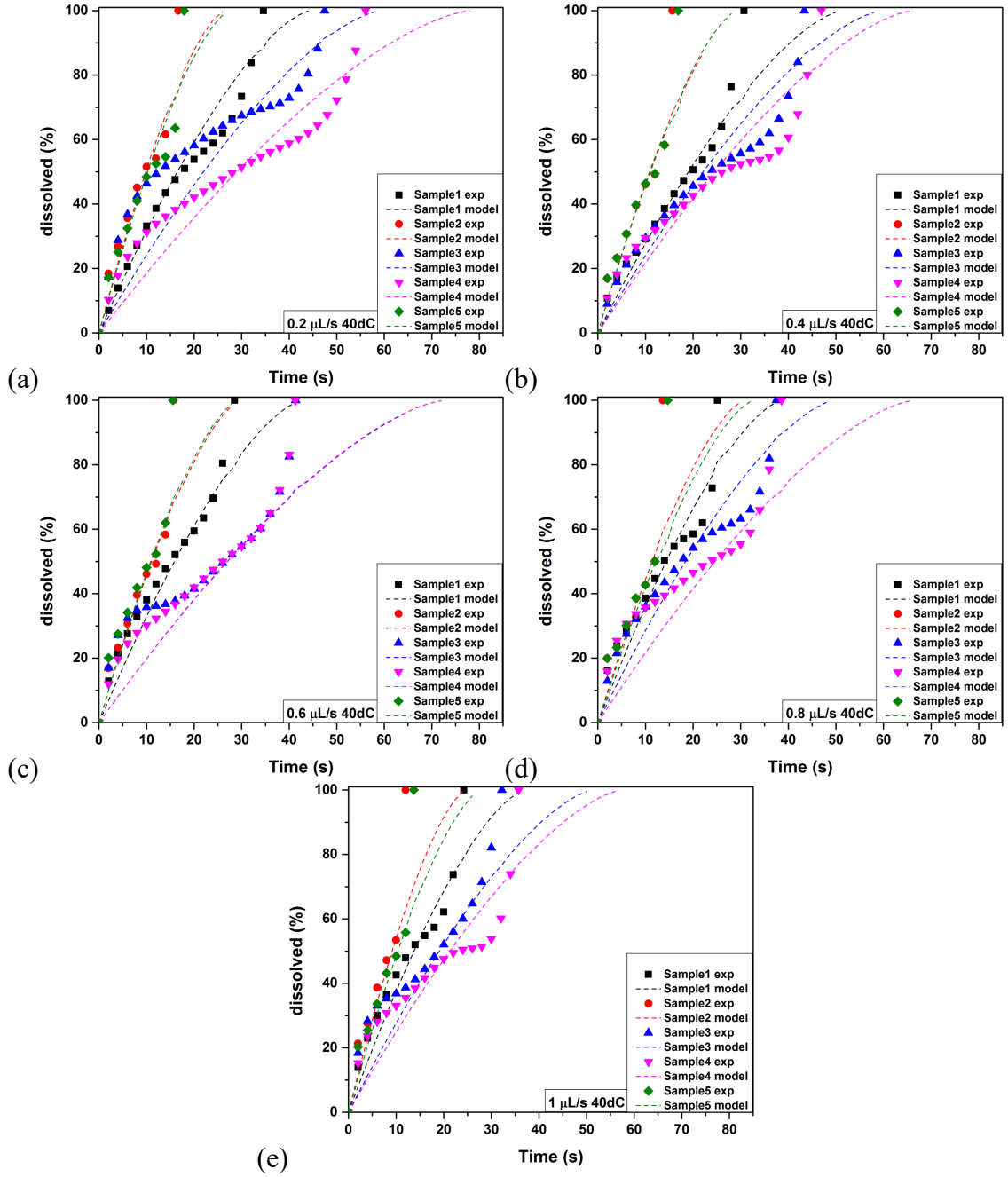

Figure 5-47 Below 250 µm dissolution profiles of experiment data vs modelling for (a) 0.2 µL/s, (b) 0.4 µL/s, (c) 0.6 µL/s, (d) 0.8 µL/s and 1 µL/s at 40dC for each powder sample.

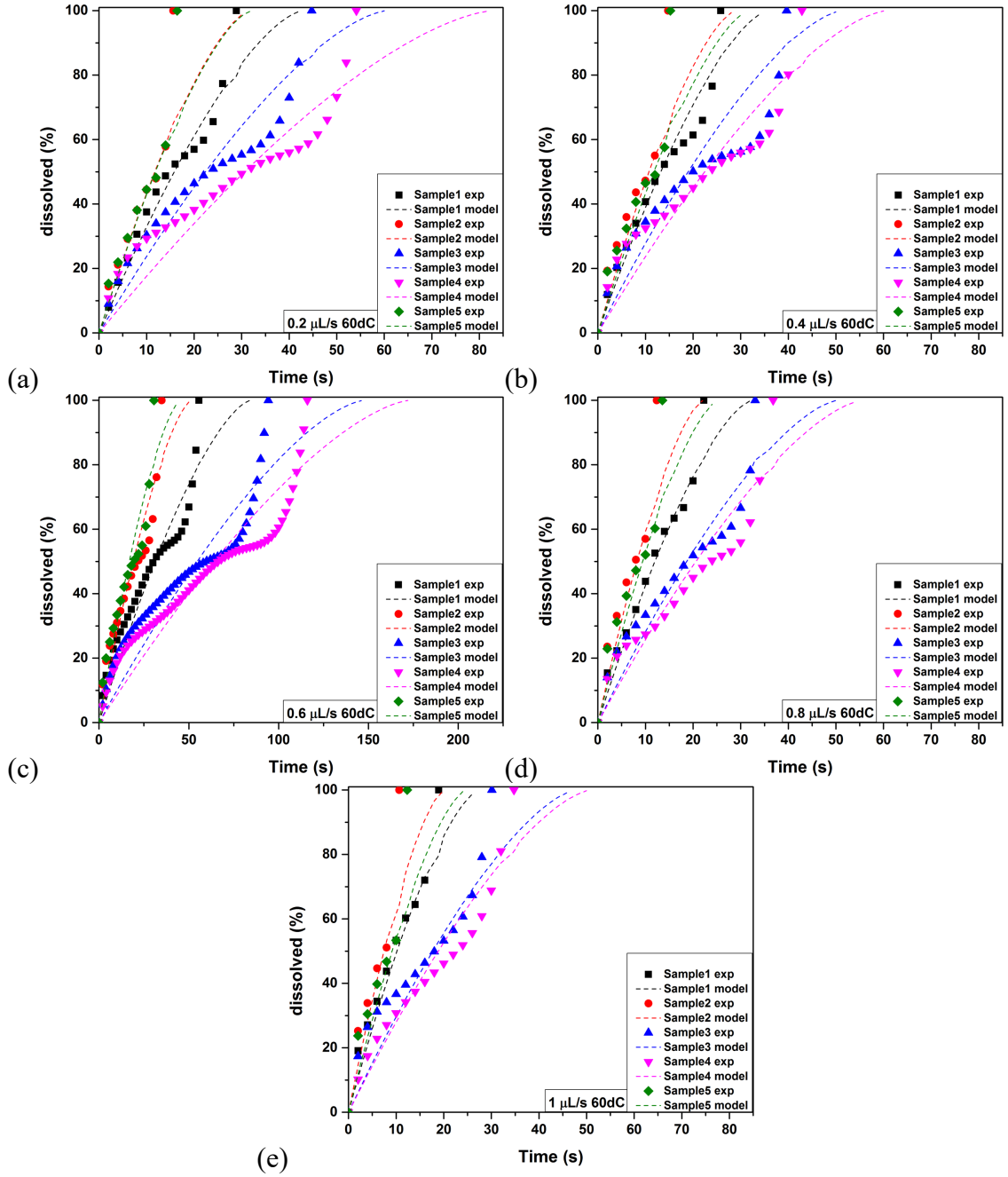

Figure 5-48 Below 250 µm dissolution profiles of experiment data vs modelling for (a) 0.2 µL/s, (b) 0.4 µL/s, (c) 0.6 µL/s, (d) 0.8 µL/s and 1 µL/s at 60dC for each powder sample.

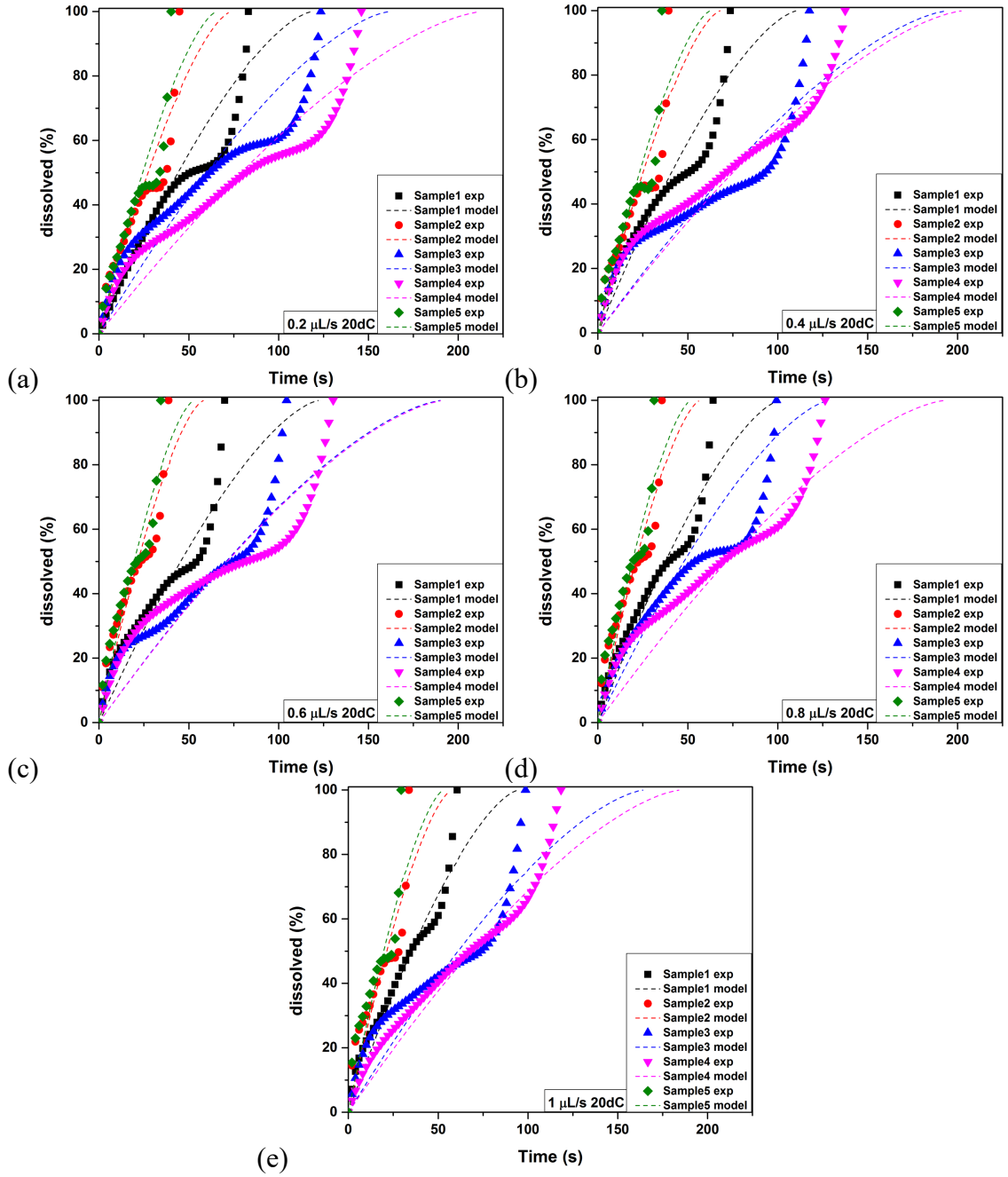

Figure 5-49 250-500 µm dissolution profiles of experiment data vs modelling for (a) 0.2 µL/s, (b) 0.4 µL/s, (c) 0.6 µL/s, (d) 0.8 µL/s and 1 µL/s at 20dC for each powder sample.

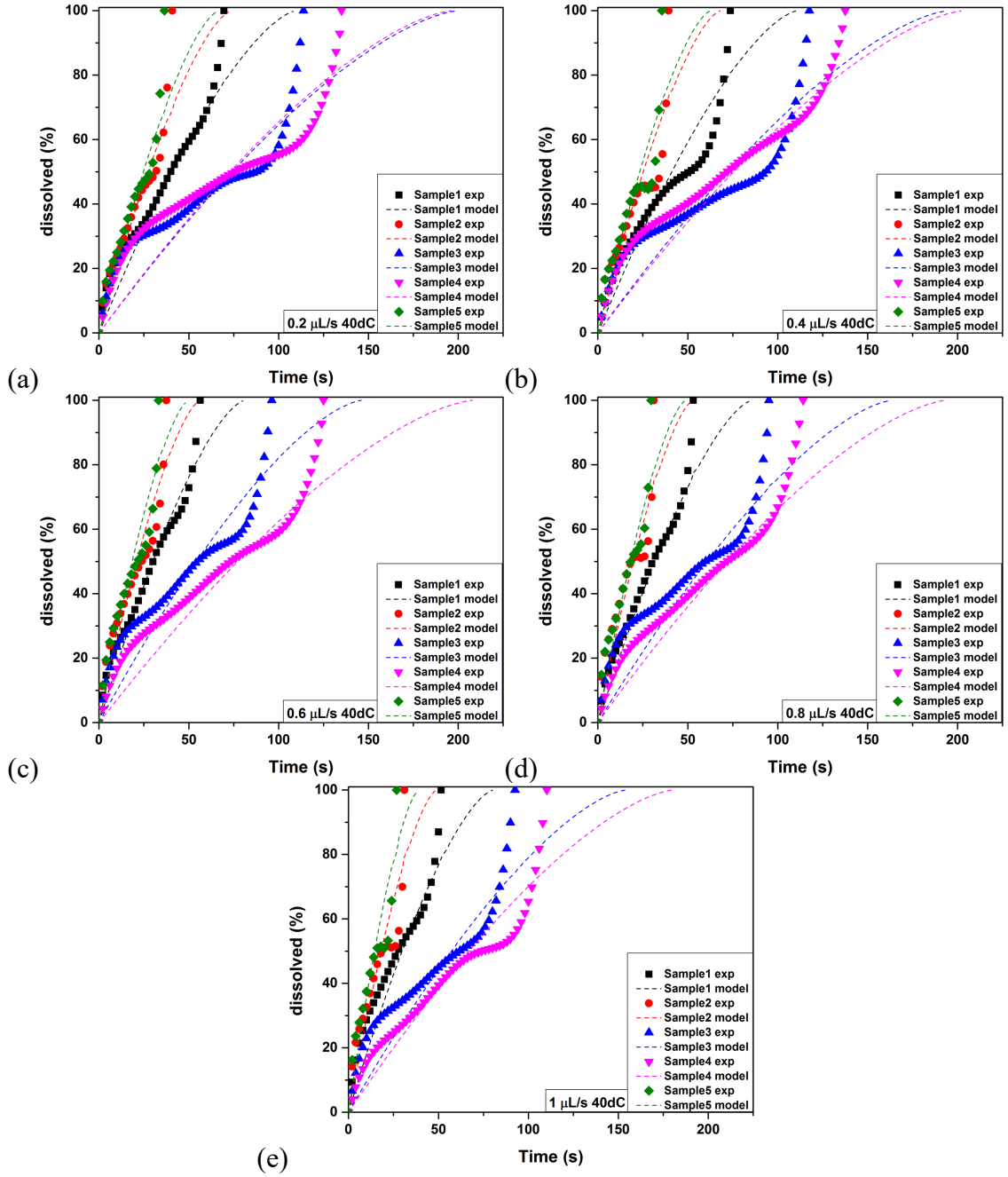

Figure 5-50 250-500 µm dissolution profiles of experiment data vs modelling for (a) 0.2 µL/s, (b) 0.4 µL/s, (c) 0.6 µL/s, (d) 0.8 µL/s and 1 µL/s at 40dC for each powder sample.

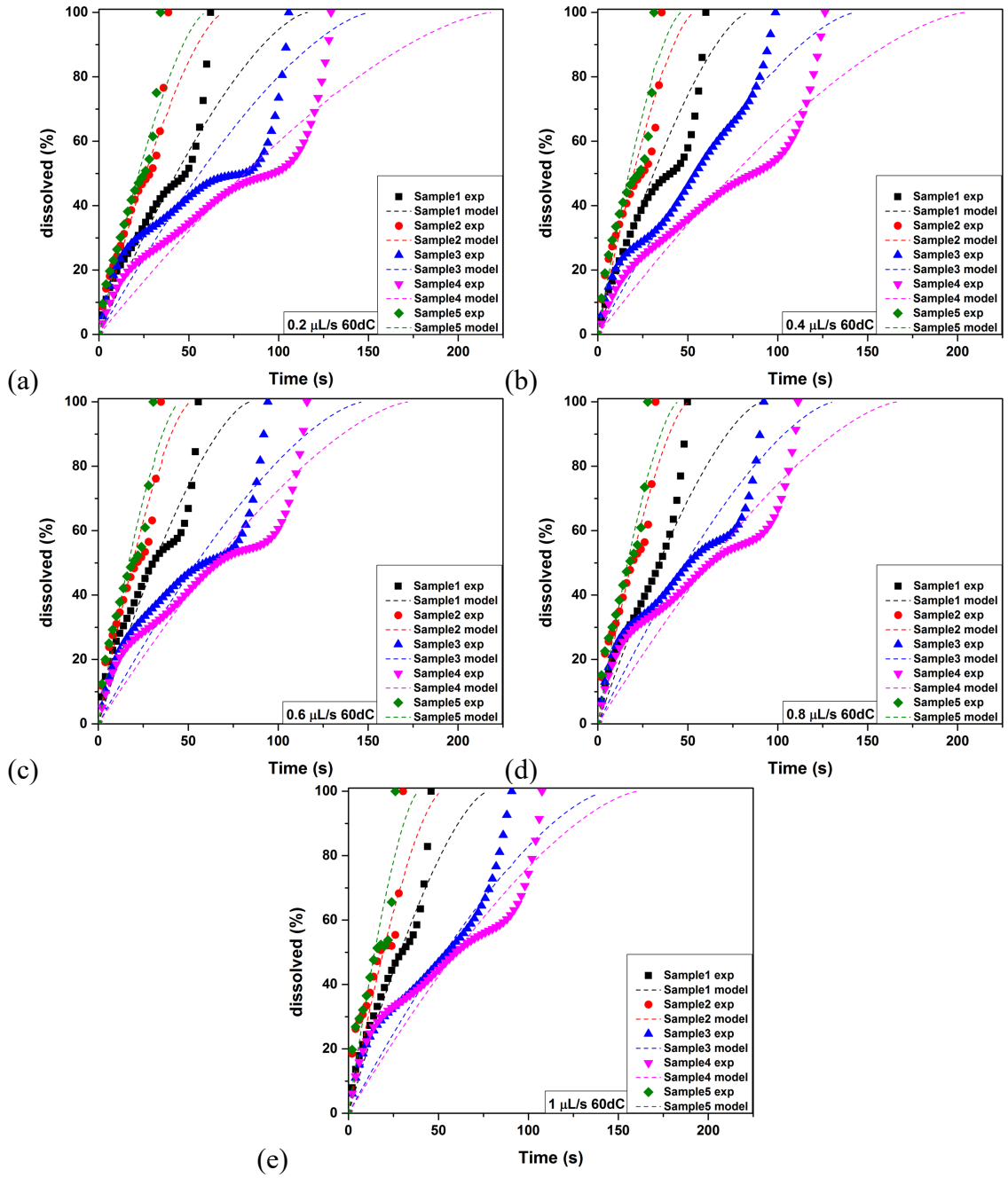

Figure 5-51 250-500 µm dissolution profiles of experiment data vs modelling for (a) 0.2 µL/s, (b) 0.4 µL/s, (c) 0.6 µL/s, (d) 0.8 µL/s and 1 µL/s at 60dC for each powder sample.

A relatively good agreement between experimental and modelling data of Sample1, Sample2 and Sample5 can be observed, especially at 20dC for all the flow rates. Slight differences appear when the temperature increases to 40dC and 60dC. However, a lack of fit is presented for Sample3 and 4, mostly in first moments of the dissolution and during

the disintegration stage. This can occur as the shrinking stage of both samples is very slow compared to Sample1, 2 and 5. Furthermore, the model shows a weakness to predict the instant mass transfer at the disintegration stage, as it does not take into account the particle porosity. The total experimental dissolution time is much shorter than predicted from the model. This is probably because of some parameters used in the modelling like the diffusivity (multi compounds) or solubility (experimental accuracy). A necessary assumption that had to be made was that the particles are spherical instead of highly agglomerated and irregular shaped as Figure 3-11 and Figure 3-16 have shown. Therefore, the area of an equivalent diameter sphere was used in the model. This happened because using the actual surface area of the granule, the particle diffusivity which is the only unknown parameter that can be modified to fit experimental and modelling results will be too small (order of magnitude 10^{-12}). The modelling results obtained using the calculated diffusivities of Figure 3-4 were not sufficient. Thus, modification on diffusivities (see Table 5.6-Table 5.15) had to be made to make the modelling results agree with experimental data. This difference in diffusivity values could be either due to particle microstructure or the distribution of the ingredients in the granule. In general, the model shows total confidence of 93.5 ± 3.1 % (see Table 5.6-Table 5.15). Specifically, for Sample1, 2 and 5 the level of confidence is 95.3 ± 1.9 % while for Sample3 and 4 is 90.9 ± 2.8 %, across the different experimental conditions as it is illustrated in Table 5.6-Table 5.15.

Table 5.6 Comparison of diffusivity from Figure 3-4 and experiment fitting results D_{fit} at different temperatures for Sample1 below 250 µm. The R^2 for each experimental condition is also presented.

	20dC			40dC			60dC		
Q (µL/s)	**Diffusivity (10^{-10} m/s)**		**R^2**	**Diffusivity (10^{-10} m/s)**		**R^2**	**Diffusivity (10^{-10} m/s)**		**R^2**
	D	**D_{fit}**		**D**	**D_{fit}**		**D**	**D_{fit}**	
0.2		6.31	0.964		2.81	0.968		4.28	0.947
0.4		-	0.969		1.49	0.925		4.58	0.949
0.6	3.11	7.11	0.974	5.09	2.00	0.970	7.58	3.18	0.921
0.8		6.11	0.928		2.51	0.941		3.98	0.962
1		4.1	0.971		1.65	0.952		4.78	0.954

Table 5.7 Comparison of diffusivity from Figure 3-4 and experiment fitting results D_{fit} at different temperatures for Sample1 250-500 µm. The R^2 for each experimental condition is also presented.

	20dC			40dC			60dC		
Q (µL/s)	**Diffusivity (10^{-10} m/s)**		**R^2**	**Diffusivity (10^{-10} m/s)**		**R^2**	**Diffusivity (10^{-10} m/s)**		**R^2**
	D	**D_{fit}**		**D**	**D_{fit}**		**D**	**D_{fit}**	
0.2		18.1	0.923		21.0	0.952		13.1	0.940
0.4		15.8	0.923		15.8	0.951		11.9	0.915
0.6	3.11	14.8	0.921	5.09	12.9	0.963	7.58	12.1	0.926
0.8		23.8	0.927		6.09	0.961		11.1	0.925
1		36.8	0.942		14.8	0.944		19.2	0.925

Table 5.8 Comparison of diffusivity from Figure 3-4 and experiment fitting results D_{fit} at different temperatures for Sample2 below 250 µm. The R^2 for each experimental condition is also presented.

	20dC			40dC			60dC		
Q (µL/s)	**Diffusivity (10^{-10} m/s)**		**R^2**	**Diffusivity (10^{-10} m/s)**		**R^2**	**Diffusivity (10^{-10} m/s)**		**R^2**
	D	**D_{fit}**		**D**	**D_{fit}**		**D**	**D_{fit}**	
0.2		14.1	0.995		6.09	0.972		5.78	0.988
0.4		11.8	0.971		3.55	0.981		5.18	0.962
0.6	3.11	10.3	0.961	5.09	2.65	0.981	7.58	3.58	0.961
0.8		10.3	0.975		2.25	0.955		3.28	0.955
1		10.3	0.935		4.05	0.967		4.75	0.944

Table 5.9 Comparison of diffusivity from Figure 3-4 and experiment fitting results D_{fit} at different temperatures for Sample2 250-500 µm. The R^2 for each experimental condition is also presented.

	20dC			40dC			60dC		
Q (µL/s)	**Diffusivity (10^{-10} m/s)**		**R^2**	**Diffusivity (10^{-10} m/s)**		**R^2**	**Diffusivity (10^{-10} m/s)**		**R^2**
	D	**D_{fit}**		**D**	**D_{fit}**		**D**	**D_{fit}**	
0.2		53.8	0.926		14.8	0.956		48.8	0.966
0.4		42.8	0.927		24.8	0.958		42.3	0.951
0.6	3.11	92.8	0.949	5.09	19.8	0.956	7.58	26.3	0.961
0.8		62.3	0.951		28.5	0.965		28.1	0.964
1		41.6	0.925		11.8	0.937		23.3	0.924

Table 5.10 Comparison of diffusivity from Figure 3-4 and experiment fitting results D_{fit} at different temperatures for Sample3 below 250 µm. The R^2 for each experimental condition is also presented.

	20dC			40dC			60dC		
Q (µL/s)	**Diffusivity (10^{-10} m/s)**		**R^2**	**Diffusivity (10^{-10} m/s)**		**R^2**	**Diffusivity (10^{-10} m/s)**		**R^2**
	D	**D_{fit}**		**D**	**D_{fit}**		**D**	**D_{fit}**	
0.2		9.98	0.891		6.32	0.896		5.93	0.927
0.4		9.85	0.851		2.72	0.934		-	0.893
0.6	2.64	8.03	0.901	4.32	3.02	0.963	6.43	4.13	0.948
0.8		7.64	0.926		4.12	0.936		4.63	0.919
1		5.84	0.915		4.62	0.906		3.93	0.904

Table 5.11 Comparison of diffusivity from Figure 3-4 and experiment fitting results D_{fit} at different temperatures for Sample3 250-500 µm. The R^2 for each experimental condition is also presented.

	20dC			40dC			60dC		
Q (µL/s)	**Diffusivity (10^{-10} m/s)**		**R^2**	**Diffusivity (10^{-10} m/s)**		**R^2**	**Diffusivity (10^{-10} m/s)**		**R^2**
	D	**D_{fit}**		**D**	**D_{fit}**		**D**	**D_{fit}**	
0.2		86.4	0.929		26.2	0.852		34.3	0.851
0.4		48.4	0.861		33.2	0.944		33.0	0.964
0.6	2.64	56.4	0.893	4.32	26.2	0.911	6.43	26.0	0.894
0.8		77.8	0.904		12.2	0.888		36.0	0.917
1		46.4	0.866		28.2	0.888		23.3	0.933

Table 5.12 Comparison of diffusivity from Figure 3-4 and experiment fitting results D_{fit} at different temperatures for Sample4 below 250 µm. The R^2 for each experimental condition is also presented.

	20dC			40dC			60dC		
Q (µL/s)	**Diffusivity (10^{-10} m/s)**		**R^2**	**Diffusivity (10^{-10} m/s)**		**R^2**	**Diffusivity (10^{-10} m/s)**		**R^2**
	D	**D_{fit}**		**D**	**D_{fit}**		**D**	**D_{fit}**	
0.2	2.53	12.3	0.927	4.15	4.95	0.926	6.17	5.01	0.908
0.4		11.0	0.898		5.15	0.892		5.37	0.898
0.6		10.5	0.890		-	0.918		5.47	0.928
0.8		10.3	0.886		-	0.860		5.07	0.884
1		10.3	0.901		4.55	0.845		5.17	0.916

Table 5.13 Comparison of diffusivity from Figure 3-4 and experiment fitting results D_{fit} at different temperatures for Sample4 250-500 µm. The R^2 for each experimental condition is also presented.

	20dC			40dC			60dC		
Q (µL/s)	**Diffusivity (10^{-10} m/s)**		**R^2**	**Diffusivity (10^{-10} m/s)**		**R^2**	**Diffusivity (10^{-10} m/s)**		**R^2**
	D	**D_{fit}**		**D**	**D_{fit}**		**D**	**D_{fit}**	
0.2	2.53	45.3	0.936	4.15	23.5	0.895	6.17	10.5	0.901
0.4		45.3	0.949		16.5	0.940		15.3	0.919
0.6		27.3	0.885		21.5	0.939		30.0	0.919
0.8		48.3	0.941		24.5	0.933		29.7	0.916
1		35.3	0.958		21.3	0.914		24.7	0.918

Table 5.14 Comparison of diffusivity from Figure 3-4 and experiment fitting results D_{fit} at different temperatures for Sample5 below 250 µm. The R^2 for each experimental condition is also presented.

	20dC			40dC			60dC		
Q (µL/s)	**Diffusivity (10^{-10} m/s)**		**R^2**	**Diffusivity (10^{-10} m/s)**		**R^2**	**Diffusivity (10^{-10} m/s)**		**R^2**
	D	**D_{fit}**		**D**	**D_{fit}**		**D**	**D_{fit}**	
0.2		21.7	0.992		9.82	0.975		9.87	0.986
0.4		15.0	0.965		3.30	0.981		8.17	0.964
0.6	2.57	14.7	0.950	4.22	4.42	0.967	6.27	7.97	0.959
0.8		14.7	0.965		-	0.955		4.67	0.955
1		13.7	0.927		6.98	0.970		8.03	0.945

Table 5.15 Comparison of diffusivity from Figure 3-4 and experiment fitting results D_{fit} at different temperatures for Sample5 250-500 µm. The R^2 for each experimental condition is also presented.

	20dC			40dC			60dC		
Q (µL/s)	**Diffusivity (10^{-10} m/s)**		**R^2**	**Diffusivity (10^{-10} m/s)**		**R^2**	**Diffusivity (10^{-10} m/s)**		**R^2**
	D	**D_{fit}**		**D**	**D_{fit}**		**D**	**D_{fit}**	
0.2		94.3	0.942		18.5	0.960		98.8	0.969
0.4		128	0.929		31.3	0.954		78.7	0.949
0.6	2.57	143	0.950	4.22	21.8	0.958	6.27	10.5	0.964
0.8		137	0.954		82.2	0.966		50.3	0.967
1		22.7	0.924		21.8	0.939		27.7	0.930

5.4 Conclusions

In this present study, a novel microfluidic dissolution testing device has been developed to understand single particle convective dissolution phenomena, to provide information for the explanation of the discrepancy between convective dissolution performance of spray-dried powders and to enable us to develop a new dissolution model by implementing the experimentally calculated particle velocity. The technique determines the dissolution behaviour of individual particles and could, therefore, be used to obtain information otherwise invisible due to the averaging of a large number of particles. The results indicate that the dissolution performance of single particles under convection is significant faster than diffusion (up to 42% for particle size below 250 μm and up to 79% faster for particle size 250-500 μm). This is explained by the addition of flow rate and temperature that dominate the system in contrast to diffusion where the dissolution mechanisms controlled the process. These parameters affect more, samples with a slow dissolution behaviour and especially those contain the Silicate binder rather than fast dissolving samples. This is because they do not allow the polymerised Silicate layer to be formed. Furthermore, the extracted particle velocity allowed us to develop a new dissolution framework based on Noyes-Whitney equation for the prediction of convective dissolution. Comparison of modelling and experimental data showed a level of confidence of 93.5 ± 3.1 %.

This work allows supplying a new dissolution testing device for single particle convective dissolution understanding and a new dissolution model that implements particle velocity. These tools can be of critical importance for the formulation industries on powder performance evaluation.

CHAPTER 6 INVESTIGATION OF Na_2SO_4 AND LAS DISSOLUTION FROM GRANULES

Abstract

In this work, the dissolution mechanisms of spray-dried powder samples with different binders were examined in aqueous solution under different experimental conditions. The dissolution process of the powder samples was online monitored by using in-situ electric conductivity probe. Aliquots were extracted at different time intervals and analysed using UV-Vis Spectrophotometer and Cat-SO_3 titration to determine the dissolution performance of the two basic powder compounds, linear alkyl benzene sulfonate (LAS) and sodium sulphate (Na_2SO_4). Dissolution profiles were fitted to different dissolution models to determine the most applicable to predict the chemical release of components. The results indicate that the LAS and the sodium sulphate Na_2SO_4 in detergent powders exhibit different dissolution behaviours which are influenced by the type and content of binders.

6.1 Introduction

Over the past decades, detergent manufacturers have implemented significant alterations in the manufacturing process [198]. One of the primary manufacturing methods in detergent business is spray drying. Due to the high efficiency of stain removal, spray-dried detergent powders account per 60-70% of the commercially available detergent washing powders and are the most common detergent powders sold globally [2]. However, different types of binders applied during the spray drying process will lead to differences in powder's physical and chemical properties such as diffusivity, particle size distribution [4], [75], [179], particle porosity, microstructure and morphology [4], [19], [87], [199] which affect significantly their dissolution and as a consequence affect the consumer satisfaction. Therefore, knowledge of dissolution behaviour of spray-dried detergent powders has drawn much attention. A surfactant, linear alkyl benzene sulfonate (LAS) and sodium sulphate (Na_2SO_4) are the two main ingredients used for the production of spray-dried detergent powders. Thus, the understanding of their chemical release as a function of binder type and content is of critical importance for the detergent industry.

In this study, the powders samples contain these two main ingredients as well as Silicate and Citric Acid as the two types of binders. Conductivity, UV-Vis Spectrophotometer and Cat-SO_3 titration were the analytical methods chosen to identify the dissolution behaviour of LAS and Na_2SO_4 under different hydrodynamic conditions. The effect of binder on their dissolution rate is also presented. To investigate the most suitable model for the prediction of chemical release of ingredients, experimental data were fitted in dissolution models found in the literature [200] including zero order kinetics, first-order kinetics, Higuchi, Hixson-Crowell and dissolution model proposed by Cao et al., [114].

6.2 Materials and Methods

6.2.1 Materials

Five spray-dried detergent powder samples, Sample1, 2, 3, 4 and 5 have been used for the single particle diffusion dissolution experiments. The composition of the samples have been discussed thoroughly in Section 3.2 of Chapter 3.

6.2.2 Dissolution studies

The dissolution profiles were determined by a USP rotating paddle Apparatus 2 (PTWS 1220 PharmaTest, Germany) at rotation speeds of 100 rpm and 200 rpm. The temperature was controlled by a water heater connected to the device which was set at 20dC for the first set of experiments and 40dC for the second set. The experimental setup is illustrated in Figure 2-29. 1 g of measured powder samples was poured into the beaker containing 800 mL of DI water. Meanwhile, an electric conductivity probe of a Jenway 4520 bench conductivity meter (Cole-Palmer, United Kingdom) was also equipped to online monitor the concentration of powder every second. The dissolution experiment was run for 10 minutes. After 10 minutes, the experiment was stopped. The experiment was repeated for 3 times for each powder sample on every experimental condition.

The same dissolution experimental procedure was repeated once again 3 times on each experimental condition. Aliquots of 2 mL were taken manually at 0, 5, 10, 15, 20, 25, 30, 35, 40, 45, 50, 75, 100, 125, 150, 200, 250, 300 and 1500 s for 20dC 100 rpm and 0, 5, 10, 15, 20, 25, 30, 35, 40, 45, 50, 75, 100, 125, 150 for 20dC and 40dC 200 rpm. A 60 mL syringe (Becton Dickinson, USA) containing a Whatman PVDF 0.45 μm filter was used for the extraction at each time interval (a different every time). Each removed aliquot was diluted with DI water to reach 10% v/v and then split in two pots of 10 mL each. One was analysed using UV-Vis Spectrophotometer, while the other was used for titration.

6.2.3 Conductivity

Pure LAS flakes (P&G, United Kingdom) and Na_2SO_4 (P&G, United Kingdom) were diluted in DI water and a standard calibration curve of conductivity versus concentration time was conducted using a Jenway 4520 bench conductivity meter (Cole-Palmer, United Kingdom). Then the concentration of LAS and Na_2SO_4 of each powder sample was determined by the Conductivity with the developed calibration models.

6.2.4 UV-Vis Spectrophotometer

Spectrophotometry is a technique that uses the absorbance of light by an analyte at a certain wavelength to determine the analyte concentration. UV-Vis spectrophotometry uses light in UV and visible part of the electromagnetic spectrum. Light of this wavelength is able to affect the excitation of electrons in the atomic or molecular ground state to higher energy levels, giving rise to an absorbance at wavelengths specifics to each molecule.

When a beam of radiation (light) passes through a substance or a solution, some of the light may be absorbed and the remainder transmitted through the sample. The ratio of the intensity of the light entering the sample to that exiting the sample at a particular wavelength is defined as the transmittance. The absorbance of a sample is the negative algorithm of the transmittance.6

LAS flakes (P&G, United Kingdom) and Na_2SO_4 (P&G, United Kingdom) were diluted in DI water and analysed in a Cary 60 UV-Vis (Agilent Technologies, USA) to investigate the absorbance wavelength. A standard calibration curve of absorbance versus concentration was conducted at the specific absorbance wavelength. Then the concentration of LAS of each aliquot was determined by the UV spectrophotometer with the developed calibration models.

6.2.5 $CatSO_3$ titration

5 mL of aliquot were placed in a 100 mL Nessler tube containing a magnetic stirrer. Then 10 mL of indicator mix (acidified solution) and 10 mL of Dichloromethane (DCM) were added to the tube. The experimental setup of $CatSO_3$ titration is illustrated in Figure 6-1 (a). With the addition of DCM, the solution will turn red (see Figure 6-1 (b)). Then it was titrated in hyamine slowly using Titrando titrator (Metrohm, United Kingdom) until the red coloured layer disappears and become pale grey. If it turned green, we have passed the endpoint. The concentration % was calculated as

$$\%\ concentration = \frac{T_i * N_t * Mwt * V * 100}{1000 * 2\ (g) * Al} \quad (6\text{-}1)$$

where $T_i$is the titration reading (mL), N_t is the titrant normality (N), Mwt is the analyte molecular weight (Mwt), V is the volume (mL) and Al is the amount of aliquot (mL).

The preparation procedure of mix indicator follows:

Preparation of indicator mix (stock solution)

1 g of Disulphine Blue and 2 g of Dimidium Bromide were dissolved in 50 g of alcohol. Then it was filled up to 500 g with DI water.

Preparation of indicator mix (acidified solution)

40 mL of indicator mix-stock solution were added accurately to a 2000 mL volumetric flask containing 200 mL of DI water and a magnetic stirrer. Then 50 mL of sulphuric acid (2.5M) was added accurately, and it was filled up to 2000 mL with DI water. Then it was stirred well.

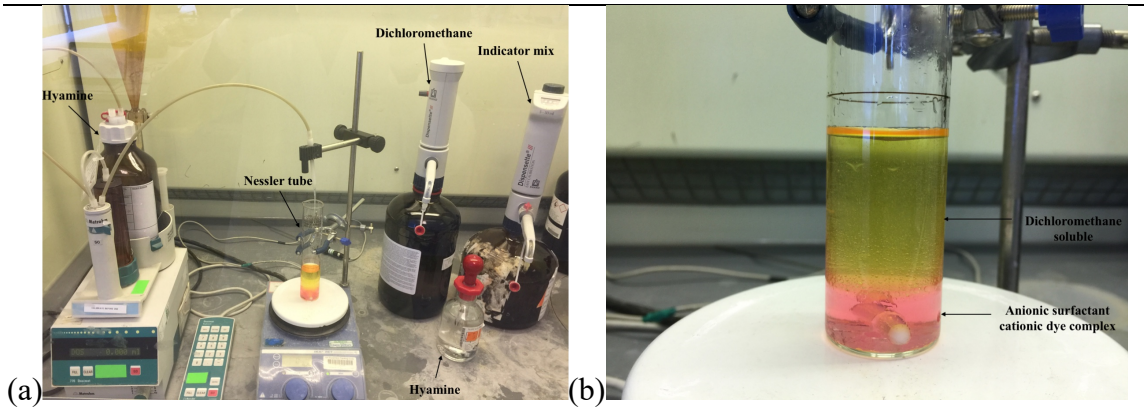

(a) (b)

Figure 6-1 (a) Experimental setup of $CatSO_3$ titration, (b) Two phases of solution before titration, yellow: soluble Dichloromethane and pink: anionic surfactant cationic dye complex.

6.3 Results and Discussion

6.3.1 Chemical release of Na_2SO_4

Pure LAS flakes and Na_2SO_4 were dissolved in DI water to make a series of standard calibration solutions of 10, 20, 40, 80, 100, 200 and 400 ppm for the development of standard calibration plots of conductivity versus concentration as presented in Figure 6-2.

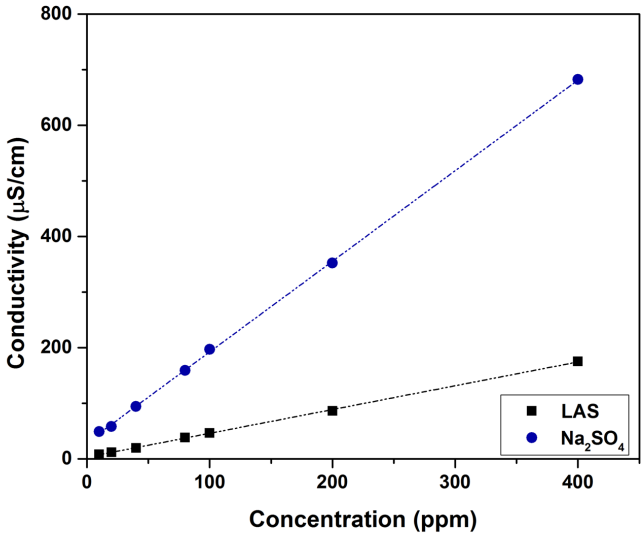

Figure 6-2 Calibration of Conductivity of LAS and Na_2SO_4.

Conductivity measurements of LAS and Na_2SO_4 solutions show that the electric conductivity of LAS is negligible in comparison with the sodium sulphate conductivity.

Therefore, the conductivity data will be used to analyse the dissolution kinetics of sodium sulphate.

The released of profiles of mainly Na_2SO_4 component of the spray-dried detergent powder samples at 20dC 100rpm, 200rpm and 40dC 100rpm are illustrated in Figure 6-3. Results show that Sample2 which contains one of the highest portions of Na_2SO_4 (77.06%), dissolves faster than Sample1 (77.06%), Sample3 (64.31%), Sample4 (61.71%) and Sample5 (63.7%) at the first 50s of the process. The main reason is the different microstructure of the powder samples. As XRT cross-sections have shown (see Figure 3-17), Sample2 has less undissolved Na_2SO_4, only 0.6% but more void space inside shell structure which is a result of the high slurry mix moisture, which allows ingredients to dissolve better in the slurry. On the other hand, the rest samples although they have a thin layered structure which should be dissolved fast, they have a significant amount of Na_2SO_4, ranging from 10 μm to 250 μm (see Figure 3-18). Except the size and the amount of undissolved Na_2SO_4, the distribution of that component in the particle affects the dissolution process where for the slow dissolving samples is mainly placed in the centre of the particle while in Sample2 can be mainly found close to the particle wall (see Figure 3-17). That allows water to dissolve Na_2SO_4 faster. The rise of temperature from 20dC to 40dC does not seem to affect the order of the release of Na_2SO_4 as Sample2 remains the faster. However, the increase of agitation speed enhances the dissolution kinetics of Na_2SO_4 for Sample2 as it can be observed from the increasement on the slope (see Figure 6-3 (b)). The effect of the binder was also studied. Sample3 and 4 which contain Silicate binder, exhibit fast bulk dissolution which is probably due to the turbulence forces generated by agitation and the particle interactions that does not allow Silicate to polymerise and slow down Na_2SO_4 dissolution. This correlates well with the

results obtained from single particle diffusion and convective dissolution (see Chapter 4 and Chapter 5), wherein the presence of other particles and laminar flow conditions the effect of Silicate in dissolution is decreasing with the increasement of particles and flow accordingly. On the other hand, the sample with the Citric Acid binder (Sample5) show similar Na_2SO_4 dissolution behaviour with Sample1, which is linked to correlations in the microstructure. Although the dissolution performance is slow, the total Na_2SO_4 dissolution time of Sample5 is the fastest.

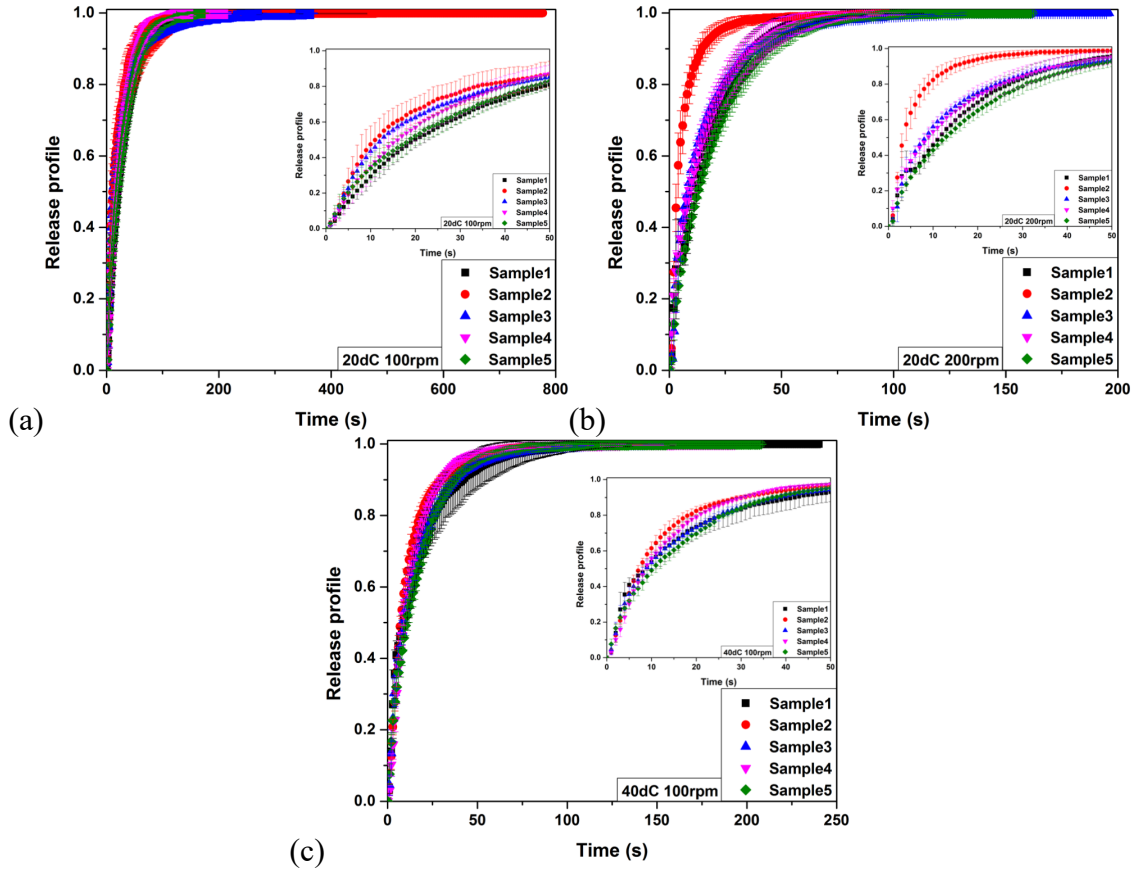

Figure 6-3 Conductivity dissolution profiles of powder samples at (a) 20dC 100rpm, (b) 20dC 200rpm and (c) 40dC 100rpm.

6.3.2 Chemical release of LAS

Pure LAS flakes and Na_2SO_4 were dissolved in DI water to make a series of standard calibration solutions of 10, 20, 40, 80, 100, 200, 400 and 800 ppm. The solutions first scanned using a UV-Vis Spectrophotometer across the UV wavelength range (200 to 400

nm) to identify the main absorbance spectra. The analysis of Na_2SO_4 did not present any absorbance. Thus UV-Vis data will be used to study the chemical release of LAS. Figure 6-4 (a) shows that LAS has an absorbance peak at 225 nm, which correlates well with results found in the literature [201]. However, the solution needs to be at a concentration of 100 ppm and below for this peak to be revealed.

Based on the results of Figure 6-4 (a) a calibration model of absorbance versus concentration was developed (see Figure 6-4 (b)). Two different regions of linear trends can be noticed. The first one is from 10 ppm to 80 ppm and the second from 100 ppm to 800 ppm. This behaviour is explained by the noise caused by absorbance of LAS at concentrations above 100 ppm (see Figure 6-4 (a)). In our dissolution experiments, the concentration of the system was 125 ppm, for this reason, each aliquot diluted to 10% v/v to be able to target the first linear region where R^2=0.994.

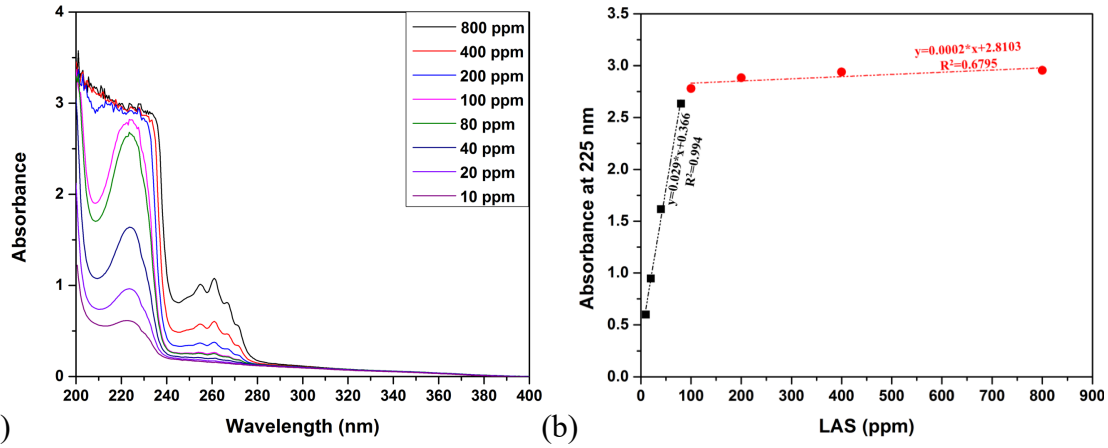

(a) (b)

Figure 6-4 (a) UV-Vis absorption spectra of LAS; (b)UV-Vis absorbance at 225 nm versus LAS concentration (ppm).

The chemical release of the two main spray-dried detergent powder ingredients, LAS and Na_2SO_4 at 20dC 100rpm, 20dC 200rpm and 40dC 100rpm is illustrated in Figure 6-5, Figure 6-6, Figure 6-7 respectively. A significant difference on measurements obtained from Conductivity method and those acquired by UV-Vis can be observed. This can be

translated as a difference in the dissolution behaviour of the two main compounds of a spray-dried detergent powder, LAS and Na_2SO_4 across the different experimental conditions. Results show that the chemical release of the compounds can be divided into two regions. The first region is in the initial moments of dissolution, where LAS dissolves faster than Na_2SO_4 and the second region where LAS releases slower or equal than Na_2SO_4. The orientation of these regions depends on the temperature, agitation speed and binder content. Keeping the agitation speed steady at 100rpm and increasing the temperature from 20dC to 40dC the time that LAS releases faster than Na_2SO_4 decreases by more than half (see Figure 6-5 and Figure 6-7). Specifically, at 20dC is from 0 s to 25 s while for 40dC is from 0 to 10 s. However, retaining the temperature at 20dC and increasing the agitation speed from 100rpm to 200rpm it can be noticed that for Sample1, 3 and 4, LAS is completely released in the first 30 s as it is enhanced by the hydrodynamic forces (see Figure 6-5 and Figure 6-6). Thus, the second region does not exist. However, for Sample2 and 5 this mechanism does not occur as from 0 s to 10 s LAS releases faster than Na_2SO_4 and then they are equally dissolving. The hypothesis concerning the fast dissolution of LAS compared to Na_2SO_4 is that the Na_2SO_4 crystals are encapsulated/coated with the LAS surfactant. Besides, if a sample contains a binder, then it surrounds the Na_2SO_4 and makes LAS more accessible to water. The release of Na_2SO_4 will start once the binder material that surrounds it is fully dissolved. Therefore, the water dissolves first the amount of LAS and then the Na_2SO_4. However, in the case of Sample5 where the binder is a disintegrant, Citric Acid, its release is enhanced [153], [154]. Moreover, LAS has higher solubility, 250 kg/m^3 compared to Na_2SO_4, 192.3 kg/m^3 at 20dC. The difference in dissolution behaviour of the compounds at 40dC can be explained by the change in solubility levels where Na_2SO_4 increases to 478.2 kg/m^3 while LAS rises

to 280 kg/m^3. Further chemical analysis on the phase transitions occurred in surfactant during release could potential further reveal the complexity of the phenomena taking place.

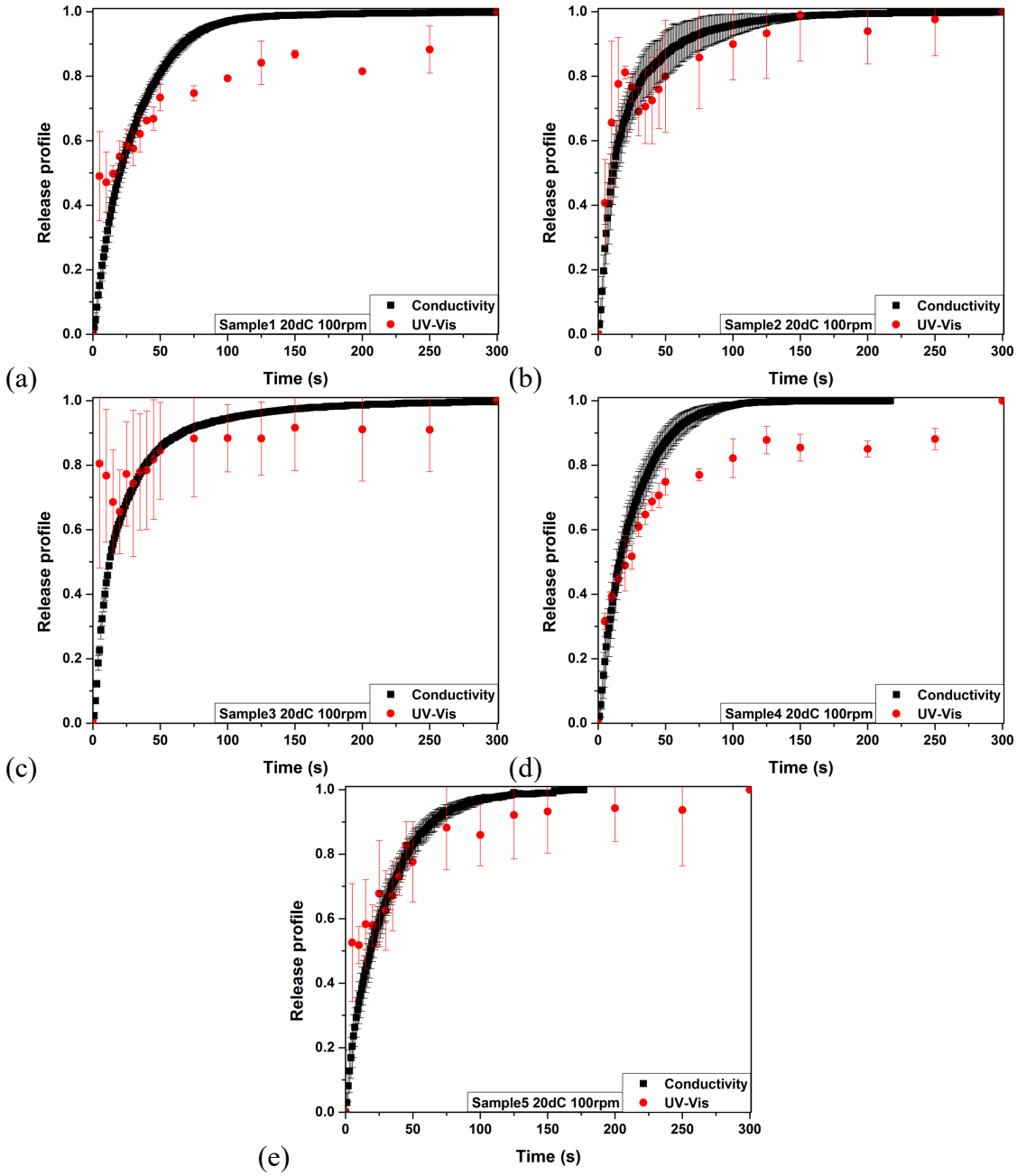

Figure 6-5 Comparison of chemical release of Na_2SO_4 (conductivity) and LAS (UV-Vis) for (a) Sample1, (b) Sample2, (c) Sample3, (d) Sample4 and (e) Sample5 at 20dC 100 rpm.

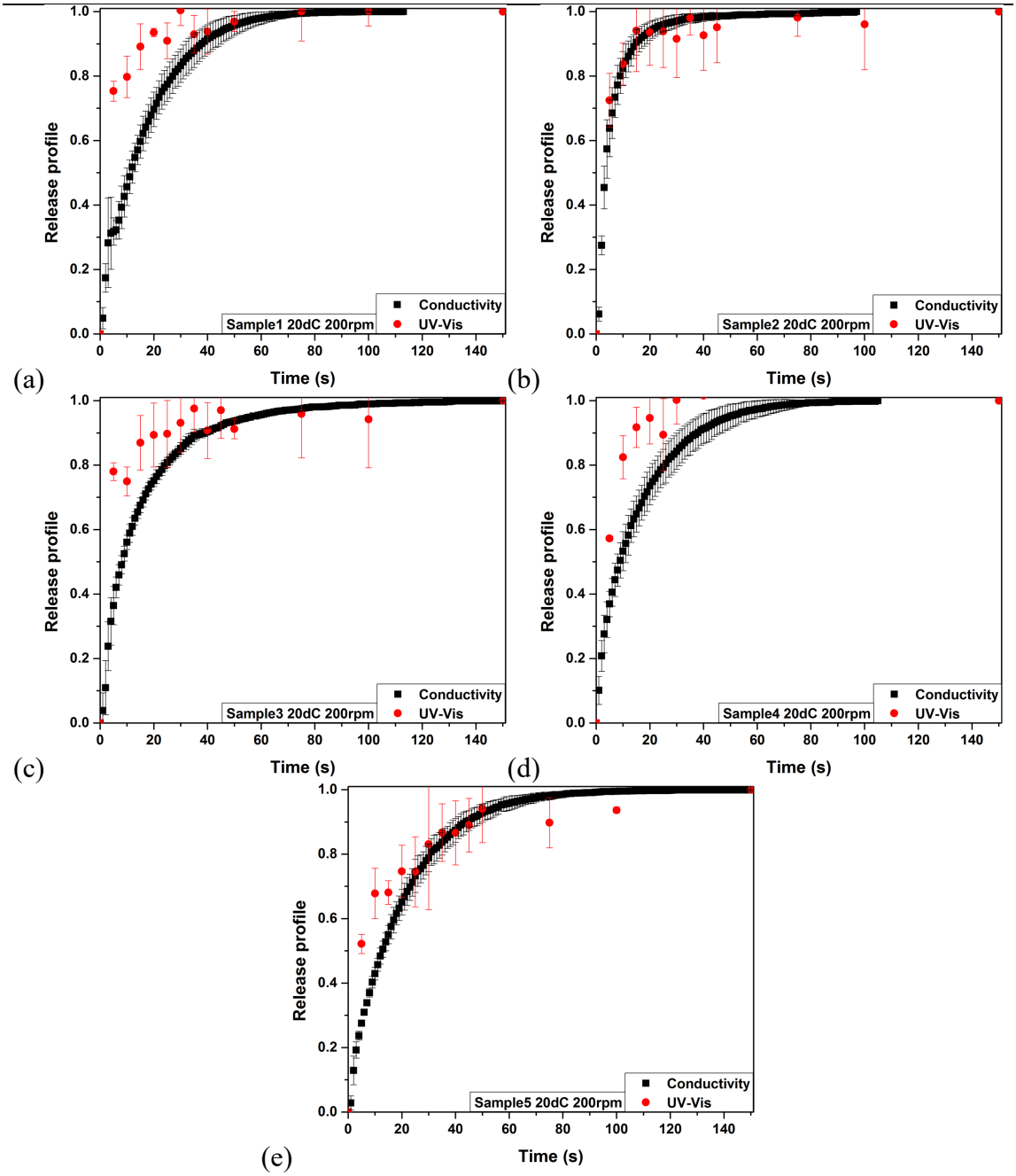

Figure 6-6 Comparison of chemical release of Na_2SO_4 (conductivity) and LAS (UV-Vis) for (a) Sample1, (b) Sample2, (c) Sample3, (d) Sample4 and (e) Sample5 at 20dC 200 rpm.

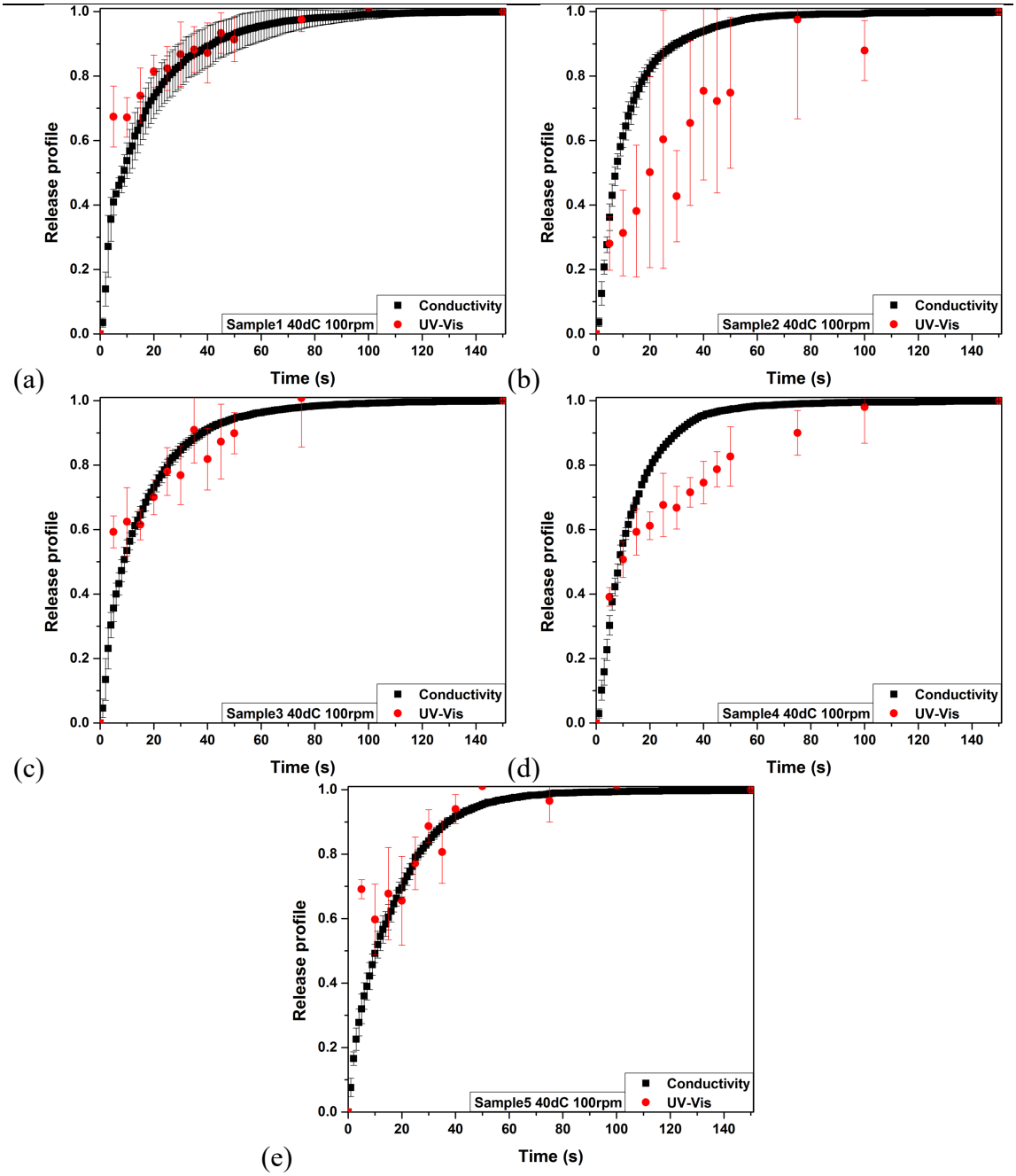

Figure 6-7 Comparison of chemical release of Na_2SO_4 (conductivity) and LAS (UV-Vis) for (a) Sample1, (b) Sample2, (c) Sample3, (d) Sample4 and (e) Sample5 at 40dC 100 rpm.

To validate the results obtained from UV-Vis experiments on the chemical release of LAS the aliquots were analysed using the $CatSO_3$ titration method. This method can be used for the direct determination of surfactants. The method is based on the dye-complexing property of cationic and anionic surfactants. The aliquot containing the sodium sulphate

and a mixed indicator of cationic and anionic complexing dyes are mixed in a water dichloromethane system. The anionic surfactant cationic dye complex is pink to red and dichloromethane soluble (see Figure 6-1 (b)). Upon titration with a cationic quaternary, Hyamine, the pink-dye surfactant complex is broken and is replaced by a colourless anionic surfactant – cationic titrant complex. A colour change from pink to grey in the non-aqueous layer indicates the endpoint. If excess Hyamine is added, it complexes the anionic dye, giving a blue colour to the non-aqueous layer.

Figure 6-8, Figure 6-9 and Figure 6-10 show the comparison of the $CatSO_3$ titration analysis with conductivity and UV-Vis measurements for the three different experimental conditions. UV-Vis and $CatSO_3$ methods shows high compatibility which means that LAS can be detected accurately by both these methods. $CatSO_3$ validates the dissolution performance of LAS. The two regions of LAS release that identified by UV-Vis can also be observed by $CatSO_3$ measurements. Both measurements show Sample2 and 5, exhibit quite similar chemical release of compounds at 20dC 100rpm and 200rpm, which can be the answer of why these samples are the fastest dissolving samples observed from the single particle dissolution experiments (see Chapter 4 and Chapter 5). The error bars on UV-Vis and $CatSO_3$ values represent the standard deviation obtained from three replicates.

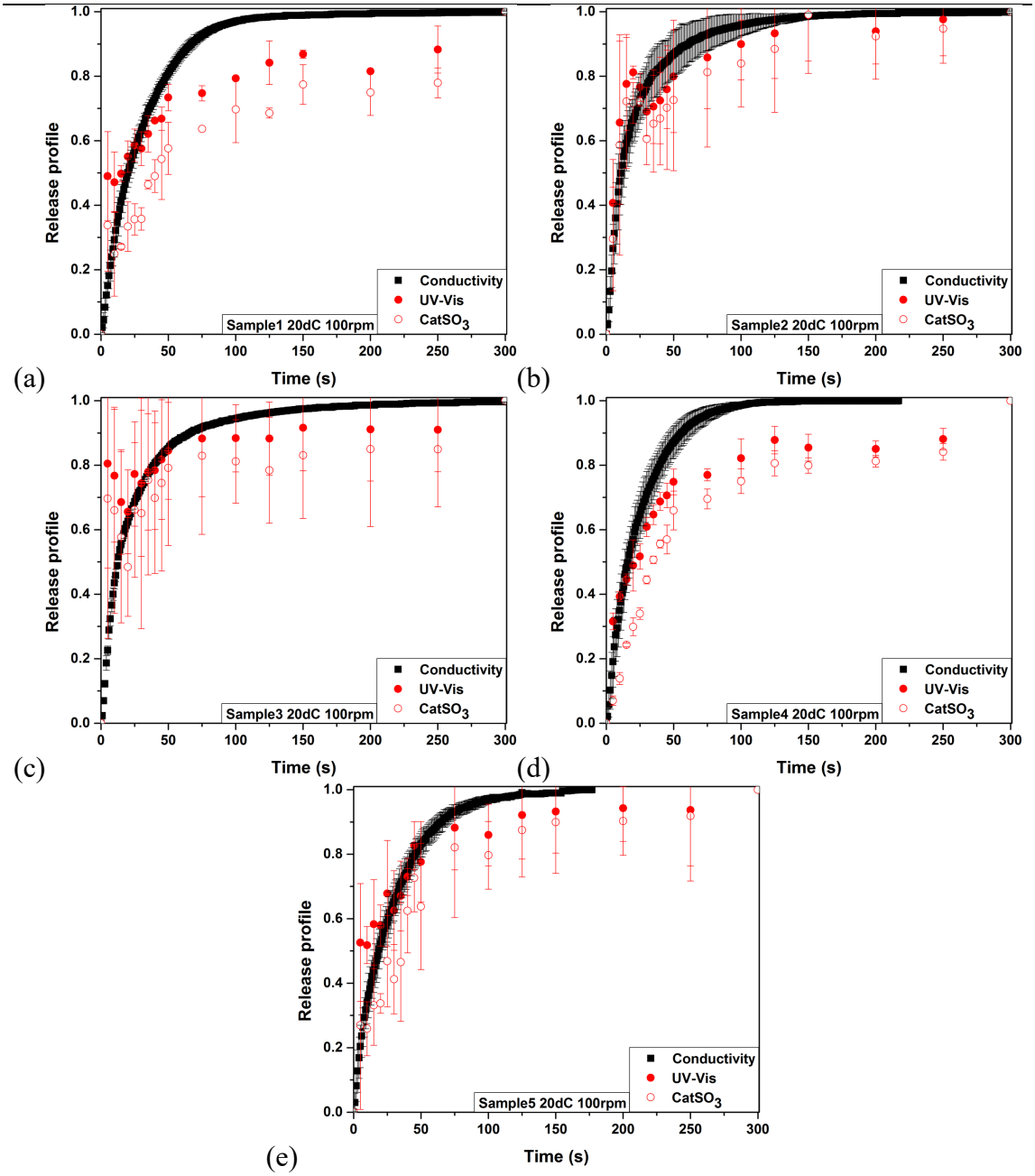

Figure 6-8 Comparison of chemical release of Na_2SO_4 (conductivity) and LAS (UV-Vis and $CatSO_3$ titration) for (a) Sample1, (b) Sample2, (c) Sample3, (d) Sample4 and (e) Sample5 at 20dC 100 rpm.

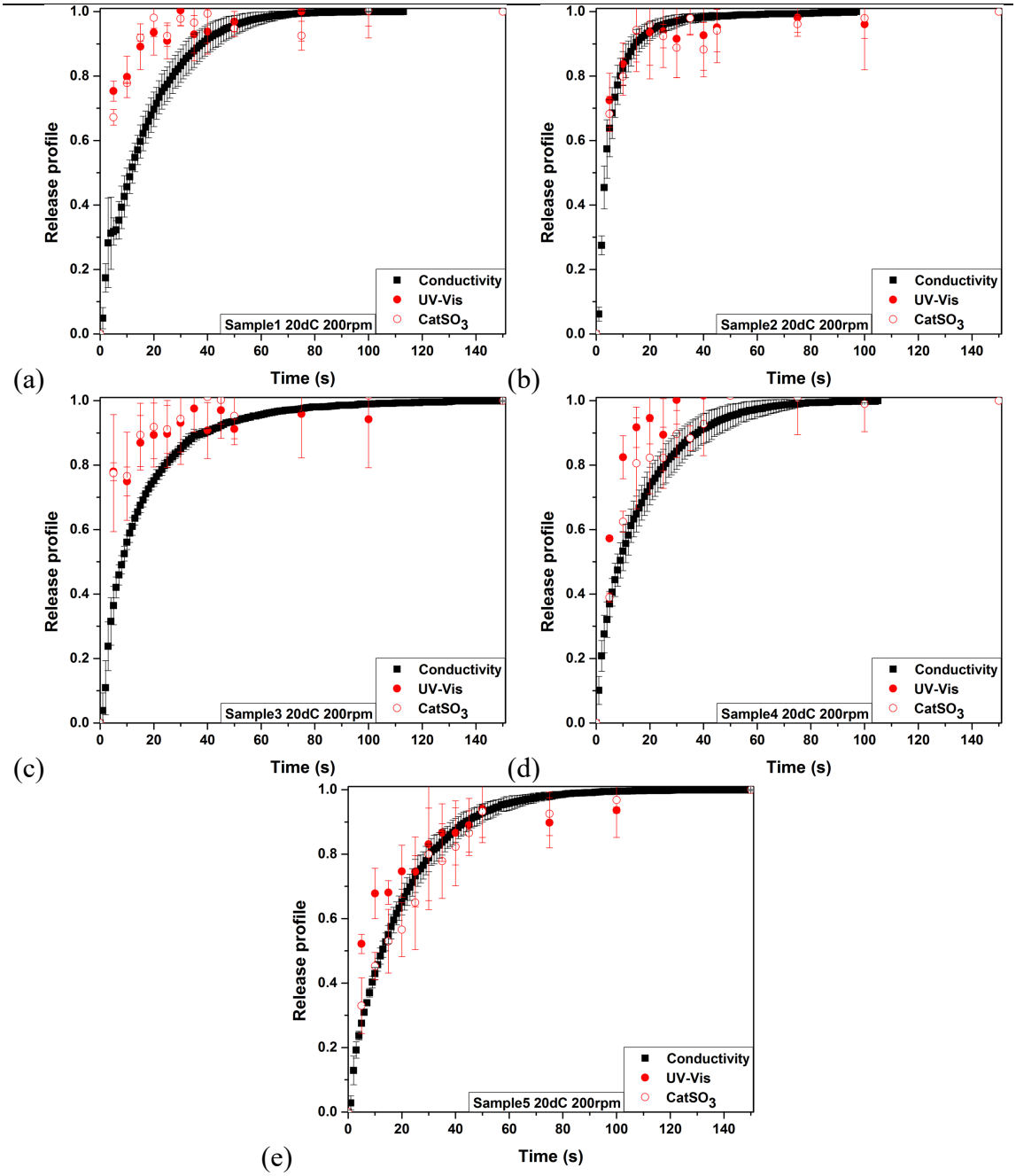

Figure 6-9 Comparison of chemical release of Na_2SO_4 (conductivity) and LAS (UV-Vis and $CatSO_3$ titration) for (a) Sample1, (b) Sample2, (c) Sample3, (d) Sample4 and (e) Sample5 at 20dC 200 rpm.

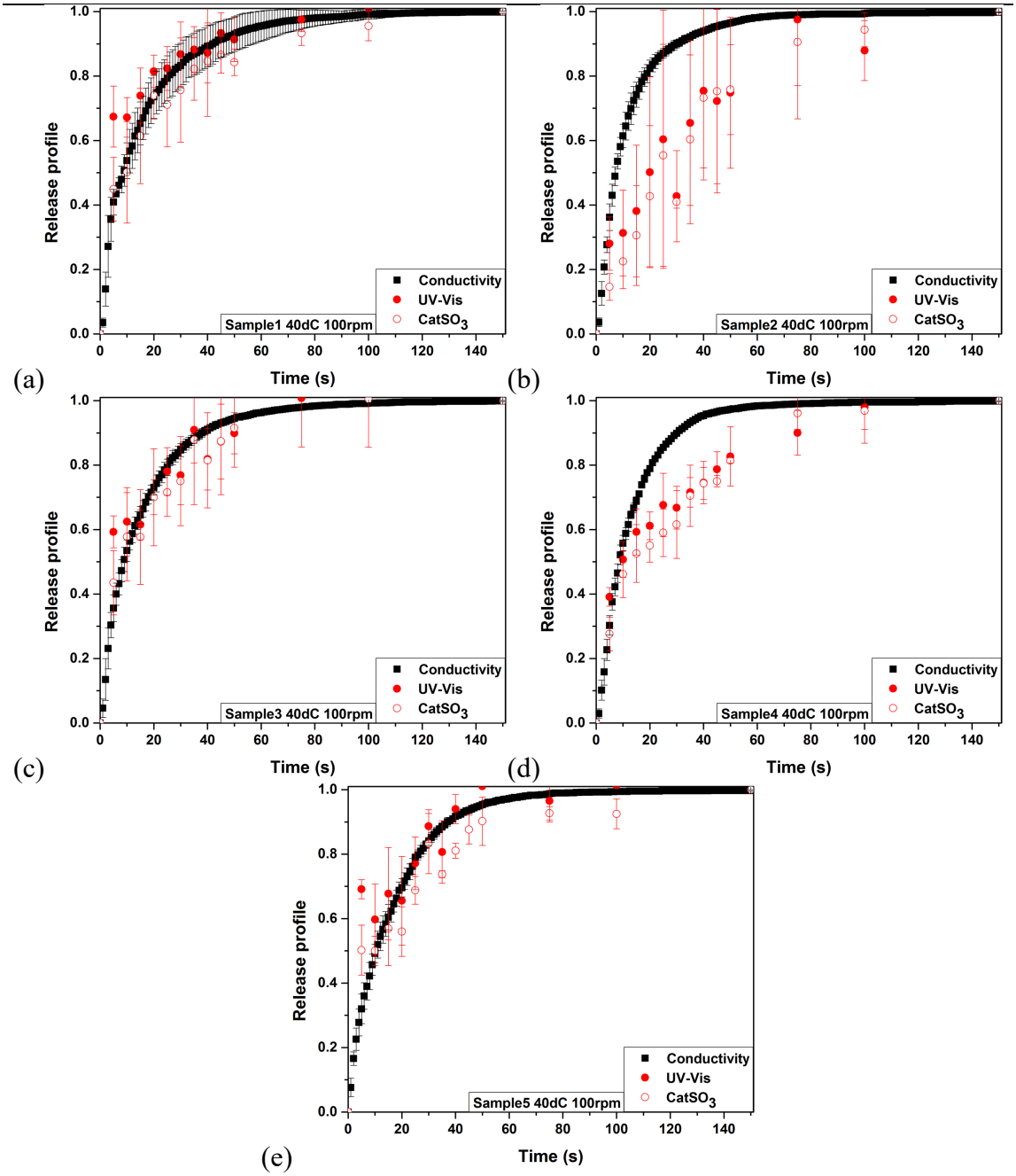

Figure 6-10 Comparison of chemical release of Na_2SO_4 (conductivity) and LAS (UV-Vis and $CatSO_3$ titration) for (a) Sample1, (b) Sample2, (c) Sample3, (d) Sample4 and (e) Sample5 at 40dC 100 rpm.

6.3.3 Dissolution rate of LAS and Na_2SO_4

Dissolution rate is commonly acquired in bulk measurements [9], [12], [19], [180] to investigate the dissolution kinetics of the samples tested. In this study, the dissolution rate

of the two main spray-dried detergent powder compounds, LAS and Na_2SO_4 were evaluated for each powder sample at the different experimental conditions.

The dissolution rate dW/dt was obtained by differentiating the changes in ingredient weight during time. The weight of LAS and Na_2SO_4 at each time interval $W_{i,t}$ was evaluated by multiplying the initial weight of the ingredient W_i with the amount dissolved at that moment, $dissolved_{i,t}$ measured from the Conductivity for the LAS and UV-Vis and $CatSO_3$ titration for the Na_2SO_4 data

$$W_{i,t} = W_i dissolved_{i,t} \tag{6-2}$$

Each powder sample has a different composition of ingredients thus the W_i of each ingredient will not be the same. The W_i was evaluated by multiplying the initial weight of powder in bulk dissolution testing, 1 g, with the composition of the ingredient in dry powder based on Table 3.2 (see Table 6.1).

Table 6.1 g of LAS and Na_2SO_4 in bulk dissolution testing.

Samples	g of compounds in bulk dissolution testing	
	Na_2SO_4	**LAS**
Sample1	0.7706	0.195
Sample2	0.7706	0.195
Sample3	0.6431	0.195
Sample4	0.6171	0.195
Sample5	0.6377	0.204

The dW/dt (kg/s) of LAS and Na_2SO_4 of the powder samples based on the three analytical methods, Conductivity, UV-Vis and $CatSO_3$ titration, at 20dC 100rpm, 200rpm and 40dC 100rpm are presented in Figure 6-11, Figure 6-12 and Figure 6-13 accordingly. UV-Vis and $CatSO_3$ results present that the rate of release of LAS is slower than Na_2SO_4

across the powder samples at different temperatures and agitation speed, although in some cases it might has the same or higher starting point than Na_2SO_4. This is due to the higher amount of sodium sulphate in the formulation of each powder sample. They also illustrate that at 20dC 100rpm LAS releases its amount instantly from the beginning of dissolution and it reaches a plateau in the first 5 s to 25 s of the process. In contrast from the Conductivity measurements we observe that Na_2SO_4 starts increasing progressively the release rate until it reaches a maximum value and then decreases until it stabilizes. This process takes from 50 s to 100 s depends on the powder sample. Increasing the temperature from 20dC to 40dC, the rate of release for both ingredients increases, while the time of release decreases. However, the effect of agitation speed is more dominant compared to temperature as it further enhances the release of ingredients. Both fluid related properties influence more the dW/dt of Na_2SO_4 (from 10^{-5} to 10^{-4} order of magnitude) than LAS which is probably due to the fact that they decrease the release time of LAS and as a consequence accelerate the dW/dt of sodium sulphate. This comes in agreement with the hypothesis stated in the previous Section 6.3.2 .

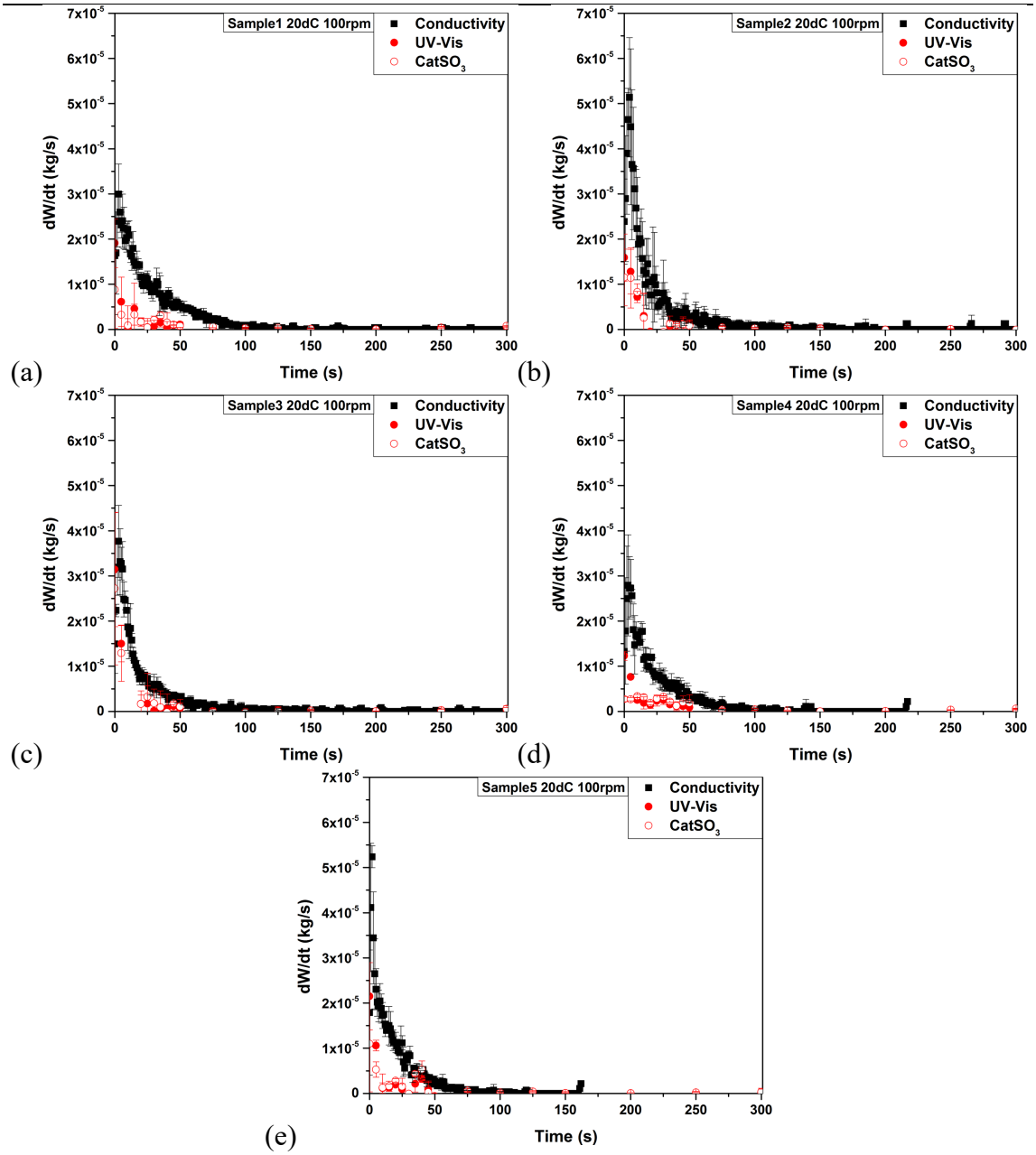

Figure 6-11 Comparison of dW/dt (kg/s) of Na_2SO_4 (conductivity) and LAS (UV-Vis and $CatSO_3$ titration) for (a) Sample1, (b) Sample2, (c) Sample3, (d) Sample4 and (e) Sample5 at 20dC 100 rpm.

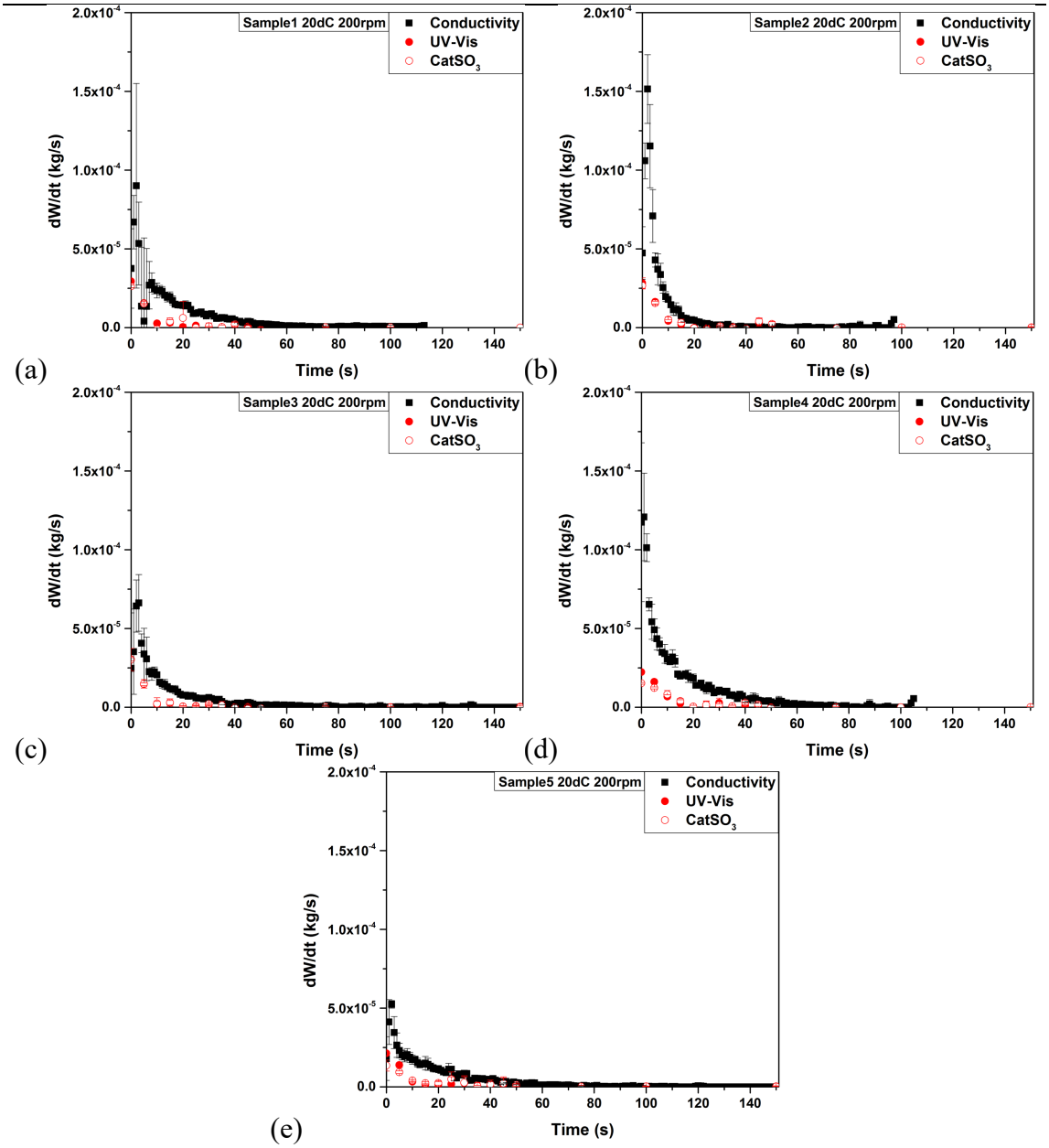

Figure 6-12 Comparison of dW/dt (kg/s) of Na_2SO_4 (conductivity) and LAS (UV-Vis and $CatSO_3$ titration) for (a) Sample1, (b) Sample2, (c) Sample3, (d) Sample4 and (e) Sample5 at 20dC 200 rpm.

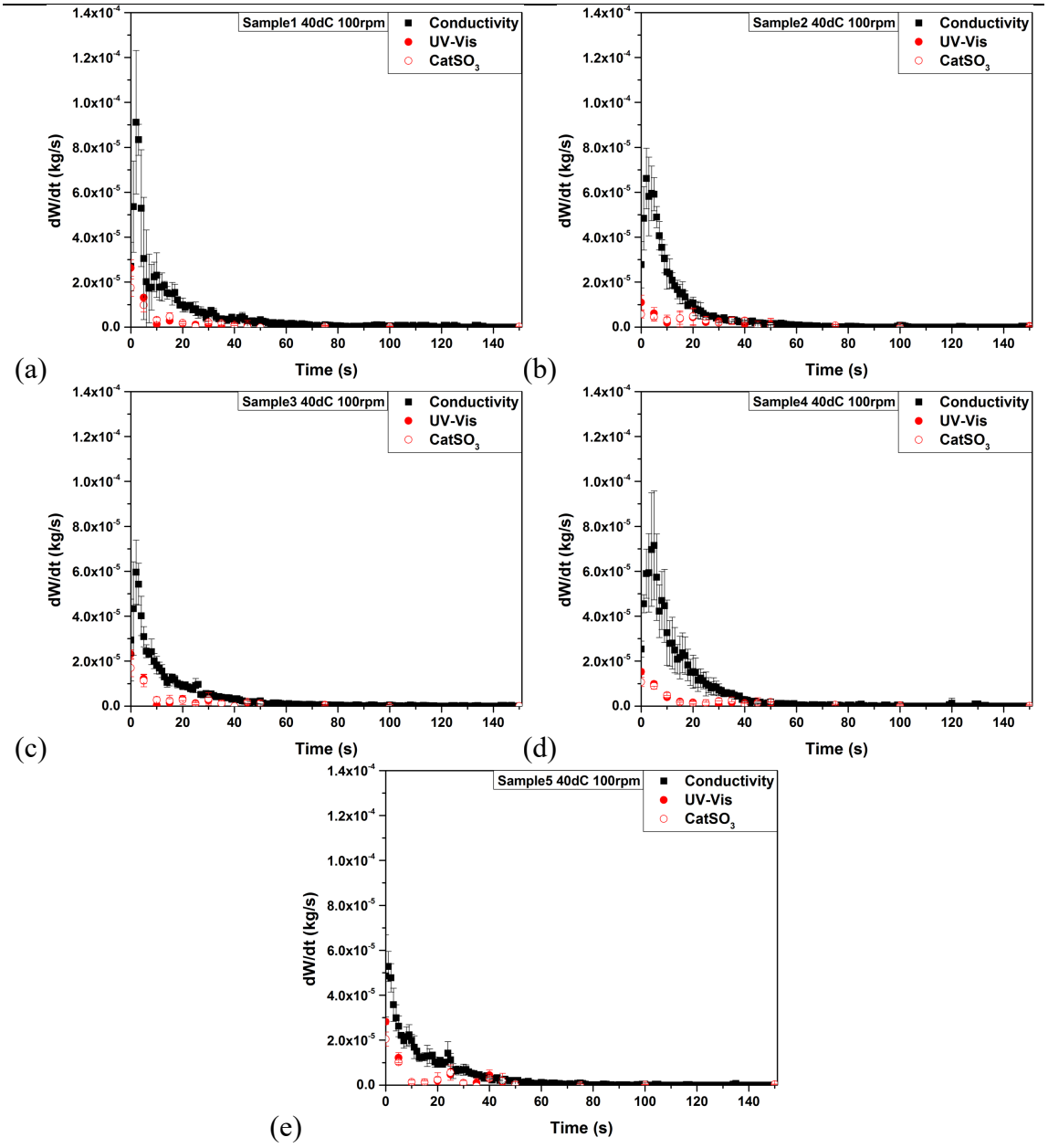

Figure 6-13 Comparison of dW/dt (kg/s) of Na_2SO_4 (conductivity) and LAS (UV-Vis and $CatSO_3$ titration) for (a) Sample1, (b) Sample2, (c) Sample3, (d) Sample4 and (e) Sample5 at 40dC 100 rpm.

6.3.4 Model to predict dissolution of LAS and Na_2SO_4

One of the primary goals as formulation scientists is to be able to design products that will meet the consumer requirements from the performance point of view. To do that we need tools that will allow us to predict how our products behave before they arrive in shelves of supermarkets. Precisely, in the detergent industry to achieve that we need

models to predict the dissolution behaviour of washing powders. Many dissolution models have been developed through the years. Some of them they were based in the theoretical analysis of the process, such as the first-order kinetics model, Higuchi model, and Hixson-Crowell model. While, some other were based on semi-empirical, empirical, such as the Korsmeyer-Peppas, Weibull, and logistic approaches to fit the dissolution data. A comprehensive analysis of the numerical dissolution expressions is expressed in Section 2.1.5 of Chapter 2. However, one of the main challenges of the industry is not only to model the dissolution performance of the product but to be able to predict the chemical release of its components. That will give it the ultimate power to be able to control dissolution.

In this study, we compared different dissolution models existed in the literature to find the most appropriate one for modelling of LAS and Na_2SO_4 release. The first order kinetics model, Weibull model, Hixson-Crowell model and Higuchi model were fitted to dissolution curves obtained from Conductivity for LAS and UV-Vis, $CatSO_3$ for Na_2SO_4 data as presented in Figure 6-8, Figure 6-9 and Figure 6-10 using the Curve Fitting Toolbox application of Matlab (Matlab R2017a, The MathWorks Inc., Natick, MA, 2017). In general, the method of selecting the most appropriated dissolution model is based on descriptive statistics of regression. The most widely used method is the comparison of determination coefficient (R^2). For a well-fitting model, R^2 should be close to 1.

However, none of the above models was able to predict the chemical release of LAS and Na_2SO_4 at 20dC 100rpm, 200rpm and 40dC 100rpm with a high level of confidence. Characteristic results of the poor fitting of the models at 20dC 100rpm are presented in

Table 6.2. Overall the confidence of these dissolution models was below 50%. Therefore, these models can not be used for this purpose.

Table 6.2 Values of determination coefficient R^2 from measurement data of the ingredients of each powder sample for dissolution models at 20dC 100rpm.

Samples	Ingredients	Determination coefficient R^2			
		First order kinetics	Weibull	Hixson-Crowell	Higuchi
Sample1	Na_2SO_4	0.266	0.295	0.324	0.426
	LAS	0.253	0.275	0.315	0.385
Sample2	Na_2SO_4	0.255	0.296	0.384	0.435
	LAS	0.215	0.238	0.268	0.326
Sample3	Na_2SO_4	0.240	0.275	0.326	0.415
	LAS	0.222	0.225	0.305	0.363
Sample4	Na_2SO_4	0.236	0.250	0.315	0.401
	LAS	0.196	0.216	0.296	0.370
Sample5	Na_2SO_4	0.241	0.265	0.333	0.428
	LAS	0.235	0.231	0.275	0.393

The lack of fitting is due to the limited amount of information that can be implanted in the model. So, a dissolution model that takes into account, particle size, the temperature of solvent, agitation speed and mass transfer coefficient would be an ideal candidate. The dissolution model developed by Cao et al., [114] for the prediction of bulk dissolution on turbulent conditions where all the granules are well distributed in the dissolution vessel, contains the information described above. This model combines CFD simulation and Noyes-Whitney equation with initial granule parameters such as density, solubility, size

distribution and diffusivity. Moreover, the power input of the dissolution system is linked with particle mass transfer by Sherwood number which is obtained through energy dissipation rate in the system. The modelling framework is presented in Figure 2-25. The fluid related properties were acquired from Table 3.3 and Table 3.4, while systems conditions were defined based on Table 6.3. Table 6.1 was used for the amount of ingredients in each powder sample. The values of bulk density ρ_b and solubility C_s of ingredients used in this model are presented in Table 6.4. An important assumption that had to be made was that the ingredients are homogeneously dispersed in the granule. So, the mass distribution of each size fraction obtained from the PSD technique for each sample (see Figure 3-6) was used as a reference for fitting the model for each ingredient.

Table 6.3 Power input *P* (W) and turbulent energy dissipation rate *ε* (W/kg) in mixing tank with 800 mL of water [114].

Temperature (dC)	Agitation speed *N* (rpm)	Power input *P* (W)	Turbulent energy dissipation rate *ε*(W/kg)
20	**100**	0.010	0.012
	200	0.077	0.097
40	**100**	0.010	0.012

Table 6.4 Bulk density ρ_b (kg/m^3) and solubility C_s (kg/m^3) of LAS and Na_2SO_4 (values provided by P&G).

Ingredient	Physical Property		
	ρ_b (kg/m^3)	C_s (kg/m^3)	
		20dC	40dC
Na_2SO_4	2664	192.3	478.2
LAS	1060	250	280

The comparison of experimentally acquired (Conductivity, UV-Vis and $CatSO_3$) and modelled release profiles of the main spray-dried detergent powder compounds, LAS and Na_2SO_4 for each powder sample at 20dC 100rpm, 200rpm and 40dC 100rpm are illustrated in Figure 6-14 - Figure 6-16 respectively. A very good correlation between experimental and modelling data of Sample1, Sample2 and Sample5 can be observed, across the different experimental conditions for Na_2SO_4. However, a significant lack of fit is presented for the prediction of LAS from both UV-Vis and $CatSO_3$ experimental results. The model can predict very well only the initial stage (first 5 s) of the chemical release of LAS but not the full curve. This has occurred because the total experimental dissolution time is longer than the predicted as some physicochemical parameters (e.g. particle size, diffusivity, solubility) used in the modelling might not be accurate. An important assumption that had to be made was that the components are spherical instead of irregularly shaped as and Figure 3-16 have shown for Na_2SO_4 crystals. Therefore, the

area of an equivalent diameter sphere was used in the model. Furthermore, although the diffusivity of Na_2SO_4 was obtained from Nernst equation (2-10) and Table 2.1 was not sufficient, and the diffusivity of LAS was unknown. Thus, modification on diffusivities (see Table 6.5) had to be made to make the modelling results agree with experimental data. Overall the model shows a confidence of 97.2 ± 1.50% (see Table 6.5) for the prediction of Na_2SO_4. While for LAS the level of confidence is 83.3 ± 18.6% (see Table 6.5).

Table 6.5 Comparison of diffusivity obtained from Nernst equation (2-10) and Table 2.1 and experiment fitting results D_{fit} at 20dC 100rpm, 200rpm and 40dC 100rpm for LAS and Na_2SO_4 each powder sample. The R^2 is also presented.

Samples and compounds		Experimental conditions								
		20dC 100rpm			20dC 200rpm			40dC 100rpm		
		Diffusivity (10^{-10} m/s)		R^2	Diffusivity (10^{-10} m/s)		R^2	Diffusivity (10^{-10} m/s)		R^2
		D	D_{fit}		D	D_{fit}		D	D_{fit}	
Sample1	**Na_2SO_4**	4.03	40.3	0.982	4.03	42.1	0.977	6.61	40.3	0.944
	LAS	-	40.3	0.204	-	71.1	0.911	-	61.1	0.816
Sample2	**Na_2SO_4**	4.03	61.1	0.950	4.03	311	0.981	6.61	31.1	0.974
	LAS	-	41.1	0.869	-	71.1	0.948	-	31.1	0.791
Sample3	**Na_2SO_4**	4.03	61.1	0.954	4.03	71.1	0.956	6.61	31.1	0.965
	LAS	-	161	0.929	-	81.1	0.861	-	61.1	0.798
Sample4	**Na_2SO_4**	4.03	61.1	0.988	4.03	71.1	0.969	6.61	31.1	0.984
	LAS	-	55.5	0.921	-	51.1	0.981	-	51.1	0.954
Sample5	**Na_2SO_4**	4.03	61.1	0.989	4.03	71.1	0.989	6.61	31.1	0.984
	LAS	-	65.5	0.789	-	51.1	0.928	-	91.1	0.806

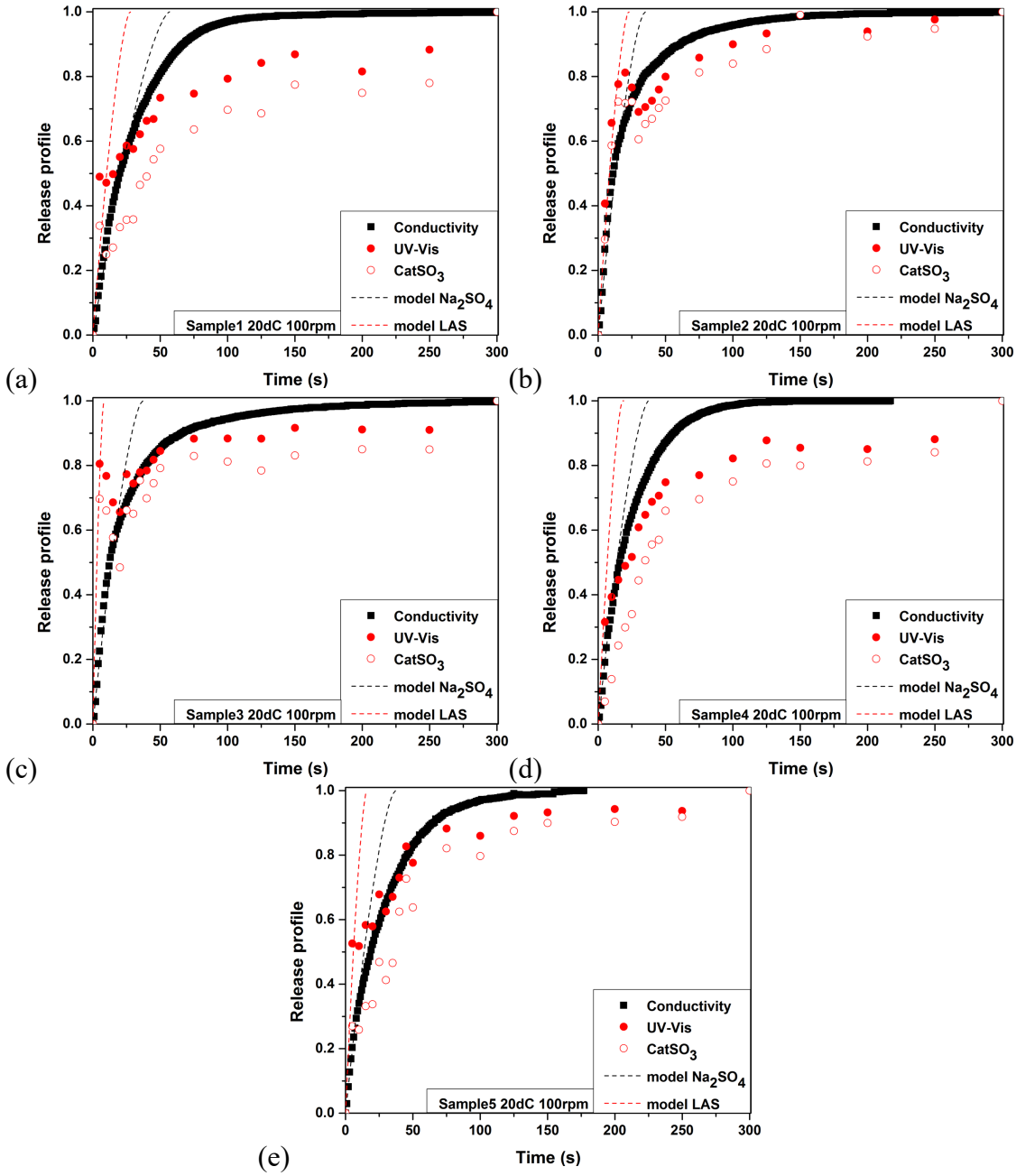

Figure 6-14 Dissolution profiles of experiment data vs modelling of Na_2SO_4 and LAS for (a) Sample1, (b) Sample2, (c) Sample3, (d) Sample4 and (e) Sample5 at 20dC 100 rpm.

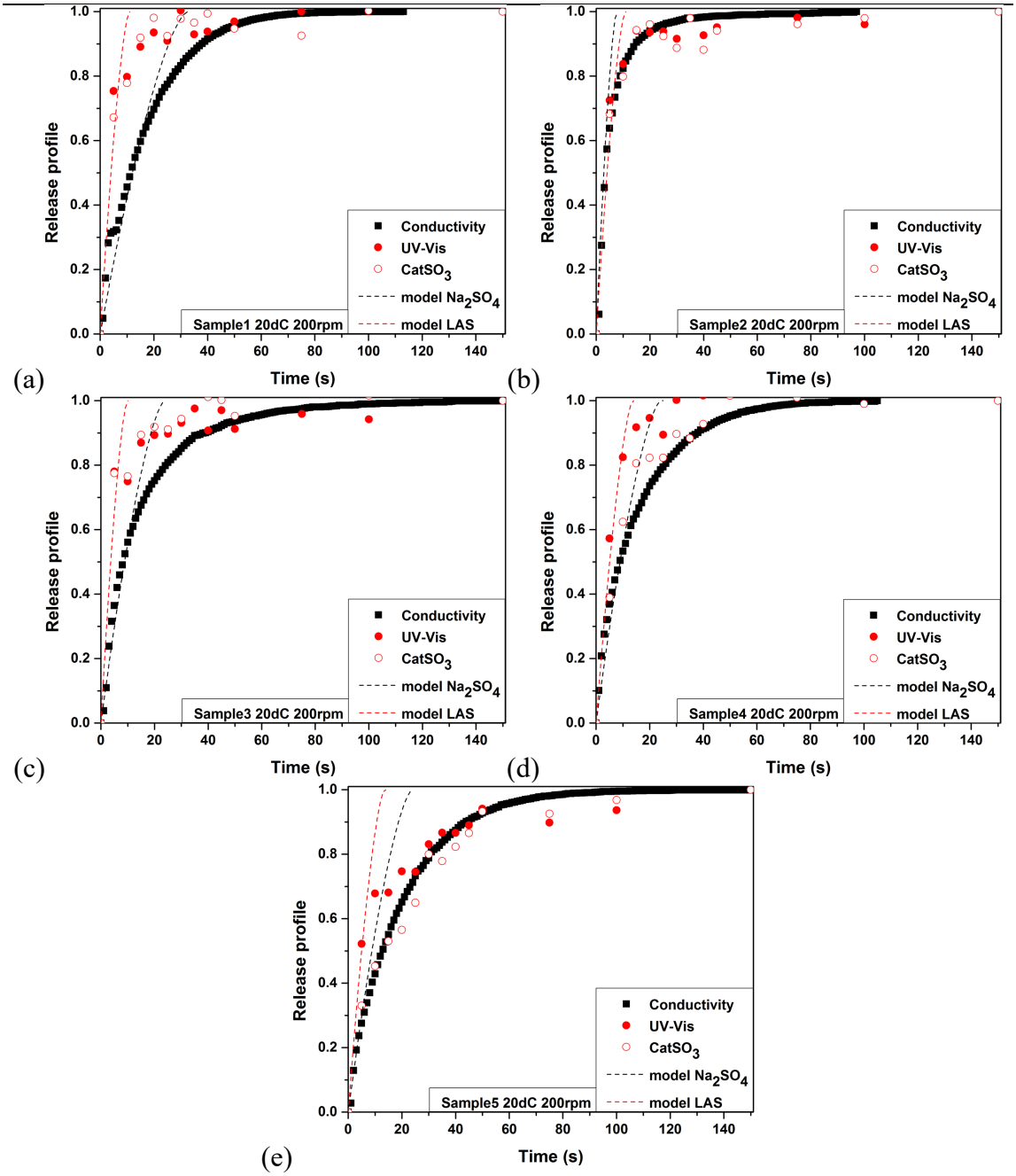

Figure 6-15 Dissolution profiles of experiment data vs modelling of Na_2SO_4 and LAS for (a) Sample1, (b) Sample2, (c) Sample3, (d) Sample4 and (e) Sample5 at 20dC 200 rpm.

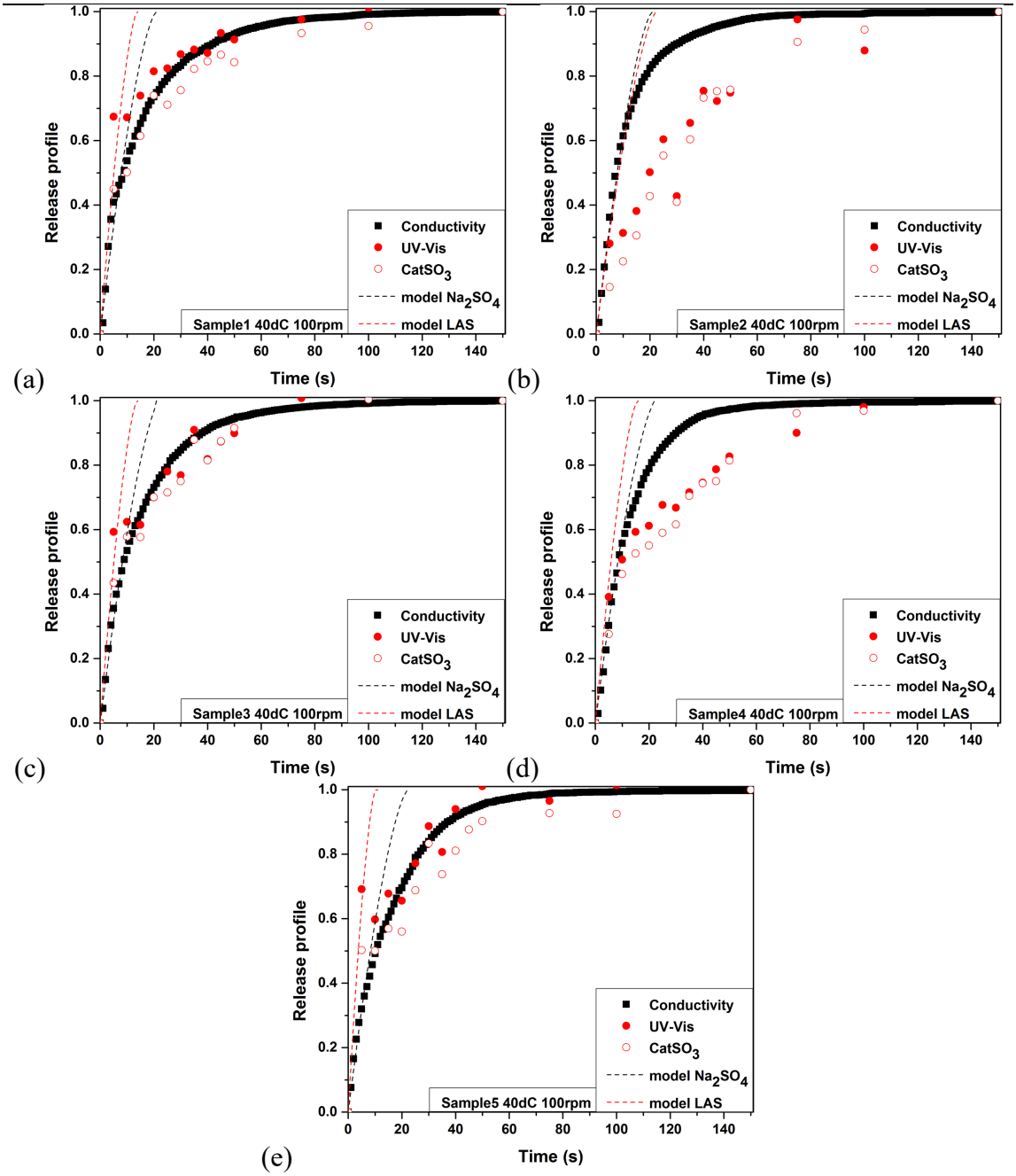

Figure 6-16 Dissolution profiles of experiment data vs modelling of Na_2SO_4 and LAS for (a) Sample1, (b) Sample2, (c) Sample3, (d) Sample4 and (e) Sample5 at 40dC 100 rpm.

6.4 Conclusions

In this present study, three different analytical methods, Conductivity, UV-Vis and $CatSO_3$ were compared to investigate the chemical release of the main components of a spray-dried detergent powder, LAS and Na_2SO_4 in turbulent conditions. Then, release

profiles of the compounds were fitted to different dissolution models to determine the most applicable. Results showed two distinct phases of the chemical release of LAS and Na_2SO_4. In the first phase, that LAS dissolves faster than Na_2SO_4 while in the second the opposite lies. The timescale of each phase depends on the type and the content of the binder and the fluid related properties. UV-Vis showed good agreement with $CatSO_3$ titration results and can be regarded as a feasible method for studying dissolution of LAS. From the comparison of the experimental results with the different dissolution models found in the literature, a bulk dissolution model that implements the energy dissipation rate of the system [114] regarded as the most appropriate for the prediction of Na_2SO_4 (R^2=0.972 ± 0.01) and LAS release (R^2=0.833 ± 0.18).

CHAPTER 7 OVERALL CONCLUSIONS AND FUTURE WORK

7.1 Overall conclusions

Dissolution is a key consumer perceivable property of both laundry hand wash and machine wash detergents. Granule dissolution can be influenced by particle size and composition, but these can be only varied within certain fixed constraints dictated by performance criteria, consumer acceptance and cost. This makes dissolution behaviour a prime candidate for optimisation via manipulation of granule microstructure and material components. In particular, it is essential to develop solutions as we understand that stress is placed on dissolution as:

- we move to shorter wash times and lower wash temperatures
- we move to lower water consumption
- we move to concentrate powders.

This whole study was aimed to establish new design rules for the formulation of highly soluble, fast releasing, leaving no residue spray-dried detergent particles. Building an ideal particle is the ultimate goal which industry has been pursuit for a long time.

Therefore, an optical methodology has been applied to understand single particle diffusion dissolution mechanisms. A significant variance has been observed from particle to particle due to the diversity in particle size, shape, surface morphology (e.g. agglomeration level), internal structure (e.g. thin layer shell structure vs foam shape shell structure, existence of undissolved salt) and binder materials. Raw dissolution data were implemented into the Mont Carlo statistical analysis to predict bulk particle dissolution profiles with particle size distribution information. Such results were compared to chemical analytical measurement of bulk particle dissolution profiles. The comparison between these two approaches reveals for the first time the binder materials impact on inter-particle cohesive effect on particle dissolution. For the investigated particle system,

the effect of silicate polymerization during dissolution can be significantly reduced by increasing salt concentration in the local area around particles. While citric acid works as a disintegrant besides binder function and shows the best performance overall even with a lower porosity (73%) than particles without binder but much higher porosity (85%).

To provide an understanding of the dissolution mechanisms of spray-dried detergent particles within a "micro wash environment" under standard conditions a novel microfluidic dissolution testing device was developed. The comparison of GPV experimental data and COMSOL simulation measurements has been used of the calibration of the system. In single particle convective dissolution, the hydrodynamic conditions rather than the phenomena control the process which results in up to 79% faster performance of the particles. Furthermore, convection does not allow polymerisation of Silicate to take place. A new dissolution framework was developed for the prediction of single particle convective dissolution. The direct link between particle velocity and dissolution performance enables the industry to minimize the amount of experimental work when extrapolating particle dissolution performance from bench scale measurements to any washing system/condition, which eventually could significantly shorter product design process.

Another challenge of the formulation industry is the controlled release of the powder components. Bulk dissolution experiments showed that Conductivity could be used as a valuable tool for the detection of the release of Na2SO4 while the combination of UV-Vis and CatSO3 titration can measure accurately the release of LAS. Two regions constitute the release of the components. The first region (in the initial moments of dissolution, from 0 s up to 30 s) where LAS dissolves faster than Na2SO4 and the second region where LAS releases slower or equal than Na2SO4. The orientation of these regions

depends on the temperature, agitation speed and binder content. A bulk dissolution model that combines Noyes-Whitney equation and the energy dissipation rate of the system considered as the most suitable for the prediction of Na2SO4 ($R2=0.972 \pm 0.01$) and LAS release ($R2=0.833 \pm 0.18$). The manipulation of LAS and Na2SO4 release will deliver better powder performance, no residues to consumers clothes and higher profit margin for the detergent industry.

7.2 Future Work

A significant amount of interesting research can be followed based on the work presented in this thesis.

- Chapter 4 showed that the particle interactions have a significant effect on dissolution kinetics of multi-component powders as they can prevent the polymerization of Silicate and accelerate the dissolution process. However, a limited amount of study has been conducted as it was not one of the aims of this research. Thus, a proper study on understanding of particle-particle interactions, the physics behind it (DLVO theory) and the link with the dissolution kinetics is suggested.
- In Chapter 5, a dissolution testing device was developed for laminar flow dissolution studies and the extracted particle velocity was used to build a model. In addition, it will be of interest to study both experimentally and numerical the relative velocity around the particle surface under turbulent conditions and then use it as implementation to the model that developed in Chapter 5. This will allow the prediction of bulk dissolution with different agitation speed and temperature by studying a single granule.

- The methodologies that has been developed in Chapter 4 and Chapter 5, are based on a 2D observation of particle dissolution and a consequence a lot of morphological information are missing. A 3D optical observation is suggested for the assessment of single particle dissolution. The 3D data could be used to build virtual models of the single particles. This will allow the exact in silico observation of surface topographic dissolution rates, as well as an accurate simulation of particle size dependent dissolution rates.
- Finally, the use of ATR-FTIR spectroscopic imaging is suggested for the visualization of the chemical release of the spray-dried detergent powder main components. This research work will validate the hypothesis that has been stated in this thesis about the mechanisms of chemical release of ingredients.

BIBLIOGRAPHY

[1] A. Marabi, G. Mayor, A. Burbidge, R. Wallach, and I. S. Saguy, "Assessing dissolution kinetics of powders by a single particle approach," *Chem. Eng. J.*, vol. 139, no. 1, pp. 118–127, May 2008.

[2] S. Thakur, H. Ahmadian, J. Sun, and J. Ooi, "An experimental and numerical study of packing, compression, and caking behaviour of detergent powders," *Particuology*, vol. 12, no. 1, pp. 2–12, Feb. 2014.

[3] J. P. K. Seville, A. D. Salman, and M. J. Hounslow, *Handbook of Powder technology - Granulation*. 2007.

[4] R. Boerefijn, P. R. Dontula, and R. Kohlus, "Chapter 14 Detergent granulation," *Handb. Powder Technol.*, vol. 11, pp. 673–703, 2007.

[5] V. F. Frolov, "Dissolution of disperse materials," *Theor. Found. Chem. Eng.*, vol. 32, no. 4, 1998.

[6] W. L. Hsu, M. J. Lin, and J. P. Hsu, "Dissolution of Solid Particles in Liquids:A Shrinking Core Model," *World Acad. Sci. Eng. Technol.*, vol. 3, no. i, pp. 2009-05-21, 2009.

[7] H. Schubert, "Food particle technology. Part I: Properties of particles and particulate food systems," *J. Food Eng.*, vol. 6, no. 1, pp. 1–32, 1987.

[8] L. Forny, A. Marabi, and S. Palzer, "Wetting, disintegration and dissolution of agglomerated water soluble powders," *Powder Technol.*, vol. 206, no. 1–2, pp. 72–78, Jan. 2011.

[9] M. Nicklasson, A. Brodin, and L. O. Sundelof, "On the determination of true dissolution rate parameters from rotating disc experiments," *Int. J. Pharm.*, vol. 1, pp. 87–95, 1983.

[10] S. N. Bhattachar, J. A. Wesley, A. Fioritto, P. J. Martin, and S. R. Babu, "Dissolution testing of a poorly soluble compound using the flow-through cell dissolution apparatus," *Int. J. Pharm.*, vol. 236, no. 1–2, pp. 135–143, 2002.

[11] E. Kaunisto, B. Nilsson, and A. Axelsson, "Drug dissolution rate measurements--evaluation of the rotating disc method.," *Pharm. Dev. Technol.*, vol. 14, no. December 2008, pp. 400–408, 2009.

[12] A. Gianfrancesco, C. Casteran, J. C. Andrieux, M. I. Giardiello, and G. Vuataz, "Assessment of physical characteristics and dissolution behavior of protein based powders," *Procedia Food Sci.*, vol. 1, pp. 601–607, 2011.

[13] T. P. Kravtchenko, J. Renoir, a. Parker, and G. Brigand, "A novel method for determining the dissolution kinetics of hydrocolloid powders," *Food Hydrocoll.*, vol. 13, no. 3, pp. 219–225, May 1999.

[14] Q. Wang, P. R. Ellis, and S. B. Ross-Murphy, "Dissolution kinetics of guar gum powders. I. Methods for commercial polydisperse samples," *Carbohydr. Polym.*, vol. 49, no. 2, pp. 131–137, 2002.

[15] Q. Wang, P. R. Ellis, and S. B. Ross-Murphy, "Dissolution kinetics of guar gum powders - II. Effects of concentration and molecular weight," *Carbohydr. Polym.*, vol. 53, no. 1, pp. 75–83, 2003.

[16] Q. Wang, P. R. Ellis, and S. B. Ross-Murphy, "Dissolution kinetics of guar gum powders-III. Effect of particle size," *Carbohydr. Polym.*, vol. 64, no. 2, pp. 239–246, 2006.

[17] C. K. Larsen, O. Gåserød, and O. Smidsrød, "A novel method for measuring hydration and dissolution kinetics of alginate powders," *Carbohydr. Polym.*, vol. 51, no. 2, pp. 125–134, 2003.

[18] A. Marabi, G. Mayor, A. Raemy, I. Bauwens, J. Claude, A. S. Burbidge, R. Wallach, and I. S. Saguy, "Solution calorimetry: A novel perspective into the dissolution process of food powders," *Food Res. Int.*, vol. 40, no. 10, pp. 1286–1298, 2007.

[19] M. A. Ansari and F. Stepanek, "The effect of granule microstructure on dissolution rate," *Powder Technol.*, vol. 181, no. 2, pp. 104–114, Feb. 2008.

[20] W. L. Hulse, J. Gray, and R. T. Forbes, "A discriminatory intrinsic dissolution study using UV area imaging analysis to gain additional insights into the dissolution behaviour of active pharmaceutical ingredients," *Int. J. Pharm.*, vol. 434, no. 1–2, pp. 133–139, 2012.

[21] A. Avdeef, K. Tsinman, O. Tsinman, N. Sun, and D. Voloboy, "Miniaturization of powder dissolution measurement and estimation of particle size," *Chem. Biodivers.*, vol. 6, no. 11, pp. 1796–1811, 2009.

[22] M. Mosharraf and C. Nyström, "The effect of particle size and shape on the surface specific dissolution rate of microsized practically insoluble drugs," *Int. J. Pharm.*, vol. 122, no. 1–2, pp. 35–47, 1995.

[23] J. Wang and D. R. Flanagan, "General solution for diffusion-controlled dissolution of spherical particles. 1. Theory," *J. Pharm. Sci.*, vol. 88, no. 7, pp. 731–738, 1999.

[24] T. Allen, *Particle Size Measurement*, 5th ed. Padstow, Cornwall: T.J. Press (Padstow) Ltd., 1997.

[25] B. Bechtloff, P. Jüsten, and J. Ulrich, "The Kinetics of Heterogeneous Solid-Liquid Reaction Crystallizations—An Overview and Examples," *Chemie Ing. Tech.*, no. 73, pp. 453–460, 2001.

[26] B. R. Bhandari and Y. H. Roos, "Dissolution of sucrose crystals in the anhydrous

sorbitol melt," *Carbohydr. Res.*, vol. 338, no. 4, pp. 361–367, 2003.

[27] J. Ostergaard, H. Jensen, S. W. Larsen, C. Larsen, and J. Lenke, "Microenvironmental pH measurement during sodium naproxenate dissolution in acidic medium by UV/vis imaging.," *J. Pharm. Biomed. Anal.*, vol. 100, pp. 290–3, Nov. 2014.

[28] S. Svanbäck, H. Ehlers, and J. Yliruusi, "Optical microscopy as a comparative analytical technique for single-particle dissolution studies.," *Int. J. Pharm.*, vol. 469, no. 1, pp. 10–6, Jul. 2014.

[29] C. Li, C. Amador, and Y. Ding, "An investigation on dissolution kinetics of single sodium carbonate particle with image analysis method," *Chinese J. Chem. Eng.*, vol. 24, no. 10, pp. 1487–1496, 2016.

[30] S. Dorozhkin, "Fundamentals of the wet-process phosphoric acid production. 1. Kinetics and mechanism of the phosphate rock dissolution," *Ind. Eng. Chem. Res.*, vol. 5885, no. Figure 1, pp. 4328–4335, 1996.

[31] S. L. Raghavan, R. I. Ristic, D. B. Sheen, and J. N. Sherwood, "Dissolution kinetics of single crystals of α-lactose monohydrate," *J. Pharm. Sci.*, vol. 91, no. 10, pp. 2166–2174, 2002.

[32] K. V. R. Prasad, R. I. Ristic, D. B. Sheen, and J. N. Sherwood, "Dissolution kinetics of paracetamol single crystals," *Int. J. Pharm.*, vol. 238, no. 1–2, pp. 29–41, 2002.

[33] E. Börjesson, F. Innings, C. Trägårdh, B. Bergenståhl, and M. Paulsson, "The dissolution behavior of individual powder particles," *Dairy Sci. Technol.*, vol. 93, no. 4–5, pp. 357–371, 2013.

[34] S. Svanback, H. Ehlers, O. Antikainen, and J. Yliruusi, "High-Speed Intrinsic

Dissolution Rate in One Minute Using the Single-Particle Intrinsic Dissolution Rate Method," *Anal. Chem.*, vol. 87, no. 21, pp. 11058–11064, 2015.

[35] D. Smrčka, J. Dohnal, and F. Štěpánek, "Dissolution and disintegration kinetics of high-active pharmaceutical granules produced at laboratory and manufacturing scale," *Eur. J. Pharm. Biopharm.*, 2016.

[36] A. A. Noyes and W. R. Whitney, "The Rate of Solution of Solid Substances in Their Own Solutions," *J. Am. Chem. Soc.*, vol. 19, no. 12, pp. 930–934, 1897.

[37] J. Wang and D. R. Flanagan, "General solution for diffusion-controlled dissolution of spherical particles. 2. Evaluation of experimental data," *J. Pharm. Sci.*, vol. 91, no. 2, pp. 534–542, 2002.

[38] W. Nernst, "Theorie der Reaktionsgeschwindigkeit in heterogenen Systemen," *Z. Phys. Chem.*, vol. 47, pp. 52–55, 1904.

[39] C. G. Varelas, D. G. Dixon, and C. A. Steiner, "Zero-order release from biphasic polymer hydrogels," *J. Control. Release*, vol. 34, no. 3, pp. 185–192, 1995.

[40] W. I. Higuchi, "Diffusional models useful in biopharmaceutics. Drug release rate processes," *J. Pharm. Sci.*, vol. 56, no. 3, pp. 315–324, 1967.

[41] L. Brunner and S. Tolloczko, "Über die Auflösungsgeschwindigkeit fester Körper," *Zeitschrift für Anorg. Chemie*, vol. 28, no. 1, pp. 314–330, Nov. 1901.

[42] E. Brunner, "Reaktionsgeschwindigkeit in heterogenen Systemen," *Zeitschrift für Phys. Chemie*, vol. 43, p. 47, 1904.

[43] A. W. Hixson and J. H. Crowell, "Dependence of Reaction Velocity upon Surface and Agitation," *Ind. Eng. Chem.*, vol. 23, no. 8, pp. 923–931, 1931.

[44] M. Wildermann, "Über die Geschwindigkeit molekularer und chemischer Reaktionen in heterogenen Systemen," *Zeitschrift für Phys. Chemie*, vol. 66, no.

1, pp. 445–495, 1909.

[45] C. Wilke and P. Chang, “Correlations of diffusion coefficients in dilute solutions,” *AICHE J.*, vol. 1, no. 2, pp. 264–270, 1955.

[46] J. Frenkel, *Kinetic Theory of Liquids*. Oxford: Clarendon Press, 1946.

[47] G. Wypych, *Handbook of Solvents*. 2001.

[48] W. Nernst, “Zur Kinetik der in Lösung befindlichen Körper,” *Zeitschrift für Phys. Chemie*, vol. 2, p. 613, 1888.

[49] A. B. Zdanovskii, “The role of the interphase solution in the kinetics of the solution of salts,” *Zhur. Fiz. Khim.*, no. 20, pp. 869–880, 1946.

[50] R. A. Robinson and R. H. Stokes, *Electrolyte solutions*, 2nd editio. Dover Publications, 2002.

[51] E. L. Cussler, *Diffusion Mass Transfer in Fluid Systems*, 3rd editio. Cambridge University Press, 2009.

[52] M. Nicklasson and A. B. Magnusson, “Program for Evaluating Drug Dissolution Kinetics in Preformulation,” *Pharm. Res.*, vol. 2, no. 6, pp. 262–266, Nov. 1985.

[53] D. E. Wurster and P. W. Taylor, “Dissolution Rates,” *J. Pharm. Sci.*, vol. 54, no. 2, pp. 169–175, Feb. 1965.

[54] R. G. Van Name and D. U. Hill, “On the influence of alcohol and of cane sugar upon the rate of solution of cadmium in dissolved iodine,” *Am. J. Sci.*, no. 36, pp. 543–554, 1913.

[55] R. G. Van Name and D. U. Hill, “On the rates of solution of metals in ferric salts and in chromic acid,” *Am. J. Sci.*, no. 42, p. 32, 1916.

[56] C. V King, “Reaction Rates at Solid—Liquid Interfaces,” *J. Am. Chem. Soc.*, vol. 57, no. 5, pp. 828–831, 1935.

[57] A. Fage and H. C. H. Townend, "An Examination of Turbulent Flow with an Ultramicroscope," *Proc. R. Soc. London. Ser. A*, vol. 135, no. 828, p. 656, Apr. 1932.

[58] J. Crank, *The Mathematics of Diffusion*, 2nd editio. Uxbridge: Oxford: Clarendon Press, 1979.

[59] V. Koganti, F. Carroll, R. Ferraina, R. Falk, Y. Waghmare, M. Berry, Y. Liu, K. Norris, R. Leasure, and J. Gaudio, "Application of Modeling to Scale-up Dissolution in Pharmaceutical Manufacturing," *AAPS PharmSciTech*, vol. 11, no. 4, pp. 1541–1548, 2010.

[60] D. M. Levins and J. R. Glastonbury, "Particle-Liquid Hydrodynamics and Mass Transfer in a Stirred Vessel. Part 2. Mass Transfer," *Trans. Inst. Chem. Eng.*, vol. 50, no. 1, pp. 32–46, 1972.

[61] V. Pillay and R. Fassihi, "Unconventional dissolution methodologies," *J. Pharm. Sci.*, vol. 88, no. 9, pp. 843–851, 1999.

[62] Y. Chen, J. Wang, and D. R. Flanagan, *Chapter 9 – Fundamental of Diffusion and Dissolution*. Elsevier Inc., 2017.

[63] W. Weibull, "A statistical distribution function of wide applicability," *J. Appl. Mech.*, vol. 18, pp. 293–297, 1951.

[64] P. J. Niebergall, "Dissolution rate studies II. Dissolution of particles under conditions of rapid agitation," *J. Pharm. Sci.*, vol. 52, no. 3, pp. 236–241, 1963.

[65] W. I. Higuchi and E. N. Hiestand, "Dissolution rates of finely divided drug powders I. Effect of a distribution of particle sizes in a diffusion-controlled process," *J. Pharm. Sci.*, vol. 52, no. 1, pp. 67–71, 1963.

[66] W. I. Higuchi, E. L. Rowe, and E. N. Hiestand, "Dissolution rates of finely divided

drug powders II. Micronized methylprednisolone," *J. Pharm. Sci.*, vol. 52, no. 2, pp. 162–164, Oct. 1963.

[67] R. W. Baker and H. K. Lonsdale, "Controlled release: mechanisms and release," in *Controlled release of biologically active agents*, New York: Plenum Press, 1974, pp. 15–71.

[68] R. W. Korsmeyer, R. Gurny, E. Doelker, P. Buri, and N. A. Peppas, "Mechanisms of solute release from porous hydrophilic polymers," *Int. J. Pharm.*, 1983.

[69] H. B. Hopfenberg, "Controlled Release from Erodible Slabs, Cylinders, and Spheres," in *Controlled Release Polymeric Formulations*, vol. 33, Americal Chemical Society, 1976, pp. 26–32.

[70] M. Gibaldi and S. Feldman, "Establishment of sink conditions in dissolution rate determinations. Theoretical considerations and application to nondisintegrating dosage forms," *J. Pharm. Sci.*, vol. 56, no. 10, pp. 1238–1242, Oct. 1967.

[71] J. G. Wagner, "Interpretation of percent dissolved-time plots derived from in vitro testing of conventional tablets and capsules," *J. Pharm. Sci.*, vol. 58, no. 10, pp. 1253–1257, Oct. 1969.

[72] F. Langenbucher, "Letters to the Editor: Linearization of dissolution rate curves by the Weibull distribution," *J. Pharm. Pharmacol.*, vol. 24, no. 12, pp. 979–981, Dec. 1972.

[73] M. Bisrat and C. Nystrom, "Physicochemical aspects of drug release. VIII. The relation between particle size and surface specific dissolution rate in agitated suspensions," *Int. J. Pharm.*, vol. 47, no. 1–3, pp. 223–231, 1988.

[74] C. Galli, "Experimental determination of the diffusion boundary layer width of micron and submicron particles," *Int. J. Pharm.*, vol. 313, no. 1–2, pp. 114–122,

2006.

[75] R. J. Hintz and K. C. Johnson, “The effect of particle size distribution on dissolution rate and oral absorption,” *Int. J. Pharm.*, vol. 51, no. 1, pp. 9–17, 1989.

[76] E. Sneed and R. Folk, “Pebbles in the Lower Colorado River, Texas a Study in Particle Morphogenesis,” *J. Geol.*, vol. 66, no. 2, pp. 114–150, 1958.

[77] T. Zingg, “Beitrag zur schotteranalyse,” Eidgenössische Technische Hochschule Zürich, 1935.

[78] A. Keith and P. Bouza, “The Impact of Dissolution on Particle Size and Particle Shape of Multi-Component Drug Delivery Systems,” p. 30093.

[79] X. Jia and R. A. Williams, “From microstructures of tablets and granules to their dissolution behaviour,” *Dissolution Technol.*, vol. 13, no. 2, pp. 11–19, 2006.

[80] Q. Yuan, X. Jia, and R. A. Williams, “Validation of a multi-component digital dissolution model for irregular particles,” *Powder Technol.*, vol. 240, pp. 25–30, May 2013.

[81] C. Nyström, M. I. Barnett, J. Mazur, and M. Glazer, “Determination of the solubility and teh dissolution rate of polydispersed materials from particle weight and surface area data using a TAII Coulter counter,” in *Proceedings of the 5th Conference on Particle Size Analysis*.

[82] J. T. Carstensen, *Solid Pharmaceutics: Mechanical Properties and Rate Phenomena*. London: Academic Press, 1980.

[83] M. Nicklasson and A. Brodin, “The relation between intrinsic dissolution rates and solubilities in water-ethanol binary solvent system,” *Int. J. Pharm.*, no. 18, pp. 149–155, 1984.

[84] G. Barbosa-Canovas, E. Ortega- Rivas, P. Juliano, and H. Yan, *FOOD POWDERS*

Physical Properties, Processing, and Functionality. 2005.

[85] C. Cavallari, B. Abertini, M. L. González-Rodríguez, and L. Rodriguez, "Improved dissolution behaviour of steam-granulated piroxicam," *Eur. J. Pharm. Biopharm.*, vol. 54, no. 1, pp. 65–73, 2002.

[86] L. Schenck, S. Jain, M. Moaddeb, N. Birringer, B. Sell, L. Kline, M. Kenning, and R. Plank, "Application of correlation between granule porosity and tablet dissolution to process development and scale-up of wet granulated formulations," in *AAPS 2004 Annual Meeting*, 2004.

[87] F. Stepanek, "Computer-aided product design - Granule dissolution," *Chem. Eng. Res. Des.*, vol. 82, no. A11, pp. 1458–1466, 2004.

[88] A. Juppo and J. Yliruusi, "Effect of amount of granulation liquid on total pore volume and pore size distribution of lactose, glucose and mannitol granules," *Eur. J. Pharm. Biopharm.*, vol. 40, pp. 299–309, 1994.

[89] L. F. Huang and W. Q. (Tony) Tong, "Impact of solid state properties on developability assessment of drug candidates," *Adv. Drug Deliv. Rev.*, vol. 56, no. 3, pp. 321–334, 2004.

[90] A. T. M. Serajuddin and C. I. Jarowski, "Effect of Diffusion Layer pH and Solubility on the Dissolution Rate of Pharmaceutical Acids and Their Sodium Salts II: Salicylic Acid, Theophylline, and Benzoic Acid," *J. Pharm. Sci.*, vol. 74, no. 2, pp. 148–154, Feb. 1985.

[91] A. T. M. Serajuddin and C. I. Jarowski, "Effect of Diffusion Layer pH and Solubility on the Dissolution Rate of Pharmaceutical Bases and their Hydrochloride Salts I: Phenazopyridine," *J. Pharm. Sci.*, vol. 74, no. 2, pp. 142–147, Feb. 1985.

[92] M. Brigante, G. Zanini, and M. Avena, "On the dissolution kinetics of humic acid particles. Effects of pH, temperature and Ca2+ concentration," *Colloids Surfaces A Physicochem. Eng. Asp.*, vol. 294, no. 1–3, pp. 64–70, 2007.

[93] M. Brigante, G. Zanini, and M. Avena, "Effect of pH, anions and cations on the dissolution kinetics of humic acid particles," *Colloids Surfaces A Physicochem. Eng. Asp.*, vol. 347, no. 1–3, pp. 180–186, 2009.

[94] P. Sway, G. Clarke, and S. Kazarian, "Application of FTIR Spectroscopic Imaging to Study the Effects of Modifying the pH Microenvironment on the Dissolution of Ibuprofen from HPMC Matrices," *J. Pharm. Sci.*, vol. 100, no. 11, pp. 4745–4755, 2011.

[95] D. E. Wurster and P. W. Taylor, "Dissolution kinetics of certain crystalline forms of prednisolone," *J. Pharm. Sci.*, vol. 54, no. 5, pp. 670–676, May 1965.

[96] A. W. Hixson and S. J. Baum, "Agitation. Mass Transfer Coefficients in Liquid-Solid Agitation Systems," *Ind. Eng. Chem.*, vol. 33, no. 4, pp. 478–485, 1941.

[97] A. W. Hixson and S. J. Baum, "Agitation. Performance of Propellers in Liquid-Solid Systems," *Ind. Eng. Chem.*, vol. 34, no. 1, pp. 120–125, 1942.

[98] K. G. Nelson and A. C. Shah, "Convective diffusion model for a transport-controlled dissolution rate process," *J. Pharm. Sci.*, vol. 64, no. 4, pp. 610–614, Apr. 1975.

[99] P. V. Pedersen and K. F. Brown, "Dissolution profile in relation to initial particle distribution," *J. Pharm. Sci.*, vol. 64, no. 7, pp. 1192–1195, Apr. 1975.

[100] J. Østergaard, F. Ye, J. Rantanen, A. Yaghmur, S. W. Larsen, C. Larsen, and H. Jensen, "Monitoring lidocaine single-crystal dissolution by ultraviolet imaging," *J. Pharm. Sci.*, vol. 100, no. 8, pp. 3405–3410, 2011.

[101] D. W. Readey and A. R. Copper, “Molecular diffusion with a moving boundary and spherical symmetry,” *Chem. Eng. Sci.*, vol. 21, no. 10, pp. 917–922, 1966.

[102] J. S. Vrentas and D. Shin, “Perturbation solutions of spherical moving boundary problems-I Slow growth or dissolution rates,” *Chem. Eng. Sci.*, vol. 35, no. 8, pp. 1687–1696, 1980.

[103] J. S. Vrentas and D. Shin, “Perturbation solutions of spherical moving boundary problems-II. Rapid growth or dissolution rates,” *Chem. Eng. Sci.*, vol. 35, no. 8, pp. 1697–1705, 1980.

[104] F. J. Vermolen and Mourik, “Analytical approach to particle dissolution in a finite medium: MST MST,” *S Mater. Sci. Technol. Apr*, vol. 13, no. 4, 1997.

[105] S. Prokop’ev, A. Okunev, and Y. Aristov, “A Monte Carlo Simulation of the Development of Surface Roughness and Its Effect on the Dissolution Kinetics of SiO2 Aerogels,” *Colloid J.*, vol. 64, no. 1, pp. 95–100, 2002.

[106] A. Mgaidi, F. Jendoubi, D. Oulahna, M. El Maaoui, and J. A. Dodds, “Kinetics of the dissolution of sand into alkaline solutions: Application of a modified shrinking core model,” *Hydrometallurgy*, vol. 71, no. 3–4, pp. 435–446, 2004.

[107] M. A. Ansari and F. Stepanek, “Design of granule structure: Computational methods and experimental realization,” *AIChE J.*, vol. 52, no. 11, pp. 3762–3774, Nov. 2006.

[108] Y. Wang, B. Abrahamsson, L. Lindfors, and J. G. Brasseur, “Analysis of Diffusion-Controlled Dissolution from Polydisperse Collections of Drug Particles with an Assessed Mathematical Model,” *J. Pharm. Sci.*, vol. 104, no. 9, pp. 2998–3017, 2015.

[109] V. G. Levich, *Physicochemical hydrodynamics*, 2nd ed. Englewood Cliffs, N.J.:

Prentice Hall, 1962.

[110] G. E. Hodges, E. K. Lowe, and A. H. J. Paterson, "A mathematical model for lactose dissolution," *Chem. Eng. J.*, vol. 53, pp. 25–33, 1993.

[111] E. K. Lowe and A. H. J. Paterson, "A Mathematical Model for Lactose Dissolution, Part II. Dissolution Below the Alpha Lactose Solubility Limit," *J. Food Eng.*, vol. 38, no. 5, pp. 15–2, 1998.

[112] T. Koiranen, T. Kilpiö, J. Nurmi, and H. V Nordén, "The modelling and simulation of dissolution of sucrose crystals," *J. Cryst. Growth*, vol. 198, pp. 749–753, 1999.

[113] F. Štěpánek and M. A. Ansari, "Computer simulation of granule microstructure formation," *Chem. Eng. Sci.*, vol. 60, no. 14, pp. 4019–4029, Jul. 2005.

[114] H. Cao, C. Amador, X. Jia, Y. Li, and Y. Ding, "A modelling framework for bulk particles dissolving in turbulent regime," *Chem. Eng. Res. Des.*, vol. 114, no. ii, pp. 108–118, 2016.

[115] D. Brooke, "Sieve Cuts as Monodisperse Powders in Dissolution Studies," *J. Pharm. Sci.*, vol. 64, no. 8, pp. 1409–1412, Apr. 1975.

[116] W. I. Higuchi, E. L. Rowe, and E. N. Hiestand, "Dissolution Rates of Finely Divided Drug Powders. II. Micronized methyl-prednisolone," *J. Pharm. Sci.*, vol. 52, no. 2, pp. 162–164, Apr. 1963.

[117] D. Brooke, "Dissolution Profile of Log-Normal Powders: Exact Expression," *J. Pharm. Sci.*, vol. 62, no. 5, pp. 795–798, Apr. 1973.

[118] D. Brooke, "Dissolution profile of log-normal powders II: Dissolution before critical time," *J. Pharm. Sci.*, vol. 63, no. 3, pp. 344–347, Sep. 1974.

[119] J. W. Mauger, S. A., Howard, and K. Amin, "Dissolution Profiles for Finely Divided Drug Suspensions," *J. Pharm. Sci.*, vol. 72, no. 2, pp. 190–193, Apr. 1983.

[120] L. P. De Almeida, S. Simões, P. Brito, A. Portugal, and M. Figueiredo, "Modeling dissolution of sparingly soluble multisized powders," *J. Pharm. Sci.*, vol. 86, no. 6, pp. 726–732, 1997.

[121] A. T. K. Lu, M. E. Frisella, and K. C. Johnson, "Dissolution Modeling: Factors Affecting the Dissolution Rates of Polydisperse Powders," *Pharm. Res. An Off. J. Am. Assoc. Pharm. Sci.*, vol. 10, no. 9, pp. 1308–1314, Sep. 1993.

[122] J. T. Carstensen and M. Dali, "Determination of mass transfer dissolution rate constants from critical time of dissolution of a powder sample," *Pharm. Dev. Technol.*, vol. 4, no. 1, 1999.

[123] A. Parker, F. Vigouroux, and W. F. Reed, "Dissolution of polymer powders," *Fluid Mech. Transp. Phenom.*, vol. 218, no. 7, pp. 1290–1299, 1999.

[124] E. Smulders, W. von Rybinski, E. Sung, W. Rähse, J. Steber, F. Wiebel, and A. Nordskog, "Laundry Detergents," in *Ullmann's Encyclopedia of Industrial Chemistry*, Wiley-VCH Verlag GmbH & Co. KGaA, 2000.

[125] U. Zoller, "HANDBOOK of DETERGENTS, Part E: Applications," *All-Purpose Cleaners their Formul.*, 2007.

[126] S. G. Kazarian and K. L. A. Chan, "'Chemical photography' of drug release," *Macromolecules*, 2003.

[127] K. L. A. Chan, S. V. Hammond, and S. G. Kazarian, "Applications of attenuated total reflection infrared spectroscopic imaging to pharmaceutical formulations," *Anal. Chem.*, 2003.

[128] J. van der Weerd, K. L. A. Chan, and S. G. Kazarian, "An innovative design of compaction cell for in situ FT-IR imaging of tablet dissolution," *Vib. Spectrosc.*, vol. 35, no. 1, pp. 9–13, 2004.

[129] J. van der Weerd and S. G. Kazarian, “Combined approach of FTIR imaging and conventional dissolution tests applied to drug release,” *J. Control. Release*, vol. 98, no. 2, pp. 295–305, 2004.

[130] S. G. Kazarian and J. Van Der Weerd, “Simultaneous FTIR spectroscopic imaging and visible photography to monitor tablet dissolution and drug release,” *Pharm. Res.*, 2008.

[131] P. Wray, K. L. A. Chan, J. Kimber, and S. G. Kazarian, “Compaction of pharmaceutical tablets with different polymer matrices studied by FTIR imaging and X-ray microtomography,” *J. Pharm. Sci.*, vol. 97, no. 10, pp. 4269–4277, Apr. 2008.

[132] P. Wray, J. Li, L. Q. Li, and S. G. Kazarian, “Combined study of biphasic and zero-order release formulations with dissolution tests and ATR-FTIR spectroscopic imaging,” *J. Pharm. Sci.*, vol. 103, no. 7, pp. 1995–2004, Apr. 2014.

[133] P. S. Wray, W. E. Sinclair, J. W. Jones, G. S. Clarke, and D. Both, “The use of in situ near infrared imaging and Raman mapping to study the disproportionation of a drug HCl salt during dissolution,” *Int. J. Pharm.*, vol. 493, no. 1, pp. 198–207, 2015.

[134] A. V. Ewing and S. G. Kazarian, “Recent advances in the applications of vibrational spectroscopic imaging and mapping to pharmaceutical formulations,” *Spectrochim. Acta - Part A Mol. Biomol. Spectrosc.*, vol. 197, pp. 10–29, 2017.

[135] K. Punčochová, A. V. Ewing, M. Gajdošová, T. Pekárek, J. Beránek, S. G. Kazarian, and F. Štěpánek, “The Combined Use of Imaging Approaches to Assess Drug Release from Multicomponent Solid Dispersions,” *Pharm. Res.*, vol. 34, no. 5, pp. 990–1001, 2017.

[136] B. Pan, R. Shen, Z. Guan, L. Dang, and H. Wei, "Insights into the dissolution mechanisms of detergent agglomerates: An approach to assess dissolution heterogeneity," *Adv. Powder Technol.*, vol. 28, no. 10, pp. 2658–2664, 2017.

[137] C. M. Riley, T. W. Rosanske, and S. R. R. Riley, *Specification of Drug Substances and Products*. Elsevier Ltd, 2013.

[138] PharmaTest, "PTWS 610 – USP / EP Tablet Dissolution Testing Instrument Vessel Centering System." pp. 1–8.

[139] I. Borst, S. Ugwu, and A. H. Beckett, "New and extended applications for USP drug release apparatus 3," *Dissolution Technol.*, vol. 4, no. 1, pp. 11–18, 1997.

[140] L. X. Yu, J. T. Wang, and A. S. Hussain, "Evaluation of USP apparatus 3 for dissolution testing of immediate-release products.," *AAPS PharmSci*, vol. 4, no. 1, p. E1, 2002.

[141] N. Fotaki, "Flow-through cell apparatus (USP Apparatus 4): Operation and features," *Dissolution Technol.*, vol. 18, no. 4, pp. 46–49, 2011.

[142] G. B. Crist, "Trends in Small-Volume Dissolution Apparatus for Low-Dose Compounds," *Dissolution Technol.*, vol. 16, no. 1, pp. 19–22, 2009.

[143] C. R. Gardner, C. T. Walsh, and Ö. Almarsson, "Drugs as materials: valuing physical form in drug discovery," vol. 3, p. 926, Nov. 2004.

[144] S. Emmanuel, L. Marc, B. Eric, and C. Jean-Michel, "Small volume dissolution testing as a powerful method during pharmaceutical development," *Pharmaceutics*, vol. 2, no. 4, pp. 351–363, 2010.

[145] S. Klein and V. P. Shah, "A Standardized Mini Paddle Apparatus as an Alternative to the Standard Paddle," *AAPS PharmSciTech*, vol. 9, no. 4, pp. 1179–1184, 2008.

[146] A. Avdeef, "Solubility of sparingly-soluble ionizable drugs," *Adv. Drug Deliv.*

Rev., vol. 59, no. 7, pp. 568–590, 2007.

[147] S. Almeida-Prieto, J. Blanco-Méndez, and F. J. Otero-Espinar, "Microscopic image analysis techniques for the morphological characterization of pharmaceutical particles: Influence of process variables," *J. Pharm. Sci.*, vol. 95, no. 2, pp. 348–357, 2006.

[148] N. Sandler, "Photometric imaging in particle size measurement and surface visualization," *Int. J. Pharm.*, vol. 417, no. 1–2, pp. 227–234, 2011.

[149] R. A. Carlton, *Pharmaceutical Microscopy*, 1st ed. New York, NY: Springer New York, 2011.

[150] M. Aulton and K. Taylor, *Aultons Pharmaceutics: The design and manufacture of medicines*, 4th ed. Elsevier Ltd, 2013.

[151] C. S. Handscomb, "Simulating Droplet Drying And Particle Formation in Spray Towers," *Thesis*, p. 237, 2008.

[152] K. Masters, *Spray drying handbook*, 5th ed. Longman Scientific & Technical, 1991.

[153] G. Akay, A. Paul, P. Robert, P. Corry, and J. W. H., "Detergent powders and process for preparing them," EP0534525A2, 1991.

[154] P. M. Desai, C. V. Liew, and P. W. S. Heng, "Review of Disintegrants and the Disintegration Phenomena," *J. Pharm. Sci.*, vol. 105, no. 9, pp. 2545–2555, 2016.

[155] W. F. Linke and A. Seidell, *Solubilities of Inorganic and Metal Organic Compounds*, 4th ed. van Nostrand, 1965.

[156] Sympatec GmbH, "QICPIC Dynamic Image Analysis-Particle Measurement," pp. 1–12.

[157] P. Webb, "An introduction to the physical characterization of materials by mercury

intrusion porosimetry with emphasis on reduction and presentation of experimental data," ... *Instrum. Corp, Norcross, Georg.*, no. January, 2001.

[158] D. H. Huntington, "The Influence of the Spray Drying Process on Product Properties," *Dry. Technol.*, vol. 22, no. 6, pp. 1261–1287, 2004.

[159] F. E. Baptan, E. Demiralp, Y. Y. Özbek, and F. Üstel, "The effect of binder on chemically precipitated hydroxyapatite during spray drying," *Mater. Tehnol.*, vol. 47, no. 3, pp. 303–306, 2013.

[160] P. A. Webb and C. Orr, *Analytical Methods in Fine Particle Technology*. Micromeritics Instrument Corporation, 1997.

[161] G. van Dalen, P. Nootenboom, and P. C. M. Heussen, "Correlative microscopy of detergent granules.," *J. Microsc.*, vol. 241, no. 3, pp. 273–81, Mar. 2011.

[162] X. Fu, M. Dutt, A. C. Bentham, B. C. Hancock, R. E. Cameron, and J. A. Elliott, "Investigation of particle packing in model pharmaceutical powders using X-ray microtomography and discrete element method," *Powder Technol.*, vol. 167, no. 3, pp. 134–140, 2006.

[163] R. Moreno-Atanasio, R. A. Williams, and X. Jia, "Combining X-ray microtomography with computer simulation for analysis of granular and porous materials," *Particuology*, vol. 8, no. 2, pp. 81–99, 2010.

[164] R. Mousavi, T. Miri, P. W. Cox, and P. J. Fryer, "A Novel Technique for Ice Crystal Visualization in Frozen Solids Using X-Ray Micro-Computed Tomography," *J. Food Sci.*, vol. 70, no. 7, pp. 437–442, 2005.

[165] I. C. Sinka, S. F. Burch, J. H. Tweed, and J. C. Cunningham, "Measurement of density variations in tablets using X-ray computed tomography," *Int. J. Pharm.*, vol. 271, no. 1–2, pp. 215–224, 2004.

[166] Skyscan NV, "NRecon User Manual," 2011.

[167] Bruker-MicroCT, "Introduction to porosity analysis Method note," *Method note*, no. June, pp. 1–17, 2014.

[168] W. Rasband and T. Ferreira, "ImageJ User Guide," *IJ 1.46r*, p. 187, 2003.

[169] A. D. Edelstein, M. A. Tsuchida, N. Amodaj, H. Pinkard, R. D. Vale, and N. Stuurman, "Advanced methods of microscope control using μManager software," *J. Biol. Methods*, vol. 1, no. 2, pp. 1–10, 2014.

[170] E. A. Gorrepati, P. Wongthahan, S. Raha, and H. S. Fogler, "Silica precipitation in acidic solutions: Mechanism, pH effect, and salt effect," *Langmuir*, vol. 26, no. 13, pp. 10467–10474, 2010.

[171] A. A. Hamouda and H. A. A. Amiri, "Factors affecting alkaline sodium silicate gelation for in-depth reservoir profile modification," *Energies*, vol. 7, no. 2, pp. 568–590, 2014.

[172] H. Yotsumoto and R. H. Yoon, "Application of Extended DLVO Theory: I, Stability of Rutile Suspensionsitle," *J. Colloid Interface Sci.*, vol. 157, pp. 426–433, 1993.

[173] H. Yotsumoto and R. H. Yoon, "Application of Extended DLVO Theory: II, Stability of Silica Suspensions," *J. Colloid Interface Sci.*, vol. 157, pp. 434–441, 1993.

[174] R. G. Horn, D. T. Smith, and W. Haller, "Surface forces and viscosity of water measured between silica sheets," *Chem. Phys. Lett.*, vol. 162, no. 4–5, pp. 404–408, 1989.

[175] V. Valmacco, M. Elzbieciak-Wodka, C. Besnard, P. Maroni, G. Trefalt, and M. Borkovec, "Dispersion Forces Acting between Silica Particles across Water:

Influence of Nanoscale Roughness," *Nanoscale Horiz.*, vol. 1, pp. 325–330, 2016.

[176] J. Israelachvili and H. Wennerström, "Role of hydration and water structure in biological and colloidal interactions," *Nature*, vol. 379, p. 219, Jan. 1996.

[177] A. Yokoyama, K. R. Srinivasan, and H. S. Fogler, "Stabilization mechanism by acidic polysaccharides. Effects of electrostatic interactions on stability and peptization," *Langmuir*, vol. 5, no. 2, pp. 534–538, Mar. 1989.

[178] E. Scheubel, "Predictive in vitro dissolution tools : application during formulation development," 2010.

[179] M. M. De Villiers, "Influence of agglomeration of cohesive particles on the dissolution behaviour of furosemide powder," *Int. J. Pharm.*, vol. 136, no. 1–2, pp. 175–179, 1996.

[180] E. Kaunisto, M. Marucci, and A. Axelsson, "Dissolution Kinetics or Pure Mass Transfer? A Mechanistic Study of Dissolution," 2010.

[181] P. Faldt, B. Bergenstahl, and G. Carlsson, "The Surface Coverage of Fat on Food Powders Analyzed by Esca (Electron Spectroscopy for Chemical Analysis)," *Food Struct.*, vol. 12, no. 12, pp. 225–234, 1993.

[182] S. Svanbäck, "Miniaturized single particle dissolution testing," University of Helsinki, 2013.

[183] A. I. Moshinskii, "Dissolution of a Polydisperse Ensemble of Particles in a Flow Apparatus," *Theor. Found. Chem. Eng. Transl. from Teor. Osn. Khimicheskoi Tekhnologii Orig. Russ. Text*, vol. 38, no. 4, pp. 375–385, 2004.

[184] B. V. Derjaguin and L. Landau, "Theory of the stability of strongly charged lyophobic sols and of the adhesion of strongly charged particles in solutions of electrolytes," *Acta Phys Chim URSS*, no. 14, pp. 633–662, 1941.

[185] E. J. W. Verwey and J. T. G. Overbeek, *Theory of the stability of lyophobic colloids*. New York: Elsevier Publishing Company Inc., 1948.

[186] E. Kaunisto, A. Rasmuson, J. Bergenholtz, J. Remmelgas, L. Lindfors, and S. Folestad, "Fundamental mechanisms for tablet dissolution: Simulation of particle deaggregation via brownian dynamics," *J. Pharm. Sci.*, vol. 102, no. 5, pp. 1569–1577, 2013.

[187] S. Buzzaccaro, E. Secchi, and R. Piazza, "Ghost Particle Velocimetry: Accurate 3D Flow Visualization Using Standard Lab Equipment," *Phys. Rev. Lett.*, vol. 111, no. 4, p. 48101, Jul. 2013.

[188] R. Cerbino and V. Trappe, "Differential Dynamic Microscopy: Probing Wave Vector Dependent Dynamics with a Microscope," *Phys. Rev. Lett.*, vol. 100, no. 18, p. 188102, May 2008.

[189] W. Thielicke and E. J. Stamhuis, "PIVlab – Towards User-friendly, Affordable and Accurate Digital Particle Image Velocimetry in MATLAB," *J. Open Res. Softw.*, vol. 2, 2014.

[190] P. Yu, Y. Zeng, T. S. Lee, X. B. Chen, and H. T. Low, "Numerical simulation on steady flow around and through a porous sphere," *Int. J. Heat Fluid Flow*, vol. 36, pp. 142–152, 2012.

[191] H. Darcy, *Recherches Experimentales Relatives au Mouvement de L'Eau dans les Tuyaux*. Paris: Mallet-Bachelier, 1857.

[192] J. Weisbach, *Lehrbuch der Ingenieur- und Maschinen-Mechanik*. Braunschweig, 1845.

[193] M. J. Fuerstman, A. Lai, M. E. Thurlow, S. S. Shevkoplyas, H. A. Stone, and G. M. Whitesides, "The pressure drop along rectangular microchannels containing

bubbles," *Lab Chip*, vol. 7, no. 11, p. 1479, 2007.

[194] C. J. Morris and F. K. Forster, "Oscillatory flow in microchannels: Comparison of exact and approximate impedance models with experiments," *Exp. Fluids*, vol. 36, no. 6, pp. 928–937, 2004.

[195] M. Akbari, D. Sinton, and M. Bahrami, "Pressure Drop in Rectangular Microchannels as Compared With Theory Based on Arbitrary Cross Section," *J. Fluids Eng.*, vol. 131, no. 4, p. 041202, 2009.

[196] B. R. Bird, W. E. Stewart, and E. N. Lightfoot, *Transport Phenomena*, 2nd Ed. New York, NY: John Wiley & Sons, Inc., 2002.

[197] A. Sinha, R. Ganguly, K. A. De, and K. I. Puri, "Single magnetic particle dynamics in a microchannel," *Phys. Fluids*, vol. 19, no. 11, 2007.

[198] P. W. Appel, "Modern methods of detergent manufacture," *J. Surfactants Deterg.*, vol. 3, no. 3, pp. 395–405, Jul. 2000.

[199] F. Štěpánek, "Effect of microstructure and pure component properties on the dissolution rate of a binary composite material," *Comput. Mater. Sci.*, vol. 44, no. 1, pp. 145–151, Nov. 2008.

[200] P. Costa and J. M. Sousa Lobo, "Modeling and comparison of dissolution profiles.," *Eur. J. Pharm. Sci.*, vol. 13, no. 2, pp. 123–33, May 2001.

[201] T. Ramcharan and A. Bissessur, "Analysis of Linear Alkylbenzene Sulfonate in Laundry Wastewater by HPLC-UV and UV-Vis Spectrophotometry," *J. Surfactants Deterg.*, vol. 19, no. 1, pp. 209–218, 2016.

APPENDIX A

Image Processing code

```
// Saves name+Part.jpg to the output directory:

//
==========================================================================
==========

    // Setup
    // =====
    //run("Set Measurements...", "area centroid  bounding shape feret's  redirect=None
decimal=2");          // No labels
    indir = getDirectory("Input: select a directory");
    list = getFileList(indir);
    outdir = getDirectory("Output: create or select a directory");
    //setBatchMode(true);
    start = getTime;

    // Loop over input images
    // ======================
    for (i=0; i<list.length; i++) {
        path = indir+list[i];
        open(path);

        id = getTitle();
        run("Duplicate...", "title=A");
        run("Duplicate...", "title=Open5");

                run("Gray Morphology", "radius=5 type=circle operator=open");
           setAutoThreshold("Default dark");
                //run("Threshold...");
                //setThreshold(98, 255);
                run("Convert to Mask");
                run("Invert");

                imageCalculator("Subtract create", "A","Open5");

        // save Particle
        dotIndex = lastIndexOf(id, ".");
        if (dotIndex!=-1)
            name = substring(id, 0, dotIndex);
        //saveAs("tiff", outdir+name+"Part.tif");
        saveAs("Jpeg", outdir+name+"Part.jpg");

                imageCalculator("Subtract create", "A","Open5");
                selectWindow("Result of A");
```

```
                rename("particle");

                imageCalculator("Subtract create", "A","particle");
                selectWindow("Result of A");
                rename("BubblesRemoved");
        // save BubblesRemoved
        dotIndex = lastIndexOf(id, ".");
        if (dotIndex!=-1)
             name = substring(id, 0, dotIndex);
        //saveAs("tiff", outdir+name+"Part.tif");
        saveAs("Jpeg", outdir+name+"BBL.jpg");

        // Clean Up
        // Close unneeded images
        while(nImages>0) {
            selectImage(nImages());
            run("Close");
        }

    }    // End looping over images

    if (isOpen("ROI Manager")) {
        selectWindow("ROI Manager");
        run("Close");
    }
    if (isOpen("Results")) {
        selectWindow("Results");
        run("Close");
    }

    print(list.length);
    print((getTime - start)/1000, " seconds");
    setBatchMode("exit and display");
    wait(5000);

    if (isOpen("Log")) {
        selectWindow("Log");
        run("Close");
    }


//

============================================================

==========

// end
```

APPENDIX B

Monte Carlo model

```
clear all

M_folder ='/Users/dxk499/Documents/MATLAB/Single to Bulk/Sample1';
% get distribution of particle sizes
P_size =
xlsread([M_folder,'/Sample1_ParticleSizeDistribution'],'psd','A2:A32')
;
freq   =
xlsread([M_folder,'/Sample1_ParticleSizeDistribution'],'psd','B2:B32')
;
%get mass data
Time = xlsread([M_folder,'/Sample1_Diffusion
dissolution'],'Mass','A2:A79');
Mass = xlsread([M_folder,'/Sample1_Diffusion
dissolution'],'Mass','B2:E79');
Size_m = xlsread([M_folder,'/Sample18_Diffusion
dissolution'],'Mass','B81:E81');

% set NaNs to max mass in experiment. i.e., once all mass is dissolved
it
% stays in solution
for ii = 1:numel(Size_m)
    Mass(isnan(Mass(:,ii)),ii)=max(Mass(:,ii));
end

% Cant have negative mass--Set mass to zeros for negatives
Mass(Mass<0)=0;

for ii =1:numel(Size_m)
M_frac(:,ii) = Mass(:,ii)./Mass(end,ii);
end

 [Size_unique idx_uni,idx_all] = unique(Size_m,'Stable');        %
stable prevents sorting by order

for ii =1 :numel(idx_uni)
        check_idx(:,ii) = (idx_all==ii);
end

Mi_dis = zeros(numel(Time),numel(P_size));
M_mean_frac = zeros(numel(Time),numel(Size_unique));

for ii = 1:numel(P_size)
    for jj = 1:numel(Time)
        M_mean_frac(jj,:)
=sum(M_frac(jj,:).*check_idx',2)./sum(M_frac(jj,:).*check_idx'>0,2);
        M_mean_frac(jj,isnan(M_mean_frac(jj,:)))=0;
        Mi_dis(jj,ii) =
interp1(Size_unique,M_mean_frac(jj,:),P_size(ii),'nearest','extrap');
    end
end

Mi_dis(Mi_dis<0)=0;
Mi_dis(Mi_dis>1)=1;
```

```
mass_per_size = freq/100;

mass_dist = mass_per_size'.*Mi_dis;
mass_dist_sum = sum(mass_dist,2);

figure(1)
plot(Time,mass_dist_sum)

% load bulk data
exp_t = xlsread([M_folder,'/Sample18_Bulk dissolution'],'A2:A156');
exp_data = xlsread([M_folder,'/Sample18_Bulk
dissolution'],'B2:B156')/100;

figure(1)
hold on
plot(exp_t,exp_data,'r')

ylabel('Fraction dissolved')
xlabel('Time [min]')
legend('Single to bulk','Experimental','Location','southeast')
title('Using all data points minus repeats + pchip')
set(gca,'Fontsize',12)

% get MSE
for ii = 1:numel(exp_t)
    [v idx(ii)] = min(abs(exp_t(ii)-Time));
end

% square diff
SSE = sum((exp_data-mass_dist_sum(idx)).^2);
MSE = SSE/numel(exp_t);
```

APPENDIX C

Manufacturing protocol of the microfluidic device

1. Mix PDMS (Sylgard 184, Dow Corning) with the cross-linking agent (ratio 10:1 w/w) and degas it.
2. Cast PDMS over the aluminium mould, cure for 2 days at room temperature.
    - this forms positive PDMS mould
3. Peel positive PDMS mould from aluminium mould, place in oven at 70C for 12hrs.
4. Wash positive PDMS mould thoroughly with isopropyl alcohol cleaning solvent (IPA) and warm DI water, then dry thoroughly.
5. Treat positive PDMS mould with 1 minute O_2 plasma.
6. Submerge positive PDMS mould in 5% PFOS in IPA solution for 1hr at room temperature.
7. Dry coating solution from positive PDMS mould (no rinsing).
8. Let positive PDMS mould surface treatment cure for 2 days at room temperature.
9. Cast PDMS over positive PDMS mould, cure for 2 days at room temperature.
    - this forms negative PDMS mould
10. Peel negative PDMS mould from positive PDMS mould.
    - if peeling is difficult, place a drop of ethanol between epoxy and PDMS
    - Prepare a flat substrate layer of epoxy inside a container, let it cure for 12 hours
    - see guideline below about forming thick layers
11. Pour epoxy over the negative PDMS mould, ensure that all channels are filled, and no bubbles are present.

12. Gently lower the cured epoxy substrate upside down onto the epoxy-covered negative PDMS mould, ensuring no bubbles form.
13. Flip the substrate, and negative PDMS mould up side up.
14. Fill the remainder of the container with epoxy so that the epoxy surface is flush with the PDMS surface.
    - see guideline below about forming thick layers
15. Leave to cure at room temperature for 36 hours.
16. Peel the negative PDMS mould from the epoxy - this leaves behind the positive epoxy mould.
    - if peeling is difficult, place a drop of ethanol between epoxy and PDMS
17. To make devices, pour PDMS over the positive epoxy mould, let it cure for 2 days at room temperature. The poured PDMS should be first mixed with its cross-linking agent (ratio 10:1 w/w) and degassed for about 30 minutes at 150 mbar to allow air bubbles to be removed.
18. Bind it to a thin layer of PDMS by exposing both surfaces to a corona discharge (ETP, USA). The corona discharge treatment is a surface modification technique that uses a low-temperature air plasma to change the properties of polymeric surfaces.

Notes about working with epoxy:

1. Never apply a vacuum to get rid of bubbles, it will just create more.
2. Avoid making layers more than ~ 2 mm thick in one casting. To make thick layers, cast 2 mm thickness, let cure for 12 hrs; repeat 2 mm at a time until desired thickness is reached.

Avoid placing epoxy moulds in the oven. This may warp them.